Title
Chemical Transformations of Nanocrystals: Theory and Molecular Simulation

Author
Frechette, Layne Braedon

Publication Date
2020

Peer reviewed|Thesis/dissertation

Chemical Transformations of Nanocrystals: Theory and Molecular Simulation

by

Layne B. Frechette

A dissertation submitted in partial satisfaction of the

requirements for the degree of

Doctor of Philosophy

in

Chemistry

in the

Graduate Division

of the

University of California, Berkeley

Committee in charge:

Professor Phillip L. Geissler, Chair
Professor Eran Rabani
Professor Kranthi K. Mandadapu

Spring 2020

Chemical Transformations of Nanocrystals: Theory and Molecular Simulation

Abstract

Chemical Transformations of Nanocrystals: Theory and Molecular Simulation

by

Layne B. Frechette

Doctor of Philosophy in Chemistry

University of California, Berkeley

Professor Phillip L. Geissler, Chair

Many of the intriguing optical, electronic, and mechanical properties of nanoparticles and their assemblies are strongly influenced by their size, shape, and composition. The range of different nanoparticles accessible by direct synthesis, however, is currently limited. Post-synthetic modification is thus an important avenue for chemists to tailor the properties of nanocrystals and to guide their assembly into functional materials. Yet, tuning such properties as nanocrystal shape and composition is often difficult because procedures for doing so take place far from equilibrium. In this thesis, we will discuss the progress we have made in understanding two such processes using statistical mechanical theory and computer simulation: (i) chemical etching, which produces concentration-dependent transformations of nanocrystal shape, and (ii) cation exchange, in which spontaneous swapping of ions of different identities effects compositional change.

For nanocrystal etching, we propose a simple kinetic model of etching which emphasizes the interplay between the concentration of etchant in the surrounding solution and the local energetics of the crystal surface. Monte Carlo simulations of this model reproduce experimentally observed etching trajectories over a broad range of parameters. We explain the observed transient nanocrystal shapes in terms of a balance between the external driving force for etching and the coordination number of nanocrystal surface atoms. Anisotropic particles such as nanorods present shape transformations which this kinetic model is unable to capture on its own. When we introduce additional kinetic moves which allow for mass transfer across the nanocrystal surface, we are able to capture nanorod shape transformations. Our microscopic explanation for this success invokes Ostwald ripening between distinct crystal facets on the nanoparticle surface.

For cation exchange, we develop an elastic Ising model which highlights the role of elastic strain due to lattice mismatch between different cation species. In its bulk incarnation, Monte Carlo simulations of this model reveal rich phase behavior featuring modulated order and surprising coexistence scenarios. These result from the extensive cost for coexistence between elastic phases. Based on this observation, we combine mean field theory with a modified Maxwell construction to predict a phase diagram which captures key features of

our simulations. If we switch to an ensemble where the net composition can fluctuate freely, the behavior of our model is vastly different. In lieu of modulated order, there is a single, mean-field critical point associated with spontaneous symmetry breaking of the net composition. We show that the long-ranged interactions responsible for this behavior arise naturally upon integrating out mechanical fluctuations. Mean field theory applied to the resulting effective Hamiltonian quantitatively captures both the thermodynamics and kinetics observed in Monte Carlo simulations. For nanocrystals, which break translational symmetry, a straightforward extension of mean field theory yields similarly accurate results. We further interrogate nanocrystal energetics by diagonalizing the nanocrystal effective Hamiltonian and its corresponding spin correlation function, revealing surface-localized soft modes. Detailed knowledge of nanocrystal energetics informs a nonequilibrium kinetic model for ion exchange focusing on surface exchange reactions and bulk diffusion of ions. Kinetic Monte Carlo simulations of this model for different choices of parameters reproduce a variety of nanocrystal morphologies seen in cation exchange experiments. Overall, our findings in this thesis demonstrate that the interplay between thermodynamics, kinetics, and geometry is key in determining the outcomes of nonequilibrium nanocrystal transformations.

To my family.

Contents

List of Figures

List of Tables

Acknowledgments

There are many people who shaped my graduate education and to whom I wish to express my gratitude.

Phill Geissler has been an excellent mentor to me. His passion for science and its communication, always on display in both the research and teaching we did together, has been inspiring. Phill taught me how crucial it is to be careful – to make sure that one fully understands a result, to do one last confirmatory calculation. Not only is it our moral duty as scientists to seek the closest approximation to the truth, but also we never know whether we might uncover something interesting and unexpected. Phill has trained me to approach science with precision and rigor, and with genuine curiosity. I am grateful to have worked closely with him over the past five years.

I have greatly benefitted from many interactions with members of the Geissler group, current and former. At the beginning of my Ph.D. I was lucky to have the guidance and friendship of Dayton Thorpe and Steve Cox. I'm especially thankful for their patience in teaching me about numerous different aspects of theoretical chemistry. I also have many fond memories from our daily lunches and the wide-ranging discussions we had there. Andreana Rosnik has been a supportive scientific big sister and friend throughout my Ph.D., from her role as my GSI in first semester stat mech, to her insights on lattice models, coding, and writing, to venting about the tough parts of grad school. Grant Rotskoff was a helpful colleague with whom I collaborated on my early work in the group and who challenged me to think more critically and to push myself harder. I have greatly enjoyed Jaffar Hasnain's enthusiasm and willingness to engage on a variety of topics. Nathan Odendahl has been an excellent coworker; I particularly appreciate his curiosity and willingness to ask questions (as well as his many puns.) Julia Rogers has been a very close friend and respected colleague. I greatly admire her persistence and attention to detail, and she has taught me a lot about science and how to give an outstanding presentation. My officemate and friend of two and a half years, Georg Menzl has been a kind and supportive figure. I am especially grateful for his camaraderie and the generous time he has given to talking both shop and about the state of the world.

My graduate work (and that of our entire group) would not have been possible without considerable logistic effort behind the scenes. I am very grateful to Lisa Littlejohn and Leslie Dietterick for all they have done – from making sure I got my paycheck on time, to coordinating conference travel, to making sure the office was well-stocked with supplies. I also appreciate having the chance to try out many of the (always excellent) outcomes of Leslie's baking experiments. Lisa will be missed – I will always remember her warmth and her protectiveness of us all.

I benefitted significantly from interactions with many other people in the Pitzer Center (both upper and lower.) I had the pleasure of collaborating with Eran Rabani early on in graduate school. His ideas and advice throughout my Ph.D. have been very valuable. I also had a number of enlightening and enjoyable conversations with both David Limmer and Kranthi Mandadapu. Moreover, I shared many lunches, drinks, and scientific chats with

various members of the Rabani, Limmer, and Mandadapu groups. Lyran Kidon in particular has been a great friend and colleague throughout my time at Berkeley. Her care and kindness did a lot to help make the Pitzer Center a good place to work.

Beyond the Pitzer Center, I had the opportunity to collaborate with Paul Alivisatos and his group. I had a lot of fun working with Matt Jones, Xingchen Ye, and Matt Hauwiller, whose hard work, positive attitude, and patience in walking me through their experiments were quite inspiring, especially in the early years of my Ph.D.

I would not have embarked on my Ph.D. were it not for the fantastic mentors I had as an undergraduate. Derek Stein was kind enough take me on as a novice student researcher. In his lab, Joe Bush taught me a lot about science and life, and gently steered me from experiment to theory. Rich Stratt trained me in theoretical chemistry, sharpened my scientific reasoning, and helped me build the foundation which has allowed me to be successful in graduate school. Vale Cofer-Shabica helped me immensely along the way. His continued friendship and caring have helped me get through grad school as well. I hope to share many more conversations and good times with him when I'm back on the East Coast.

To my union siblings in UAW 2865: working with you all has been one of the most meaningful aspects of my time in Berkeley. I'm so proud of all the work our union has done to improve the lives and strengthen the power of student-workers. I want to thank Val McGraw specifically for getting me involved.

Finally, my family – Dad, Mom, Tim, Gareth, Callean, Emily, Rachel, Grammie Maxine, Nana and George, Papa Arnold and Grammie Pat. Thanks for encouraging me, for coming out to visit, for understanding me being so far away for 5 years. I look forward to being closer to you all.

Chapter 1

Introduction

A central goal of materials science is to understand how to design materials with specific physical and chemical properties. Such knowledge would allow scientists and engineers to tailor novel materials to particular applications. Contemporary research in this field is increasingly focused on fulfilling this goal using nanoscale building blocks [117]. Nanoparticles, whose dimensions are barely larger than those of individual molecules, show significant promise as the ingredients of modern energy devices such as solar cells and LEDs, as well as for use as medical imaging tools [63]. The excitement over nanoparticles stems from their unique properties, which differ significantly from those of their macroscopic counterparts. Their miniscule size discourages the formation of structural defects which often plague bulk materials [3]. Nanoparticles also exhibit striking optical and electronic properties [63]. Perhaps the most famous illustration of this is the size-dependent light emission of CdS quantum dots [2]. This example highlights a crucial point: because nanoparticles are so small, their properties can be highly dependent on such features as their size and shape. Their small size means that a significant fraction of their constituent atoms lies at or near their surfaces, which experience environments quite different their interiors. Moreover, distinct nanoparticle shapes yield distinct arrangements of surface atoms. Such variations are often important in processes such as surface catalysis [68] and self-assembly [54]. Nanoparticles with heterogeneous compositions also exhibit distinct optical and electronic properties, and these properties often depend on the precise spatial arrangement of atoms of differing chemical identity [24].

The diversity of possible nanoparticles suggests the tunability of their properties, which makes them promising candidates for serving as the basis of custom-designed materials. However, much work remains to be done in understanding how to control such features as their shape and composition. A large part of what makes this task difficult is the fact that protocols for synthesizing and modifying nanoparticles typically operate far from equilibrium. The products of such procedures are thus usually not under thermodynamic control, but rather are heavily influenced by nonequilibrium kinetics. This renders simple thermodynamic models for transformation mechanisms suspect and forces scientists to instead confront the full, microscopic dynamics. While experimental techniques for monitoring nanoparticle

transformations continue to advance [122], their resolution remains far too low to reveal these atomic details in liquid environments which colloidal nanoparticles inhabit.[1] On the other hand, computer simulations can fully resolve the motions of individual atoms. They are limited instead by the computer time and memory required to obtain representative sampling on relevant physical time and length scales.

In this thesis, we use computer simulation and statistical mechanical theory to interrogate two transformations that significantly expand the diversity of synthetically accessible nanocrystals. The first – chemical etching – provides a way to alter the shape and size of nanocrystals. The second – cation exchange – offers an avenue to tune the composition of nanocrystals. We focus on the essential physical features of nanocrystals known to be important in these transformations. For etching, in which a metal nanocrystal is dissolved by oxidant molecules [121], the coordination and hence energetic stability of surface atoms ought to govern how easily they are stripped away. For cation exchange, in which the positively charged constituents of a semiconductor nanocrystal swap places with a different ionic species in the surrounding solution [108], the elastic strain associated with compositional defects is thought to significantly bias their spatial arrangement [102, 25]. Focusing on these aspects, we construct and study lattice models for both processes. By concentrating on simplified microscopic models, which intentionally omit what we expect (or hope) to be irrelevant features, we sacrifice some realism in exchange for the ability to thoroughly sample microscopic dynamics over long timescales. Such sampling is crucial for correctly capturing key features of reactions in these small and hence highly fluctuating systems.

This remainder of this thesis is organized as follows:

In chapter 2, we discuss our model for etching. Our collaborators have performed liquid cell TEM experiments to monitor the dissolution of gold nanocrystals [121, 52]. The nonequilibrium shape transformations which a nanocrystal undergoes depend both on the initial shape of the crystal and on the concentration of the oxidizing species. We construct a kinetic model for etching which accounts for the driving force for dissolution as well as the energetic stability associated with bonds between neighboring surface atoms. Monte Carlo simulations of this model reproduce the experimentally observed shape transformations quite well. Moreover, we are able to explain the shape transformations and their concentration-dependence microscopically, as a consequence of the balance between the magnitude of the driving force and the energy of nearest-neighbor contacts. An exception to this success occurs for nanorods. For these crystals, agreement with experiment is obtained only upon introduction of additional mechanisms of surface relaxation, namely mass transport of atoms across the crystal surface. Detailed inspection of the associated simulation trajectories suggests that altered shape transformations are largely a consequence of Ostwald ripening between different crystal facets.

Chapters 3-5 concern our elastic Ising model for ion exchange. In Chapter 3, we thoroughly investigate the bulk phase behavior of this model. Models which couple mechanical fluctuations to spin or composition variables have a rich history [4, 5, 36, 37, 79, 80]. We

[1] In vacuum, *in situ* TEM can directly reveal atomic dynamics: see, for example, [125].

build significantly upon extant work by using Monte Carlo simulations to survey phase behavior across a wide range of temperature and composition, revealing surprising coexistence scenarios. Specifically, we observe coexistence between phases without microscopic structure and phases with modulated order, but never coexistence between unstructured phases. We show that this is a consequence of the extensive energetic penalty for coexistence between elastic phases. By creating a graphical construction akin to the double-tangent construction of conventional thermodynamics, we fashion a mean-field phase diagram which captures the structures observed in our simulations. Such structures are strikingly absent when we switch ensembles in Chapter 4. Specifically, when the net composition is not held fixed but rather is allowed to fluctuate, Monte Carlo simulations of our model exhibit spontaneous symmetry breaking consistent with mean field universality. This behavior originates from long-ranged effective interactions, which we reveal by integrating out mechanical fluctuations of atoms about their lattice sites. Armed with this knowledge, we construct a mean field theory which quantitatively captures not only free energies and the critical temperature for spontaneous symmetry breaking, but also the dynamics of quenching and hysteresis. Having firmly established the behavior of our elastic Ising model in bulk, we turn to nanocrystals. A straightforward extension of mean field theory to incorporate spatial variations of the average composition allows us to accurately predict phase transitions in nanocrystals. In Chapter 5, we delve further into the energetics and dynamics of nanocrystals. Numerical energy minimization shows that compositional defects preferentially reside at the crystal surface rather than well within the interior. As a result, soft modes – which have very low or even zero energy – appear in the spectra of the nanocrystal effective potential and spatial correlation function. Turning to dynamics with these observations in mind, we propose a kinetic model for ion exchange reactions in which exchange events occur exclusively at the nanocrystal surface and diffusion transports different kinds of atoms throughout the crystal. Kinetic Monte Carlo simulations of this model exhibit patterns which resemble experimentally observed heterostructures, and which appear to be biased by bulk phase behavior. Notably, these nonequilibrium patterns are far different from nanocrystal configurations that minimize free energy.

Chapter 2

Etching: A Nonequilibrium Route to New Nanocrystal Shapes

The work described here draws significantly from *Science* 354 (6314), 874-877 [121]. Reprinted with permission from AAAS. The work is also reproduced in part from *Nano Letters* 18 (9), 5731-5737 [52].

2.1 Introduction

Understanding nanoparticle dynamics and reactivity remains a major challenge in physical chemistry. Recently, Alivisatos and co-workers developed a novel technique – liquid cell TEM (transmission electron microscopy) – for imaging nanoscale reactions in liquid environments in real time [122]. As in conventional TEM, the sample is imaged via irradiation with an electron beam. What makes the technique novel is the ability to sample liquid phase environments, an advancement made possible by "sandwiching" the sample and its liquid environment between two graphene sheets. This has allowed the real-time imaging of such fundamental phenomena as nanoparticle nucleation and growth and inter-nanoparticle interactions [122, 93, 19]. Although such studies provide a new window into nanoscale transformations, they still do not operate at a sufficiently high resolution to fully unveil microscopic details. Theory and computer simulation can give additional microscopic insights into such processes that are unavailable even with the most advanced imaging techniques.

In this chapter, we show how theory and computer simulation of simple models shed light on the mechanisms of nanocrystal dissolution. This process can be initiated and observed directly in a liquid cell TEM setup. The liquid cell sample consists of an aqueous solution of ligand-coated gold nanoparticles as well as the compound $FeCl_3$. Interaction between the electron beam and $FeCl_3$ leads to the creation of hydroxyl radical species, which oxidize gold atoms, initiating dissolution or "etching" of the nanocrystals (see Fig. 2.1). In dissolution trajectories observed with TEM, nanocrystals transform from their initial shapes into distinct "transient intermediate" shapes which persist while the nanocrystals shrink. At very

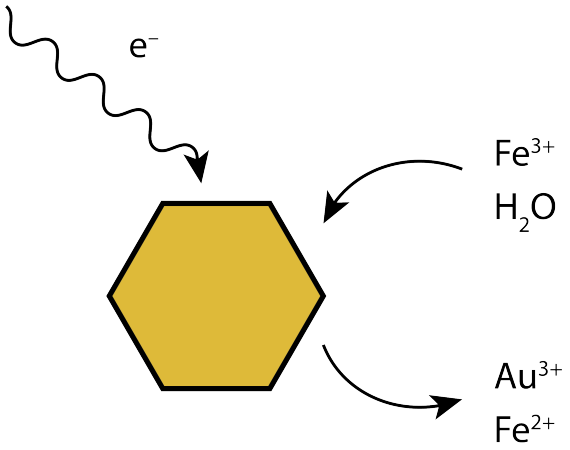

Figure 2.1: Schematic of the electron beam-initiated oxidation reaction.

low etchant concentrations, nanocrystals tend towards a truncated octahedron (TO) shape, while at elevated concentrations the dominant shape motif is that of a tetrahexahedron (THH); see Ref. [121]. Notably, the precise intermediate shape depends both on the etchant concentration and on the initial shape of the nanoparticle.

We explain these shape transformations via a simple microscopic lattice model which takes into account the nanocrystal lattice geometry, local atomic coordination, and the driving force for etching. Monte Carlo (MC) simulations of this model reproduce the experimentally observed shape changes over a broad range of concentrations. These shape changes can be explained as a straightforward consequence of the interplay between local crystal geometry and nonequilibrium kinetics. Faithfully capturing the etching dynamics of anisotropic shapes such as nanorods appears to require the introduction of additional mechanisms of surface relaxation which compete with etching. Our results demonstrate how simple physical models can yield mechanistic insights into what appear to be complex nanoscale dynamics.

2.2 Kinetic Model of Etching

Our model for nanocrystal etching resolves only the collection C of FCC lattice sites that are occupied by gold atoms at a given time. This list changes as a result of stochastic microscopic events whose rate constants we prescribe.

The dynamics of an atom detaching from the surface of a nanoparticle is shaped by many factors: the local surface structure, presence and arrangement of passivating ligand molecules, and the spatial distribution of oxidizing species, among others. We focus exclusively on the expectation that more highly coordinated atoms face higher energetic barriers to detachment, and are therefore etched less rapidly. Specifically, the removal rate constant

$k(n)$ of a particular surface atom is taken to depend only on the number n of its nearest-neighbor lattice sites that are occupied.

Many features of the resulting etching trajectories are insensitive to the precise form of $k(n)$, requiring only that it declines sharply with n for highly coordinated sites. The particular form we choose follows from a simple kinetic description of the association between oxidizing species in solution and the nanoparticle surface: oxidants bind to a given surface atom with rate constant k_{on}; upon binding, a surface atom (denoted Au) becomes activated for etching. The activated surface atom (denoted Au^*) may either deactivate (through unbinding of the oxidant, which occurs with rate constant k_{off}) or detach from the nanoparticle with rate constant k_{detach}, as represented in the chemical equation:

$$\text{Au} \underset{k_{\text{off}}}{\overset{k_{\text{on}}}{\rightleftharpoons}} \text{Au}^* \xrightarrow{k_{\text{detach}}} \emptyset.$$

The resulting rate of detachment, $r = k_{\text{detach}} p(\text{Au}^*)$, thus depends on the probability $p(\text{Au}^*)$ that the atom is activated. The quantity $p(\text{Au}^*)$ is generally time-dependent; for simplicity, we employ a steady-state approximation $dp(\text{Au}^*)/dt \approx 0$, which leads to:

$$k_{\text{on}} p(\text{Au}) - (k_{\text{off}} + k_{\text{detach}}) p(\text{Au}^*) \approx 0, \tag{2.1}$$

yielding a effective rate constant for etching $k = r/p(\text{Au})$,

$$k = \frac{k_{\text{on}}}{1 + k_{\text{off}}/k_{\text{detach}}}. \tag{2.2}$$

Surface atoms that detach readily once activated (relative to the rate of oxidant unbinding) thus etch at essentially the same rate, i.e., oxidant binding is the rate-limiting step. Sites that detach slowly even when activated etch at much lower rates.

We take an Arrhenius form for detachment kinetics,

$$k_{\text{detach}}(n) = k_0 e^{-\beta \epsilon n}, \tag{2.3}$$

with an energetic barrier that grows linearly with coordination number n, where the inverse temperature is $\beta = 1/k_B T$ (k_B is Boltzmann's constant). Assuming k_{off} to be independent of n, and defining parameters μ and n^* through:

$$e^{\beta \mu} = k_{\text{off}}/k_0 \tag{2.4}$$

$$\mu = -n^* \epsilon, \tag{2.5}$$

we finally have:

$$k(n) = \frac{k_{\text{on}}}{1 + e^{\beta \epsilon (n - n^*)}}, \tag{2.6}$$

or equivalently,

$$k(n) = \frac{k_{\text{on}}}{1 + e^{\beta (\epsilon n + \mu)}}. \tag{2.7}$$

We anticipate that reaction barriers are high, $\beta\epsilon \gg 1$, so that the Fermi function form of Eq. 2.6 implies:

$$k(n) \approx k_{\text{on}}, \qquad n < n^* \tag{2.8}$$

$$k(n) \approx k_{\text{on}} e^{-\beta\epsilon(n-n^*)}, \; n > n^*. \tag{2.9}$$

The second expression for the effective etching rate, Eq. 2.7, highlights an isomorphism between our kinetic model and Monte Carlo sampling of a classic statistical mechanics model for phase separation, namely the lattice gas [18].

We generated a collection of stochastic etching trajectories for several different values of n^* using the Gillespie algorithm [41] for kinetic Monte Carlo sampling with the rates given in Eq. 2.6. We obtain essentially indistinguishable results using a discrete-time Monte Carlo scheme based on the aforementioned lattice gas analogy (an explicit comparison between these two methods for $n^* = 6.5$ is shown in Appendix A.1.) The latter approach offers significant practical advantages when the model is elaborated to describe surface diffusion. For this reason, most of the trajectories we report (except where noted) were generated with lattice gas Monte Carlo methods, which we detail below.

2.3 Lattice Gas Monte Carlo

The dynamical variables of a lattice gas specify the presence ($\rho_i = 1$) or absence ($\rho_i = 0$) of material at each of a collection of lattice sites i. Their equilibrium fluctuations in a grand canonical ensemble are governed by a distribution of $C = \{\rho_1, \rho_2, ...\}$ given by:

$$P(C) \propto e^{-\beta\mathcal{H}}, \tag{2.10}$$

with the Hamiltonian

$$\mathcal{H} = -\mu \sum_i \rho_i - \epsilon \sum_{\langle i,j \rangle} \rho_i \rho_j, \tag{2.11}$$

where μ is an externally imposed chemical potential. The second summation in $\mathcal{H}$ includes all distinct pairs of nearest neighbor lattice sites, which contribute an attractive energy $-\epsilon$ when both are occupied.[1]

The simplest Monte Carlo scheme for sampling the distribution Eq. 2.10 would (i) select a lattice site i at random, (ii) attempt to change its occupation state $\rho_i \to 1 - \rho_i$ and (iii) accept the change with probability $A(C \to C')$, where C and C' are the states of the system before and after the proposed change. Any choice of A that satisfies detailed balance suffices for this purpose. The Glauber acceptance probability [43]:

$$A(C \to C') = \frac{1}{1 + e^{\beta(\mathcal{H}(C') - \mathcal{H}(C))}} \tag{2.12}$$

[1] More realistic interaction potentials for gold exist and have a more complex structure [83, 105]; however the excellent agreement between our results and experiment indicate our simple Hamiltonian suffices.

is a common choice, particularly when trajectories are given a dynamical interpretation (associating a small time interval with each MC step). If the configurational distribution changes smoothly in time, then this discrete-time scheme is equivalent to a continuous-time kinetics with transition rates:

$$k(C \to C') = w_0 A(C \to C'), \tag{2.13}$$

where w_0 is a constant with units of inverse time. In the particular case of a deletion move, which takes $\rho_i = 1$ to $\rho_i = 0$, this rate becomes:

$$k(C \to C') = \frac{w_0}{1 + e^{\beta(\epsilon n + \mu)}}, \tag{2.14}$$

where n is the coordination number of site i in configuration C. This rate corresponds precisely to the etching rate $k(n)$ described in the previous section, establishing an equivalence between our kinetic model of nanocrystal etching and the deletion moves of a discrete-time grand canonical Glauber Monte Carlo sampling. (In the limit $\beta\epsilon \gg 1$ of Eqs. 2.8 and 2.9, the rate takes the form of Metropolis dynamics [114]; see Appendix A.1 for a comparison with Glauber dynamics.) In light of this equivalence, we interpret the chemical potential $\mu = -\epsilon n^*$ as a proxy for the driving force for etching. While it could be related in a complicated way to such underlying factors as etchant concentration and the electron beam strength, we treat it as an effective parameter that determines which coordination-number-dependent etching events are facile.

The precise lattice gas sampling scheme sketched above is not well-suited for etching trajectories, since for a given configuration only a small fraction of lattice sites – those at the nanocrystal surface – participate in etching reactions. We therefore propose Monte Carlo moves that attempt only to modify the occupation state of interfacial lattice sites. For deletion moves, the number of such changeable sites is $N_{\text{surf}}(C)$, i.e., the number of atoms that are incompletely coordinated. For insertion moves, the number of changeable sites is instead the number $N_{\text{vac}}(C)$ of vacancies that are adjacent to occupied sites (though in the strongly non-equilibrium etching regime, the probabilities of insertion moves are so small that these moves are insignificant.)

Our primary scheme for simulating the etching of a nanoparticle is thus as follows:

1. Determine whether to attempt deleting an atom or inserting an atom, with probability 1/2 for either move.

2. If attempting insertion, select one vacancy j at random from the $N_{\text{vac}}(C)$ vacancies associated with the configuration. Then, accept the "trial move" of changing the current configuration C into another configuration C' by changing $\rho_j = 0$ to $\rho_j = 1$ with probability:

$$A_{\text{insert}}(C \to C') = \frac{1}{1 + (f(C, C'))^{-1}} \tag{2.15}$$

where:

$$f(C, C') = \frac{N_{\text{vac}}(C)}{N_{\text{surf}}(C')} e^{-\beta \Delta \mathcal{H}} \tag{2.16}$$

$$\Delta \mathcal{H} = \mathcal{H}(C') - \mathcal{H}(C) = -\mu - \epsilon n. \tag{2.17}$$

The ratio of Ns in the function f preserves detailed balance (see Appendix A.2).

If attempting deletion, select one atom j at random from the $N_{\text{surf}}(C)$ atoms associated with the configuration. Then, accept the trial move $C \to C'$ by changing $\rho_j = 1$ to $\rho_j = 0$ with probability:

$$A_{\text{delete}}(C \to C') = \frac{1}{1 + (g(C, C'))^{-1}}, \tag{2.18}$$

where:

$$g(C, C') = \frac{N_{\text{surf}}(C)}{N_{\text{vac}}(C')} e^{-\beta \Delta \mathcal{H}}, \tag{2.19}$$

$$\Delta \mathcal{H} = \mathcal{H}(C') - \mathcal{H}(C) = \mu + \epsilon n. \tag{2.20}$$

3. Repeat until the nanoparticle has been fully etched – i.e., no atoms remain.

This scheme saves us significant computational expense and allows us to simulate large systems consisting of tens of millions of sites. We note that as a consequence of this choice of dynamics, the ensemble we consider only includes configurations in which a single interface separates occupied from unoccupied regions of the lattice.

In all simulations, the temperature was set to $k_B T = 0.0259$eV (corresponding to room temperature,) and the bond energy ϵ was set to 0.3275eV, one-twelfth the bulk sublimation energy of gold [23], so that $\beta\epsilon \approx 12.6$. [2]

2.4 Simulations of Nanocrystal Shape Change

Despite its simplicity, our model produces a THH intermediate from an initially cube-shaped nanoparticle for a relatively wide range of chemical potentials, $-8 < \mu/\epsilon < -6$. In the language of the kinetic model, this corresponds to etching rates for which $6 < n^* < 8$. In Fig. 2.2 we show experimental and simulation (using $\mu/\epsilon = -6.5$) trajectories. The nonequilibrium THH structure is thus unlikely to be a consequence of the electron beam, the particular oxidation chemistry employed in the liquid cell, or the presence of surface-bound ligands, because these effects are not explicitly considered in our simulations. When

[2] While the solution-phase environment likely has a significant influence on the thermodynamics of surface atom removal and hence on the value of ϵ, we anticipate reaction barriers will still be high relative to $k_B T$, and so the precise value of ϵ should not have a significant impact on our conclusions. Simulations performed with different values of $\beta\epsilon$ support this assertion.

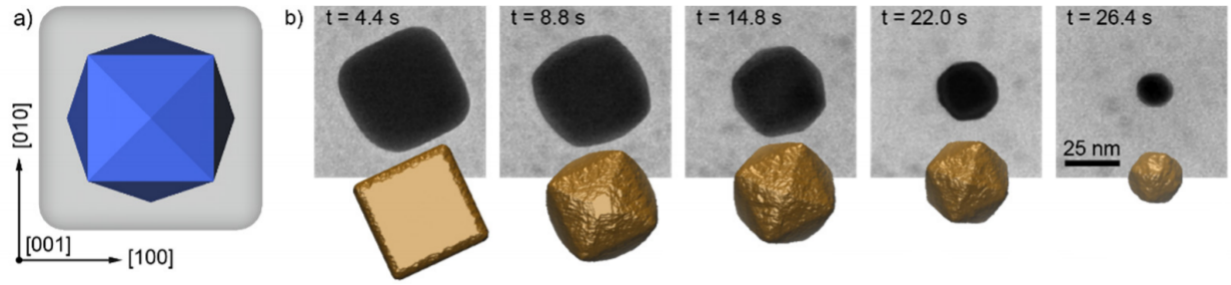

Figure 2.2: **a**: Idealized THH shape, viewed along the [001] axis. **b**: Snapshots from nonequilibrium etching trajectories from experiment (top) and simulation (bottom.) Etching simulation was performed on an initially cubic $\approx$ 7-million atom nanoparticle with $\mu/\epsilon = -6.5$.

the driving force for oxidation is reduced in experiments, cubes transform into truncated octahedra [121], the shape predicted by the Wulff construction for an FCC lattice [119, 56, 120, 74]. This same equilibrium transformation is observed in simulations near $\mu/\epsilon = -6$ or when additional mechanisms of surface relaxation are introduced (see Section 2.5.).

Mechanism of THH Formation

The formation of a THH intermediate is driven by the interplay between the value of the driving force μ and the coordination number of surface sites. Specifically, the value of μ (or $n^* = -\mu/\epsilon$) determines which atoms are etched quickly and which are not. Surface atoms with $n < n^*$ all etch at approximately the same (rapid) rate k_{on}, while those with $n > n^*$ etch much more slowly, with a rate which becomes exponentially smaller with n (see Eqs. 2.8 and 2.9.) For example, when $\mu/\epsilon = -6.5$, $n^* = 6.5$, atoms with $n \leq 6$ are all etched with rate $\approx k_{on}$, while those with $n > 6$ etch only very slowly. The formation of a THH intermediate thus appears to be contingent on the rapid removal of surface atoms with $n = 6$. This can be understood by examining the geometry of an idealized nanocrystal surface (see Fig. 2.3). A perfect cube-shaped FCC crystal is bound by {100} facets consisting of atoms with $n = 8$ (see Appendix A.3 for a description of different facets). Atoms on the edges adjoining such facets have coordination number $n = 5$, while those on the corners have $n = 3$. Removal of all atoms with $n \leq 6$ reveals new edges with coordination $n = 6$ (see Fig. 2.3). Another removal of all atoms with $n \leq 6$ exposes additional $n = 6$ surface atoms on the perimeter of the {100} facets as well as another $n = 6$ edge on the layer of atoms just beneath the receding top layer on each face of the cube (see Fig. 2.3). Clearly, repetition of this procedure will lead to a "train" of receding stepped "terraces," a mechanism which we have called "step-recession" by analogy to the well-known inverse process of step-flow [12, 64]. Continued step-recession creates square pyramid-shaped features on each side of the shrinking cube – which constitutes the THH shape. Once this shape is attained, additional etching serves mainly to reduce the size of the THH rather than change its shape. The

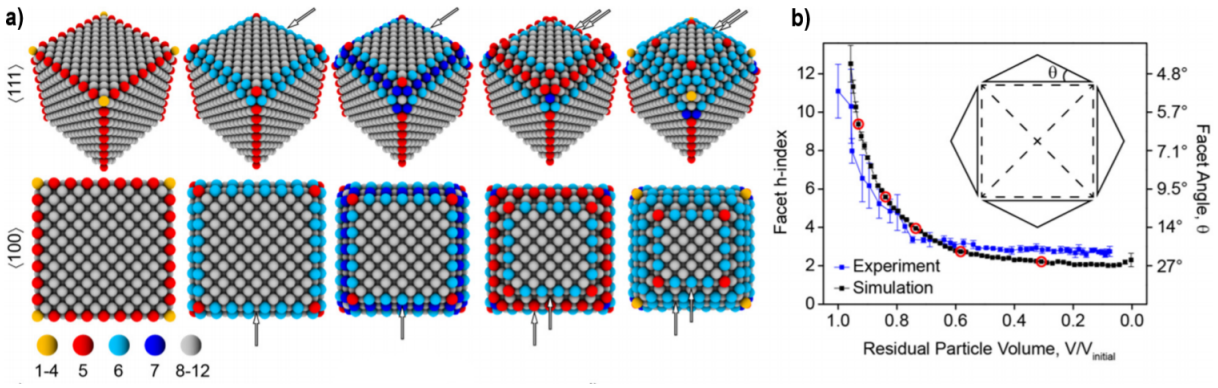

(a)

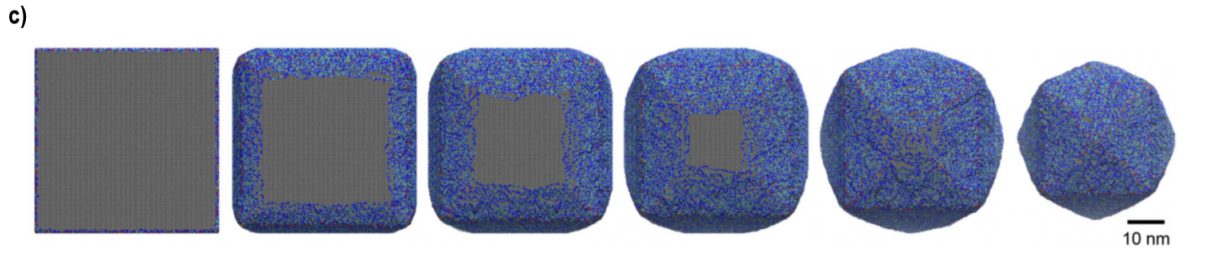

(b)

Figure 2.3: **a**: Idealized model of the first few steps of cubic nanoparticle etching, with atoms colored according to their coordination number n, viewed along two different directions. Arrows guide the eye to where etching is taking place. **b**: h-index (proportional to facet angle) over the course of a trajectory, as monitored by fraction of initial volume remaining. Schematic shows how the facet angle is defined. Simulation result is averaged over each of 24 possible angles (see Appendix A.4 for details.) **c**: Snapshots from a simulation etching trajectory of an initially $\approx$ 7-million atom nanoparticle with $\mu/\epsilon = -6.5$. Atoms are colored as in the idealized etching steps in **a**; snapshots are taken at remaining volumes corresponding to the red circles in **b**.

THH shape might thus be thought of as a kind of transient "steady state." Although the stochasticity of our MC simulations prevents the steps from being atomically flat as they are in the idealized etching scenario, the sequence of shape changes we observe in simulations is largely consistent with the step-recession mechanism (see Fig. 2.3).

The THH is further characterized by the angle θ of each of its pyramidal features with respect to the $\{100\}$ plane. At an atomic level, this angle is determined by the ratio of step height to terrace width in the step train. Equivalently, one could describe the faces of the pyramid as "vicinal" $\{hk0\}$ facets, where $h > k$ and:

$$\cos\theta = \frac{h}{\sqrt{h^2 + k^2}}. \tag{2.21}$$

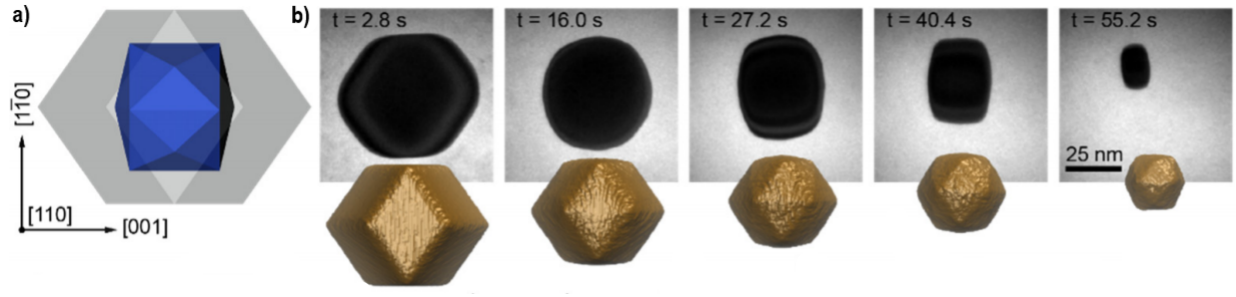

Figure 2.4: **a**: Idealized THH shape, viewed along the [110] axis. **b**: Snapshots from nonequilibrium etching trajectories from experiment (top) and simulation (bottom.) Etching simulation was performed on an initially $\approx$ 7-million atom RDD nanoparticle with $\mu/\epsilon = -6.5$.

Assuming facets with $k = 1$, we measured the quantity h (which we henceforth refer to as the "h index;" see Appendix A.4 for the details of its calculation) as a function of remaining nanoparticle mass (a proxy for time) in our simulations and compared the result to that of experiment. The general shapes of the curves are very similar, and they are quantitatively in fairly good agreement. (That the "asymptotic" value of the h index is slightly higher in experiment than in simulation may have to do with etchant concentration; see following section.)

We also performed simulations of nanocrystals initially in the shape of rhombic dodecahedra (RDD). At a chemical potential $\mu/\epsilon = -6.5$, the RDD etched into a transient THH intermediate, just like the cube. Configurations along etching trajectories (viewed along the [110] axis) are very similar between experiment and simulation (see Fig. 2.4). The h index trajectory is also qualitatively very similar to that of experiment (see Fig. 2.5). However, while the experimental results show an asymptotic value of $h \approx 3$, simulations show $h \approx 2$ for the THH and RDD. This suggests that additional factors that are not considered in simulations (e.g., ligand binding to the larger {100} terrace area of {310} facets [121]) may be important in dictating the precise facet morphology. Nonetheless, the THH transient intermediate appears to be a common motif for etching FCC nanocrystals.

Dependence of Transient Intermediates on Concentration

The precise shape of the transient intermediate depends on oxidant concentration. As noted previously, for small enough concentrations, nanocrystals initially shaped like cubes and RDD transform to their equilibrium, TO shape in experiments. In simulations, at $\mu/\epsilon = -6$,[3] the FCC lattice gas exhibits coexistence between macroscopic high-density and low-density phases, so that the crystal surfaces can relax substantially on the time scale of growth or

[3]The classic lattice gas model exhibits coexistence between macroscopic high-density and low-density phases at a chemical potential $\mu/\epsilon = -Z/2$, where Z is the coordination number of the bulk lattice [18]. For the FCC lattice, $Z = 12$.

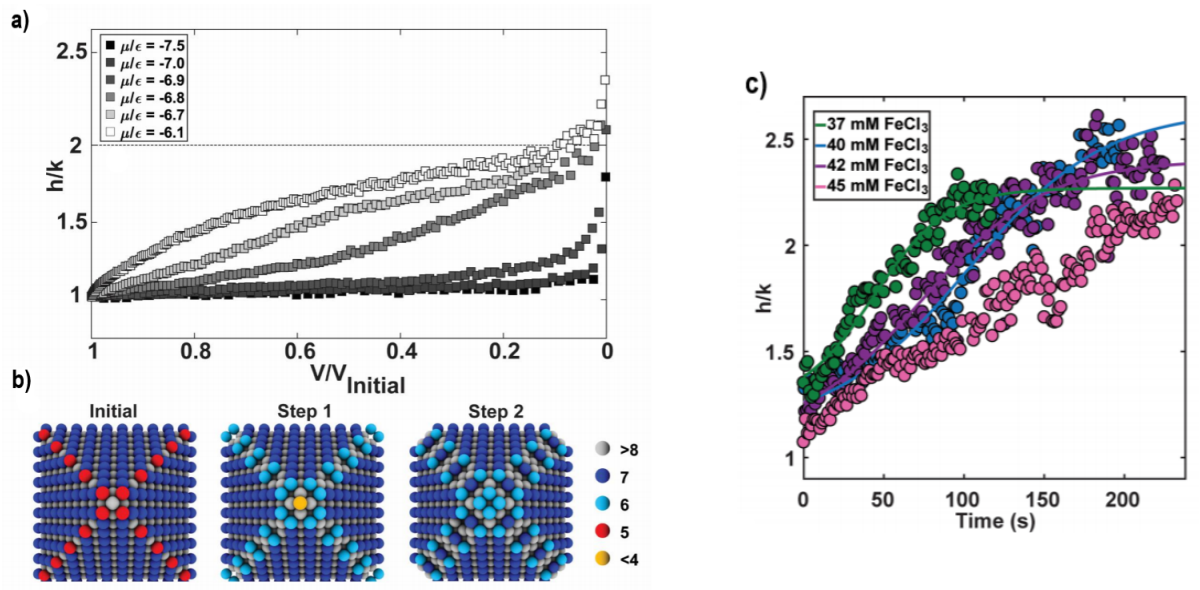

Figure 2.5: **a**: h-index versus remaining nanoparticle volume computed from simulations of $\approx$ 7-million atom RDD nanoparticles at different values of μ/ϵ. **b**: Idealized model of the first few steps of RDD nanoparticle etching, with atoms colored according to their coordination number n, viewed along the [100] axis. **c**: h-index versus time for RDD nanoparticles etched in experiments, for different concentrations.

etching. We find that the equilibrium truncated octahedron emerges in etching simulations at a value of μ/ϵ slightly above coexistence, e.g. $\mu/\epsilon = -5.98$. For significantly higher values than this (around $\mu/\epsilon = -5.9$ and above), the shape evolution is instead dominated by growth of the nanoparticle. Precisely at $\mu/\epsilon = -6$, any finite initial structure constitutes a sub-critical nucleus, which dissolves as a consequence of interfacial tension on time scales that hinder surface relaxation [91]. (See Fig. 2.7 for snapshots at each of these conditions.) We also observe this shape when alternative mechanisms of surface relaxation are introduced (see subsequent section.)

At elevated concentrations the THH is the dominant motif, but the h index which characterizes its pyramidal faces depends on the precise value of the concentration. In experiments [52], exposing cubes to higher oxidant concentrations produces transient THH shapes with higher values of h ("shorter" pyramids). At the highest concentrations, cubes simply shrink, maintaining their shape. RDD, on the other hand, exhibit THH intermediates whose h index is less sensitive to concentration. Like the cube, though, at the highest concentrations the RDD simply shrinks while retaining its shape. These observations can be understood, again, by considering the coordination of surface atoms.

As the cube etches, stochastic etching events on the {100} terraces reveal $n = 7$ surface atoms. For $\mu/\epsilon = -6.5$ these atoms are essentially inaccessible to etchant, but for $\mu/\epsilon = -7$

they are somewhat labile (though they etch less rapidly than $n = 6$ atoms). For an even higher value of $\mu/\epsilon = -7.5$, atoms with $n = 7$ are readily etched. The fact that a higher number of exposed atoms are rapidly etched leads to higher values of h, as well as rougher steps (see Fig. 2.6). For $\mu/\epsilon \leq -8$, even $n = 8$ atoms etch at an appreciable rate. In that case, all atoms on the {100} facets etch at similar rates, causing the cube shape to be maintained as the nanocrystal shrinks (see Fig. 2.7).

To understand the concentration-dependence of RDD etching, note that the RDD surface consists entirely of {110} facets. These facets contain surface atoms with $n = 7$ and $n = 11$, and the edges separating these facets consist of $n = 5$ atoms. For $-7 < \mu/\epsilon < -6$, these $n = 5$ atoms are readily removed, exposing rows of $n = 6$ surface atoms which are also readily etched (see Fig. 2.5). Continued step-recession from the edges leads to the observed THH shape. The trajectory of the h index does depend on the exact value of μ in this regime, but the asymptotic value of h appears to be 2. (Occasionally, thermal fluctuations will cause one of the $n = 7$ surface atoms to be removed, exposing two $n = 6$ atoms which readily etch and lead to the entire row of atoms receding, somewhat akin to snapping a rubber band; see Fig. 2.8.) For $\mu/\epsilon \leq -7$, the $n = 7$ atoms which comprise much of the exposed {110} surfaces etch approximately as readily as atoms with $n \leq 6$, leading to a preservation of the RDD shape (reflected in the constant h value of 1,) much like the situation for the cube for $\mu/\epsilon \leq -8$.

2.5 Surface Relaxation

In the lattice gas scheme described previously, the equilibrium truncated octahedron shape is obtained only when the rate of insertion of atoms is approximately equal to the rate of deletion of atoms, which occurs within a narrow range of chemical potential. By contrast, in experiments the equilibrium shape is observed under a wider range of driving forces. This indicates that the dominant mechanism of surface relaxation may not be insertion moves as controlled by a chemical potential, but rather surface diffusion mediated by ligands and/or etchant. (In the absence of oxidizing conditions, surface diffusion on a nanoparticle is very slow) [103]. We therefore also performed simulations where we attempted to relax nanoparticles via such diffusion moves.

Monte Carlo Moves

Diffusive surface relaxation moves consisted of attempts to swap the positions of randomly selected surface atoms and randomly selected surface vacancies; alternative surface relaxation moves are considered in Appendix A.5. For such moves the acceptance probability is given by:

$$A(C \to C') = \frac{1}{1 + (d(C, C'))^{-1}}, \tag{2.22}$$

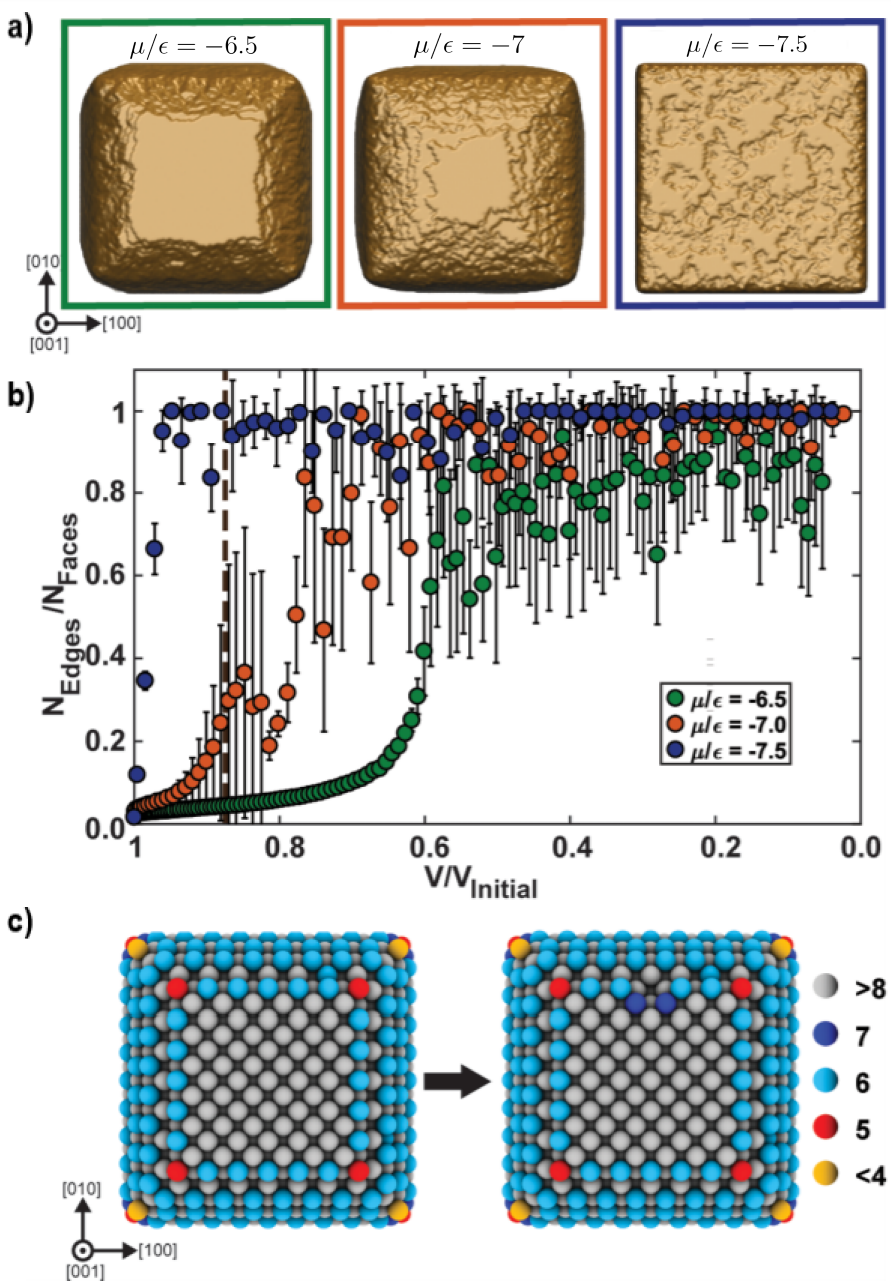

Figure 2.6: **a**: Snapshots of the initial steps of cube etching at different chemical potentials. Steps become more rough at more negative chemical potential. **b**: Ratio of number atoms on the perimeter of the topmost layer of atoms on a cube face (N_{Edges}) to the total number of atoms on that face (N_{Faces}), averaged over each face of the cube. As μ/ϵ becomes more negative, this ratio increases more rapidly with time, reflecting the surface roughness observed in simulations. **c**: Stochastic etching events remove an $n = 6$ atom on the perimeter of a face and reveal two atoms with $n = 7$. If $-6 > \mu/\epsilon > -7$, then such atoms are not readily etched; if $\mu/\epsilon \leq -7$ then atoms with $n = 7$ etch nearly as readily as those with $n < 7$, leading to a rough perimeter.

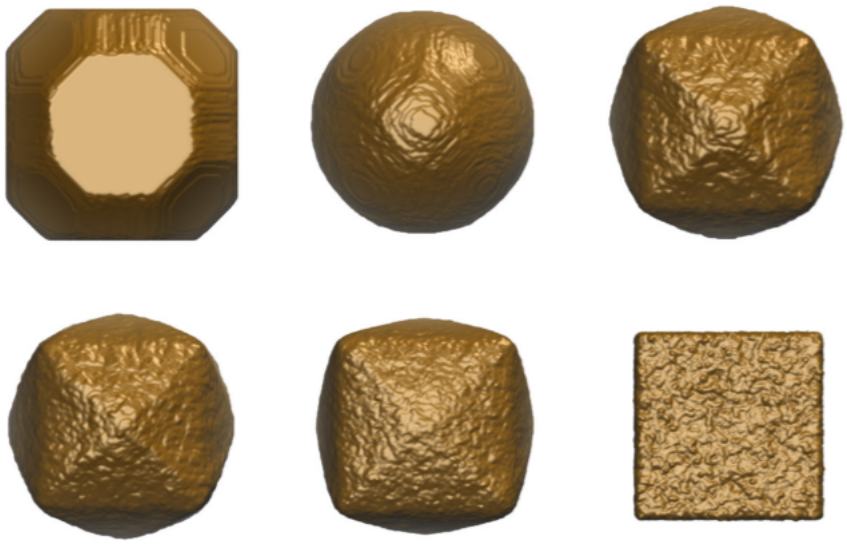

Figure 2.7: Snapshots from MC trajectories at different chemical potentials. Top row, left to right: $\mu/\epsilon = -5.98, -6, -6.25$. Bottom row, left to right: $\mu/\epsilon = -6.75, -7, -8$.

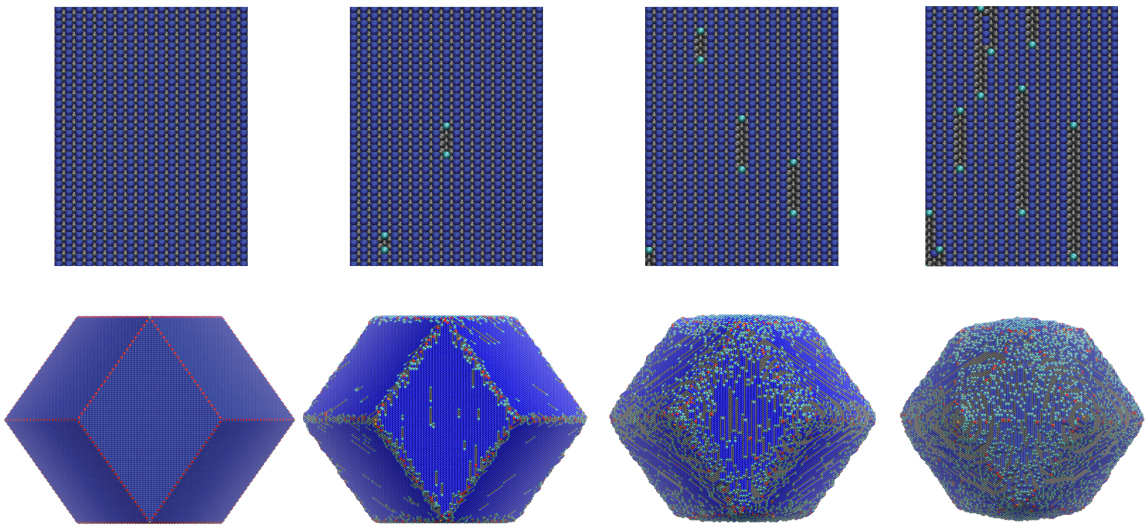

Figure 2.8: Top row: recession of a single row of atoms on a (110) surface initiated by the thermally-activated, stochastic removal of a single atom with $n = 7$. The removal of this single atom reveals two atoms with $n = 6$, which etch readily and reveal more $n = 6$ atoms. Bottom row: Etching of an RDD nanocrystal. Row-recession is clearly visible on the {110} facets.

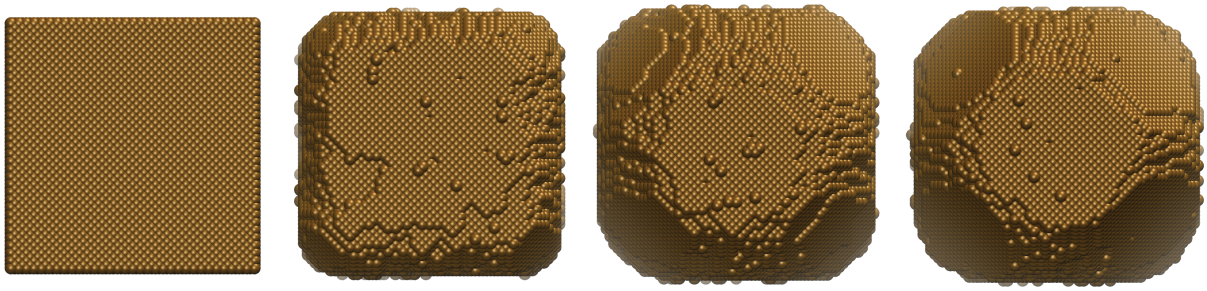

Figure 2.9: Relaxation to the equilibrium FCC nanocrystal shape via surface relaxation moves.

where:

$$d(C, C') = \frac{N_{\text{surf}}(C) N_{\text{vac}}(C)}{N_{\text{surf}}(C') N_{\text{vac}}(C')} e^{-\beta \Delta E}, \tag{2.23}$$

$$\Delta E = E(C') - E(C) = -\epsilon \Delta n, \tag{2.24}$$

where Δn is the total change in the number of bonds.

Simulations of Surface Relaxation

To test our surface relaxation moves, we performed MC simulations consisting only of such moves (i.e. with no insertion or deletion moves.) Initially cubic nanocrystals steadily relax to the equilibrium TO shape expected from the Wulff construction [119] via mass transfer from low-coordination corners to high-coordination {100} faces (see Fig. 2.9.)

We also performed simulations where both insertion/deletion and diffusion moves were allowed. Here, we set the chemical potential to $\mu/\epsilon = -6.5$ and attempted diffusion moves with a probability R for values $R = 0.9, 0.99, 0.999$. (For values much less than 0.9, the inclusion of diffusion moves had essentially no effect on the shape evolution.) Deletion moves and insertion moves were both attempted with probability $(1-R)/2$, though insertion moves were accepted at a rate so small as to be negligible. As can be seen in Fig. 2.10, for sufficiently large R, surface diffusion dominates over etching, resulting in the attainment of the equilibrium shape. For the smaller values of R, diffusion appears to "smooth out" sharp corners and edges of the intermediate THH shape compared to simulations using only insertion and deletion moves. Since experimental etching trajectories exhibit THH intermediates with more "smoothed out" features than simulation trajectories using only insertion and deletion moves, this suggests that the inclusion of surface relaxation moves may be important for capturing etching shape transformations precisely.

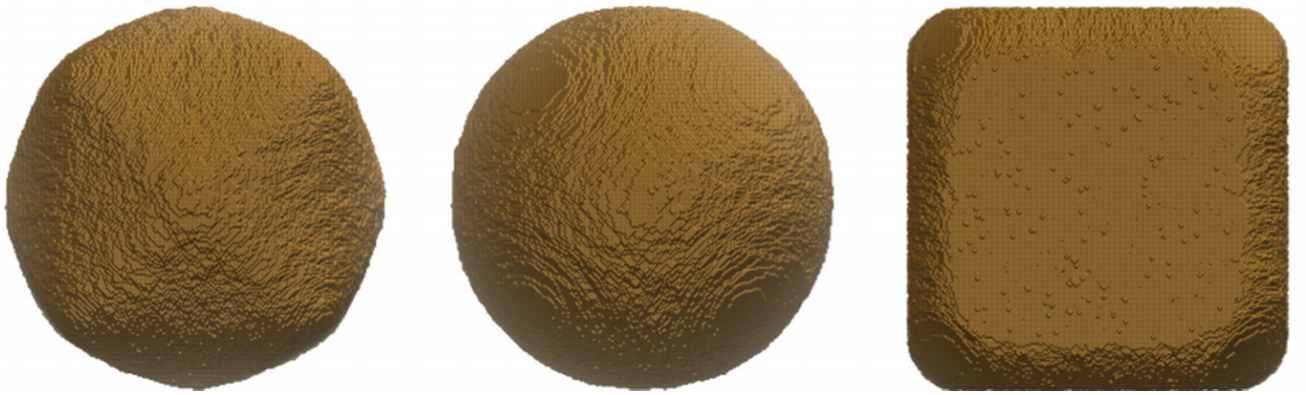

Figure 2.10: Snapshots from simulations of etching with surface relaxation moves included. Left to right: $R = 0.9, 0.99, 0.999$.

Simulations of Rod Etching

In the absence of surface relaxation moves, MC simulations of rod etching fail to capture nonequilibrium shape transformations observed in experiments. While near coexistence ($\mu/\epsilon = -5.98$) MC simulations do capture the experimentally observed elongated TO shape, for $\mu/\epsilon = -6.5$ simulations deviate significantly from experiments. Specifically, while in experiments nonequilibrium rods dissolve mainly at their tips, becoming "shorter", in simulations rods etch primarily on their sides, becoming "skinnier" ([121]). Snapshots from simulations consisting solely of insertion/deletion moves are shown in Figs. 2.11 and 2.12.

The addition of surface relaxation moves to rod simulations brings them into qualitative agreement with experiment. In Fig. 2.13 we show snapshots from a rod etching trajectory which includes surface relaxation moves with $R = 0.99$. Clearly, the rod now loses mass from its tips rather than from its sides. The shape transformation that is effected is that of an ellipsoid whose aspect ratio gradually shrinks to 1. To understand the origin of this change in behavior, we mapped out the mass transfer process by tracking individual diffusion moves, in the form of a score s for each site. If an atom has most recently diffused from that site, we assign a score $s = -1$; if an atom has most recently diffused to that site, we assign a score $s = 1$. Else, $s = 0$. In Fig. 2.14, we show snapshots colored according to this scheme. There is clearly mass transfer from the tips of the rod to its edges.

We also break down diffusion moves by coordination number change (i.e., moving from an n_0-coordinate site to an n_1-coordinate site) to see what kinds of diffusion moves contributed most to the mass transfer. Histograms of these moves are shown in Fig. 2.15. Clearly, from-6-to-6 moves are the most dominant. However, when only from-6-to-6 moves are allowed, the rods fail to exhibit the ellipsoidal transformation. If we also allow from-5-to-6 moves, then we recover the ellipsoidal transformation. These 5- and 6-coordinate atoms are highly

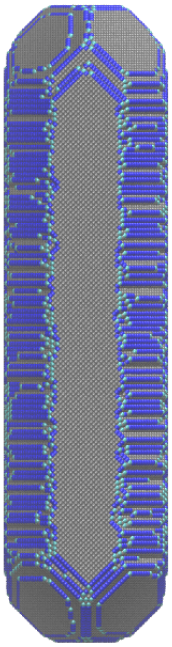

Figure 2.11: Snapshot from an equilibrium simulation of nanorod (etching at $\mu/\epsilon = -5.98$).

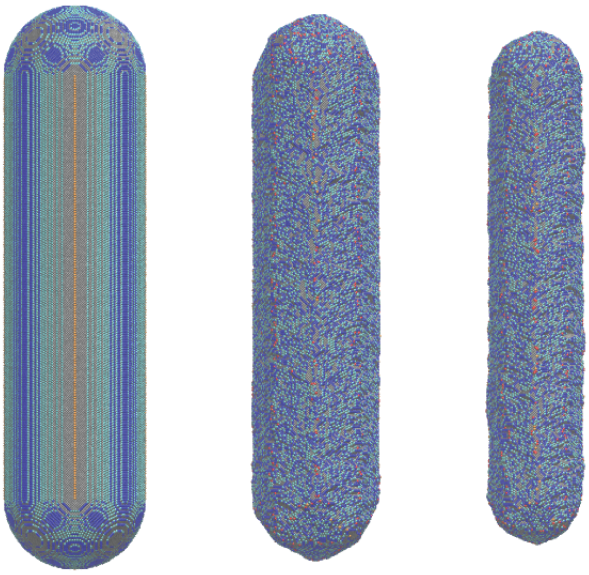

Figure 2.12: Snapshots from a simulation of nanorod etching at $\mu/\epsilon = -6.5$ in the absence of surface relaxation.

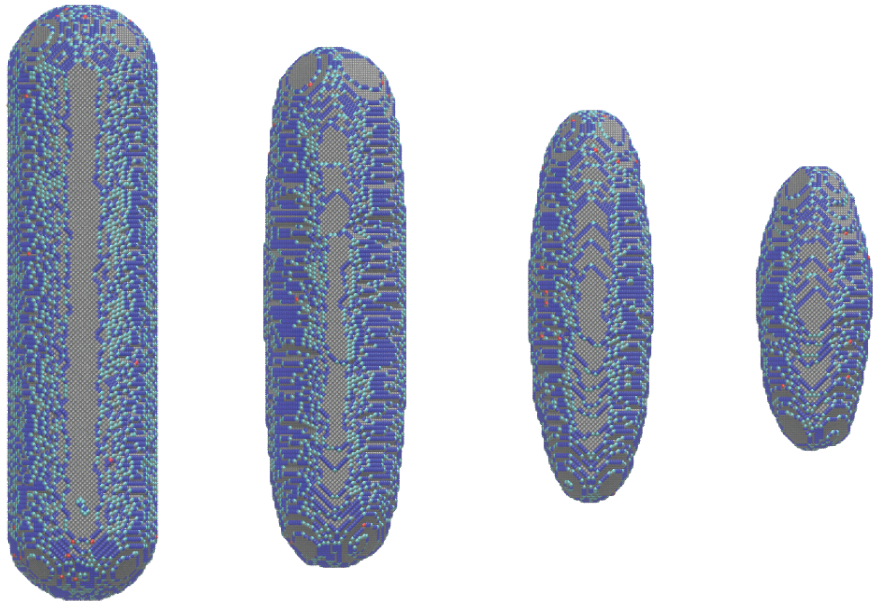

Figure 2.13: Ellipsoid transformation.

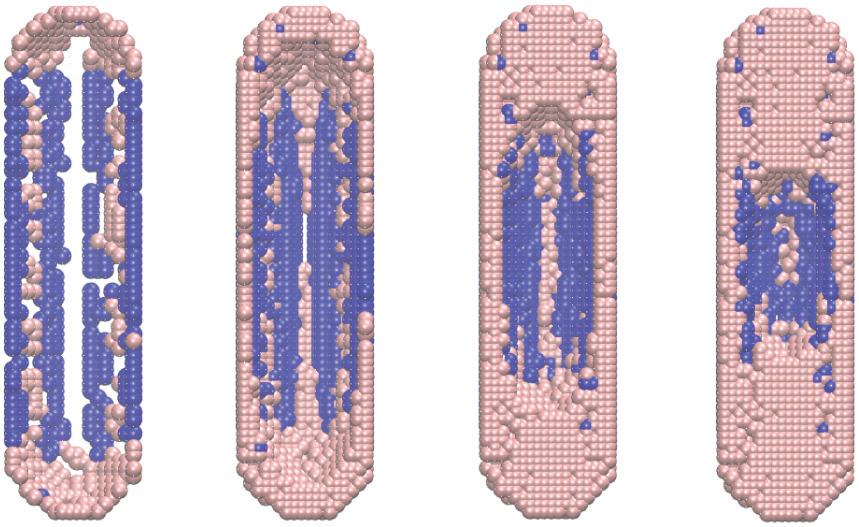

Figure 2.14: Maps of diffusion during an etching+surface relaxation trajectory ($\mu/\epsilon = -6.5$, $R = 0.99$). Sites are colored pink for $s = -1$ and blue for $s = 1$.

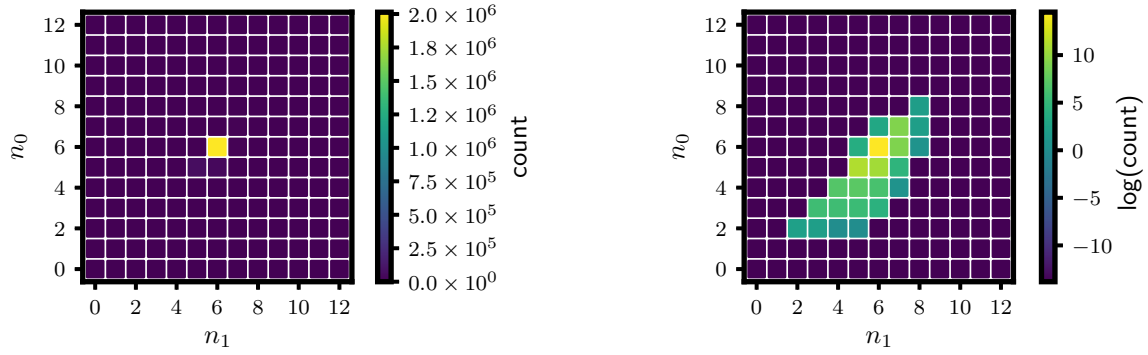

Figure 2.15: Histograms of diffusion moves from a site with $n = n_0$ to a site with $n = n_1$ over the course of an etching+surface relaxation trajectory ($\mu/\epsilon = -6.5$, $R = 0.99$). The plot on the left shows the number of moves, while the plot on the right shows the logarithm of the number of moves.

concentrated along terrace steps (see Fig. 2.16). In other words, the ellipsoid transformation appears to be driven by energetically neutral or favorable mass transfer at terraces. Combined with the observation of mass transfer from nanorod tips to edges, we conjecture that there is an energetically downhill transfer of mass from {111} edges to {100} edges which promotes the ultimate etching away of the tips (where {111} facets are located) and the preservation of {100} facets on the sides of the rod.

We test this hypothesis in a simpler setting. Specifically, we consider a finite {100} adlayer on an infinite {100} substrate and a finite {111} adlayer on an infinite {111} substrate. Each of these adlayers is initialized in a shape that maximized the coordination number of surface atoms: a square with faces oriented along [110] directions for the (100) surface, and a hexagon for the (111) surface. In the absence of any driving force, there are no energetically favorable ways to modify these adlayers with single-atom moves. Indeed, when we perform MC simulations in which we attempted to swap atoms both within and between these adlayers using the diffusion moves of Eqs. 2.22, 2.23, and 2.24, we observe that at $T = 0$ no such moves are accepted. Once a driving force is introduced (in the form of etching moves at $\mu/\epsilon = -6.5$,) removal of atoms with $n \leq 6$ by etching moves opens up new possibilities for energetically neutral or favorable movement of atoms between the (100) and (111) adlayers. Indeed, most of the trajectories we sampled exhibit growth of one adlayer at the expense of the other (though the driving force causes the net population of adlayer atoms to decrease.) Which adlayer grows at the expense of the other depends strongly on their relative initial sizes. In Fig. 2.18 we plot the population of the adlayers over time for a large number of trajectories and for several different choices of initial adlayer sizes, and in Fig. 2.19 we plot the fraction of trajectories exhibiting growth of (100) adlayers at the expense of (111) adlayers versus the ratio of the initial sizes of those adlayers. For a (100)

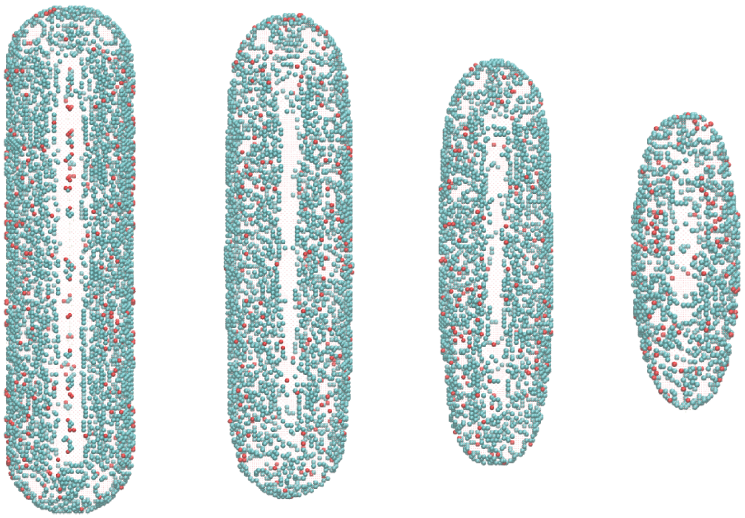

Figure 2.16: Snapshots from an etching+surface relaxation trajectory ($\mu/\epsilon = -6.5$, $R = 0.99$) showing only atoms with $n = 6$ (light blue) and $n = 5$ (red.)

adlayer with $N_{100} = 100$, the probability that the (100) adlayer will grow at the expense of the (111) layer (rather than the reverse) is roughly 1/2 when $N_{111} \approx 2.3N_{100}$. The fact that this point does not occur when $N_{111} \approx N_{100}$ as in standard Ostwald ripening reflects the fact that the density of low-coordination perimeter atoms depends on the geometry of the facet. (The (100) square adlayer has four perimeter atoms with $n = 6$, while the (111) hexagon has six such atoms.)

What the preceding analysis suggests is that unless the number of atoms comprising its (111) facets is at least ≈ 2 times the number comprising its (100) facets, an etching nanocrystal will exhibit mass transfer from (111) facets to (100) facets. This is consistent with the etching trajectories of nanorods, which have a large number of atoms on their (100)-dominated sides compared to their (111)-dominated tips. To test the hypothesis that Ostwald ripening underlies the difference between etching trajectories with and without diffusion, one could simulate etching with diffusion of a nanocrystal very rich in (111) atoms compared to (100) atoms. If our hypothesis is correct, then the resulting shape transformation should feature mass transfer from (100) facets to (111) facets. Such a simulation would also provide a prediction for an even more important test – comparison with an experimental etching trajectory.

Confirmation of this proposed mechanism awaits more systematic experiments on the shape-dependence of rod etching. It is possible that an anisotropic distribution of ligands on the nanorod surface also contributes to the discrepancy between simulations without diffusion and experiment.

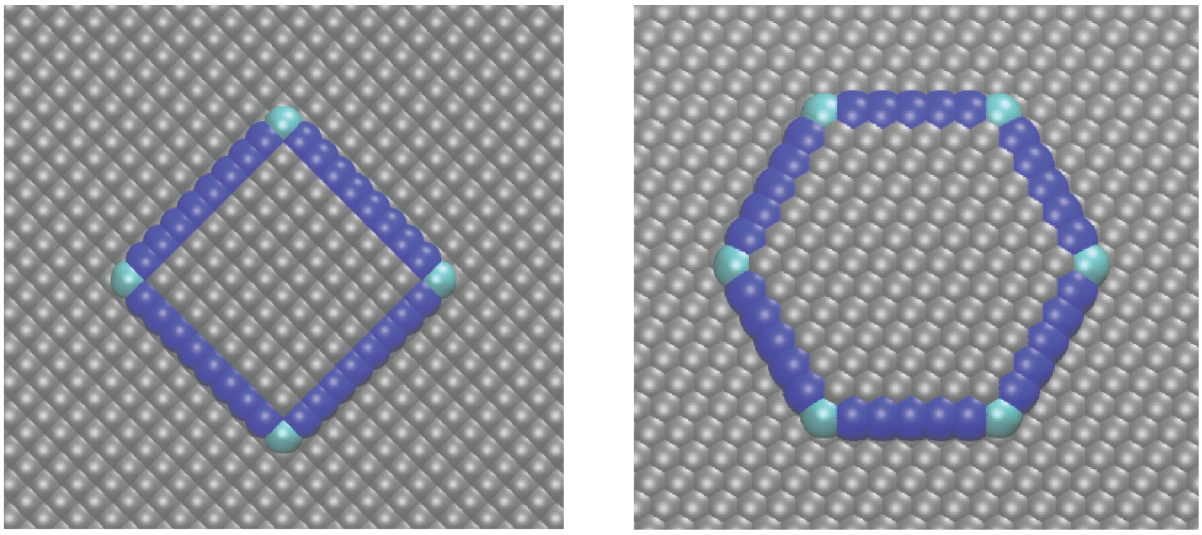

Figure 2.17: Left: low-energy adlayer on (100) substrate. Right: low-energy adlayer on (111) substrate.

2.6 Conclusion

Our simple model for nanocrystal etching explains a surprising number of features observed in experimental dissolution trajectories. There are, however, a number of extensions which could be pursued to enhance its realism. Given the importance of surface-bound ligands in preventing nanoparticle aggregation and in modulating the accessibility of certain surface sites, one might try to include a description of them in the etching process. Additionally, surface reconstruction is known to be an important aspect of nanocrystal surface chemistry, but due to the assumption of a fixed lattice structure our model cannot capture this phenomenon. Allowing atoms to move off-lattice would certainly enhance the realism of our model, but would also make it significantly more time-consuming to simulate. It would, however, be very straightforward to investigate the nonequilibrium etching of nanocrystals with different lattice structures. In any case, the success of our rather generic model for crystal shape transformations should make it a good starting point for future investigations.

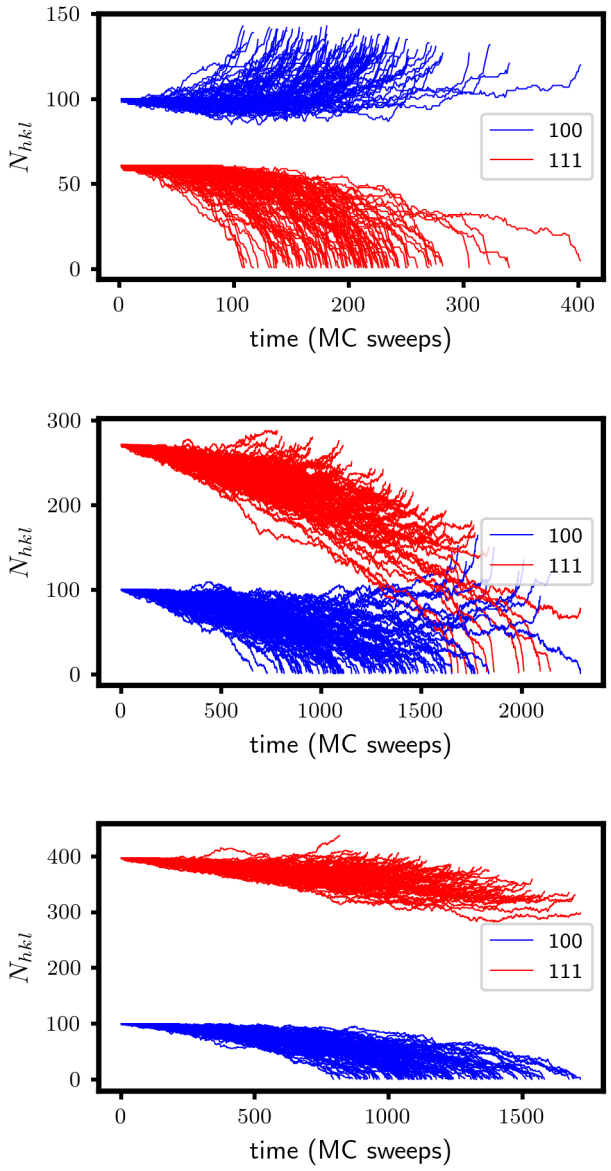

Figure 2.18: Plots of 100 independent trajectories of (100) and (111) adlayers with both etching (at $\mu/\epsilon = -6.5$) and surface relaxation moves ($R = 0.99$) for different relative initial sizes. In the top plot all trajectories result in (100) growth; in the middle plot 57% of trajectories result in (100) growth; in the bottom plot no trajectories result in (100) growth. Trajectories end once one adlayer has vanished.

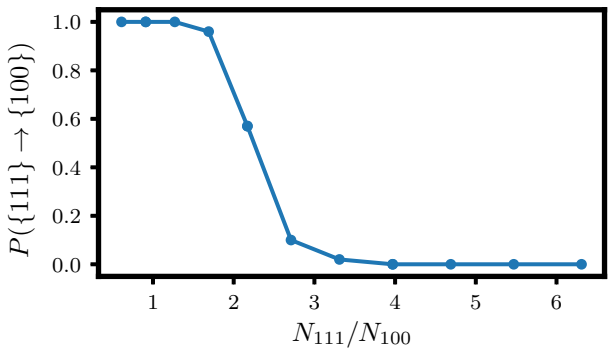

Figure 2.19: Fraction $P(\{111\} \to \{100\})$ of trajectories which end in (100) adlayer growth at the expense of the (111) adlayer versus the ratio N_{111}/N_{100} between initial (100) and (111) adlayer sizes. Here, $N_{100} = 100$.

Chapter 3

Consequences of Lattice Mismatch for Phase Equilibrium in Heterostructured Solids

3.1 Introduction

Lattice mismatch – the difference in preferred bond length between adjoining regions of a heterogeneous solid – is a natural consequence of mixing diverse components to build complex materials. It is well recognized that juxtaposing domains with different lattice spacings introduces local strain, significantly impacting material properties such as electronic structure [107, 20, 95] and the propensity to form dislocations [76, 94]. The resulting elastic energy can also significantly bias the spatial arrangement of compositional defects and interfaces. How these biases influence the thermodynamic stability of mixed phases, however, has not been thoroughly characterized. Here, we examine the phase behavior of a microscopic model for such systems, motivated by intriguing heterostructures adopted by CdS/Ag_2S nanocrystals [102] in the course of cation exchange reactions [108, 71, 101, 24]. Their alternating stripes of Cd-rich and Ag-rich domains have been attributed to lattice mismatch between the CdS and Ag_2S domains [25], but an understanding of how they form, and whether they are thermodynamically stable, has been lacking.

Our model and analysis draw from those introduced by Fratzl and Penrose [36, 37], who represented a two-component solid by atoms on a flexible square lattice with bond length preferences that depend on local composition. By integrating out mechanical fluctuations, they obtained an approximate effective Hamiltonian for the composition field, whose atomic identities interact in a pairwise and anisotropic fashion. For the special case of a 1:1 mixture of the two species, they used mean field theory (MFT) to predict a second-order phase tran-

sition between a high-temperature disordered phase and a low-temperature ordered phase characterized by stripes of alternating composition.

This Chapter surveys the composition-temperature phase diagram of a similar model much more broadly, revealing an unanticipated richness with interesting implications for nanoscale transformations. Monte Carlo (MC) simulations confirm the predicted appearance of modulated-order phases with spontaneously broken symmetry. They further point to unusual scenarios of phase separation, with well-defined interfaces but a non-convex free energy. This behavior can be understood as a consequence of elastic energies for phase separation that scale extensively with system size. For this situation we devise a procedure, akin to the conventional Maxwell construction, to determine the boundaries of coexistence regions given equations of state for the corresponding bulk phases. Although the high temperature phase behavior is dominated by fluctuations on the triangular lattice, a straightforward mean field theory describes the required bulk properties quite faithfully at low temperature. We combine these approaches to predict a phase diagram that accounts for the full set of structures observed in our MC simulations, including those with system-spanning interfaces.

3.2 Model

We consider a model in which N atoms are situated near the sites of a completely occupied two-dimensional triangular lattice, with periodic boundary conditions in both Cartesian directions. The atom at site $\mathbf{R}$ has two possible types ("spins"), indicated $\sigma_{\mathbf{R}} = +1$ (type A) and $\sigma_{\mathbf{R}} = -1$ (type B). These atom types are distinguished by their size, so that nearest neighbor atoms at sites $\mathbf{R}$ and $\mathbf{R} + a\hat{\boldsymbol{\alpha}}$ prefer a bond distance l dictated by their identities,

$$l(\sigma_{\mathbf{R}}, \sigma_{\mathbf{R}+a\hat{\boldsymbol{\alpha}}}) = \begin{cases} l_{AA}, & \text{for } \sigma_{\mathbf{R}} = \sigma_{\mathbf{R}+a\hat{\boldsymbol{\alpha}}} = 1 \\ l_{AB}, & \text{for } \sigma_{\mathbf{R}} \neq \sigma_{\mathbf{R}+a\hat{\boldsymbol{\alpha}}} \\ l_{BB}, & \text{for } \sigma_{\mathbf{R}} = \sigma_{\mathbf{R}+a\hat{\boldsymbol{\alpha}}} = -1, \end{cases} \tag{3.1}$$

where a is the lattice constant and $\hat{\boldsymbol{\alpha}}$ is a unit bond vector. We take $l_{BB} < l_{AA}$ and adopt the simple mixing rule $l_{AB} = (l_{AA} + l_{BB})/2$. The lattice mismatch $\Delta = (l_{AA} - l_{BB})/2$ will serve as our basic unit of length.

Both the atoms' identities and their displacements ($\mathbf{u}_{\mathbf{R}}$) away from ideal lattice positions fluctuate according to a Boltzmann distribution $P(\{\mathbf{u}_{\mathbf{R}}\}, \{\sigma_{\mathbf{R}}\}) \propto e^{-\beta\mathcal{H}}$, where $T = (k_B\beta)^{-1}$ is temperature and $\mathcal{H}(\{\mathbf{u}_{\mathbf{R}}\}, \{\sigma_{\mathbf{R}}\})$ is the energy of a given configuration. The net displacement $\sum_{\mathbf{R}} \mathbf{u}_{\mathbf{R}} = 0$ and the net fraction of A atoms $c = (2N)^{-1} \sum_{\mathbf{R}} (\sigma_{\mathbf{R}} + 1)$ are both implicitly held fixed. Fluctuations in the lattice constant a (at zero external pressure), however, are included in the ensemble we consider; for large systems and small lattice mismatch, this freedom primarily allows the macroscopic geometry to adapt to the imposed composition, $a \approx l_{AB} + \Delta(2c-1) + O(N^{-1/2})$. The free energy $F(c)$ for this ensemble encodes the model's response to changing proportions of atom types, and in particular its phase transitions.

Deviations of bond distances away from their locally preferred lengths incur energy that grows quadratically,

$$\mathcal{H} = \frac{K}{4} \sum_{\mathbf{R},\hat{\boldsymbol{\alpha}}} \left[|a\hat{\boldsymbol{\alpha}} + \mathbf{u}_{\mathbf{R}} - \mathbf{u}_{\mathbf{R}+a\hat{\boldsymbol{\alpha}}}| - l(\sigma_{\mathbf{R}}, \sigma_{\mathbf{R}+a\hat{\boldsymbol{\alpha}}}) \right]^2 , \tag{3.2}$$

where K is a positive constant that sets the natural energy scale $\epsilon = K\Delta^2/8$. All energies and lengths will henceforth be expressed in units of ϵ and Δ, respectively. The ground states of Eq. 3.2 clearly occur in the absence of heterogeneity, i.e., $c = 0$ or $c = 1$. At intermediate composition, fixed connectivity prevents the collection of bonds from simultaneously attaining their preferred lengths. We have explored the resulting compositional correlations using MC simulations, as well as analytically using small-mismatch and mean-field approximations.

3.3 Monte Carlo simulations

Protocol

We used MC simulations to explore the equilibrium properties of Eq. 3.2. Periodic boundary conditions were imposed in order to simulate bulk behavior. The numbers of unit cells in the x and y directions, N_x and N_y, were chosen so as to make the dimensions L_x, L_y of the box nearly equal. Many of the simulations were carried out with $N_x = 12$, $N_y = 14$ (making the total number of atoms $N = 168$,) so that $L_x/L_y \approx 0.990$. A number of simulations were also performed at different system sizes, the largest being $N_x = 36$, $N_y = 40$, in order to assess finite-size effects. These will be described in more detail later.

Most simulations were conducted in the isothermal-isobaric (NPT) ensemble. This ensemble was sampled using two basic MC moves: spin flips and displacement moves. In both cases, an atom at lattice site $\mathbf{R}$ was selected at random. An attempt was then made to change either its spin, $\sigma_{\mathbf{R}} \to -\sigma_{\mathbf{R}}$, or its position, $\mathbf{R}+\mathbf{u}_{\mathbf{R}} = \mathbf{r}_{\mathbf{R}} \to \mathbf{r}_{\mathbf{R}}+\boldsymbol{d}$, where $\boldsymbol{d} = (d_x, d_y)$ is a two dimensional vector. The components of the vector were selected uniformly at random from an interval $[-d_{\max}, d_{\max}]$. The requisite random numbers were generated using the Mersenne Twister algorithm [75] as implemented in the GNU Scientific Library (GSL) [73]. For most of our simulations, $d_{\max}$ was chosen to be $0.1l_{AA}$, although at the lowest temperatures we considered it was more efficient to use a smaller value of $0.05l_{AA}$. After a move (either displacement or spin) was proposed, it was either accepted or rejected according to a Metropolis criterion [21]:

$$P(C \to C') = \min \left[1, e^{-\beta(\mathcal{H}(C)-\mathcal{H}(C'))} \right], \tag{3.3}$$

where C and C' represent configurations $\{\sigma_{\mathbf{R}}\}, \{\mathbf{r}_{\mathbf{R}}\}$ before and after the proposed move, respectively, and $\beta = 1/k_B T$. The above form of the acceptance probability ensures that the MC algorithm satisfies detailed balance and hence properly samples the equilibrium distribution at temperature T.

Simulation runs consisted of performing a large number of MC sweeps. A single MC sweep consisted of N attempted spin flips and N attempted displacement moves. Constant pressure was maintained using a standard algorithm in which attempts to change the system's volume were proposed and then accepted or rejected according to a Metropolis criterion [21]. In our simulations, proposed volume moves consisted of changing the total volume by an amount δV, selected uniformly at random from the interval $[-\delta V_{\max}, \delta V_{\max}]$. We chose $\delta V_{\max} = 0.01 V_0$, where V_0 is the volume at the beginning of a simulation run. Such volume moves were performed once every MC sweep.

Before collecting data from any molecular simulation, it is necessary to equilibrate the system in order to remove artifacts due to its initial preparation. In our simulations, initial configurations consisted of atoms arranged on a perfect triangular lattice, with a random distribution of spins, and with a volume consistent with the net composition. Before obtaining statistics, we equilibrated the system by running for 10^7 MC sweeps without collecting any data. Statistics were then collected for different observables once every sweep, over 10^7 sweeps.

A central quantity of interest is the free energy as a function of composition, $F(c)$. We used umbrella sampling [21, 113] to obtain this quantity. For calculations at temperatures $T \geq 2.0$ we biased the system with a set of hard wall window potentials spaced equally over the range of possible compositions [21]. For the system size $N_x = 12$, $N_y = 14$, we used 100 overlapping windows. Within each window, statistics were collected as described in the previous paragraph. We then used the Weighted Histogram Analysis Method (WHAM) [65] to construct the full probability distribution (and hence free energy) as a function of composition. For lower temperatures ($k_B T/\epsilon < 2.0$), large free energy barriers necessitated a somewhat more involved procedure. Here we used the inverted free energy profile obtained at $k_B T = 2.0$, in combination with a set of evenly spaced harmonic windows with spring constant $K' = 20\epsilon/\Delta^2$, as a bias potential. For $N_x = 12$, $N_y = 14$, 100 harmonic windows were used. Larger systems required more windows - for $N_x = 24$, $N_y = 28$, we used 400 windows. We again used WHAM to construct free energy profiles from this data.

The majority of our simulations were carried out with a mismatch of $\Delta = 0.1$. The MC results presented here and in the main text were obtained using this value. However, we also ran the same simulations at a much smaller value of $\Delta = 0.005$ and obtained essentially identical results.

In some cases we computed thermodynamic quantities at an explicitly fixed composition. This necessitated the use of Kawasaki (rather than Metropolis) dynamics [61]. In Kawasaki dynamics, one performs a spin *exchange* rather than a spin flip. Explicitly, two atoms are selected at random and, if their spins are different, an exchange of their values is attempted. This proposed move is accepted with the detailed balance-preserving probability of Eq. 3.3.

Results

At high temperature, equilibrium states of this model are macroscopically uniform but exhibit suggestive microscopic correlations. A few such disordered configurations, selected

randomly from MC simulations, are shown in the top row of Fig. 3.1A. For nearly pure mixtures at modest T (≈ 1.4,) defects cluster in space, but not compactly. Motifs of microscopically alternating composition are even more evident at intermediate net composition, where typical equilibrium states resemble interpenetrating networks of A and B atoms. At low temperature these structural tendencies produce four phases. The "superlattice" phases S_1 and S_2 feature periodic modulation of atom types with wavelengths on the order of a single lattice spacing. In the vein of previous studies of modulated order [66, 26] we characterize these phases by their average composition on three distinct sublattices. In S_1 two sublattices are enriched in atom type A, while the third is enriched in type B. Roles of A and B are reversed in S_2. The ideal forms of these phases, where the net composition per site $2c_\gamma - 1 = (3/N)\sum_{\mathbf{R}}^{(\gamma)} \sigma_{\mathbf{R}}$ is ± 1 on each sublattice γ, occur at $c = 1/3$ and $c = 2/3$. In the "unstructured" phases U_1 and U_2, whose zero-temperature forms are compositionally pure, the average composition is independent of sublattice. Previous work anticipated the appearance of modulated order phases like S_1 and S_2 [36, 37], but not their competition with unstructured phases.

The emergence of superlattice phases as temperature decreases at intermediate composition involves a breaking of symmetry between A- and B-rich states. This symmetry is suggested by the form of Eq. 3.2, but not precisely implied. Despite its Hookean form, $\mathcal{H}$ is an anharmonic function of atomic displacements, with nonlinearities of order Δ/a that favor one atom type (B) for all $c \neq 0, 1$. Symmetry with respect to a global transformation of the composition $\{\sigma_{\mathbf{R}}\} \to \{-\sigma_{\mathbf{R}}\}$ is thus not guaranteed. Nevertheless, MC simulations suggest symmetry of thermodynamic quantities about c very near $1/2$ even for the substantial lattice mismatch $\Delta/a = 0.15$, indicating that nonlinearities in $\mathcal{H}$ are intrinsically weak in effect (see Appendix B.1 for more information.)

MC sampling further reveals states of coexistence among these four phases, as depicted in the bottom row of Fig. 3.1A. Specifically, S_1 and S_2 coexist at low temperature over a range of composition centered near $c = 1/2$. Coexistence between S_1 and U_1, and between S_2 and U_2, are also observed. But under no conditions do simulations exhibit coexistence between U_1 and U_2.

The usual quantitative signature of phase separation in d spatial dimensions is a subextensive non-convexity in the corresponding free energy, i.e., a barrier of $O(N^{-(d-1)/d})$ in $F(c)/N$ as a function of c that approaches the convex envelope in the thermodynamic limit. The free energies $F_{\mathrm{MC}}(c)$ we have determined from simulation (using methods of umbrella sampling and histogram reweighting [21, 113, 65]) do not follow this expectation. Specifically, plots of $F_{\mathrm{MC}}(c)/N$ in Fig. 3.1B show non-convex regions that persist as N becomes large. We will argue that this behavior is generic to the coexistence of geometrically mismatched solids with a fixed macroscopic shape, and that the resulting negative curvature of $F(c)$ is simply related to their elastic properties.

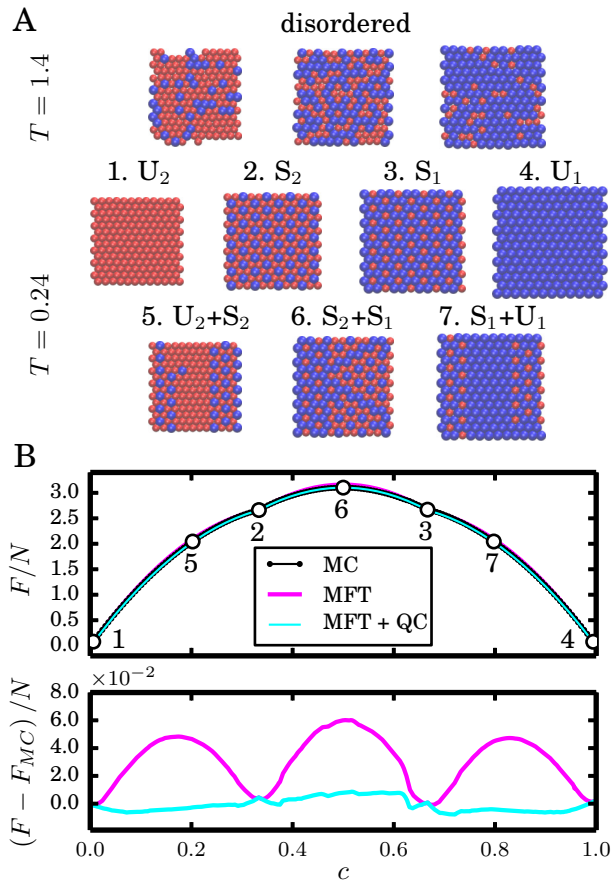

Figure 3.1: Monte Carlo (MC) simulation results for the elastic model in Eq. 3.2. **A**: Survey of configurations exemplifying the disordered, unstructured (U_1 and U_2), and superlattice (S_1 and S_2) phases. Blue and red spheres represent A and B atoms, respectively. **B**: Free energy per particle $F(c)/N$ as a function of composition c at $T = 0.24$. Circles numbered 1 to 7 refer to the corresponding configurations in **A**. Results are shown in black for MC sampling, in pink for the mean field theory (MFT) of Eq. 3.70, and in blue for application of the quadratic construction (QC, Eq. 3.82) to mean-field thermodynamics. Lower panel shows the difference between MFT and MC results (pink), and the difference between MFT+QC and MC (blue).

3.4 Small mismatch approximation

For atom types that differ only slightly in size, $\Delta/a \ll 1$, the energy $\mathcal{H}$ is approximately quadratic in the displacement field $\mathbf{u_R}$. This approximation makes our Hamiltonian analytically tractable. To see this, note that the natural bond length, Eq. 3.1, can be rewritten as:

$$l(\sigma_{\mathbf{R}}, \sigma_{\mathbf{R}'}) = l_{AB} + \frac{\Delta}{2}(\sigma_{\mathbf{R}} + \sigma_{\mathbf{R}'}). \tag{3.4}$$

We then rewrite Eq. 3.2 as:

$$\mathcal{H}/\epsilon = \bar{\mathcal{H}} = 2\sum_{\mathbf{R},\hat{\boldsymbol{\alpha}}} \left[\frac{a}{\Delta}\left|\hat{\boldsymbol{\alpha}} + \left(\frac{\Delta}{a}\right)(\bar{\mathbf{u}}_{\mathbf{R}} - \bar{\mathbf{u}}_{\mathbf{R}+a\hat{\boldsymbol{\alpha}}})\right| - \left(\frac{l_{AB}}{\Delta} + \frac{1}{2}(\sigma_{\mathbf{R}} + \sigma_{\mathbf{R}+a\hat{\boldsymbol{\alpha}}})\right)\right]^2. \tag{3.5}$$

Here we have defined a scaled Hamiltonian $\bar{\mathcal{H}} = \mathcal{H}/\epsilon$ and scaled displacement $\bar{\mathbf{u}}_{\mathbf{R}} = \mathbf{u}_{\mathbf{R}}/\Delta$. Now, let $\boldsymbol{\delta} = (\Delta/a)(\bar{\mathbf{u}}_{\mathbf{R}} - \bar{\mathbf{u}}_{\mathbf{R}+a\hat{\boldsymbol{\alpha}}})$. Then,

$$\begin{aligned} |\hat{\boldsymbol{\alpha}} + \boldsymbol{\delta}|^2 &= |\hat{\boldsymbol{\alpha}}|^2 + 2\hat{\boldsymbol{\alpha}}\cdot\boldsymbol{\delta} + |\boldsymbol{\delta}|^2 \\ &= 1 + 2\hat{\boldsymbol{\alpha}}\cdot\boldsymbol{\delta} + \mathcal{O}(\delta^2) \\ \implies |\hat{\boldsymbol{\alpha}} + \boldsymbol{\delta}| &= \sqrt{1 + 2\hat{\boldsymbol{\alpha}}\cdot\boldsymbol{\delta} + \mathcal{O}(\delta^2)}. \end{aligned} \tag{3.6}$$

For small x, we have $\sqrt{1+x} = 1 + \frac{x}{2} + \mathcal{O}(x^2)$, so:

$$|\hat{\boldsymbol{\alpha}} + \boldsymbol{\delta}| \approx 1 + \hat{\boldsymbol{\alpha}}\cdot\boldsymbol{\delta}. \tag{3.7}$$

Therefore,

$$\begin{aligned} \bar{\mathcal{H}} &\approx 2\sum_{\mathbf{R},\hat{\boldsymbol{\alpha}}} \left[\frac{a}{\Delta} + \frac{a}{\Delta}\hat{\boldsymbol{\alpha}}\cdot\boldsymbol{\delta} - \frac{l_{AB}}{\Delta} - \frac{1}{2}(\sigma_{\mathbf{R}} + \sigma_{\mathbf{R}+a\hat{\boldsymbol{\alpha}}})\right]^2 \\ &= 2\sum_{\mathbf{R},\hat{\boldsymbol{\alpha}}} \left[\hat{\boldsymbol{\alpha}}\cdot(\bar{\mathbf{u}}_{\mathbf{R}} - \bar{\mathbf{u}}_{\mathbf{R}+a\hat{\boldsymbol{\alpha}}}) + \frac{a - l_{AB}}{\Delta} - \frac{1}{2}(\sigma_{\mathbf{R}} + \sigma_{\mathbf{R}+a\hat{\boldsymbol{\alpha}}})\right]^2. \end{aligned} \tag{3.8}$$

We define the quantity:

$$\delta\sigma_{\mathbf{R}} = \sigma_{\mathbf{R}} - \frac{a - l_{AB}}{\Delta}, \tag{3.9}$$

allowing us to write our small-mismatch Hamiltonian as:

$$\bar{\mathcal{H}} \approx 2\sum_{\mathbf{R},\hat{\boldsymbol{\alpha}}} \left(\hat{\boldsymbol{\alpha}}\cdot(\bar{\mathbf{u}}_{\mathbf{R}} - \bar{\mathbf{u}}_{\mathbf{R}+a\hat{\boldsymbol{\alpha}}}) - \frac{1}{2}(\delta\sigma_{\mathbf{R}} + \delta\sigma_{\mathbf{R}+a\hat{\boldsymbol{\alpha}}})\right)^2. \tag{3.10}$$

From the above expression it is clear that, in the small-mismatch limit, our Hamiltonian is quadratic in both displacement and spin variables, and that the displacements and spins are linearly coupled. We drop the overbar on the displacements and Hamiltonian in what follows.

3.5 Fourier Space Hamiltonian

In our Hamiltonian, variables at different sites are coupled. We can take advantage of translational symmetry to locate uncoupled modes, by writing our Hamiltonian in Fourier space. We first write the displacement and spin fields in terms of their Fourier coefficients:

$$\mathbf{u}_{\mathbf{R}} = \frac{1}{N}\sum_{\mathbf{q}} \tilde{\mathbf{u}}_{\mathbf{q}} e^{-i\mathbf{q}\cdot\mathbf{R}} \tag{3.11a}$$

$$\delta\sigma_{\mathbf{R}} = \frac{1}{N}\sum_{\mathbf{q}} \delta\tilde{\sigma}_{\mathbf{q}} e^{-i\mathbf{q}\cdot\mathbf{R}}, \tag{3.11b}$$

where the sum is taken over values within the first Brillouin zone, specifically $\mathbf{q} = n_1\mathbf{b}_1/N_1 + n_2\mathbf{b}_2/N_2$, where $N_1N_2 = N$; $n_1 = 0, 1, \ldots, N_1 - 1$; $n_2 = 0, 1, \ldots, N_2 - 1$; and the reciprocal lattice vectors for the triangular lattice are given by [77]:

$$\mathbf{b}_1 = \frac{2\pi}{\sqrt{3}a}\left(\sqrt{3}, -1\right) \tag{3.12a}$$

$$\mathbf{b}_2 = \frac{4\pi}{\sqrt{3}a}\left(0, 1\right). \tag{3.12b}$$

Inserting eqs. 3.11a and 3.11b into eq. 3.10, and using the relation:

$$\sum_{\mathbf{R}} e^{-i(\mathbf{q}+\mathbf{q}')\cdot\mathbf{R}} = N\delta_{-\mathbf{q},\mathbf{q}'}, \tag{3.13}$$

where $\delta_{-\mathbf{q},\mathbf{q}'}$ denotes the Kronecker delta function, we obtain a Fourier-space version of our Hamiltonian:

$$\mathcal{H} = \frac{2}{N}\sum_{\mathbf{q}}\left[\tilde{\mathbf{u}}_{\mathbf{q}}\cdot\mathbf{F}_{\mathbf{q}}\cdot\tilde{\mathbf{u}}_{-\mathbf{q}} + \frac{1}{4}g_{\mathbf{q}}\delta\tilde{\sigma}_{\mathbf{q}}\delta\tilde{\sigma}_{-\mathbf{q}} - \frac{1}{2}\mathbf{h}_{\mathbf{q}}\cdot\left(\tilde{\mathbf{u}}_{\mathbf{q}}\delta\tilde{\sigma}_{-\mathbf{q}} - \tilde{\mathbf{u}}_{-\mathbf{q}}\delta\tilde{\sigma}_{\mathbf{q}}\right)\right]. \tag{3.14}$$

The quantities $\mathbf{F}$, $\mathbf{h}$, and g encode information about the lattice structure:

$$\mathbf{F}_{\mathbf{q}} = \sum_{\hat{\boldsymbol{\alpha}}} f_{\hat{\boldsymbol{\alpha}},\mathbf{q}}\hat{\boldsymbol{\alpha}}\hat{\boldsymbol{\alpha}} \tag{3.15a}$$

$$\mathbf{h}_{\mathbf{q}} = \sum_{\hat{\boldsymbol{\alpha}}} h_{\hat{\boldsymbol{\alpha}},\mathbf{q}}\hat{\boldsymbol{\alpha}} \tag{3.15b}$$

$$g_{\mathbf{q}} = \sum_{\hat{\boldsymbol{\alpha}}} g_{\hat{\boldsymbol{\alpha}},\mathbf{q}}, \tag{3.15c}$$

where:

$$f_{\hat{\boldsymbol{\alpha}},\mathbf{q}} = \left(e^{-ia\mathbf{q}\cdot\hat{\boldsymbol{\alpha}}} - 1\right)\left(e^{ia\mathbf{q}\cdot\hat{\boldsymbol{\alpha}}} - 1\right) \tag{3.16a}$$

$$h_{\hat{\boldsymbol{\alpha}},\mathbf{q}} = \left(e^{-ia\mathbf{q}\cdot\hat{\boldsymbol{\alpha}}} - 1\right)\left(e^{ia\mathbf{q}\cdot\hat{\boldsymbol{\alpha}}} + 1\right) \tag{3.16b}$$

$$g_{\hat{\boldsymbol{\alpha}},\mathbf{q}} = \left(e^{-ia\mathbf{q}\cdot\hat{\boldsymbol{\alpha}}} + 1\right)\left(e^{ia\mathbf{q}\cdot\hat{\boldsymbol{\alpha}}} + 1\right). \tag{3.16c}$$

It is revealing to single out the longest-wavelength ($\mathbf{q} = 0$) component of the Hamiltonian. In particular, we write:

$$\mathcal{H} = \mathcal{H}_{\mathbf{q}\neq 0} + \mathcal{H}_{\mathbf{q}=0}, \tag{3.17}$$

where $\mathcal{H}_{\mathbf{q}\neq 0}$ is simply Eq. 3.14 with the $\mathbf{q} = 0$ term excluded, and $\mathcal{H}_{\mathbf{q}=0}$ is:

$$\mathcal{H}_{\mathbf{q}=0} = \frac{2Z}{N}\delta\hat{\sigma}_0^2, \tag{3.18}$$

since $f_{\hat{\boldsymbol{\alpha}},\mathbf{q}}$ and $h_{\hat{\boldsymbol{\alpha}},\mathbf{q}}$ are both zero when $\mathbf{q} = 0$, and $g_0 = 4Z$, where Z is the coordination number of the lattice. Now, by taking the Fourier transform of $\delta\sigma_{\mathbf{R}} = \sigma_{\mathbf{R}} - (a - l_{AB})/\Delta$, we obtain:

$$\delta\tilde{\sigma}_{\mathbf{q}} = \tilde{\sigma}_{\mathbf{q}} - N\delta_{\mathbf{q},0}\left(\frac{a - l_{AB}}{\Delta}\right), \tag{3.19}$$

where $\tilde{\sigma}_{\mathbf{q}} = \sum_{\mathbf{R}} \sigma_{\mathbf{R}} e^{i\mathbf{q}\cdot\mathbf{R}}$. (This fact allows us to drop the δ in front of σ for all but the $\mathbf{q} = 0$ mode.) Using the fact that $\tilde{\sigma}_0 = \sum_{\mathbf{R}} \sigma_{\mathbf{R}} = N\langle\sigma\rangle$, where $\langle\cdots\rangle$ denotes a spatial average, we can substitute Eq. 3.19 into Eq. 3.18 to obtain:

$$\mathcal{H}_{\mathbf{q}=0} = 2ZN\left(\langle\sigma\rangle - \left(\frac{a - l_{AB}}{\Delta}\right)\right)^2. \tag{3.20}$$

Thus, if the composition c is fixed (so $\langle\sigma\rangle = 2c - 1$), the lattice constant a will exhibit harmonic fluctuations about the minimum-energy value:

$$a = l_{AB} + \Delta(2c - 1). \tag{3.21}$$

However, the energy penalty for these fluctuations is manifestly extensive and so such fluctuations can be neglected in the thermodynamic limit. We thus see that the net composition effectively sets the system's volume. Finite-sized simulations exhibit fluctuations in a that are consistent with this prediction.

3.6 Effective Hamiltonian

Mechanical fluctuations in the small-mismatch (Gaussian) limit can be integrated out exactly [36], yielding marginal statistics of the composition field that corresponds to a Boltzmann distribution with effective energy $\mathcal{H}_{\text{eff}}$. To derive this energy function, we first write the composition and displacement fields in terms of their real and imaginary parts:

$$\tilde{\mathbf{u}}_{\mathbf{q}} = \mathbf{a}_{\mathbf{q}} + i\mathbf{b}_{\mathbf{q}} \tag{3.22a}$$

$$\tilde{\mathbf{u}}_{-\mathbf{q}} = \mathbf{a}_{\mathbf{q}} - i\mathbf{b}_{\mathbf{q}} \tag{3.22b}$$

$$\tilde{\sigma}_{\mathbf{q}} = c_{\mathbf{q}} + id_{\mathbf{q}} \tag{3.22c}$$

$$\tilde{\sigma}_{-\mathbf{q}} = c_{\mathbf{q}} - id_{\mathbf{q}}. \tag{3.22d}$$

Plugging these into the Hamiltonian yields:

$$\mathcal{H}_{\mathbf{q}\neq 0} = \frac{2}{N}\sum_{\mathbf{q}\neq 0}\left[\mathbf{a_q}\cdot\mathbf{F_q}\cdot\mathbf{a_q} + \mathbf{b_q}\cdot\mathbf{F_q}\cdot\mathbf{b_q} + \frac{1}{4}(c_\mathbf{q}^2 + d_\mathbf{q}^2)g_\mathbf{q} - i\Delta\mathbf{h_q}\cdot(c_\mathbf{q}\mathbf{b_q} - d_\mathbf{q}\mathbf{a_q})\right]. \quad (3.23)$$

Now we need to integrate out the fields $\mathbf{a_q}$ and $\mathbf{b_q}$. This is equivalent (up to an unimportant constant) to minimizing the Hamiltonian with respect to $\mathbf{a_q}$ and $\mathbf{b_q}$, since their fluctuations are harmonic. Setting the derivatives of Eq. 3.23 with respect to $\mathbf{a_q}$ and $\mathbf{b_q}$ equal to zero, we find:

$$\mathbf{a_q} = -i\frac{1}{2}d_\mathbf{q}\mathbf{F_q}^{-1}\cdot\mathbf{h_q} \quad (3.24)$$

$$\mathbf{b_q} = i\frac{1}{2}c_\mathbf{q}\mathbf{F_q}^{-1}\cdot\mathbf{h_q}. \quad (3.25)$$

Plugging these values into our Hamiltonian and simplifying gives us an effective Hamiltonian:

$$\mathcal{H}_{\text{eff}} = \frac{1}{2N}\sum_{\mathbf{q}\neq 0}|\tilde{\sigma}_\mathbf{q}|^2\left(\mathbf{h_q}\cdot\mathbf{F_q}^{-1}\cdot\mathbf{h_q} + g_\mathbf{q}\right). \quad (3.26)$$

where we have used the fact that $c_\mathbf{q}^2 + d_\mathbf{q}^2 = |\tilde{\sigma}_\mathbf{q}|^2$. We identify the term in parentheses as a Fourier-space effective potential:

$$\tilde{U}_\mathbf{q} = \mathbf{h_q}\cdot\mathbf{F_q}^{-1}\cdot\mathbf{h_q} + g_\mathbf{q}, \quad (3.27)$$

so we can write the effective Hamiltonian as:

$$\mathcal{H}_{\text{eff}} = \frac{1}{2N}\sum_{\mathbf{q}\neq 0}\tilde{U}_\mathbf{q}|\tilde{\sigma}_\mathbf{q}|^2. \quad (3.28)$$

Instead of excluding the $\mathbf{q} = 0$ term from the sum, it is convenient to define a new effective potential:

$$\tilde{V}_\mathbf{q} = \begin{cases}\tilde{U}_\mathbf{q}, & \mathbf{q}\neq 0\\ 0, & \mathbf{q} = 0,\end{cases} \quad (3.29)$$

so that our effective Hamiltonian is:

$$\mathcal{H}_{\text{eff}} = \frac{1}{2N}\sum_{\mathbf{q}}\tilde{V}_\mathbf{q}|\tilde{\sigma}_\mathbf{q}|^2. \quad (3.30)$$

In real space, $\mathcal{H}_{\text{eff}}$ is a sum of pair interactions:

$$\mathcal{H}_{\text{eff}} = \frac{1}{2}\sum_{\mathbf{R},\mathbf{R}'\neq\mathbf{R}}\sigma_\mathbf{R}V_{\mathbf{R}-\mathbf{R}'}\sigma_{\mathbf{R}'}, \quad (3.31)$$

where $V_{\mathbf{R}} = \sum_{\mathbf{q}} \tilde{V}_{\mathbf{q}} e^{-i\mathbf{q}\cdot\mathbf{R}}/N$. In order to examine the features of the effective potential in more detail, we must specify a lattice structure. For the triangular lattice, the bond vectors are:

$$\hat{\boldsymbol{\alpha}}_1 = \begin{pmatrix} 1/2 \\ \sqrt{3}/2 \end{pmatrix} \tag{3.32a}$$

$$\hat{\boldsymbol{\alpha}}_2 = \begin{pmatrix} 1 \\ 0 \end{pmatrix} \tag{3.32b}$$

$$\hat{\boldsymbol{\alpha}}_3 = \begin{pmatrix} 1/2 \\ -\sqrt{3}/2 \end{pmatrix}, \tag{3.32c}$$

as well as their additive inverses $-\hat{\boldsymbol{\alpha}}_1$, $-\hat{\boldsymbol{\alpha}}_2$, $-\hat{\boldsymbol{\alpha}}_3$. The sum over bond vectors $\hat{\boldsymbol{\alpha}}$ includes all six of these vectors. For this choice, the Fourier components of the effective interaction potential $V_{\mathbf{R}}$ is given by:

$$\tilde{V}_{\mathbf{q}} = \frac{4\left(2\cos\frac{q_x a}{2}\cos\frac{\sqrt{3}q_y a}{2} + \cos q_x a - 3\right)^2}{(\cos q_x a - 2)\left(4\cos\frac{q_x a}{2}\cos\frac{\sqrt{3}q_y a}{2} - 3\right) + \cos\sqrt{3}q_y a}, \tag{3.33}$$

where x and y indicate Cartesian components. The real-space effective potential is computed as the (numerical) inverse Fourier transform of Eq. 3.33; it asymptotically scales as $1/|\mathbf{R}|^4$ (see Appendix B.2.) Fig. 3.2 shows the effective compositional potential in both real- and reciprocal-space representations. Like the result of Ref. [36] for more complicated mechanical coupling on a square lattice, $\tilde{V}_{\mathbf{q}}$ has local minima near the boundary of the first Brillouin zone. Periodic variations in composition are thus least costly at microscopic wavelengths and along particular lattice directions, echoing the stability of superlattice phases observed in simulations. The modulated microstructure of these phases is suggested even more strongly by the dependence of $V_{\mathbf{R}}$ on atom separation, which we obtain by numerical inversion of the Fourier transform. Elastic interactions clearly disfavor the placement of defects on neighboring lattice sites (see Appendix B.3 for a detailed analysis of defect configurations.)

It is worth noting that the potential is discontinuous at $\mathbf{q} = 0$. We have $\lim_{\mathbf{q}\to 0} \tilde{V}_{\mathbf{q}} = 8$, but $\tilde{V}_{\mathbf{q}=0} = 0$. This results in an infinitely long-ranged contribution to the potential whose magnitude scales with $1/N$. We will explore the implications of this contribution in more detail in Chapter 4; here, at fixed net composition, the value of $\tilde{V}_0$ is irrelevant.

3.7 Energetic Stability of Phase Coexistence

The structures observed in MC simulations suggest that phases with modulated order, and coexistence among such phases, are stable at low temperatures. Here we assess the stability of coexisting elastic phases of different compositions with respect to the creation of interfaces. To do so, we explicitly evaluate the energy of configurations with macroscopic spatial

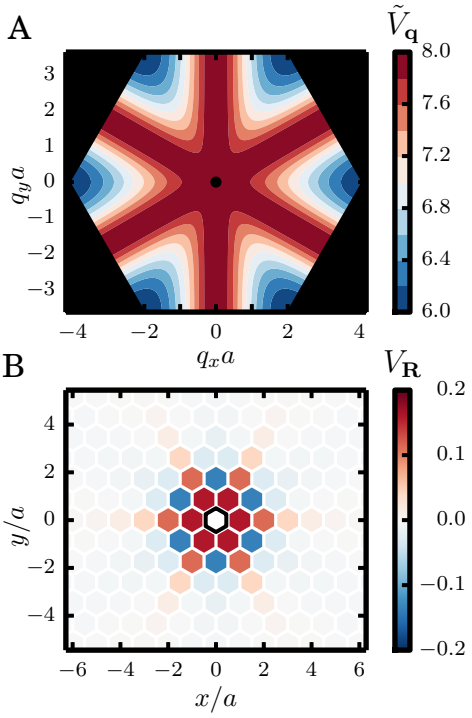

Figure 3.2: Effective pair potential V for the composition field in the small-mismatch approximation of Eq. 3.10. **A**: Reciprocal space representation $\tilde{V}_{\boldsymbol{q}}$, plotted in the first Brillouin zone. The black dot in the center indicates the discontinuity at $\boldsymbol{q} = \mathbf{0}$, where $\tilde{V}_{\mathbf{0}} = 0$. **B**: Effective interaction between an A (or B) atom at the origin (marked by the outlined hexagon) and another A (or B) atom at $\mathbf{R}$. Mixed interactions between A and B have opposite sign.

modulations of varying wavelength λ. If this energy decreases with increasing λ, then coexistence is energetically stable. The stability of coexistence will turn out to depend on the internal structure of the phases. In particular, we will see that while superlattice phases can stably coexist with each other or with an unstructured phase (at least at zero temperature,) coexistence between two unstructured phases is energetically unstable.

Form of the spatial modulations in Fourier space

We first write the spatially modulated composition field in Fourier space. In real space, a composition field $\sigma(\mathbf{r})$ which consists of a series of domains of alternating composition separated by sharp interfaces ("stripes") can be written as:

$$\sigma(\mathbf{r}) = \frac{1}{2}\left(\sigma_1(\mathbf{r}) + \sigma_2(\mathbf{r})\right) + s(\mathbf{r})\left(\sigma_1(\mathbf{r}) - \sigma_2(\mathbf{r})\right), \tag{3.34}$$

where $s(\mathbf{r})$ is a square wave whose direction of modulation is along an as-yet-unspecified axis, and where $\sigma_\mu(\mathbf{r})\,(\mu = 1, 2)$ are the (potentially spatially-dependent) composition fields of the two different macroscopic phases. In Fourier space, this field can be written as:

$$\tilde{\sigma}(\mathbf{q}) = \frac{1}{2}\left(\tilde{\sigma}_1(\mathbf{q})\right) + \tilde{\sigma}_2(\mathbf{q})) + \frac{1}{N}\sum_{\mathbf{q}'}\tilde{s}(\mathbf{q}-\mathbf{q}')\left(\tilde{\sigma}_1(\mathbf{q}') - \tilde{\sigma}_2(\mathbf{q}')\right), \tag{3.35}$$

where we have used the fact that the Fourier transform of a product of two functions in real space is their convolution in Fourier space. Before we can go any further, we need to determine the forms of $\tilde{\sigma}_\mu(\mathbf{q})$. In real space, since we allow for the possibility that the individual macroscopic phases can have periodic microscopic order, we write the composition field as:

$$\sigma_\mu(\mathbf{r}) = \sum_{\mathbf{b}_\mu} c_{\mathbf{b}_\mu} e^{i\mathbf{b}_\mu\cdot\mathbf{r}}, \tag{3.36}$$

where $\mathbf{b}_\mu$ are reciprocal lattice vectors. In Fourier space, this becomes:

$$\tilde{\sigma}_\mu(\mathbf{q}) = \sum_{\mathbf{b}_\mu} N c_{\mathbf{b}_\mu}\delta(\mathbf{q}, \mathbf{b}_\mu). \tag{3.37}$$

This expression can be derived straightforwardly:

$$\begin{aligned}
\tilde{\sigma}_\mu(\mathbf{q}) &= \sum_{\mathbf{r}} \sigma_\mu(\mathbf{r}) e^{-i\mathbf{q}\cdot\mathbf{r}} \\
&= \sum_{\mathbf{r}} \left(\sum_{\mathbf{b}_\mu} c_{\mathbf{b}_\mu} e^{i\mathbf{b}_\mu\cdot\mathbf{r}}\right) e^{-i\mathbf{q}\cdot\mathbf{r}} \\
&= \sum_{\mathbf{b}_\mu} c_{\mathbf{b}_\mu} \left(\sum_{\mathbf{r}} e^{i(\mathbf{b}_\mu - \mathbf{q})\cdot\mathbf{r}}\right) \\
&= \sum_{\mathbf{b}_\mu} N c_{\mathbf{b}_\mu}\delta(\mathbf{q}, \mathbf{b}_\mu).
\end{aligned}$$

The Fourier coefficients $c_{\mathbf{b}_\mu}$ can be determined by examining the real space composition field. For a phase with spatially uniform composition, $\sigma_\mu(\mathbf{r}) = \bar{\sigma}$, we have:

$$c_{\mathbf{b}_\mu} = \bar{\sigma}\delta(\mathbf{b}_\mu, 0), \tag{3.38}$$

while for a superlattice phase, where $\sigma_\mu(\mathbf{r}) = -\frac{1}{3} + \frac{4}{3}\cos\left(\Delta\mathbf{G}\cdot\mathbf{r}\right)$ (or its negative): [1]

$$c_{\mathbf{b}_\mu} = -\frac{1}{3}\delta(\mathbf{b}_\mu, 0) + \frac{2}{3}\delta(\mathbf{b}_\mu, \Delta\mathbf{G}) + \frac{2}{3}\delta(\mathbf{b}_\mu, -\Delta\mathbf{G}). \tag{3.39}$$

[1] The quantity $\Delta\mathbf{G} = \mathbf{G}_1 - \mathbf{G}_2$ is determined by $\mathbf{r}\cdot\Delta\mathbf{G} = \frac{2\pi}{3}(n_1 - n_2)$.

Now, for both spatially uniform and superlattice phases, $c_{\mathbf{b}_\mu} = c_{-\mathbf{b}_\mu}$, so we can write:

$$\tilde{\sigma}_\mu(\mathbf{q}) = {\sum_{\mathbf{b}_\mu}}' N c_{\mathbf{b}_\mu} \left(\delta(\mathbf{q}, \mathbf{b}_\mu) + \delta(\mathbf{q}, -\mathbf{b}_\mu)\right), \tag{3.40}$$

where the prime symbol indicates that the sum is to be taken over the positive half space, and implies a factor of 1/2 when $\mathbf{b}_\mu = 0$. Furthermore we separate the $\mathbf{b}_\mu = 0$ component from the sum and write:

$$\tilde{\sigma}_\mu(\mathbf{q}) = N c_{0,\mu} \delta(\mathbf{q}, 0) + {\sum_{\mathbf{b}_\mu}}'' N c_{\mathbf{b}_\mu} \left(\delta(\mathbf{q}, \mathbf{b}_\mu) + \delta(\mathbf{q}, -\mathbf{b}_\mu)\right), \tag{3.41}$$

where the extra prime symbol indicates that the $\mathbf{b}_\mu = 0$ term is excluded from the sum. The Fourier coefficient $c_{0,\mu}$ is equal to $\bar{\sigma}_\mu$, the net composition of phase μ. With this expression for the single-phase, Fourier-space composition fields in hand, we can write the overall Fourier-space composition field as:

$$\begin{aligned}\tilde{\sigma}(\mathbf{q}) = {} & N\left(\frac{\bar{\sigma}_1 + \bar{\sigma}_2}{2}\right)\delta(\mathbf{q}, 0) + (\bar{\sigma}_1 - \bar{\sigma}_2)\tilde{s}(\mathbf{q}) \\ & + {\sum_{\mathbf{b}_1}}'' c_{\mathbf{b}_1}\left(\frac{N}{2}\delta(\mathbf{q}, \mathbf{b}_1) + \frac{N}{2}\delta(\mathbf{q}, -\mathbf{b}_1) + \tilde{s}(\mathbf{q} - \mathbf{b}_1) + \tilde{s}(\mathbf{q} + \mathbf{b}_1)\right) \\ & + {\sum_{\mathbf{b}_2}}'' c_{\mathbf{b}_2}\left(\frac{N}{2}\delta(\mathbf{q}, \mathbf{b}_2) + \frac{N}{2}\delta(\mathbf{q}, -\mathbf{b}_2) - \tilde{s}(\mathbf{q} - \mathbf{b}_2) - \tilde{s}(\mathbf{q} + \mathbf{b}_2)\right)\end{aligned} \tag{3.42}$$

where $\tilde{s}(\mathbf{q})$ is given by (see Appendix B.4):

$$\tilde{s}(k_1, k_2) = (1 - e^{2\pi i k_2/N_2})^{-1}\delta(k_1, 0)\frac{N_1 N_2}{\lambda}\sum_{j=\pm1,\pm3,\ldots}^{\lambda} -\delta\left(k_2, \frac{N_2 j}{2\lambda}\right).$$

Evaluating stripe energies

Now we evaluate the energies for stripes with different kinds of microscopic structure.

Case 1: No microscopic structure

In the case of no microscopic structure in either phase, we have $c_{\mathbf{b}_\mu} = \bar{\sigma}_\mu \delta(\mathbf{b}_\mu, 0)$. Hence the composition field is given by:

$$\tilde{\sigma}(\mathbf{q}) = N\left(\frac{\bar{\sigma}_1 + \bar{\sigma}_2}{2}\right)\delta(\mathbf{q}, 0) + (\bar{\sigma}_1 - \bar{\sigma}_2)\tilde{s}(\mathbf{q}). \tag{3.43}$$

The energy of this field is:

$$\begin{aligned}
E &= \frac{1}{2N}\sum_{\mathbf{q}} |\tilde{\sigma}(\mathbf{q})|^2 \tilde{V}(\mathbf{q}) \\
&= \frac{(\bar{\sigma}_1 - \bar{\sigma}_2)^2}{2N}\sum_{\mathbf{q}} |\tilde{s}(\mathbf{q})|^2 \tilde{V}(\mathbf{q}) \\
&= \frac{\Delta\bar{\sigma}^2}{2}\sum_{k_1,k_2} \frac{\delta(k_2,0)}{2-2\cos\left(2\pi k_1/N_1\right)} \frac{1}{\lambda^2} \sum_{j=\pm 1,\ldots}^{\lambda} \delta\left(k_1, \frac{N_1 j}{2\lambda}\right) \tilde{V}(k_1,k_2) \\
&= \frac{\Delta\bar{\sigma}^2}{2\lambda^2}\sum_{k_1} \frac{1}{2-2\cos\left(2\pi k_1/N_1\right)} \sum_{j=\pm 1,\ldots}^{\lambda} \delta\left(k_1, \frac{N_1 j}{2\lambda}\right) \tilde{V}(k_1,0) \\
&= \boxed{\frac{\Delta\bar{\sigma}^2}{2\lambda^2} \sum_{j=\pm 1,\ldots}^{\lambda} \frac{\tilde{V}\left(\frac{N_1 j}{2\lambda},0\right)}{2-2\cos\left(\pi j/\lambda\right)}.}
\end{aligned}$$

(In the above we made the definition $\Delta\bar{\sigma} = \bar{\sigma}_1 - \bar{\sigma}_2$.) If we view $\tilde{V}$ as a function of q_x, q_y rather than k_1, k_2, then since $\mathbf{q}\cdot\hat{\mathbf{x}} = 2\pi j/\lambda$, we have:

$$\boxed{E(\lambda) = \frac{\Delta\bar{\sigma}^2}{2\lambda^2} \sum_{j=\pm 1,\ldots}^{\lambda} \frac{\tilde{V}\left(\frac{2\pi j}{\lambda},0\right)}{2-2\cos\left(\pi j/\lambda\right)}.} \tag{3.44}$$

Case 2: One spatially uniform phase, one superlattice phase

In the case of one spatially uniform phase and one superlattice phase, we have:

$$\begin{aligned}
c_{\mathbf{b}_1} &= \delta(\mathbf{b}_1, 0) \\
c_{\mathbf{b}_2} &= \frac{1}{3}\delta(\mathbf{b}_2,0) - \frac{2}{3}\delta(\mathbf{b}_2,\Delta\mathbf{G}) - \frac{2}{3}\delta(\mathbf{b}_2,-\Delta\mathbf{G}).
\end{aligned}$$

The composition field is then given by:

$$\begin{aligned}
\tilde{\sigma}(\mathbf{q}) = N\left(\frac{\bar{\sigma}_1+\bar{\sigma}_2}{2}\delta(\mathbf{q},0)\right) + \Delta\bar{\sigma}^2|\tilde{s}(\mathbf{q})|^2 \\
- \frac{2}{3}\left(\frac{N}{2}\delta(\mathbf{q},\Delta\mathbf{G}) + \frac{N}{2}\delta(\mathbf{q},-\Delta\mathbf{G}) - \tilde{s}(\mathbf{q}-\Delta\mathbf{G}) - \tilde{s}(\mathbf{q}+\Delta\mathbf{G})\right).
\end{aligned} \tag{3.45}$$

Taking the square modulus of the field (noting that many of the possible terms vanish due to the factor $\delta(k_2,0)$ contained in $\tilde{s}$,) we have:

$$\begin{aligned}
|\tilde{\sigma}(\mathbf{q})|^2 = N^2\left(\frac{\bar{\sigma}_1+\bar{\sigma}_2}{2}\right)^2\delta(\mathbf{q},0) + \Delta\bar{\sigma}^2|\tilde{s}(\mathbf{q})|^2 \\
+ \frac{4}{9}\left(N^2\delta(\mathbf{q},\Delta\mathbf{G}) + N^2\delta(\mathbf{q},-\Delta\mathbf{G}) + |\tilde{s}(\mathbf{q}-\Delta\mathbf{G})|^2 + |\tilde{s}(\mathbf{q}+\Delta\mathbf{G})|^2\right).
\end{aligned} \tag{3.46}$$

The energy is:

$$\begin{aligned} E(\lambda) &= \frac{1}{2N}\sum_{\mathbf{q}} |\tilde{\sigma}(\mathbf{q})|^2 \tilde{V}(\mathbf{q}) \\ &= \frac{\Delta\bar{\sigma}^2}{2N}\sum_{\mathbf{q}} |\tilde{s}(\mathbf{q})|^2 \tilde{V}(\mathbf{q}) + \frac{1}{9}N\left(\tilde{V}(\Delta\mathbf{G}) + \tilde{V}(-\Delta\mathbf{G})\right) \\ &+ \frac{2}{9}\frac{1}{N}\sum_{\mathbf{q}} \left(|\tilde{s}(\mathbf{q}-\Delta\mathbf{G})|^2 + |\tilde{s}(\mathbf{q}+\Delta\mathbf{G})|^2\right)\tilde{V}(\mathbf{q}). \end{aligned}$$

Writing:

$$\Delta\mathbf{G} = \frac{\alpha_1}{N_1}\mathbf{b}_1 + \frac{\alpha_2}{N_2}\mathbf{b}_2, \tag{3.47}$$

we have:

$$\begin{aligned} \tilde{s}(\mathbf{q}-\Delta\mathbf{G}) &= \tilde{s}(k_1-\alpha_1, k_2-\alpha_2) \\ &= \left(1 - e^{2\pi i(k_1-\alpha_1)/N_1}\right)^{-1} \delta(k_2,\alpha_2)\frac{N_1}{\lambda}\sum_{j=\pm1,\ldots}^{\lambda} \delta\left(k_1, \alpha_1 + \frac{N_1 j}{2\lambda}\right). \end{aligned}$$

Thus we can write the energy as:

$$\begin{aligned} E(\lambda) = \frac{\Delta\bar{\sigma}^2}{2\lambda^2}\sum_{j=\pm1,\ldots}^{\lambda} \frac{\tilde{V}\left(\frac{N_1 j}{2\lambda}, 0\right)}{2-2\cos\left(\pi j/\lambda\right)} + \frac{2}{9}N\tilde{V}(\Delta\mathbf{G}) \\ + \frac{2}{9\lambda^2}\left(\sum_{j=\pm1,\ldots}^{\lambda} \frac{\tilde{V}\left(\alpha_1 + \frac{N_1 j}{2\lambda}, \alpha_2\right)}{2-2\cos\left(\pi j/\lambda\right)} + \sum_{j=\pm1,\ldots}^{\lambda} \frac{\tilde{V}\left(-\alpha_1 + \frac{N_1 j}{2\lambda}, -\alpha_2\right)}{2-2\cos\left(\pi j/\lambda\right)}\right). \end{aligned}$$

Collecting terms,

$$\boxed{\begin{aligned} E(\lambda) = \frac{1}{9}N\tilde{V}(\Delta\mathbf{G}) + \frac{1}{2\lambda^2}\sum_{j=\pm1,\ldots}^{\lambda}\left(\frac{\Delta\bar{\sigma}^2\tilde{V}\left(\frac{N_1 j}{2\lambda}, 0\right)}{2-2\cos\left(\pi j/\lambda\right)}\right. \\ \left. + \frac{4}{9}\frac{\left(\tilde{V}\left(\alpha_1 + \frac{N_1 j}{2\lambda}, \alpha_2\right) + \tilde{V}\left(-\alpha_1 + \frac{N_1 j}{2\lambda}, -\alpha_2\right)\right)}{2-2\cos\left(\pi j/\lambda\right)}\right). \end{aligned}} \tag{3.48}$$

Again, we could express $\tilde{V}$ in terms of q_x and q_y instead of k_1 and k_2. To do so, note that:

$$\begin{aligned} 3\Delta\mathbf{G} &= 2\pi(1, -\sqrt{3}) \\ &= -3\mathbf{b}_2 - \mathbf{b}_1 \\ \implies \Delta\mathbf{G} &= -\frac{1}{3}\mathbf{b}_1 - \mathbf{b}_2 \\ &= -\frac{N_1/3}{N_1}\mathbf{b}_1 - \frac{N_2}{N_2}\mathbf{b}_2. \end{aligned}$$

So,

$$\alpha_1 = -N_1/3$$
$$\alpha_2 = -N_2.$$

Then it is just a matter of computing $\mathbf{q} \cdot \hat{\mathbf{x}}$ and $\mathbf{q} \cdot \hat{\mathbf{y}}$ from the definition of $\mathbf{q}$.

Case 3: Two superlattice phases in register

In the case of two superlattice phases, we have:

$$c_{\mathbf{b}_1} = \frac{1}{3}\delta(\mathbf{b}_2, 0) - \frac{2}{3}\delta(\mathbf{b}_2, \Delta\mathbf{G}) - \frac{2}{3}\delta(\mathbf{b}_2, -\Delta\mathbf{G})$$
$$c_{\mathbf{b}_2} = -\frac{1}{3}\delta(\mathbf{b}_2, 0) + \frac{2}{3}\delta(\mathbf{b}_2, \Delta\mathbf{G}) + \frac{2}{3}\delta(\mathbf{b}_2, -\Delta\mathbf{G}).$$

In this section we shall assume that the two phases are "in register," i.e. that the interface between the superlattices is not offset by some vector. In this case, the composition field is:

$$\tilde{\sigma}(\mathbf{q}) = \Delta\bar{\sigma}\tilde{s}(\mathbf{q}) - \frac{4}{3}\left(\tilde{s}(\mathbf{q} - \Delta\mathbf{G}) + \tilde{s}(\mathbf{q} + \Delta\mathbf{G})\right), \tag{3.49}$$

so,

$$|\tilde{\sigma}(\mathbf{q})|^2 = \Delta\bar{\sigma}^2|\tilde{s}(\mathbf{q})|^2 + \frac{16}{9}\left(|\tilde{s}(\mathbf{q} - \Delta\mathbf{G})|^2 + |\tilde{s}(\mathbf{q} + \Delta\mathbf{G})|^2\right). \tag{3.50}$$

The energy is:

$$\begin{aligned} E(\lambda) &= \frac{1}{2N}\sum_{\mathbf{q}} |\tilde{\sigma}(\mathbf{q})|^2 \tilde{V}(\mathbf{q}) \\ &= \frac{\Delta\bar{\sigma}^2}{2N}\sum_{\mathbf{q}} |\tilde{s}(\mathbf{q})|^2 \tilde{V}(\mathbf{q}) + \frac{8}{9N}\sum_{\mathbf{q}} \left(|\tilde{s}(\mathbf{q} - \Delta\mathbf{G})|^2 + |\tilde{s}(\mathbf{q} + \Delta\mathbf{G})|^2\right)\tilde{V}(\mathbf{q}) \\ &= \boxed{\frac{1}{2\lambda^2}\sum_{j=\pm 1,\ldots}^{\lambda} \frac{\Delta\bar{\sigma}^2\tilde{V}\left(\frac{N_1 j}{2\lambda}, 0\right) + \frac{16}{9}\left(\tilde{V}\left(\alpha_1 + \frac{N_1 j}{2\lambda}, \alpha_2\right) + \tilde{V}\left(-\alpha_1 + \frac{N_1 j}{2\lambda}, -\alpha_2\right)\right)}{2 - 2\cos(\pi j/\lambda)}.} \end{aligned} \tag{3.51}$$

Case 4: Two superlattice phases out of register

In this section we shall allow for the possibility that the two phases are out of register by some vector $\mathbf{a}$. The composition fields of the individual phases are given by:

$$\sigma_1(\mathbf{r}) = \frac{1}{3} - \frac{4}{3}\cos(\mathbf{r} \cdot \Delta\mathbf{G})$$
$$\sigma_2(\mathbf{r}) = -\frac{1}{3} + \frac{4}{3}\cos((\mathbf{r} + \mathbf{a}) \cdot \Delta\mathbf{G}),$$

and so:

$$c_{\mathbf{b}_1} = \frac{1}{3}\delta(\mathbf{b}_2, 0) - \frac{2}{3}\delta(\mathbf{b}_2, \Delta\mathbf{G}) - \frac{2}{3}\delta(\mathbf{b}_2, -\Delta\mathbf{G})$$
$$c_{\mathbf{b}_2} = -\frac{1}{3}\delta(\mathbf{b}_2, 0) + \frac{2}{3}e^{i\Delta\mathbf{G}\cdot\mathbf{a}}\delta(\mathbf{b}_2, \Delta\mathbf{G}) + \frac{2}{3}e^{-i\Delta\mathbf{G}\cdot\mathbf{a}}\delta(\mathbf{b}_2, -\Delta\mathbf{G}).$$

In this case, the composition field is:

$$\tilde{\sigma}(\mathbf{q}) = \Delta\bar{\sigma}\tilde{s}(\mathbf{q}) + \frac{N}{3}(e^{i\Delta\mathbf{G}\cdot\mathbf{a}} - 1)\left(\delta(\mathbf{q}, \Delta\mathbf{G}) + \delta(\mathbf{q}, -\Delta\mathbf{G})\right) - \frac{2}{3}(e^{i\Delta\mathbf{G}\cdot\mathbf{a}} + 1)\left(\tilde{s}(\mathbf{q} - \Delta\mathbf{G}) + \tilde{s}(\mathbf{q} + \Delta\mathbf{G})\right),$$

so,

$$|\tilde{\sigma}(\mathbf{q})|^2 = \Delta\bar{\sigma}^2|\tilde{s}(\mathbf{q})|^2 + \frac{N^2}{9}(2 - 2\cos(\Delta\mathbf{G}\cdot\mathbf{a}))\left(\delta(\mathbf{q}, \Delta\mathbf{G}) + \delta(\mathbf{q}, -\Delta\mathbf{G})\right) + \frac{4}{9}(2 + 2\cos(\Delta\mathbf{G}\cdot\mathbf{a}))\left(|\tilde{s}(\mathbf{q} - \Delta\mathbf{G})|^2 + |\tilde{s}(\mathbf{q} + \Delta\mathbf{G})|^2\right),$$

and hence the energy is:

$$\begin{aligned} E(\lambda) &= \frac{1}{2N}\sum_{\mathbf{q}} |\tilde{\sigma}(\mathbf{q})|^2\tilde{V}(\mathbf{q}) \\ &= \frac{\Delta\bar{\sigma}^2}{2N}\sum_{\mathbf{q}} |\tilde{s}(\mathbf{q})|^2\tilde{V}(\mathbf{q}) + \frac{N}{18}(2 - 2\cos(\Delta\mathbf{G}\cdot\mathbf{a}))\left(\tilde{V}(\Delta\mathbf{G}) + \tilde{V}(-\Delta\mathbf{G})\right) \\ &\quad + \frac{2}{9N}(2 + 2\cos(\Delta\mathbf{G}\cdot\mathbf{a}))\sum_{\mathbf{q}}\left(|\tilde{s}(\mathbf{q} - \Delta\mathbf{G})|^2 + |\tilde{s}(\mathbf{q} + \Delta\mathbf{G})|^2\right)\tilde{V}(\mathbf{q}). \end{aligned}$$

Plugging in $\tilde{s}$ and simplifying we have, finally,

$$\boxed{E(\lambda) = \frac{1}{9}N(2 - 2\cos(\Delta\mathbf{G}\cdot\mathbf{a}))\tilde{V}(\Delta\mathbf{G}) + \frac{1}{2\lambda^2}\sum_{j=\pm1,\ldots}^{\lambda}\left(\frac{\Delta\bar{\sigma}^2\tilde{V}\left(\frac{N_1 j}{2\lambda}, 0\right)}{2 - 2\cos(\pi j/\lambda)} + \frac{4}{9}\frac{(2 + 2\cos(\Delta\mathbf{G}\cdot\mathbf{a}))\left(\tilde{V}\left(\alpha_1 + \frac{N_1 j}{2\lambda}, \alpha_2\right) + \tilde{V}\left(-\alpha_1 + \frac{N_1 j}{2\lambda}, -\alpha_2\right)\right)}{2 - 2\cos(\pi j/\lambda)}\right).} \tag{3.52}$$

A single superlattice domain

We need the energy of a single bulk superlattice in order to compare stripe energies. To do so, note that for a superlattice the composition field is given by:

$$\tilde{\sigma}(\mathbf{q}) = -\frac{1}{3}N\delta(\mathbf{q}, 0) + \frac{2}{3}N\delta(\mathbf{q}, \Delta\mathbf{q}) + \frac{2}{3}N\delta(\mathbf{q}, -\Delta\mathbf{q}), \tag{3.53}$$

so the energy is:

$$\begin{aligned} E_{\text{super}} &= \frac{1}{2N}\sum_{\mathbf{q}} |\tilde{\sigma}(\mathbf{q})|^2 \tilde{V}(\mathbf{q}) \\ &= \frac{2}{9} N\tilde{V}\left(\Delta\mathbf{G}) + \tilde{V}(-\Delta\mathbf{G})\right) \\ &= \frac{4}{9} N\tilde{V}(\Delta\mathbf{G}). \end{aligned}$$

Numerical evaluation of energies

Now we can numerically evaluate the energies of different stripe configurations. Since $\tilde{V}(\Delta\mathbf{G}) = 6$, the energy, per atom, of a single superlattice domain is:

$$E_{\text{super}}/N = \frac{4}{9}\tilde{V}(\Delta\mathbf{G}) = \frac{8}{3}. \tag{3.54}$$

Our theoretical results for $E(\lambda)$ agree essentially exactly with the results of energy minimization of our simulated system. Plots comparing these results are shown in Figs. 3.3, 3.4 and 3.5. We see that the energy of stripes consisting of unstructured phases increases with λ, but that of stripes consisting of an unstructured phase and a superlattice phase, or of two superlattice phases, decreases with λ. This means that coexistence between large unstructured domains is energetically unstable, while coexistence between a large unstructured domain and a large superlattice domain or between two large superlattice domains is energetically stable. These results are consistent with the observations of coexistence in MC simulations between two modulated phases and between a modulated and an unstructured phase, but not between two unstructured phases.

In the limit $\lambda \to \infty$, the expressions for $E(\lambda)$ above yield the energies associated with coexistence between two different macroscopic domains present in equal proportions. We compute these energies numerically, truncating their associated sums at large λ (we choose $\lambda = 10000$; including further terms only change the sums by fractions of a percent.)[2] They are given by:

$$\begin{aligned} E_{\text{unstruct+unstruct}}/N &\approx 4.01492 \\ E_{\text{unstruct+super}}/N - \frac{1}{2}E_{\text{super}}/N &\approx 0.446148 \\ E_{\text{super+super}}/N - E_{\text{super}}/N &\approx 0.446280. \end{aligned}$$

These are the energy penalties associated with coexistence between two unstructured phases, an unstructured and a superlattice phase, and two (in-register) superlattice phases, respectively. (Note that we have subtracted off the energies of the bulk phases.) These calculations tell us that, unlike in conventional systems, the energy of coexistence scales linearly with

[2]The exact energy of phase separation can in fact be evaluated analytically; see Appendix B.5.

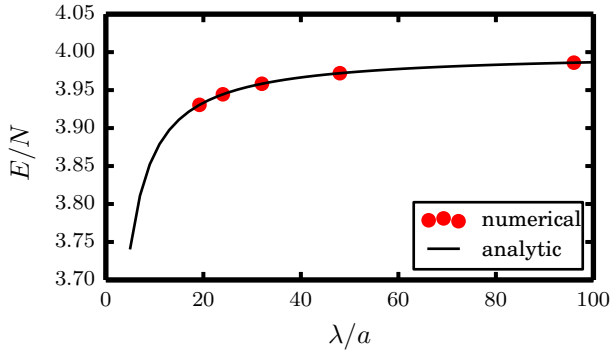

Figure 3.3: Energy associated with unstructured stripes (with uniform compositions.)

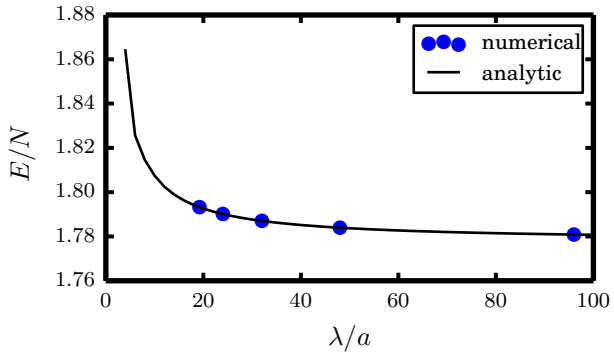

Figure 3.4: Energy of superlattice/unstructured stripes.

system size N rather than with the interfacial area between domains. Furthermore, the fact that $E_{\text{unstruct+unstruct}} > E_{\text{super+super}}$ even though the net composition is the same in both coexistence scenarios provides a reason for why we do not see coexistence between unstructured phases in simulations.

3.8 Mean Field Theory

While the preceding analysis of perfectly ordered phases reveals the energetically preferred patterns of composition at zero temperature, it cannot tell us about the stability of phases at finite temperature. For that, we turn to mean field theory (MFT.) The effective Hamiltonian

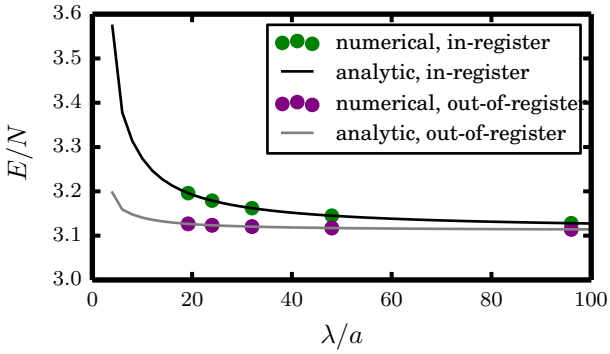

Figure 3.5: Energy of superlattice/superlattice stripes. The black line and green dots are for an in-register interface; the gray line and purple dots are for an out-of-register interface.

$\mathcal{H}_{\text{eff}}(\{\sigma_{\mathbf{R}}\})$ for compositional fluctuations can serve as the basis for a simple MFT.[3] Following standard treatments [18, 26], we consider a reference system of noninteracting spins in an external field that may differ among the three sublattices, subject to the requirement that the net composition c (which can take on real values between 0 and 1) be fixed:

$$\bar{m} = 2c - 1 = \frac{1}{N}\sum_{\mathbf{R}} \sigma_{\mathbf{R}}. \tag{3.55}$$

In analogy with magnetic systems, we refer to $\bar{m}$ as the net magnetization. Anticipating modulated order, we write a reference Hamiltonian in which each of n sublattices is subject to a different effective field [26]:

$$\mathcal{H}_0 = -\sum_{\gamma=1}^{n} h_\gamma \sum_{\mathbf{R}}{}^{(\gamma)} \sigma_{\mathbf{R}}, \tag{3.56}$$

where h_γ is an effective field that acts only on sublattice γ, and the γ superscript in the sum over lattice sites emphasizes that the sum is taken only over sites on sublattice γ. The corresponding reference partition function is:

$$Q_0 = \sum_{\{\sigma_{\mathbf{R}}\}}{}' e^{-\beta \mathcal{H}_0(\{\sigma_{\mathbf{R}}\})}, \tag{3.57}$$

where the prime symbol reminds us that the sum must respect the constraint $\frac{1}{N}\sum_{\mathbf{R}} \sigma_{\mathbf{R}} = \bar{m}$. Performing the constrained sum directly is difficult. Instead, we introduce a Lagrange

[3] Fratzl and Penrose [36] wrote down a very simple MFT to predict the critical temperature on a square elastic lattice; we consider an MFT in the vein of theirs in Appendix B.6.

multiplier μ and write:

$$\begin{aligned} Q_0 &= \sum_{\{\sigma_{\mathbf{R}}\}} e^{\beta\mu\left(\sum_{\mathbf{R}}\sigma_{\mathbf{R}} - N\bar{m}\right) - \beta\mathcal{H}_0} \\ &= e^{-\beta\mu N\bar{m}} \prod_{\gamma} \prod_{\mathbf{R}}{}^{(\gamma)} 2\cosh\beta(\mu + h_\gamma) \\ &= e^{-\beta\mu N\bar{m}} \prod_{\gamma} \left[2\cosh\beta(\mu + h_\gamma)\right]^{N_\gamma}, \end{aligned}$$

where N_γ is the number of sites on sublattice γ. The sublattice magnetization, defined as:

$$m_\gamma = \langle\sigma_{\mathbf{R}}\rangle^{(\gamma)} = \frac{1}{N_\gamma}\sum_{\mathbf{R}}{}^{(\gamma)}\sigma_{\mathbf{R}}, \tag{3.58}$$

is determined by the soon-to-be self-consistent equation:

$$m_\gamma = \frac{1}{N_\gamma}\frac{\partial \log Q_0}{\partial\beta h_\gamma} = \tanh\beta(\mu + h_\gamma). \tag{3.59}$$

Now we apply the Gibbs-Bogoliubov-Feynman estimate [18]:

$$Q_{\text{est}} = Q_0 e^{-\beta\langle\Delta\mathcal{H}\rangle_0}, \tag{3.60}$$

where $\Delta\mathcal{H} = \mathcal{H}_{\text{eff}} - \mathcal{H}_0$, and where $\langle\ldots\rangle_0$ indicates an average with respect to the reference Hamiltonian. To determine the optimal effective fields we maximize the logarithm of Q_{est}:

$$\begin{aligned} 0 &= \frac{\partial \log Q_{\text{est}}}{\partial\beta h_\gamma} \\ &= \underbrace{\frac{\partial \log Q_0}{\partial\beta h_\gamma}}_{(i)} - \underbrace{\beta\frac{\partial\langle\mathcal{H}_{\text{eff}}\rangle_0}{\partial\beta h_\gamma}}_{(ii)} + \underbrace{\beta\frac{\partial\langle\mathcal{H}_0\rangle_0}{\partial\beta h_\gamma}}_{(iii)}. \end{aligned} \tag{3.61}$$

We evaluate Eq. 3.61 term-by-term:

$$\begin{aligned} (i): \quad \frac{\partial \log Q_0}{\partial\beta h_\gamma} &= \left\langle \sum_{\mathbf{R}}{}^{(\gamma)}\sigma_{\mathbf{R}} \right\rangle_0 \\ &= \boxed{N_\gamma m_\gamma.} \end{aligned} \tag{3.62}$$

Next,

$$\begin{aligned}(ii): \quad \langle \mathcal{H}_{\text{eff}} \rangle_0 &= \left\langle \frac{1}{2} \sum_{\mathbf{R},\mathbf{R}' \neq \mathbf{R}} V_{\mathbf{R},\mathbf{R}'} \sigma_{\mathbf{R}} \sigma_{\mathbf{R}'} \right\rangle_0 \\ &= \frac{1}{2} \left\langle \sum_{\gamma,\delta} \sum_{\mathbf{R}}^{(\gamma)} \sum_{\mathbf{R}' \neq \mathbf{R}}^{(\delta)} V_{\mathbf{R},\mathbf{R}'} \sigma_{\mathbf{R}}^{(\gamma)} \sigma_{\mathbf{R}'}^{(\delta)} \right\rangle_0 \\ &= \frac{1}{2} \sum_{\gamma,\delta} \sum_{\mathbf{R}}^{(\gamma)} \sum_{\mathbf{R}' \neq \mathbf{R}}^{(\delta)} V_{\mathbf{R},\mathbf{R}'} \left\langle \sigma_{\mathbf{R}}^{(\gamma)} \right\rangle_0 \left\langle \sigma_{\mathbf{R}'}^{(\delta)} \right\rangle_0 \\ &= \sum_{\gamma,\delta} J_{\gamma\delta} m_\gamma m_\delta, \end{aligned} \tag{3.63}$$

where we have defined:

$$J_{\gamma\delta} = \frac{1}{2} \sum_{\mathbf{R}}^{(\gamma)} \sum_{\mathbf{R}' \neq \mathbf{R}}^{(\delta)} V_{\mathbf{R},\mathbf{R}'}, \tag{3.64}$$

which describes the net coupling between sublattices γ and δ. Now we can take the derivative:

$$\begin{aligned}\frac{\partial \langle \mathcal{H}_{\text{eff}} \rangle_0}{\partial h_\gamma} &= 2 \sum_\delta m_\delta \frac{\partial m_\delta}{\partial h_\gamma} J_{\delta\delta} + 2 \sum_{\delta,\theta \neq \delta} m_\delta \frac{\partial m_\theta}{\partial h_\gamma} J_{\delta\theta} \\ &= \boxed{2 \sum_{\delta,\theta} m_\delta \frac{\partial m_\delta}{\partial h_\gamma} J_{\delta\theta}.} \end{aligned} \tag{3.65}$$

Our last term is:

$$\begin{aligned}(iii): \quad \langle \mathcal{H}_0 \rangle_0 &= \left\langle -\sum_\gamma h_\gamma \sum_{\mathbf{R}}^{(\gamma)} \sigma_{\mathbf{R}} \right\rangle_0 \\ &= -\sum_\gamma h_\gamma m_\gamma N_\gamma \\ \implies \frac{\partial \langle \mathcal{H}_0 \rangle_0}{\partial h_\gamma} &= \boxed{-m_\gamma N_\gamma - \sum_\delta h_\delta \frac{\partial m_\delta}{\partial h_\gamma} N_\delta.} \end{aligned} \tag{3.66}$$

Putting everything together, we have:

$$0 = 2 \sum_{\delta,\theta} m_\delta \frac{\partial m_\theta}{\partial h_\gamma} J_{\delta\theta} + \sum_\delta N_\delta \frac{\partial m_\delta}{\partial h_\gamma} h_\delta, \tag{3.67}$$

or, grouping terms by derivatives,

$$0 = \sum_\delta \frac{\partial m_\delta}{\partial h_\gamma} \left(2 \sum_\theta m_\theta J_{\delta\theta} + N_\delta h_\delta \right). \tag{3.68}$$

A solution to the above is:

$$h_\delta = -\frac{2}{N_\delta}\sum_\theta m_\theta J_{\delta\theta}. \tag{3.69}$$

We thus have a set of self-consistent equations:

$$m_\gamma = \tanh\beta\left(\mu - \frac{2}{N_\gamma}\sum_\delta m_\delta J_{\gamma\delta}\right), \tag{3.70}$$

subject to the constraint:

$$\bar{m} = \sum_\gamma m_\gamma x_\gamma, \tag{3.71}$$

where $x_\gamma = N_\gamma/N$. There may be multiple possible solutions to the above self-consistent equations, but the physically acceptable ones will minimize the free energy:

$$\begin{aligned} F(\bar{m}) &= -k_B T \log Q_{\text{est}}(\bar{m}) \\ &= -k_B T \sum_\gamma N_\gamma \log\left[2\cosh\left(\tanh^{-1} m_\gamma\right)\right] - \sum_{\gamma,\delta} J_{\gamma,\delta} m_\gamma m_\delta + \mu N \bar{m}. \end{aligned} \tag{3.72}$$

Eqs. 3.70, 3.71, and 3.72 constitute the mean field solution to the problem of modulated order at a fixed net composition. To apply it, we simply need to specify the sublattices and evaluate the coupling constants $J_{\gamma\delta}$. The sublattices comprising the triangular lattice are shown in Fig. 3.6. The self-consistent equations can be solved numerically to yield the equilibrium values for the sublattice magnetizations (and μ.) We did so using Scipy's [57] root-finding routine "brentq" in the "optimize" package [10]. In Fig. 3.7 we plot our order parameter Δm, defined as the (magnitude of the) difference between the largest sublattice magnetization and the smallest sublattice magnetization, for a fixed composition of $c = 2/3$ ($\bar{m} = 1/3$.) We see that mean field theory predicts a (first-order) transition from a high temperature disordered state to a low-temperature state in which the sublattices attain net magnetizations different from $\bar{m}$. Specifically, one sublattice attains a negative magnetization, and the other two attain a positive magnetization. That is, one sublattice is occupied by predominantly B atoms, while the other two are occupied by predominantly A atoms.

Numerical solution of the mean field equations also determines an estimate $F_{\text{MFT}}(c)$ for the free energy. This mean-field approximation successfully captures some of the general features of our simulation results, particularly at low temperature. For the example plotted in Fig. 3.1B, discrepancies are small over the entire range of c, and significant only where simulations show two phases coexisting in similar proportions. Since the states considered in MFT are macroscopically uniform by construction, a failure to describe phase equilibrium is expected. From such a theory of uniform states, assessing the thermodynamics of coexistence would typically proceed by Maxwell construction, removing non-convex regions of $F_{\text{MFT}}(c)$ that usually signal instability to the formation of interfaces. For a case in which the true free

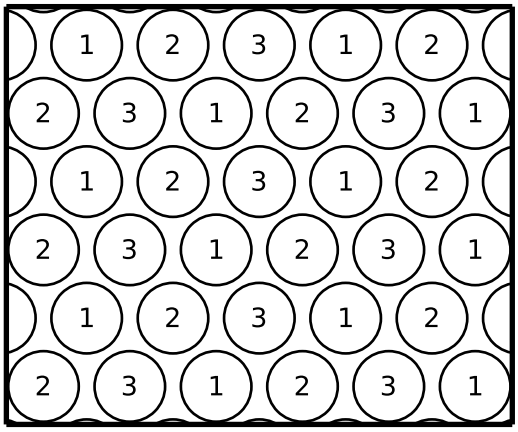

Figure 3.6: The triangular lattice naturally decomposes into three intercalating sublattices, as labeled above.

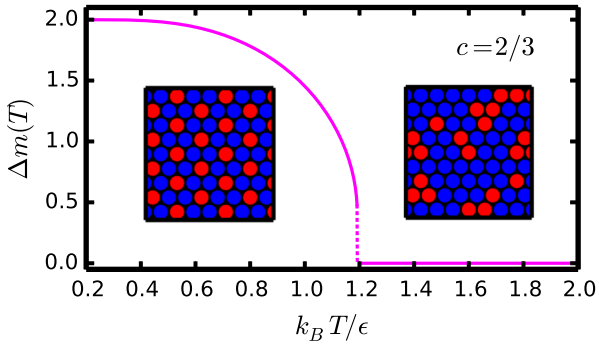

Figure 3.7: Plot of the order parameter Δm as a function of temperature, computed by solving the mean-field equations (3.70, 3.71, and 3.72) at a composition $c = 2/3$. The discontinuous jump in Δm at $k_B T/\epsilon \approx 1.2$ (indicated by the dashed line) marks a first order phase transition from a disordered phase to a superlattice phase. A schematic superlattice configuration is shown on the left, while a schematic disordered configuration is shown on the right.

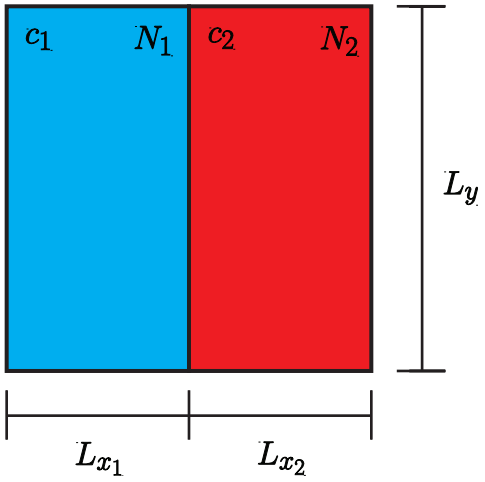

Figure 3.8: Schematic of a phase-separated configuration.

energy is non-convex, a different procedure is clearly needed. As has been noted previously in the context of capillary wave suppression in elastic solids [104], here we must specifically acknowledge an extensive thermodynamic penalty to accommodate domains with differing lattice constants in a rectangular macroscopic geometry.

3.9 Free Energy of Elastic Coexistence

Linear elasticity theory associates an energy $E = Y(L - L_0)^2$ with deforming a solid from its natural length L_0 to a length L, where Y is Young's modulus [67, 96]. From this rule we can estimate the cost of phase coexistence in a lattice-mismatched solid. Consider two phases with compositions c_1 and c_2, whose macroscopically uniform realizations have free energies per particle $f(c_1)$ and $f(c_2)$. We assume for simplicity that the interface between these domains is parallel to the y-axis. Domains 1 and 2 have numbers of atoms N_1 and N_2, and widths of L_{x_1} and L_{x_2}, respectively. Both domains have length L_y. This constraint on the dimensions of the domains causes elastic strain. A schematic of this setup is shown in Fig. 3.8. We define:

$$l_y = L_y/N_y, \tag{3.73}$$

where N_y is the number of lattice sites along the y direction, and:

$$n_i = N_i/N, \tag{3.74}$$

where $i = 1, 2$. Additionally, we have the following constraints:

$$n_1 + n_2 = 1 \tag{3.75a}$$

$$n_1 c_1 + n_2 c_2 = c. \tag{3.75b}$$

Now let us consider the free energy of coexistence. This is given by:

$$F_{\text{coex}}(c_1, c_2; c) = N_1 f(c_1, l_y) + N_2 f(c_2, l_y) + (\text{int.}), \tag{3.76}$$

where f is the free energy density of a homogeneous phase, and the final term denotes energetic contributions that scale with the interfacial length (and which we neglect in the thermodynamic limit.) Noting that in an elastic medium there is a restoring force against changes in length, and that for small enough changes the associated energy is quadratic in the change, we write the free energy density as:

$$f(c_1, l_y) = f(c_1, \bar{l}_y(c_1)) + Y_y(l_y - \bar{l}_y)^2, \tag{3.77}$$

where $\bar{l}_y(c_1)$ is the unstrained value of l_y for a homogeneous medium with composition c_1, and Y_y is a Young's modulus for stretching or compressing the medium in the y direction. In what follows, we shall drop the subscripts to make things cleaner, i.e. let $l_y = l$ and $Y_y = Y$. Now we make an assumption about the dependence of $\bar{l}$ on concentration, namely:

$$\bar{l}(c) = \bar{l}(0) + c\Delta l, \tag{3.78}$$

where $\Delta l \equiv \bar{l}(1) - \bar{l}(0)$. This assumption is known as Vegard's law [112] and we have observed in simulations that it holds for our microscopic elastic model.

Before proceeding to analyze the free energy, let us ask what the equilibrium value of l is for the phase-separated system. This is determined by minimizing the free energy with respect to l:

$$\begin{aligned}
0 = \frac{\partial F_{\text{coex}}(c_1, c_2; c)/N}{\partial l} &= 2n_1 Y(l - \bar{l}(c_1)) + 2n_2 Y(l - \bar{l}(c_2)) \\
\implies 0 &= (n_1 + n_2)l - (n_1\bar{l}(c_1) + n_2\bar{l}(c_2)) \\
&= l - n_1(\bar{l}(0) + c_1\Delta l) - n_2(\bar{l}(0) + c_2\Delta l) \\
&= l - \bar{l}(0) - (n_1 c_1 + n_2 c_2)\Delta l \\
&= l - \bar{l}(0) - c\Delta l \\
\implies l &= \bar{l}(0) + c\Delta l,
\end{aligned} \tag{3.79}$$

where we have used eqs. 3.75a and 3.75b. This shows that the phase-separated system also obeys Vegard's Law. Let us use this fact to rewrite the free energy expression. Note that:

$$\begin{aligned}
l - \bar{l}(c_j) &= \bar{l}(0) + c\Delta l - (\bar{l}(0) + c_j\Delta l) \\
&= -\Delta c_j \Delta l,
\end{aligned}$$

where we have defined $\Delta c_j = c_j - c$. The free energy of phase separation can now be rewritten as:

$$F_{\text{coex}}(c_1, c_2; c)/N = n_1\left(f(c_1) + Y\Delta l^2 \Delta c_1^2\right) + n_2\left(f(c_2) + Y\Delta l^2 \Delta c_2^2\right). \tag{3.80}$$

We can eliminate n_1 and n_2 by making use of the following:

$$\begin{aligned} c &= n_1 c_1 + n_2 c_2 \\ &= n_1(c + \Delta c_1) + n_2(c + \Delta c_2) \\ \implies n_1 \Delta c_1 &= -n_2 \Delta c_2 \\ &= (n_1 - 1)\Delta c_2 \\ \implies n_1 &= \frac{-\Delta c_2}{\Delta c_1 - \Delta c_2}. \end{aligned} \tag{3.81a}$$

Similarly,

$$n_2 = \frac{\Delta c_1}{\Delta c_1 - \Delta c_2}. \tag{3.81b}$$

Also, defining $\Delta f = f(c_2) - f(c_1)$, we write the free energy as:

$$\begin{aligned} F_{\text{coex}}(c_1, c_2; c)/N &= \frac{\Delta c_2}{\Delta c_2 - \Delta c_1}\left(f(c_1) + Y\Delta l^2 \Delta c_1^2\right) \\ &\quad - \frac{\Delta c_1}{\Delta c_2 - \Delta c_1}\left(f(c_1) + \Delta f + Y\Delta l^2 \Delta c_2^2\right) \\ &= f(c_1) - \frac{\Delta c_1}{\Delta c_2 - \Delta c_1}\Delta f + Y\Delta l^2 \frac{\Delta c_2 \Delta c_1^2 - \Delta c_1 \Delta c_2^2}{\Delta c_2 - \Delta c_1} \\ &= f(c_1) - \frac{\Delta c_1}{\Delta c_2 - \Delta c_1}\Delta f - Y\Delta l^2 \Delta c_1 \Delta c_2. \end{aligned} \tag{3.82}$$

Eq. 3.82 is our final result for the elastic free energy of coexistence. Absent lattice mismatch ($\Delta l = 0$), minimizing Eq. 3.82 with respect to c_1 and c_2 (at fixed c) corresponds to the conventional double-tangent construction. For $\Delta l \neq 0$, coexistence instead entails a free energy that connects points $(c_1^*, f(c_1^*))$ and $(c_2^*, f(c_2^*))$ in the c-f plane with a parabola of curvature $\kappa_{coex} = -Y\Delta l^2$. We term this procedure the "quadratic construction" (QC).

Quadratic Construction

We identify the equilibrium compositions c_j^* by evaluating $F_{\text{coex}}(c_1, c_2; c)$ for all values of c_1 and c_2 consistent with a given c, and selecting the pair that yields minimum free energy. Taking a graphical view of this solution, we could equivalently bring a parabola $f_0 - (\kappa_{\text{coex}}/2)(c - c_0)^2$ from below $f(c)$, varying parameters f_0 and c_0 until the two curves meet at a pair of points without crossing. All intervals of c on which $\partial^2 f(c)/\partial c^2 < 2\kappa_{\text{coex}}$ are replaced in the QC by a parabola representing coexistence. The result of applying this procedure to a fictitious homogeneous free energy profile is shown in Fig. 3.9. The value of κ_{coex} appropriate to our triangular lattice is -16; we derive this fact in Appendix B.7.

Applying the QC to our MFT estimate $F_{\text{MFT}}(c)$, correspondence with MC results can be greatly improved. In the case of Fig. 3.1B, mean-field predictions for $F(c)$ deviate from simulations by less than 1%, comparable to random sampling error. This excellent agreement

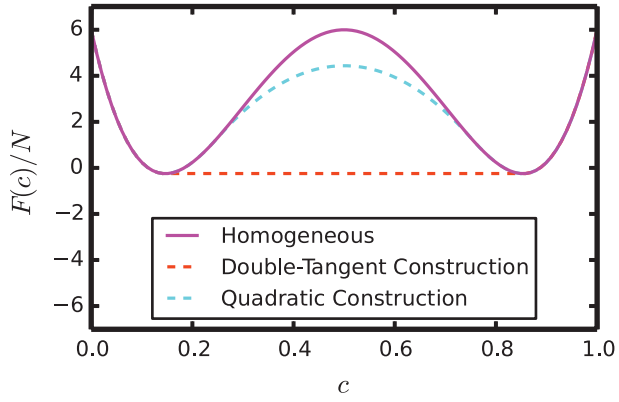

Figure 3.9: Standard double-tangent construction and quadratic construction performed on a fictitious homogeneous free energy profile. For this fictitious quadratic construction, κ_{coex} is taken to be -50.

emphasizes a predominance of macroscopically heterogeneous states in the temperature range $T \lesssim 0.4$, despite the non-convexity of $F(c)$. We attribute this agreement to the appreciable spatial range of $V_{\mathbf{R}}$, which includes substantial coupling between sites separated by several lattice spacings.

3.10 MFT vs MC: The impact of fluctuations

The low-$\mathbf{q}$ form of $\tilde{V}_{\mathbf{q}}$, which varies quadratically with q to lowest order, suggests an eventual failure of MFT near criticality [34]. Quantitative agreement indeed deteriorates with increasing temperature, and above $T \approx 0.46$ the fluctuations neglected by MFT influence phase behavior even qualitatively. The phase diagram for our elastic model, as determined from MC simulations (see Appendix B.8) and plotted in Fig. 3.10B, is equivalent in form to a spin model on the same lattice with couplings that resemble $V_{\mathbf{R}}$ at short range [66]. In contrast to predictions of MFT (see Fig. 3.10A,) (i) the loss of superlattice order upon heating is continuous, with critical properties belonging to the three-state Potts model universality class, and (ii) in the temperature range $T \approx 0.46$ to $T \approx 0.56$, phases S_1 and S_2 are separated by a line of Kosterlitz-Thouless critical points. Away from these exotic features, first order transitions are well described by Eqs. 3.70 and 3.82. The absence of a first order transition between unstructured phases U_1 and U_2 is also captured by MFT and the QC, consistent with our finding of energetic instability for this scenario in Section 3.7.

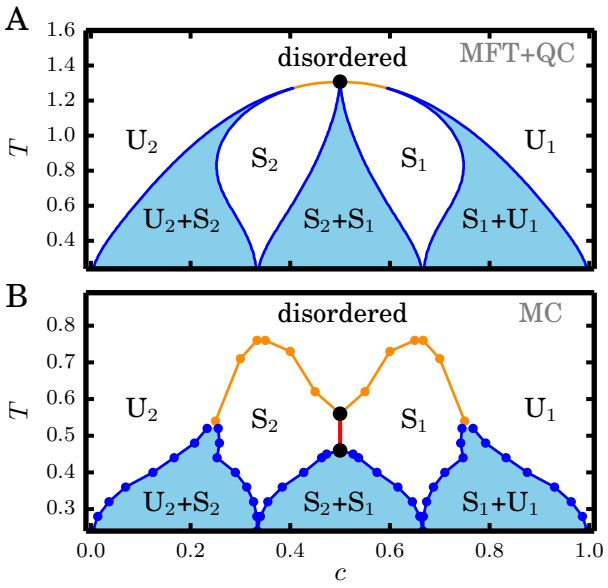

Figure 3.10: Phase diagram for our elastic model in the plane of temperature and composition. **A**: Mean-field prediction resulting from the quadratic construction of Eq. 3.82. Black circle indicates a critical point at $T \approx 1.3$; elsewhere, lines indicate first-order transitions. Orange lines separate the disordered phase from superlattice phases S_1 or S_2. Blue lines bound coexistence regions, which are shaded in light blue. **B**: Numerically exact results from Monte Carlo sampling. In this case, the disordered-to-superlattice transitions (orange lines) are continuous. A line of Kosterlitz-Thouless critical points between $T_c^{\text{lower}} \approx 0.46$ and $T_c^{\text{upper}} \approx 0.56$ is shown in red.

3.11 Conclusion

Our results demonstrate that lattice mismatch can generate more nuanced thermodynamic behaviors than was previously appreciated. They also indicate a central importance of lattice geometry and boundary conditions. The modulated order of phases S_1 and S_2 owes its stability to the fixed macroscopic shape implied by periodic boundary conditions. Such a constraint on boundary shape could arise in real systems from strong interactions that bind a nanocrystal to a substrate, a notion consistent with the observation of stable Cu superlattices within two-dimensional Bi_2Se_3 nanocrystals [11]. It could also be imposed by core-shell interactions in hetero-nanostructures, a possibility which we have explored with MC simulations (see Appendix B.9.) Core/shell arrangements, moreover, are natural intermediates in the course of exchange reactions that proceed most rapidly at surface sites [44].

The precise form of the phase diagram in Fig. 3.10B is likely specific to the dimensionality and lattice symmetry of the elastic model we have studied. Several of its interesting

features, however, we expect to be general for heterostructured solids under appropriate boundary conditions. A tendency for modulated order, for example, is evident in three-dimensional systems explored previously [47]. Additional simulations and theory, described in Appendix B.10, confirm the existence of modulated phases in three dimensional crystals. Thermodynamic potentials with indefinite convexity, and their implications for phase coexistence, are similarly anticipated as generic consequences of the elastic forces attending lattice mismatch. Testing these predictions in the laboratory may be most straightforward for materials that can be manipulated more readily than the internal structure of nanocrystals, for instance assemblies of DNA-coated nanoparticles [40] or spin-crossover compounds [30, 84, 86, 87, 106, 109], where elasticity is known to play a significant role.

Chapter 4

The Origin of Mean-Field Behavior in an Elastic Ising Model

The work described here is reproduced in part from arxiv:2004.10373 [39].

4.1 Introduction

The impact of spin-lattice interactions on materials' phase behavior has long been a topic of interest in condensed matter physics and materials science [100, 27, 4, 89]. Microscopic coupling between spin and geometry in an extended material can endow it with intriguing and useful properties, such as susceptibility of crystal structure to light or pressure [70, 51, 98, 49]. Elastic Ising models can provide a minimal representation of such materials. In a simple variant, the atoms of a crystal lattice interact with their neighbors via Hookean springs. The natural length of these springs is determined by the participating atoms' internal "spin" (which could represent either a literal spin state or a chemical identity.) This type of model has been employed in studies of lattice-mismatched semiconductor alloys [28, 115] and spin-crossover compounds [79, 80]. Despite its substantial history, one of the most basic aspects of this model's behavior remains unresolved. The aforementioned studies employed Monte Carlo (MC) simulations to demonstrate that elastic Ising models can exhibit demixing transitions governed by mean-field critical exponents. However, the microscopic origin of this behavior has not been explicitly identified, nor has a quantitative framework for predicting its consequences been developed.

Here, we present a thorough explanation for the origin of this mean-field behavior. Drawing from our recent work on a similar elastic Ising model [38], we show how the coupling of mechanical fluctuations to spins engenders effective inter-atomic interactions with infinite spatial extent. These give rise to the observed mean-field critical behavior. With an explicit form for the interactions in hand, we develop a straightforward mean field theory (MFT) which accurately predicts the free energy as a function of magnetization as well as the critical temperature for spontaneous symmetry breaking. MFT yields similarly faithful predictions

for relaxation dynamics of the magnetization in the presence of an external field. Finally, we extend our theory to describe spatially heterogeneous systems such as nanocrystals. Our results provide a theoretical basis not only for interpreting the results of a number of previous computer simulation studies, but also for the design of switchable elastic materials. The work described here draws largely from arxiv:2004.10373 [39].

4.2 Elastic Fluctuations Produce Long-Ranged Interactions

We consider a collection of N atoms located near the sites $\mathbf{R}$ of a d-dimensional crystal lattice characterized by unit bond vectors $\hat{\boldsymbol{\alpha}}$. Spin variables $\sigma_{\mathbf{R}} = \pm 1$ determine the natural bond length between neighboring atoms:

$$l(\sigma_{\mathbf{R}}, \sigma_{\mathbf{R}+a\hat{\boldsymbol{\alpha}}}) = \begin{cases} l_{AA}, \text{ for } \sigma_{\mathbf{R}} = \sigma_{\mathbf{R}+a\hat{\boldsymbol{\alpha}}} = 1 \\ l_{AB}, \text{ for } \sigma_{\mathbf{R}} \neq \sigma_{\mathbf{R}+a\hat{\boldsymbol{\alpha}}} \\ l_{BB}, \text{ for } \sigma_{\mathbf{R}} = \sigma_{\mathbf{R}+a\hat{\boldsymbol{\alpha}}} = -1, \end{cases} \tag{4.1}$$

where a is the lattice parameter, $l_{BB} < l_{AA}$, and $l_{AB} = (l_{AA} + l_{BB})/2$. We choose the lattice mismatch $\Delta = (l_{AA} - l_{BB})/2$ to be our basic unit of length. An external pressure p couples directly to the volume cNa^d, where c is a geometry-dependent constant of $\mathcal{O}(1)$. The Hamiltonian governing the system is quadratic in deviations of bond lengths from their preferred σ-dependent values:

$$\mathcal{H} = \frac{K}{4} \sum_{\mathbf{R},\hat{\boldsymbol{\alpha}}} \left[|a\hat{\boldsymbol{\alpha}} + \mathbf{u}_{\mathbf{R}} - \mathbf{u}_{\mathbf{R}+a\hat{\boldsymbol{\alpha}}}| - l(\sigma_{\mathbf{R}}, \sigma_{\mathbf{R}+a\hat{\boldsymbol{\alpha}}}) \right]^2 + pcNa^d. \tag{4.2}$$

where $\mathbf{u}_{\mathbf{R}}$ is the displacement of an atom from its ideal lattice sites. The spring constant $K > 0$ determines the elastic energy scale $\epsilon = K\Delta^2/8$. We express all quantities henceforth in units of Δ and ϵ. Eq. 4.2 manifestly couples spin and displacement variables. We will show how the effect of fluctuations in the displacements can be captured by an effective energy function $\mathcal{H}_{\text{eff}}$ of the remaining spin variables:

$$\mathcal{H}_{\text{eff}}[\{\sigma_{\mathbf{R}}\}] = \mathcal{H}^{\text{SR}} + \mathcal{H}^{\text{LR}} - h \sum_{\mathbf{R}} \sigma_{\mathbf{R}} \tag{4.3}$$

$$\mathcal{H}^{\text{SR}} = \frac{1}{2} \sum_{\mathbf{R},\mathbf{R}'} \sigma_{\mathbf{R}} V^{\text{SR}}_{\mathbf{R}-\mathbf{R}'} \sigma_{\mathbf{R}'} \tag{4.4}$$

$$\mathcal{H}^{\text{LR}} = \frac{1}{2N} V^{\text{LR}} \left(\sum_{\mathbf{R}} \sigma_{\mathbf{R}} \right)^2, \tag{4.5}$$

where "SR" and "LR" stand for "short-ranged" and "long-ranged," respectively. $V_{\mathbf{R}}^{\mathrm{SR}}$ is an effective interaction potential that decays steadily with distance $|\mathbf{R}|$, and V^{LR} is a positive constant that sets the strength of long-range coupling. This form of spin interactions guarantees mean field critical behavior, as will be discussed below.

We first simplify Eq. 4.2 by noting that if Δ is not too large, $\mathcal{H}$ can be written approximately as (see [38] and Appendix C.1):

$$\mathcal{H} \approx 2\sum_{\mathbf{R},\hat{\boldsymbol{\alpha}}}\left(\hat{\boldsymbol{\alpha}}\cdot(\mathbf{u}_{\mathbf{R}}-\mathbf{u}_{\mathbf{R}+a\hat{\boldsymbol{\alpha}}})-\frac{1}{2}(\delta\sigma_{\mathbf{R}}+\delta\sigma_{\mathbf{R}+a\hat{\boldsymbol{\alpha}}})-(\tilde{\sigma}_0/N-\delta a)\right)^2 - Nh\delta a, \tag{4.6}$$

where $h = -pcdl_{AB}^{d-1}$ is a dimensionless pressure and $\delta a = a - l_{AB}$. We have partitioned the spin variables into two components, namely the net magnetization $\tilde{\sigma}_0 = \sum_{\mathbf{R}}\sigma_{\mathbf{R}}$ and the local deviation $\delta\sigma_{\mathbf{R}} = \sigma_{\mathbf{R}} - \tilde{\sigma}_0/N$. Using $\sum_{\mathbf{R}}\mathbf{u}_{\mathbf{R}} = 0$, we expand Eq. 4.6:

$$\mathcal{H} = \Delta\mathcal{H}(\{\mathbf{u}_{\mathbf{R}}\}),\{\delta\sigma_{\mathbf{R}}\}) + 2(\tilde{\sigma}_0/N-\delta a)^2NZ - Nh\delta a, \tag{4.7}$$

where Z is the coordination number of the lattice and

$$\Delta\mathcal{H} = 2\sum_{\mathbf{R},\hat{\boldsymbol{\alpha}}}\left(\hat{\boldsymbol{\alpha}}\cdot(\mathbf{u}_{\mathbf{R}}-\mathbf{u}_{\mathbf{R}+a\hat{\boldsymbol{\alpha}}})-\frac{1}{2}(\delta\sigma_{\mathbf{R}}+\delta\sigma_{\mathbf{R}+a\hat{\boldsymbol{\alpha}}})\right)^2. \tag{4.8}$$

Gaussian fluctuations in the global lattice parameter δa evidently couple solely to $\tilde{\sigma}_0$. Working in an ensemble with fixed N, p, and inverse temperature $\beta = 1/k_BT$, where k_B is Boltzmann's constant, we integrate out these fluctuations:

$$\bar{\mathcal{H}} = -\beta^{-1}\log\left(\int d(\delta a)\exp\left(-\beta\mathcal{H}\right)\right) \tag{4.9}$$

$$= \Delta\mathcal{H} - h\tilde{\sigma}_0 + \text{const.} \tag{4.10}$$

Pressure h simply plays the role of an effective field acting on $\tilde{\sigma}_0$, and so spin coupling is contained entirely in $\Delta\mathcal{H}$. We interrogate this coupling by further integrating out Gaussian fluctuations in the displacement field (dropping the unimportant constant term in Eq. 4.10):

$$\mathcal{H}_{\mathrm{eff}} = -\beta^{-1}\log\left(\int\prod_{\mathbf{R}}d\mathbf{u}_{\mathbf{R}}\exp(-\beta\Delta\mathcal{H})\right) - h\tilde{\sigma}_0. \tag{4.11}$$

If we assume that our system is subject to periodic boundary conditions, then the required integrals are most easily performed in Fourier space. This yields (see [38]):

$$\mathcal{H}_{\mathrm{eff}}[\{\sigma_{\mathbf{R}}\}] = \frac{1}{2N}\sum_{\mathbf{q}}\tilde{V}_{\mathbf{q}}|\tilde{\sigma}_{\mathbf{q}}|^2 - h\tilde{\sigma}_0, \tag{4.12}$$

where $\tilde{f}_{\mathbf{q}}$ denotes the Fourier transform of a generic function $f_{\mathbf{R}}$ [1]. The explicit form of the effective potential $\tilde{V}_{\mathbf{q}}$ is given in Ch. 3, Eq. 3.33.

The existence of a long-ranged coupling is not immediately evident from this analysis, since the longest-wavelength component of the potential ($\tilde{V}_0$) is zero. However, the limit of the potential as $\mathbf{q} \to 0$ is not approached smoothly (see Fig. 4.1) a required condition for short-ranged interactions [22, 110]. Observe that a simple modification of $\tilde{V}_{\mathbf{q}}$ *does* vanish smoothly as $\mathbf{q} \to 0$:

$$\tilde{V}^{\mathrm{SR}}_{\mathbf{q}} = \tilde{V}_{\mathbf{q}} - (1 - \delta_{\mathbf{q},0}) \lim_{\mathbf{q}\to 0} \tilde{V}_{\mathbf{q}}. \tag{4.13}$$

Its inverse transform $V^{\mathrm{SR}}_{\mathbf{R}}$ is therefore a well-defined short-ranged interaction [2]. The remainder of $\tilde{V}_{\mathbf{q}}$ is:

$$\begin{aligned} \tilde{V}^{\mathrm{LR}}_{\mathbf{q}} &= \tilde{V}_{\mathbf{q}} - \tilde{V}^{\mathrm{SR}}_{\mathbf{q}} && (4.14)\\ &= \text{const.} - \delta_{\mathbf{q},0} \lim_{\mathbf{q}\to 0} \tilde{V}_{\mathbf{q}}, && (4.15) \end{aligned}$$

where the constant term simply generates an irrelevant self-interaction, which we drop. Plugging this back into the sum in Eq. 4.12 and writing all quantities in terms of real-space sums gives us the promised form Eq. 4.3, with:

$$V^{\mathrm{LR}} = -\lim_{\mathbf{q}\to 0} \tilde{V}_{\mathbf{q}}. \tag{4.16}$$

The value of the limit depends on the lattice structure:

$$\begin{aligned} \lim_{\mathbf{q}\to 0} \tilde{V}_{\mathbf{q}} &= 2Z - 4\mathbf{a}(\hat{\mathbf{q}}) \cdot \mathbf{A}^{-1}(\hat{\mathbf{q}}) \cdot \mathbf{a}(\hat{\mathbf{q}}) && (4.17)\\ \mathbf{a}(\hat{\mathbf{q}}) &= \sum_{\hat{\boldsymbol{\alpha}}} (\hat{\mathbf{q}} \cdot \hat{\boldsymbol{\alpha}}) \hat{\boldsymbol{\alpha}} && (4.18)\\ \mathbf{A}(\hat{\mathbf{q}}) &= \sum_{\hat{\boldsymbol{\alpha}}} (\hat{\mathbf{q}} \cdot \hat{\boldsymbol{\alpha}})^2 \hat{\boldsymbol{\alpha}}\hat{\boldsymbol{\alpha}}, && (4.19) \end{aligned}$$

where $\hat{\mathbf{q}}$ is a unit vector. For the triangular lattice, this simplifies to $\lim_{\mathbf{q}\to 0} \tilde{V}_{\mathbf{q}} = 8$.

That long-ranged interactions are operative in spin-crossover compounds has been suggested by several authors [118, 109, 62, 9, 35]. Miyashita et al. [79] conjectured that the long-ranged interactions responsible for mean-field behavior in their model had the same $1/|\mathbf{R} - \mathbf{R}'|^3$ decay as that between point defects in three-dimensional continuum elastic media. We have demonstrated that, instead, an infinitely long-ranged interaction arises from a discontinuity in the spectrum $\tilde{V}_{\mathbf{q}}$. This nonanalytic feature originates physically in a mismatch between the elastic energy associated with $\mathbf{q} = 0$ and small (but nonzero) wavevector variations in the magnetization. Schulz et al. [104] argued that precisely those long-wavelength elastic modes ought to be responsible for the mean-field behavior of elastic models of binary alloys.

[1] Note that we have dropped the δ in front of $\tilde{\sigma}_{\mathbf{q}}$. That is because $\delta\tilde{\sigma}_{\mathbf{q}} = \tilde{\sigma}_{\mathbf{q}} - \delta_{\mathbf{q},0}\tilde{\sigma}_0$, but $\tilde{V}_0 = 0$, so $\tilde{\sigma}_0$ simply does not contribute to the sum.

[2] The function $V^{\mathrm{SR}}_{\mathbf{R}}$ is generally anisotropic; for the triangular lattice, its slowest decay is $1/|\mathbf{R}|^4$ along (certain linear combinations of) triangular lattice basis vectors [38].

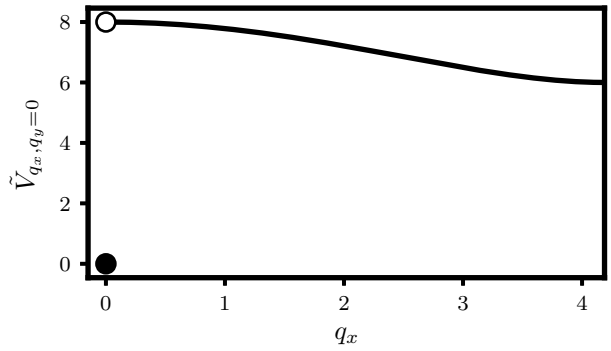

Figure 4.1: Fourier-space effective potential for the triangular lattice. Note that $\tilde{V}_{\mathbf{q}}$ is smooth everywhere except $\mathbf{q} = 0$, since $\tilde{V}_0 = 0$, but $\lim_{\mathbf{q}\to 0} = 8$.

4.3 Mean-Field Thermodynamics

A model which consists solely of interactions of the form $\mathcal{H}^{\mathrm{LR}}$ is described exactly by MFT [59, 15, 116, 81]. Its mean-field critical exponents are robust to the addition of arbitrary short-ranged interactions [16, 85] (a fact which we confirmed numerically for several different lattice structures; see Appendix C.3 for details). There is no such guarantee for non-universal quantities such as the critical temperature T_c, but if the magnitude of $V_{\mathbf{R}}^{\mathrm{SR}}$ is small, then MFT may still predict their values with reasonable accuracy. We obtained such predictions using standard techniques of MFT [18], which yield a self-consistent equation for the net magnetization per atom $m = \tilde{\sigma}_0/N$:

$$m = \tanh\left(2\beta\bar{V}m + h\right), \tag{4.20}$$

as well as a simple expression for the free energy $F(m)$:

$$F_{\mathrm{MF}}(m) = E_{\mathrm{MF}}(m) - TS_{\mathrm{MF}}(m) \tag{4.21}$$

$$E_{\mathrm{MF}} = -N\bar{V}m^2 - hm \tag{4.22}$$

$$S_{\mathrm{MF}}/k_B = -\left[\frac{1-m}{2}\log\frac{1-m}{2} + \frac{1+m}{2}\log\frac{1+m}{2}\right], \tag{4.23}$$

where $\bar{V} = -\sum_{\mathbf{R}\neq 0} V_{\mathbf{R}}/2$ characterizes both long- and short-ranged contributions to the mean field. When $h = 0$, Eq. 4.20 implies a critical temperature $T_c = 2\bar{V}$ for spontaneous symmetry breaking. To test the accuracy of MFT, we performed MC simulations of the elastic Hamiltonian Eq. 4.2 on a periodic triangular lattice (see Appendix C.2 for details.) Specifically, we employed umbrella sampling [113] combined with histogram reweighting [65] to compute free energies. In addition, we located T_c from the intersection of Binder cumulants computed at different system sizes [7]. The results agree quantitatively with our mean-field

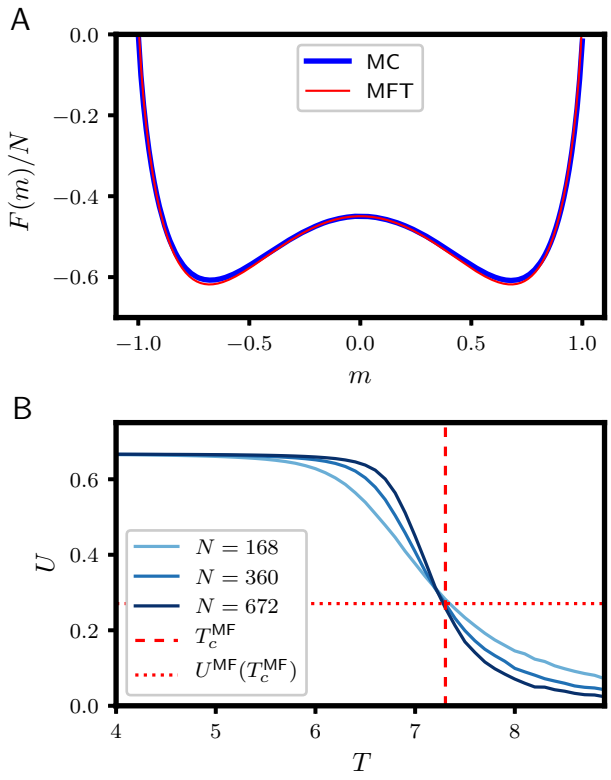

Figure 4.2: **A**: Free energy as a function of magnetization $F(m)$ at $T = 6$, $p = 0$ for a periodic triangular lattice. The MC curve was computed with umbrella sampling of Eq. 4.2, while the MFT curve was obtained from Eq. 4.21. **B**: MFT estimates for the triangular lattice critical temperature $T_c^{\mathrm{MF}} = 2\bar{V} \approx 7.31$ and the corresponding value of the Binder cumulant $U^{\mathrm{MF}}(T_c^{\mathrm{MF}})$ closely predict the intersection point of MC Binder cumulants U for different system sizes. Specifically, MC indicates $T_c^{\mathrm{MC}} \approx 7.2$, so the MFT result is accurate within $\approx 2\%$. MC results for the Binder cumulants were computed by sampling configurations generated under Eq. 4.3 rather than Eq. 4.2 so as to avoid mitigate any minor errors associated with insufficient sampling of mechanical fluctuations.

predictions, as shown in Fig. 4.2. We found similarly excellent agreement between MC and MFT for several different lattice structures in both two and three dimensions (see Appendix C.3.)

4.4 Mean-Field Kinetics

As a more stringent test of MFT, we consider dynamics of our elastic Ising model. Free energy profiles like that in Fig. 4.2 are suggestive of time-dependent response that would follow a

sudden change in external control parameters. But this relaxation advances in the high-dimensional space of spin configurations, through sequential flips of spins that are correlated in space and in time. Resolving few of these details, MFT asserts that thermodynamic driving forces determine time evolution in a simple way. Its success in a dynamical context would provide powerful tools to predict and understand nonequilibrium response.

The model energy function in Eq. 4.2 constrains microscopic rules for time evolution but does not specify them uniquely. To craft a dynamical model we must additionally assign rates to microscopic transitions which are consistent with Boltzmann statistics. As a simplification, we take relaxation of the displacement variables $\mathbf{u_R}$ to be much faster than that of spin variables. This rapid mechanical equilibration allows us to consider time variations of the spin field $\sigma_{\mathbf{R}}$ alone, biased by an effective Hamiltonian. In the small-mismatch limit this effective energy is given by Eq. 4.3. We adopt transition rates $\pi(\sigma_{\mathbf{R}} \to \sigma'_{\mathbf{R}})$ among spin configurations proportional to their Metropolis Monte Carlo acceptance probabilities, $\pi(\sigma_{\mathbf{R}} \to \sigma'_{\mathbf{R}}) = \tau^{-1} \min[1, \exp[-\beta \Delta \mathcal{H}_{\text{eff}}]]$, where τ is an arbitrary reference time scale.

The ordering dynamics that follow a rapid quench from $T > T_c$ to $T < T_c$ are strongly influenced by the long-range component of $\mathcal{H}_{\text{eff}}$. Models with exclusively short-ranged interactions, such as described by $\mathcal{H}^{\text{SR}}$, develop finite-wavelength instabilities upon such quenching [13]. These Ising-like instabilities are visually manifest in the coarsening of spin domains en route to a state of broken symmetry. By contrast, a model with exclusively infinite-range interactions, such as described by $\mathcal{H}^{\text{LR}}$, lacks finite-wavelength spatial correlations entirely and therefore does not exhibit a slowly growing length scale upon quenching. In dynamical simulations of our elastic Ising model, we observe no distinct domain growth upon quenching from $T = 8 > T_c$ to $T = 4 < T_c$, consistent with the observations of Miyashita *et al.* [79].s Indeed, our measurements of the time-dependent spin structure factor $\mathcal{M}(\mathbf{q}, t) = \langle |\tilde{\sigma}(\mathbf{q}, t)|^2 \rangle / N^2$ (where $\langle \cdots \rangle$ denotes an ensemble average) show that only the $\mathbf{q} = 0$ mode becomes unstable upon quenching (Fig. 4.3). This can be understood in detail as a consequence of the energy gap between the $\mathbf{q} = 0$ mode and the finite-wavelength modes depicted in Fig. 4.1. The lack of participation of the finite-wavelength modes in the quench dynamics suggests that a mean-field model – in which the only dynamical quantity is the net magnetization – should also provide a sensible description of other dynamical features.

In addition to changes in temperature, one can probe a system's response to a cyclically varying parameter that crosses and recrosses a phase boundary. In the resulting loop, the distinctness of forward and backward branches reports on the system's "memory" owing to a slow degree of freedom (the net magnetization, in our case.) If such an experiment were performed sufficiently slowly, one would normally expect differences between the two branches to vanish. For our model, hysteresis instead appears to persist for arbitrarily slow cycling. Normally, the free energy barrier for nucleating a stable phase is subextensive in scale, since the thermodynamic cost is interfacial in nature. For our model, finite-size scaling of MC simulation results indicate that the barrier separating minima in $F(m)$ instead scales linearly with system size N. This feature is inherent to MFT, which presumes spatial heterogeneity and thus a lack of interfaces. Thermal fluctuations are insufficient to overcome

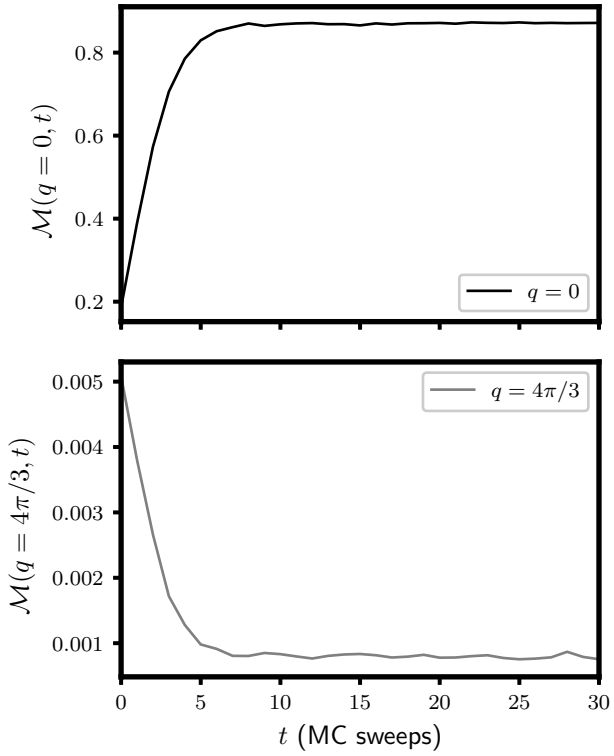

Figure 4.3: Time evolution of two Fourier components of the spin structure factor $\mathcal{M}(\mathbf{q},t) = \langle|\tilde{\sigma}(\mathbf{q},t)|^2\rangle/N^2$ after a quench. In the plots, $q = |\mathbf{q}|$. Curves were obtained by averaging over 10^3 independent trajectories initialized from equilibrium configurations sampled at $T = 8$, $p = 0$ and propagated with MC dynamics at $T = 4$, $p = 0$. Note the rapid initial growth of the $q = 0$ mode.

such an extensive barrier in the thermodynamic limit, and so the system is bistable even at long times. The mean-field nature of the barrier in $F(m)$ is reflected in Fig. 4.4, which shows excellent agreement between hysteresis loops computed from MC and the corresponding prediction of MFT.

At the ends of the hysteresis loop, $F(m)$ is no longer bistable, and a system initialized at the location of the formerly-metastable well m_i can relax to the single stable well at m_f without crossing a barrier. Within MFT, this dynamics can be regarded as a random walk of the magnetization with step length $\Delta m = 2/N$ taken in discrete time steps Δt on the mean-field energy surface. The probability distribution $p(m,t)$ for the magnetization at time

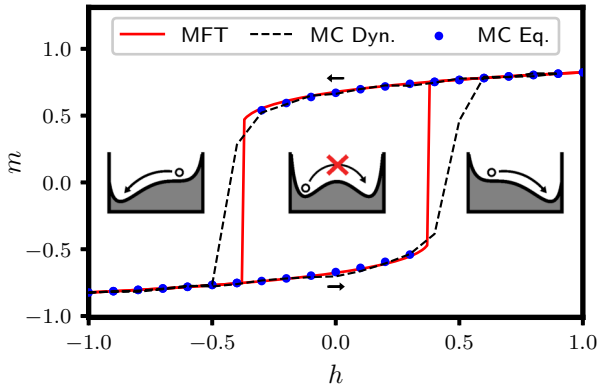

Figure 4.4: Hysteresis loop at $T = 6$ from MFT and MC. The MFT curve was obtained by numerical solution of Eq. 4.20. Solutions to this equation which are also local free energy minima (of which there are at least one and at most two) comprise the mean-field hysteresis loop. MC Dyn. (dynamic) results were obtained by sweeping the field from $h = -0.8$ to $h = 0.8$ and back again for a system with $N = 2688$. For each field value, there were 10 MC sweeps of equilibration and 10 MC sweeps of production. MC Eq. (equilibrium) results we obtained by initializing the system with all spins $+1$ (upper branch) or all spins -1 (lower branch), equilibrating for 100 MC sweeps, and then collecting data over 10^3 MC sweeps.

t is governed by a master equation [3]:

$$\begin{aligned} p(m,t) = {} & p(m-\Delta m, t-\Delta t)\Pi_+(m-\Delta m) \\ & + p(m+\Delta m, t-\Delta t)\Pi_-(m+\Delta m) \\ & + p(m,t-\Delta t)\left(1-(\Pi_+(m)+\Pi_-(m))\right). \end{aligned} \tag{4.24}$$

with transition rates

$$\Pi_\pm(m) = \frac{1 \mp m}{2} \min\left[1, e^{-\beta(E_{\mathrm{MF}}(m\pm\Delta m)-E_{\mathrm{MF}}(m))}\right], \tag{4.25}$$

for incrementally increasing (decreasing) m. The factor $(1 \mp m)/2$ accounts for the number of available down (up) spins at magnetization m, which imposes an entropic bias at the mean-field level. In the limit of large N, these rates satisfy detailed balance with respect to the probability distribution $e^{-\beta F_{\mathrm{MF}}(m)}$. Furthermore, we impose the boundary conditions:

$$p(m,0) = \begin{cases} 1, & m = m_{\mathrm{i}} \\ 0, & \text{otherwise} \end{cases} \tag{4.26}$$

$$p(m_{\mathrm{f}},t) = 0, \tag{4.27}$$

[3]Mean-field dynamics can also be accessed by directly simulating the MC dynamics of a mean-field Hamiltonian; see Appendix C.4 for details.

so that the system always begins at $m = m_{\rm i}$, and the magnetization can never exceed $m = m_{\rm f}$.

Defining the column vector $\mathbf{p}(t) = (p(-1,t), p(-1+\Delta m, t), \ldots p(1,t))^T$, we can rewrite the master equation 4.24 as:

$$\mathbf{p}(t+\Delta t) = \mathbf{\Omega} \cdot \mathbf{p}(t), \tag{4.28}$$

where the elements of the transition matrix $\mathbf{\Omega}$ are given by:

$$\Omega_{m,m'} = \delta_{m,m'}\left(1 - \Pi_+(m) - \Pi_-(m)\right) + \delta_{m,m'+\Delta m}\Pi_-(m) + \delta_{m,m'-\Delta m}\Pi_+(m). \tag{4.29}$$

Letting $t = n\Delta t$, we can write the formal solution to Eq. 4.28 as:

$$\mathbf{p}(t) = \mathbf{\Omega}^n \cdot \mathbf{p}(0). \tag{4.30}$$

Numerical propagation of Eq. 4.30 is straightforward, and with access to $p(m,t)$ we can compute the average magnetization as a function of time:

$$\langle m(t) \rangle = \sum_{m=-1}^{m_{\rm f}} m p(m,t), \tag{4.31}$$

as well as the first passage time distribution $P(t)$:

$$P(t) = \frac{\mathscr{S}(t) - \mathscr{S}(t-\Delta t)}{\Delta t}, \tag{4.32}$$

where the survival probability $\mathscr{S}(t)$ is:

$$\mathscr{S}(t) = \sum_{m=-1}^{m_{\rm f}} p(m,t). \tag{4.33}$$

We compare the quantities $\langle m(t) \rangle$ and $P(t)$ to their counterparts computed from MC simulations in Fig. 4.5. In Fig. 4.6 we plot first passage time distributions of relaxation from the formerly-metastable well to the stable well. As is evident in these figures, the dynamics of both the average magnetization and its fluctuations are captured very well by MFT.

4.5 Ensemble Inequivalence

We have thus far sidestepped a subtle, but important, caveat. Specifically, while the factor of $1/N$ in $V^{\rm LR}$ ensures that the energy is extensive, the arbitrarily-long interaction range means that the energy is no longer additive [82, 14]. In turn, this means that derivatives of the free energy $F(m)$ no longer have a definite sign, and hence its Legendre transform is no longer a single-valued function [124]. In other words, the ensemble in which m is fixed and the ensemble in which m can fluctuate are no longer equivalent [4]. Thus, the modulated structures observed in an ensemble with fixed magnetization – as in our previous work [38] – are not equilibrium states in the present ensemble, where the net magnetization can fluctuate.

[4] In a related context, Vandeworpe and Newman [115]. previously noted inequivalence between canonical and grand canonical ensembles for a Keating model of a semiconductor mixture.

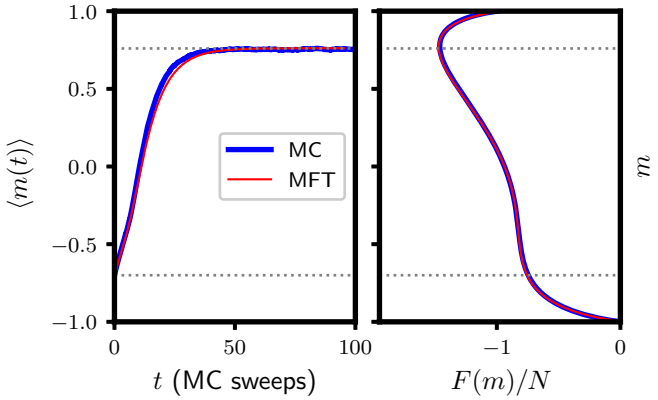

Figure 4.5: Average magnetization versus time at the end of the hysteresis loop (left) with $T = 6$ and free energy at the end of the hysteresis loop (right) with $T = 6$, $h = 0.5$. Gray dashed lines indicate the positions of the formerly-metastable well and the single stable well. The MFT result for the average magnetization was computed via Eq. 4.31. The MC result was computed by averaging over 10^4 independent trajectories, which were initialized with configurations equilibrated at a constant magnetization of $m = -0.7$ using Kawasaki dynamics [61].

4.6 Nanocrystals

In our analysis thus far we have assumed periodic boundary conditions. While this may be appropriate for a macroscopic system, many elastic materials, in particular spin-crossover compounds, have nanoscale dimensions and hence a significant fraction of atoms at the periphery [8, 46, 29, 78]. We therefore studied the impact of open boundary conditions on our model. While the analysis of fluctuations in δa is insensitive to the choice of boundary conditions, broken translational invariance means that a Fourier transform will not diagonalize $\Delta\mathcal{H}$. As a result, the required integrals in Eq. 4.11 are more complicated, but still numerically tractable. For a given nanocrystal size and shape, they can be performed numerically exactly to yield an effective Hamiltonian:

$$\mathcal{H}_{\text{eff}} = \frac{1}{2}\sum_{\mathbf{R},\mathbf{R}'} \sigma_{\mathbf{R}} V_{\mathbf{R},\mathbf{R}'} \sigma_{\mathbf{R}'} - h\sum_{\mathbf{R}} \sigma_{\mathbf{R}}, \tag{4.34}$$

where due to broken translational symmetry, the effective potential depends on both $\mathbf{R}$ and $\mathbf{R}'$, not just their difference. Plots of this potential for a hexagonally-shaped nanocrystal with triangular lattice structure are shown in Fig. 4.7. Interactions between sites towards the interior of the crystal closely resemble bulk interactions, though interactions between sites towards the perimeter of the crystal differ significantly from bulk interactions (see [38].) Importantly, these interior interactions largely retain the long-ranged component, meaning

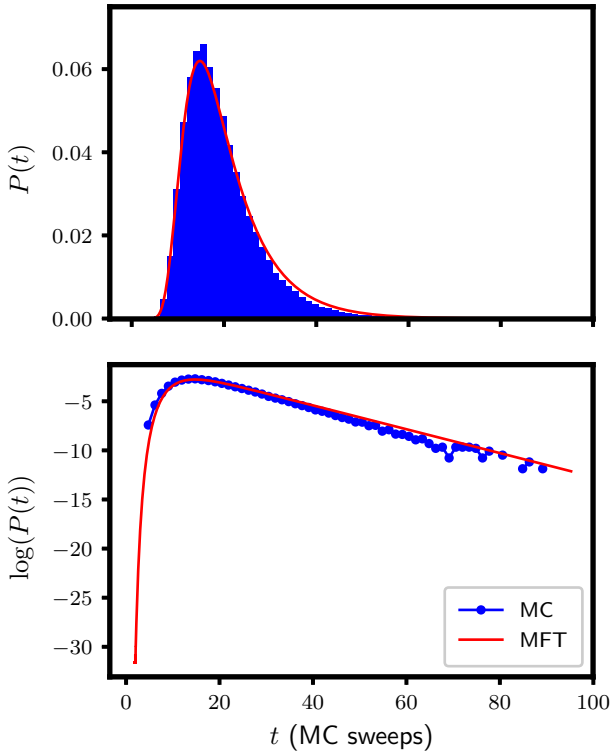

Figure 4.6: Distribution of mean first passage times at the end of the hysteresis loop plotted on linear (top) and logarithmic (bottom) scales. MFT result was computed via Eq. 4.32. For each MC trajectory, the first passage time was defined as the number of MC steps taken to go from the initial state with $m = -0.7$ to the bottom of the stable well where $m = 0.76$. The long-time exponential tail is characteristic of diffusion on a bounded interval; its timescale is governed by the smallest-magnitude eigenvalue of Eq. 4.29 [99].

that MFT might still prove reasonably accurate. Unlike in bulk, sites in the nanocrystal do not all experience the same average environment. An accurate MFT must take this spatial variation into account. A set of self-consistent equations for the average magnetization $m_{\mathbf{R}}$ of each site in the nanocrystal can be written (see Appendix C.5 for a derivation):

$$m_{\mathbf{R}} = \tanh\left(-\beta \sum_{\mathbf{R}' \neq \mathbf{R}} V_{\mathbf{R},\mathbf{R}'} m_{\mathbf{R}'}\right). \tag{4.35}$$

An example of solutions to this set of equations, computed using the same techniques as in [38], is shown in Fig. 4.8. The average net magnetization is then simply computed as:

$$m = \frac{1}{N} \sum_{\mathbf{R}} m_{\mathbf{R}}. \tag{4.36}$$

We used Eqs. 4.35 and 4.36 to compute mean-field predictions for m as a function of temperature for hexagonal nanocrystals of different sizes. Due to their finite sizes, thermal fluctuations will cause the system to cross the barrier separating degenerate free minima increasingly frequently as T_c is approached from below, so that straightforward averaging of an equilibrium MC trajectory will result in $m \approx 0$. In order to compare to MFT predictions, we instead computed MC estimates for $m(T)$ by locating the minima of free energy profiles computed with umbrella sampling. MC results obtained in this way correspond quite closely with MFT predictions (see Fig. 4.9), consistent with long-ranged interactions in the nanocrystal effective potential. Furthermore, we found that the height of the nanocrystal free energy barrier computed from umbrella sampling MC simulations for $T < T_c$ scales linearly with system size N, just as in bulk (see Fig. 4.10.) We thus anticipate similar agreement between MFT and MC for nanocrystal dynamics.

4.7 Conclusion

Our findings have significant implications for functional elastic materials. We have shown that long-ranged interactions are a generic consequence of elastic fluctuations in lattice-mismatched solids. They should thus be operative, for instance, in spin-crossover compounds. One of the intriguing features of these compounds is the bistability of their high-spin-rich and low-spin-rich phases near room temperature [51, 53, 8, 92], which makes them promising for use as molecular switches in next-generation data storage devices. Our results provide an underlying reason for this behavior: the extensive free energy barrier separating these phases means that spin-crossover materials are robust to fluctuations typically responsible for the decay of metastable states. This barrier scaling also explains why transitions between high- and low-spin phases under an applied field are macroscopically sharp. We thus anticipate that our MFT will provide a simple, quantitative framework in which to explain and predict further features of these materials.

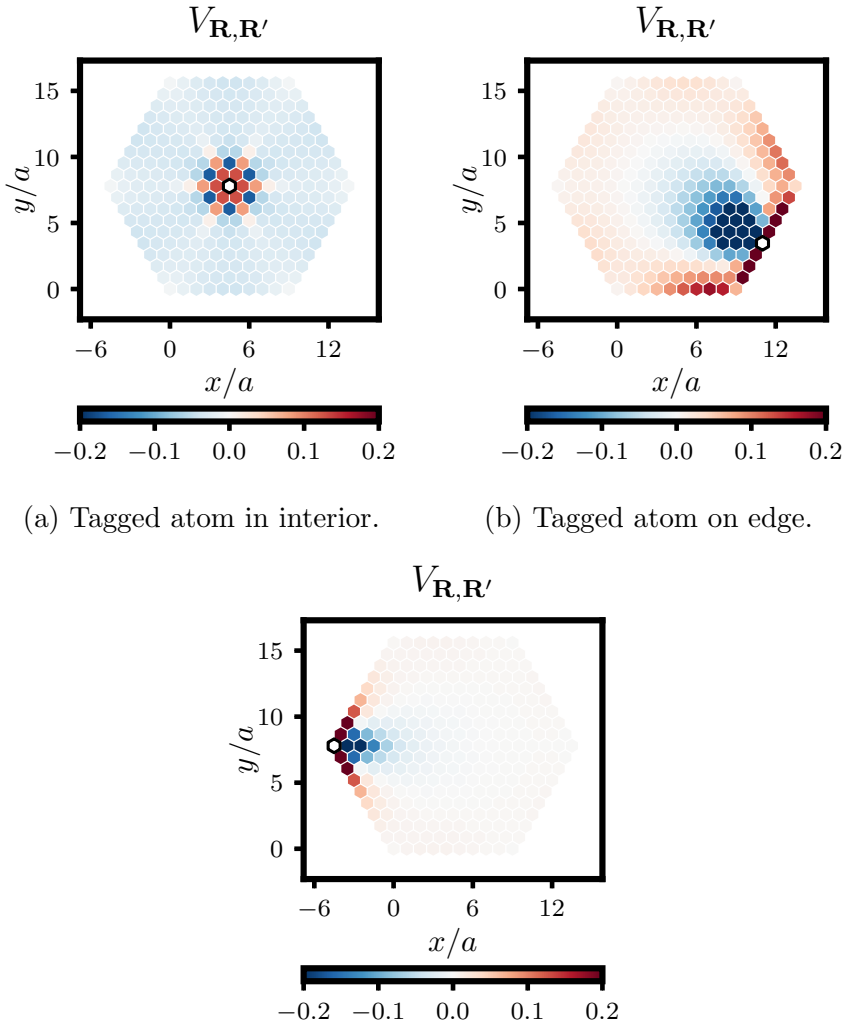

(a) Tagged atom in interior.

(b) Tagged atom on edge.

(c) Tagged atom at corner.

Figure 4.7: Pair interaction function $V_{\mathbf{R},\mathbf{R}'}$ for different locations $\mathbf{R}$ of the tagged atom (outlined in black.)

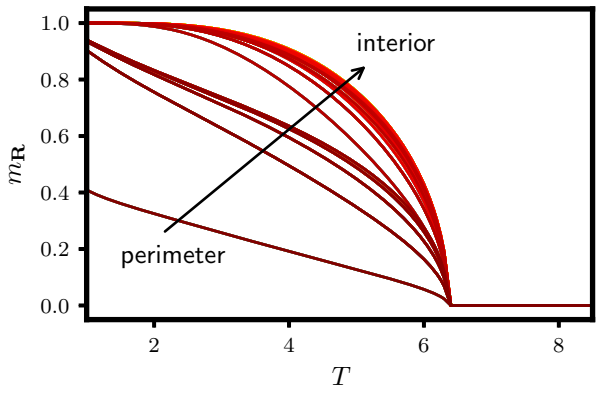

Figure 4.8: Numerical solutions to Eq. 4.35 for a hexagonal nanocrystal of size $N = 271$ with triangular lattice structure. Sites near the perimeter of the crystal have lower magnetization than sites well within the interior; all sites transition from zero to nonzero magnetization at a temperature $T_c \approx 6.2$.

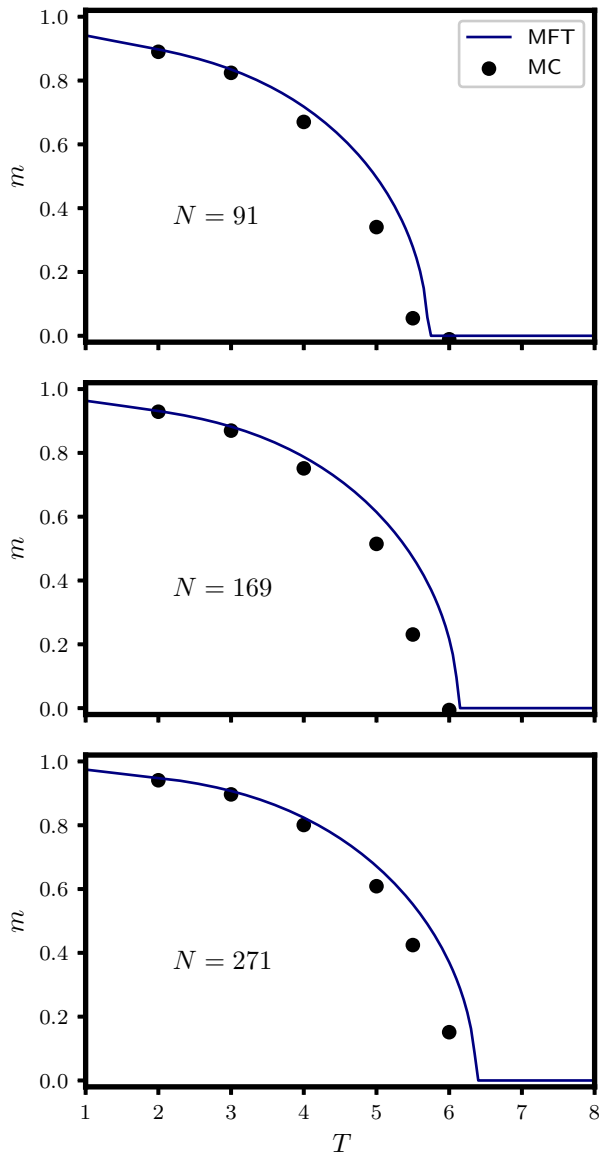

Figure 4.9: Nanocrystal magnetization as a function of temperature for different system sizes. MFT curves were obtained as the numerical solutions of Eqs. 4.35 and 4.36. MC points were obtained as the minima of free energy profiles computed *via* umbrella sampling of the effective Hamiltonian, Eq. 4.34, for each system size.

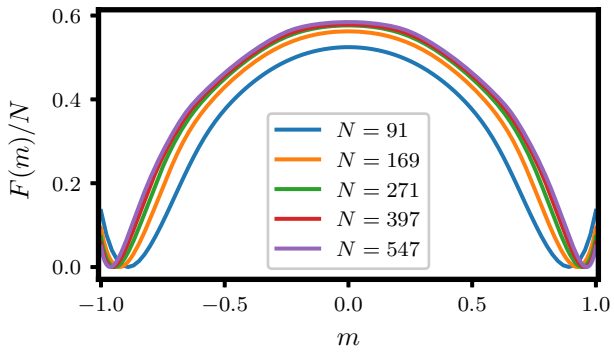

Figure 4.10: Nanocrystal free energies for different system sizes at $T = 3$, $h = 0$. Curves were computed *via* umbrella sampling of the effective Hamiltonian, Eq. 4.34, for each system size.

Chapter 5

Ion Exchange Dynamics

5.1 Introduction

Cation exchange is an important method for post-synthetic modification in which the cations in a semiconductor nanocrystal are replaced by a different type of cation, while the anion sublattice remains intact [108, 6, 101, 24]. This process has been exploited to synthesize technologically useful nanocrystal heterostructures, including metastable structures [71], that are inaccessible *via* conventional synthesis techniques [6]. However, the microscopic mechanisms by which cation exchange occurs remain unclear. We would like to understand the physical principles which govern this process using theory and molecular simulation.

One approach to understanding the dynamics of ion exchange is to simply perform straightforward molecular dynamics simulations, as some researchers have done [32]. However, there are a few pitfalls to this approach. For one, the timescales of ion exchange (milliseconds to hours or days [108, 24]) are very long compared to the timescales associated with basic molecular motions (femtoseconds to nanoseconds,) and hence are inaccessible to standard molecular dynamics simulations (which, with current technology, are capable of looking at, at most, $\sim$ 10s of microseconds.) One way to overcome this is to simply raise the temperature so as to accelerate activated, barrier-crossing events; however, the dynamics observed at such elevated temperatures may not be representative of those at lower temperatures. Moreover, there may be significant issues with standard force fields [97, 45, 31], which are largely parametrized against bulk thermodynamic properties and not necessarily designed to handle intermixing of multiple ionic species. Indeed, Michael Grünwald observed (in a personal communication) that certain unusual defect structures occur in simulations of interstitial ions in CdS using standard pair-potential-based force fields which are absent in more reliable DFT-based, ab initio simulations. (We have corroborated this observation for a couple of different interstitial ion species and force fields.) Other work has avoided the timescale problem by recognizing that changes in the spatial distribution of cations takes place on timescales much longer than that of lattice vibrations. Instead, the authors performed DFT calculations of different ion exchage defect structures and used these as input

for kinetic Monte Carlo simulations [90], although those simulations were still limited in timescale. Nevertheless, such studies have shed some light on the microscopic processes underlying ion exchange in some specific semiconductor materials.

At a higher level, though, one might ask whether there are some general physical principles which govern the fates of ion exchange in different materials. Why, for instance, do some reactions tend to produce Janus nanoparticles, while others result in core-shell structures? A particularly intriguing case is that of Ag_2S/CdS nanorods studied by Alivisatos et al. [102, 25]. There, the authors observed the formation of alternating "stripes" of Ag-rich and Cd-rich domains, which persisted over long periods of time even though DFT calculations by those authors suggested that such structures should only be metastable. The authors attributed this to the significant lattice mismatch between Ag_2S and CdS, which, their calculations indicated, led to a preferred nonzero separation distance between two Ag domains in a Cd nanorod. Meanwhile, later authors found a similar phenomenon in other materials, where materials with more lattice mismatch resulted in modulated composition, unlike those with less mismatch which resulted in phase separation [123]. Our model for ion exchange is inspired largely by these observations.

We adopt the elastic Ising model studied in Chs. 3 and 4 as a model for a nanocrystal which can undergo cation exchange. In Ising model language, ions of different types are associated with different "spins," $\sigma_{\mathbf{R}} = \pm 1$. (These are not literal spins, but simply a convenient shorthand for the variable representing the identity of an atom.) The length of the bond between neighboring atoms depends on their spins, mimicking lattice mismatch. In this chapter, we first investigate how the free surface of a nanocrystal impacts the elastic energy associated with compositional defects. It turns out, perhaps not surprisingly, that such defects face less severe energetic penalties at the surface than in the interior of the crystal. What is surprising is that this surface "softness" reflects some fairly exotic properties in the spectrum of the nanocrystal elastic Hamiltonian. Motivated by the special role of the surface, we then construct a kinetic model for cation exchange which focuses on the interplay between exchange events occuring at the surface and transport of ions through bulk diffusion. Although simple, this scheme is able to capture an array of reaction outcomes consistent with the diversity of experimentally observed nanocrystal heterostructures.

5.2 Elastic Behavior of the Nanocrystal Surface

Elastic Energy of Compositional Defects

We first calibrate our intuition regarding nanocrystal elastic energy by examining some special cases of compositional defects. The translational symmetry of a bulk crystal means that the energy of an isolated compositional defect (e.g. an atom with $\sigma_{\mathbf{R}} = -1$ in a crystal where all other atoms have $\sigma_{\mathbf{R}} = 1$) is independent of its position. The free surface of a nanocrystal breaks that symmetry. Hence, the elastic energy associated with a compositional defect is a function of its location in the nanocrystal. It is reasonable to suspect that this

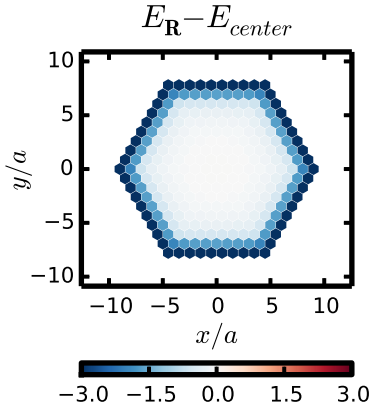

Figure 5.1: Energy $E_{\mathbf{R}}$ associated with introducing a compositional defect in an otherwise compositionally uniform nanocrystal, minus the energy E_{center} of a compositional defect placed precisely in the center of the crystal. Units of energy are ϵ, the elastic energy scale defined in Ch. 3. It is clearly more favorable to place a defect at or near the perimeter than the interior of the crystal.

energy is lowest when the defect is located at the nanocrystal surface, and indeed this is the case. In Fig. 5.1 we plot the energy associated with introducing a single compositional defect at different locations in a two-dimensional, hexagon-shaped nanocrystal cut out of a triangular lattice. The energy is clearly lowest at the surface, in particular at the corners of the hexagon. This behavior has an intuitive explanation: introducing a compositional defect causes strain in the lattice, but there are fewer nearby bonds to strain at the perimeter of the crystal than deep in its interior. We show the bond strains associated with a surface defect versus a defect at the center of the nanocrystal in Fig. 5.2. As we saw in Ch. 4, pair interactions between sites near the perimeter are also significantly different from those in bulk. However, the microscopic basis for these spatial variations is less straightforward to analyze than the energy of a single defect.

Surface Modes

In order to further interrogate the energetics of the nanocrystal surface, we shall diagonalize the nanocrystal Hamiltonian. In bulk this is accomplished with a Fourier transform, but broken translational symmetry prevents us from using this trick in the nanocrystal. We can nevertheless numerically diagonalize the nanocrystal Hamiltonian. Specifically, we diagonalize the effective potential matrix $\mathbf{V}$ whose elements are $V_{\mathbf{R},\mathbf{R}'}$:

$$\mathbf{V}\xi_k^{\mathbf{V}} = \lambda_k^{\mathbf{V}}\xi_k^{\mathbf{V}}, \quad k = 1, \ldots, N, \tag{5.1}$$

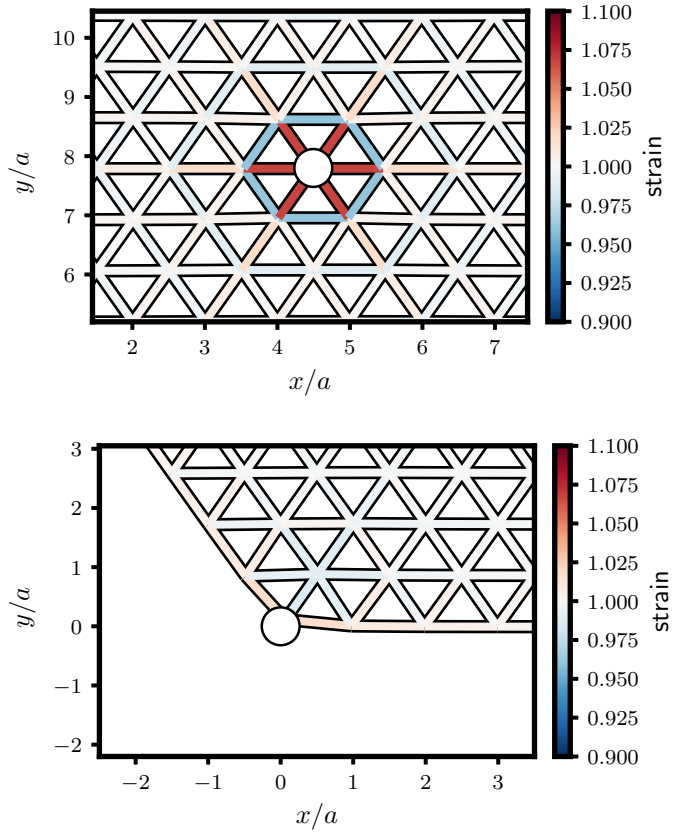

Figure 5.2: Plots illustrating strain associated with a compositional defect at the center (top) and corner (bottom) of a nanocrystal consisting of $N = 271$ atoms. Strain is defined as $|\mathbf{r}_{\mathbf{R}} - \mathbf{r}_{\mathbf{R}+a\hat{\boldsymbol{\alpha}}}|/l(\sigma_{\mathbf{R}}, \sigma_{\mathbf{R}+a\hat{\boldsymbol{\alpha}}})$, where $\mathbf{r}_{\mathbf{R}}$ is the mechanical equilibrium position of the atom at site $\mathbf{R}$ at zero temperature. Defects are marked with white circles. There is clearly much less strain at the corner than in the center of the crystal.

where $\xi_k^{\mathbf{V}}$ are eigenvectors and $\lambda_k^{\mathbf{V}}$ are eigenvalues. We plot the eigenvalues in Fig. 5.3. This yields a surprise; there are a number of modes with eigenvalue zero![1] In fact, the number of such modes is equal to the number of surface atoms (we have checked that this holds true for differently-sized and -shaped triangular lattice nanocrystals; see Appendix D.1.) The corresponding eigenvectors span a degenerate subspace, and hence are not unique. We choose to consider the eigenvectors which are maximally localized in space; the procedure for obtaining them is detailed in Appendix D.1. Some representative eigenvectors are plotted in Fig. 5.4. Clearly, these modes are localized at the surface of the nanocrystal. That the effective potential would contain low-energy surface modes is perhaps not surprising, but

[1]Note that these modes include neither the trivial modes associated with center-of-mass translation and net rotation, nor the $\mathbf{q} = 0$ compositional mode.

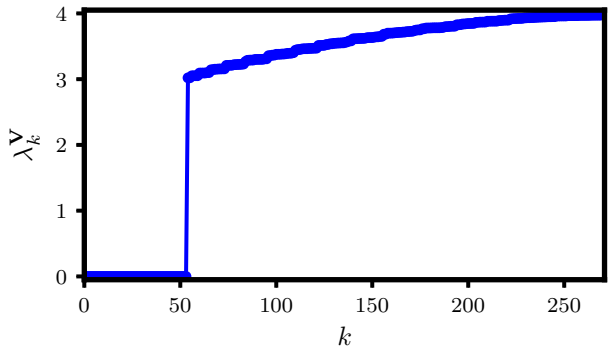

Figure 5.3: Eigenvalues of $V_{\mathbf{R},\mathbf{R}'}$ for a triangular lattice nanocrystal with $N = 271$. The quantity k indexes the modes, here from smallest to largest eigenvalue. This nanocrystal has 54 surface atoms, precisely the number of zero eigenvalues in the spectrum above.

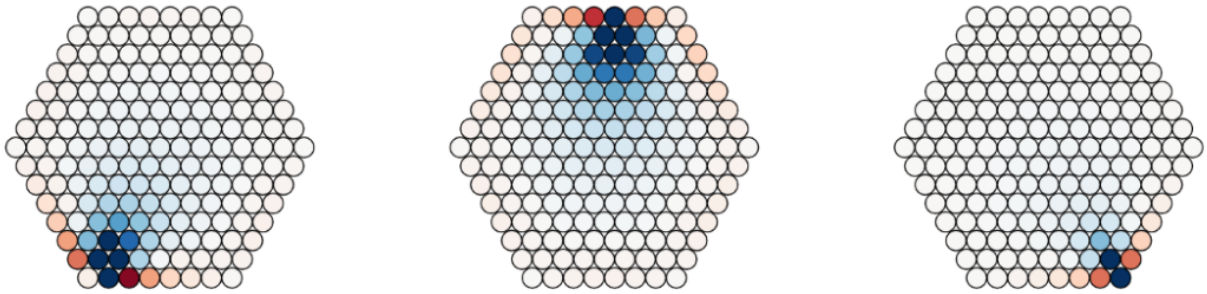

Figure 5.4: Eigenvectors of $V_{\mathbf{R},\mathbf{R}'}$ corresponding to zero eigenvalues for a triangular lattice nanocrystal with $N = 169$. White indicates a value of zero, while blue indicates negative values (darkest blue is -1) and red indicates positive values (darkest red is -1).

the fact that their eigenvalues are precisely zero suggests that there may be some deeper underlying physics at play.

Mechanical Topological Modes and Mode Counting

The aforementioned features of the surface zero modes are reminiscent of the behavior of topological insulators [50]. While the typical settings for such physics are fairly exotic, similar behavior has been identified in more prosaic, mechanical systems. In particular, Kane and Lubensky [60] showed that mechanical lattices with the special property of "isostaticity" tend to exhibit boundary-localized vibrational modes. An isostatic lattice is one which

Figure 5.5: Zero-mode eigenvectors of a nanocrystal with surface disorder.

has as many constraints as degrees of freedom. Specifically, the authors recall Maxwell's argument that a lattice in d spatial dimensions with N atoms and N_b bonds is mechanically stable if $dN - N_b > 0$. An isostatic lattice is one which lies at the threshold of mechanical stability, $dN - N_b = 0$. The square lattice with only nearest-neighbor bonds, for example, is isostatic. Furthermore, under certain conditions the boundary-localized modes are topologically protected in the same sense as electronic boundary modes in the quantum Hall effect and topological insulators [50]. A major consequence of this topological protection is that such zero modes are robust to surface disorder. Our zero eigenvectors exhibit just such a property. In Fig. 5.5 we show a few zero eigenvectors for a nanocrystal in which we have randomly deleted or inserted surface atoms. These eigenvectors are still largely localized to the surface, and the number of such zero modes is equal to the number of surface atoms in the surface-disordered crystal.

Inspired by Kane and Lubensky's framework and by our observations of robust surface zero modes, we test whether an analogous relation between isostaticity and zero modes holds for our elastic Ising model. We have two kinds of degrees of freedom (spins and displacements); for the purpose of counting, we treat them on the same footing. For the triangular lattice, for instance, our elastic Ising model has three degrees of freedom per atom

(two components of the displacement vector and one spin.) Our condition for (generalized) isostaticity is thus:

$$(d+1)N - N_b = 0 \tag{5.2}$$

We have checked whether generalized isostaticity (in bulk) is associated with zero modes (in nanocrystals) for different nanocrystal sizes and for different lattice structures. In Table 5.1 we compile information for several of the systems we have investigated. The data suggests that nanocrystals with an isostatic lattice structure exhibit a number of zero modes which scales as the number of surface atoms. Non-isostatic lattices may exhibit some zero modes, but their number does not scale with the nanocrystal surface area. Interestingly, the square lattice (with both nearest- and next-nearest-neighbor bonds) also exhibits "soft" modes which are very close to (but not exactly) zero (see Fig. 5.6.) We identify the soft modes as the set of eigenvectors whose energies appear to increase continuously from zero and are separated from the other modes by a discontinuity in the spectrum (which occurs at $k = 36$ in the plot.) The number of such modes appears to scale with the number of surface atoms. The corresponding eigenvectors, a few of which are shown in Fig. 5.7, are localized to the nanocrystal surface.

Lattice	1d		Triangular		Square		FCC		Simple Cubic		BCC	
Isostatic?	Yes		Yes		No		No		No		Yes	
Shape	chain		hexagon		square		cube		cube		sphere	
N_{atom}	10	100	7	271	16	100	108	256	64	216	65	256
N_0	2	2	6	54	4	4	14	14	0	0	50	170
N_{surf}	2	2	6	54	12	36	76	148	37	91	50	143
N_{soft}	0	0	0	0	8	32	0	0	0	0	0	0

Table 5.1: Isostaticity and zero modes for different lattices. The 1d, square, and simple cubic lattices have both nearest- and next-nearest-neighbor bonds (to ensure mechanical stability;) all other lattices have only nearest-neighbor bonds. "Isostatic?" here is understood to refer to generalized isostaticity. N_{atom} is the number of atoms in the nanocrystal; N_0 is the number of zero modes; N_{surf} is the number of surface atoms; N_{soft} is the number of soft modes. The "sphere" shape for the BCC lattice refers to the fact that the nanocrystals studied were constructed by excerpting atoms from a spherical volume of an infinite BCC lattice.

Although our evidence for association between generalized isostaticity and surface-localized zero modes is suggestive, we have yet to prove that the former implies the latter. Furthermore, while we have shown that the zero modes of the triangular lattice are robust to surface disorder D.1, we have not explicitly proven that they are topologically protected. Answering these questions will require a much more detailed analysis. Specifically, following Kane and Lubensky, we could attempt to compute the topological invariants associated with the

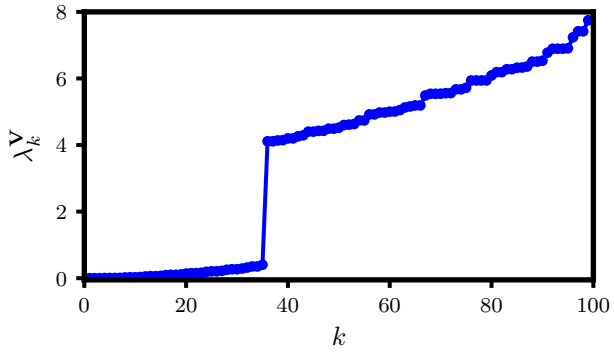

Figure 5.6: Eigenvalues of $V_{\mathbf{R},\mathbf{R}'}$ for a square lattice nanocrystal with $N = 100$. The quantity k indexes the modes, here from smallest to largest eigenvalue. Note the small but nonzero "soft" modes from $k = 4$ to $k = 36$.

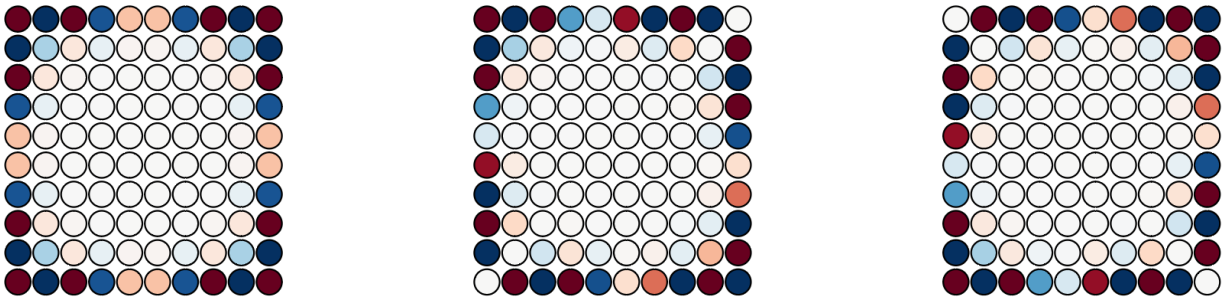

Figure 5.7: "Soft" eigenvectors of $V_{\mathbf{R},\mathbf{R}'}$ corresponding to small, nonzero eigenvalues for the square lattice. Left to right: $k = 4, 5, 6$, with eigenvalues $0.005120, 0.006831, 0.009331$, respectively (units of ϵ.) White indicates a value of zero, while blue indicates negative values (darkest blue is -1) and red indicates positive values (darkest red is 1).

"square root" of the (full, rather than effective) Hamiltonian. From this we could say something about whether the zero modes are topologically protected and perhaps derive an index theorem that indicates how many zero modes should occur in a nanocrystal. This work is still in progress; it might be aided by pursuing an analysis along the lines of other recent work on topological phases in classical systems [111].

Modes of the Correlation Matrix

An awkward feature of the analysis in the previous section is that spins are treated as continuous variables, i.e. the elements of the eigenvectors can take on a continuous range of values. By contrast, for the physical system we wish to study spin variables are restricted to the discrete values $\sigma_{\mathbf{R}} = \pm 1$ (so for a given composition, $\delta\sigma_{\mathbf{R}}$ can take on only one of two values.) In other words, the eigenvectors of the previous section are not realizable as physical states of the elastic Ising model. One way to circumvent this problem is to consider the spin correlation function rather than the interaction matrix itself. Physically, one could think of the inverse of this correlation function as an effective interaction between different spatial components of the spin field. The correlation function is given by:

$$\boldsymbol{\mathcal{X}}_{\mathbf{R},\mathbf{R}'} = \langle \delta\sigma_{\mathbf{R}} \delta\sigma_{\mathbf{R}'} \rangle, \tag{5.3}$$

where $\langle \cdots \rangle$ denotes an average with respect to the Boltzmann distribution:

$$P(\{\mathbf{u}_{\mathbf{R}}\}, \{\sigma_{\mathbf{R}}\}) = \frac{\exp(-\beta\mathcal{H})}{\prod_{\mathbf{R}} \int d\mathbf{u}_{\mathbf{R}} \sum_{\sigma_{\mathbf{R}}} \exp(-\beta\mathcal{H})}. \tag{5.4}$$

The spectrum of the correlation matrix is defined by:

$$\boldsymbol{\mathcal{X}} \xi_k = \lambda_k^{\boldsymbol{\mathcal{X}}} \xi_k, \quad k = 1, ..., N, \tag{5.5}$$

where $\lambda_k^{\boldsymbol{\mathcal{X}}}$ is the kth eigenvalue and ξ_k is the kth eigenvector. The advantage of considering the correlation matrix compared to the effective Hamiltonian is that the discreteness of the spin variables is "built in" by sampling physical configurations. It is, however, more computationally demanding than simply interrogating the potential because now the Boltzmann distribution must be sampled for each temperature (and possibly composition) of interest.

We have computed the nanocrystal correlation matrix $\boldsymbol{\mathcal{X}}$ and its spectrum for one temperature $T = 0.5$ and size $N = 169$ in an ensemble where the composition can fluctuate. Sampling of $\mathcal{H}_{\text{eff}}$ was performed with a Metropolis Monte Carlo algorithm. The system was equilibrated for 10^4 MC sweeps and data was collected every sweep for 10^5 MC sweeps. Plots of $\boldsymbol{\mathcal{X}}_{\mathbf{R},\mathbf{R}'}$ are shown for a few different values of $\mathbf{R}$ in Fig. 5.8 A plot of the eigenvalue spectrum is shown in Fig. 5.9. The spectrum exhibits "jumps" between sets of nearly degenerate modes. These different sets of eigenvalues correspond to eigenvectors localized to distinct regions of space; the highest eigenvalues correspond to eigenvectors localized to the nanocrystal corners, while the smallest eigenvalues correspond to eigenvectors localized

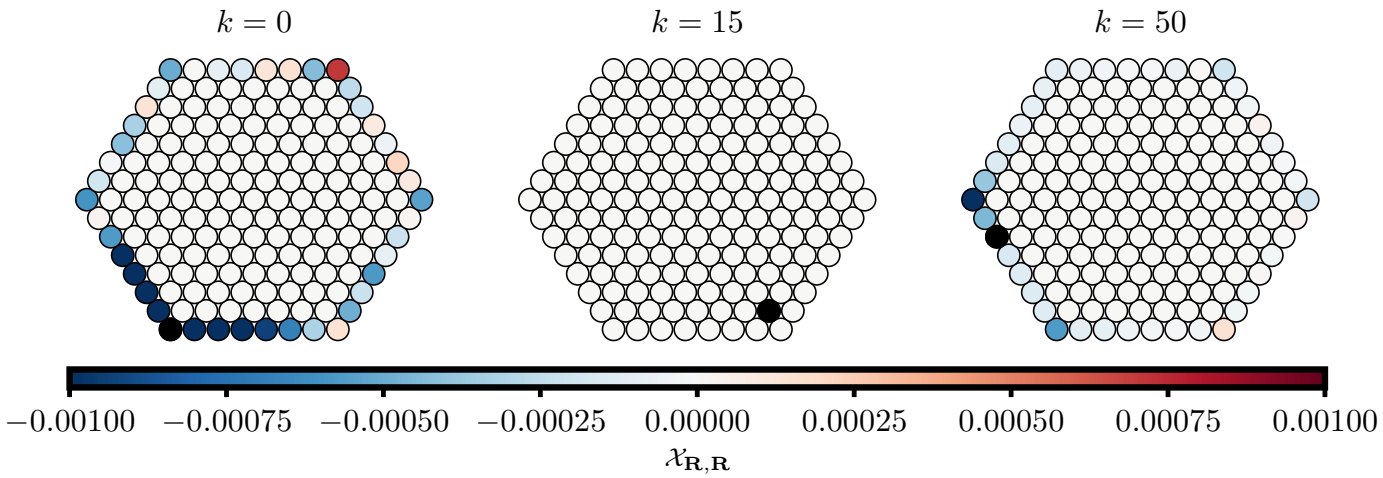

Figure 5.8: Columns of $\boldsymbol{\mathcal{X}}$ at $N = 169$, $T = 0.5$ for selected values of $\mathbf{R}$ (indexed by k.) The tagged spin at $\mathbf{R}$ is colored black. The scale of the color bar is reduced in order to emphasize spatial variations in the correlation function, but most of the entries in the columns are fairly small (magnitude ≤ 0.01.)

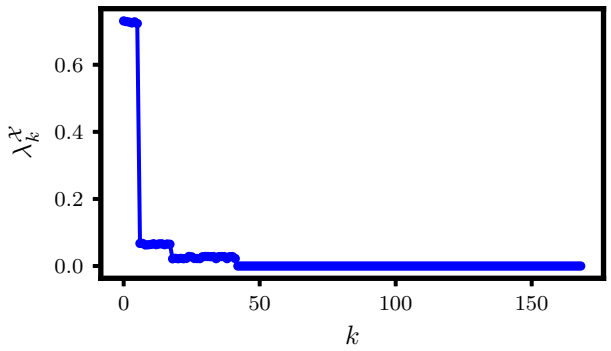

Figure 5.9: Eigenvalues of the correlation matrix $\boldsymbol{\mathcal{X}}$ for $N = 169$, $T = 0.5$. The quantity k indexes the modes.

in the interior (see Fig. 5.10.) The eigenvalues of the *inverse* correlation matrix tell us the "stiffness" or energetic cost associated with each of its eigenvectors (modes.) Thus, the lowest values of $\lambda_k^{\boldsymbol{\mathcal{X}}}$ correspond to stiff modes, while the largest values of $\lambda_k^{\boldsymbol{\mathcal{X}}}$ correspond to soft modes. The fact that these soft modes are localized at the nanocrystal surface reflects the fact that compositional defects are readily accommodated at the surface compared to bulk, and suggests that the surface should play an important role in cation exchange reactions.

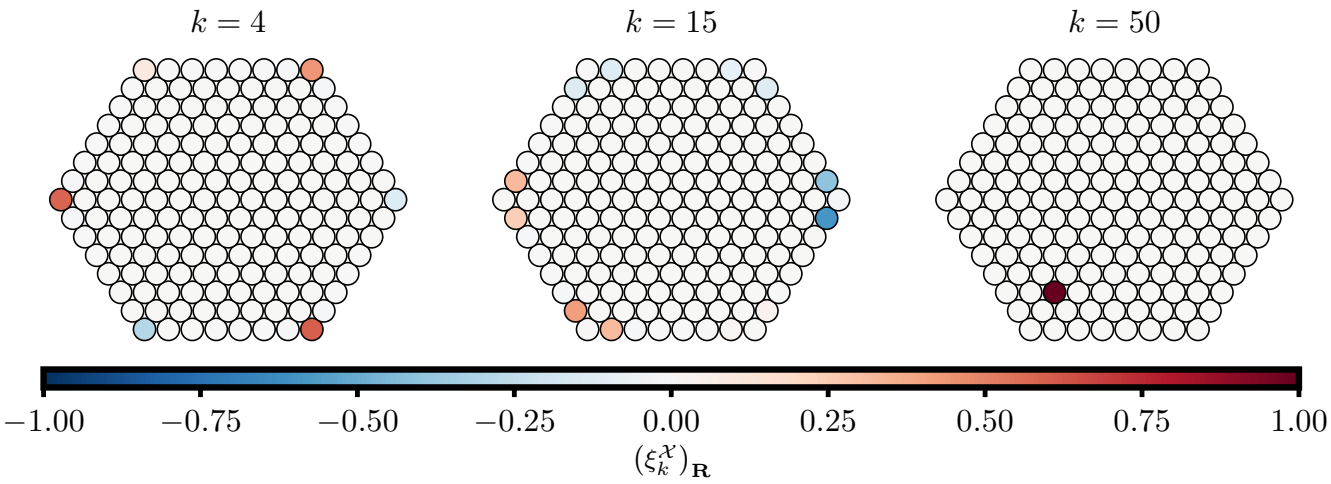

Figure 5.10: Representative eigenvectors of the correlation matrix $\boldsymbol{\mathcal{X}}$ for $N = 169$, $T = 0.5$.

5.3 Kinetic Monte Carlo Simulations

Having undertaken a detailed analysis of nanocrystal energetics, we now consider a simple model for ion exchange reactions. We assume that exchange occurs only at the surface of the nanocrystal, and that dopants can subsequently diffuse through the entire crystal by swapping identities with a neighboring host atom. These events are represented a spin flip ($\sigma_{\mathbf{R}} \to -\sigma_{\mathbf{R}}$) at a surface site $\mathbf{R}$, and a spin swap ($\sigma_{\mathbf{R}} \to \sigma_{\mathbf{R}'}$, $\sigma_{\mathbf{R}'} \to \sigma_{\mathbf{R}}$) between two adjacent sites $\mathbf{R}$ and $\mathbf{R}'$ where $\sigma_{\mathbf{R}} \neq \sigma_{\mathbf{R}'}$. We shall refer to these as "exchange" events and "diffusion" events, respectively. Such events are assumed to obey first-order kinetics with rate constants k_{ex} and k_{diff}. The rate of an event depends on the initial and final configurations C and C' through the Hamiltonian $\mathcal{H}$, and in order to be consistent with the Boltzmann distribution its associated rate constant must satisfy detailed balance:

$$k_{\text{ex}} = k_{\text{ex}}^0 e^{-\beta(\mathcal{H}(C')-\mathcal{H}(C))} \tag{5.6}$$

$$k_{\text{diff}} = k_{\text{diff}}^0 e^{-\beta(\mathcal{H}(C')-\mathcal{H}(C))}. \tag{5.7}$$

The "bare" rate constants k_{ex}^0 and k_{diff}^0 set the fundamental timescales for exchange and diffusion. Their precise values are likely to be influenced by a number of factors; here, we simply treat them as phenomenological.

We can simulate these dynamics straightforwardly via a kinetic Monte Carlo (KMC) scheme employing the Gillespie algorithm [41]. The most straightforward implementation is as follows:

1. Given an initial configuration, determine all possible exchange and diffusion moves and compute their rate constants.

2. Label each of the n events with an index $i = 1, \ldots, n$, and let the rate constant of the ith event be k_i.

3. Compute the total rate constant k_{total} as the sum of all exchange and diffusion rate constants.

4. Generate a number r uniformly at random between 0 and k_{total}, and execute the event j for which $k_{j-1} \leq r < k_j$ (defining $k_0 = 0$.)

5. Update the time $t \to t + \Delta t$, where Δt is sampled from the exponential distribution $P(\Delta t) = k_{\text{total}} \exp(-k_{\text{total}} \Delta t)$.

6. Repeat.

Our initial configuration consists of a nanocrystal with $\sigma_{\mathbf{R}} = 1$ for all $\mathbf{R}$. Enumeration of, and calculation of the rates of, all possible events at each iteration may be expensive, and more efficient versions of this algorithm exist [42]. For our purposes, the above algorithm has been sufficient.

We illustrate the basic features of these dynamics by considering the simple case of a non-interacting Hamiltonian:

$$\mathcal{H}_0 = -h \sum_{\mathbf{R}} \sigma_{\mathbf{R}}. \tag{5.8}$$

The field h, which represents the thermodynamic driving force for ion exchange, acts to bias the net composition $\sum_{\mathbf{R}} \sigma_{\mathbf{R}}$. We take $h < 0$ so that the spin state $\sigma_{\mathbf{R}} = -1$ is thermodynamically favored. The rate constants can then be written as:

$$k_{\text{ex}} = k^0_{\text{ex}} e^{\pm 2\beta h} \tag{5.9}$$

$$k_{\text{diff}} = k^0_{\text{diff}}, \tag{5.10}$$

where $\beta = 1/k_B T$ is the inverse temperature and where the $\pm$ correspond to moves $\sigma_{\mathbf{R}} = 1 \to -1$ and $\sigma_{\mathbf{R}} = -1 \to 1$, respectively. The field h acts as the natural energy scale; we choose to simulate the nanocrystal at a fairly low temperature, $\beta h = 5$. Because of the thermodynamic favorability of surface exchange, we expect that the rate of change of nanocrystal composition is limited by the rate of diffusion of -1 spins inwards (making room for exchange of new -1 spins at the surface,) even though the bare rate constants might be similar. In Fig. 5.11 we plot the composition over time, averaged over 100 independent trajectories, as well as representative configurations along a single trajectory. As can be seen, the composition exhibits exponential decay, indicative of an overall first order kinetics. By looking at the configurations, we can see how compositional change proceeds: exchange (at the surface) is rapid, and subsequent decay of the population of blue ($\sigma_{\mathbf{R}} = 1$) atoms is limited by the speed at which those atoms can randomly diffuse to the surface.

Were ion exchange reactions as simple as the non-interacting model, we would not see the variety of intriguing nanocrystal heterostructures observed in experiments. These spatial patterns arise as a result of *interactions* between atoms of different identities. The spatial

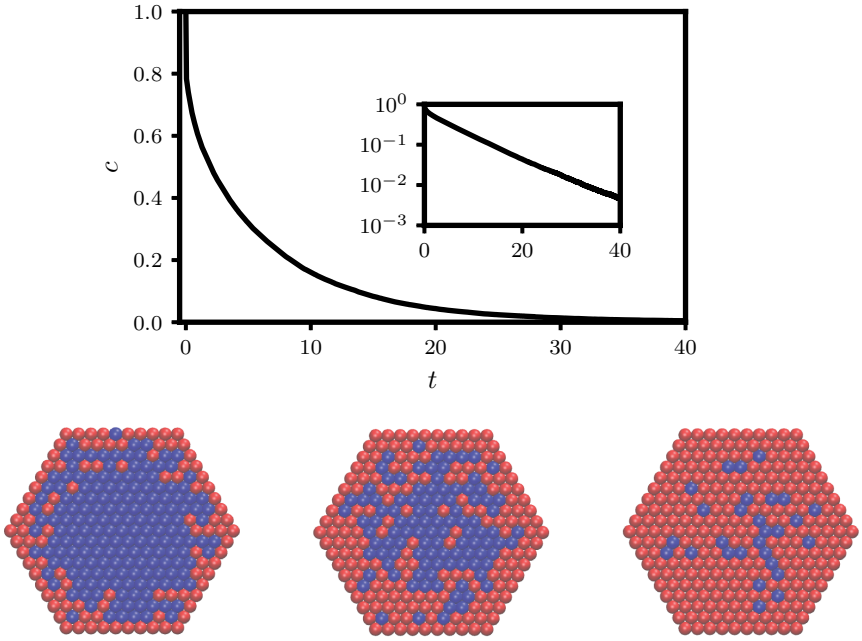

Figure 5.11: Composition vs. time, averaged over 100 independent trajectories, and representative configurations for the noninteracting model. Here $k_BT/h = 1/5$, $k^0_{\rm diff}/k^0_{\rm ex} = 1$, $N = 271$. Inset is a log-linear plot of the same data, showing exponential decay of the composition. Configurations shown are from a single trajectory at times $t \approx 1, 4, 13$ from left to right. Blue atoms have $\sigma_{\mathbf{R}} = 1$, while red atoms have $\sigma_{\mathbf{R}} = -1$.

distribution of composition in nanocrystal heterostructures has been previously thought of in terms of the interplay between short-ranged "chemical" and long-ranged elastic interactions [25]. We mimic these interactions in simulations by defining an energy function:

$$\mathcal{H} = \mathcal{H}_{\rm chemical} + \mathcal{H}_{\rm elastic} + \mathcal{H}_0 \tag{5.11}$$

where:

$$\mathcal{H}_{\rm chemical} = -\frac{J}{2}\sum_{\mathbf{R},\hat{\boldsymbol{\alpha}}} \sigma_{\mathbf{R}}\sigma_{\mathbf{R}+a\hat{\boldsymbol{\alpha}}} \tag{5.12}$$

$$\mathcal{H}_{\rm elastic} = \frac{1}{2}\sum_{\mathbf{R},\mathbf{R}'} \sigma_{\mathbf{R}} V_{\mathbf{R},\mathbf{R}'} \sigma_{\mathbf{R}'}. \tag{5.13}$$

The attractive chemical energy of strength $J > 0$ between like nearest-neighbor spins discourages the growth of interfaces between domains of differing composition. Meanwhile, as we have seen in Ch. 3, the effective elastic pair potential $V_{\mathbf{R},\mathbf{R}'}$ encourages short-wavelength modulations of the composition. One might therefore suspect that varying the relative

strengths of such interactions affects which heterostructures form as a result of cation exchange. Our goal for the remainder of this section is to test this hypothesis.

We first consider the case in which there are no elastic interactions, only the Ising-like chemical energy and the external field. Here, we measure energy in units of J, and take $k_BT/J = 2$ (below the critical temperature of the triangular lattice Ising model [33].) The field is set to $h/J = 5$. To mimic the timescales of surface exchange and bulk diffusion in nanocrystals [44], we assume that $k^0_{\text{ex}} \gg k^0_{\text{diff}}$. In Fig. 5.12 we show the composition versus time, averaged over 100 trajectories, along with representative nanocrystal configurations. As in the non-interacting case, the initial decay of the composition is rapid. After this initial perdiod of surface exchange, though, changes in the composition slow down dramatically. A survey of nanocrystal configurations reveals that the thin shell that forms due to exchange grows progressively more slowly with time. This is likely because the Ising-like interactions penalize increases in surface area between domains of differing composition. Once a shell has formed, in order for subsequent exchange to occur, a blue atom must diffuse from the core through the red shell to the surface of the crystal. Since the first step in this process – a blue atom intruding into the red shell – is energetically unfavorable, it occurs as a rare thermal fluctuation. This is underscored by the fact that dynamics gets much slower as the temperature is lowered (see Fig. 5.13.) As the shell grows, so does the distance that this atom must diffuse once it has broken through. Thus the rate of change of composition should become progressively slower as the reaction proceeds. (In this way, exchange might be thought of as "self-limiting" [58].) This behavior is strongly reminiscent of certain cation exchange reactions involving cation species which are similar in size [24] (and hence have low lattice mismatch.)

When chemical interactions are absent and elastic interactions (due to lattice mismatch) dominate instead, the observed exchange pathways are dramatically different. In Fig. 5.14 we show the composition over time, averaged over 100 trajectories run at $k_BT/\epsilon = 0.2$, $h/\epsilon = -5$. The observed dynamics is much faster than in the case of no elastic interactions. Furthermore, configurations taken from the trajectories show that even after an initial shell has formed, additional red ($\sigma_{\mathbf{R}} = -1$) atoms diffuse inward fairly quickly and form spatial patterns closely similar to those of superlattice phases observed in the bulk elastic Ising model in Ch. 3. More specifically, as the reaction proceeds, the interior of the nanocrystal exhibits motifs from each of the bulk phases in turn, from blue-rich S_1, to coexistence between S_1 and red-rich S_2, to S_2 alone. Moreover, these patterns stand in striking contrast to equilibrium nanocrystal configurations harvested from umbrella sampling simulations [113]. These configurations exhibit "phase separation" into red and blue-rich domains, similar to Janus nanostructures observed in some experiments [24] (see Fig. 5.15.) Our KMC simulations evidently produce highly nonequilibrium patterns. This is a consequence of the fast kinetics of surface exchange: if we make $k^0_{\text{diff}} \gg k^0_{\text{ex}}$, then KMC trajectories exhibit configurations which much more closely resemble those of the equilibrium umbrella sampling simulations. In effect, because diffusion is fast, spins have time to "equilibrate" after each change in composition due to an exchange event. In contrast, when exchange is fast, surface sites tend to saturate with spins of the thermodynamically favored type, and further changes

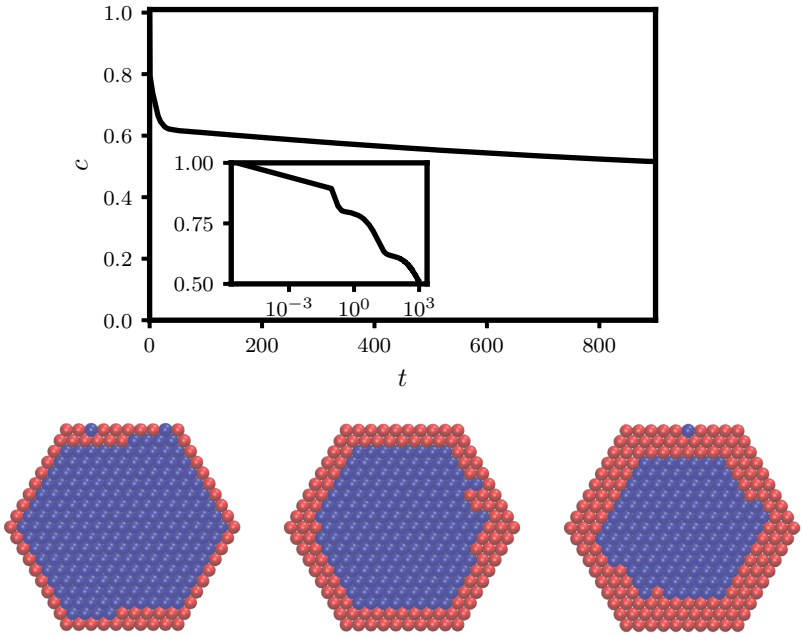

Figure 5.12: Composition vs. time, averaged over 100 independent trajectories, and representative configurations for the chemical interaction-only case. Here $k_BT/J = 2$, $h/J = -5$, $k^0_{\text{diff}}/k^0_{\text{ex}} = 10^{-2}$, $N = 271$. Inset is a semilog plot of the same data, showing "stepped" changes in the composition corresponding to the formation of new layers in the shell. Configurations shown are from a single trajectory at times $t \approx 30, 230, 900$ from left to right.

in the composition must be facilitated by diffusion of the thermodynamically disfavored spin to the surface. The shell appears to prevent deformation of the nanocrystal (evident in equilibrium simulations) and instead acts as a "frame," creating boundary conditions similar to periodic boundary conditions seen in bulk (in fact, if we perform equilibrium simulations with infinitely stiff surface sites, then nanocrystals exhibit modulated order rather than phase separation as the equilibrium state: see Appendix B.9.) This results in modulated order being energetically favorable in the interior of the nanocrystal. Though not of precisely the same form, the striped patterns observed in lattice-mismatched CdS/Ag_2S nanorods [102, 25] might share a similar origin to our superlattices.

We have not yet performed extensive simulations in which both chemical and elastic interactions are comparable in magnitude. However, one might expect that competition between short-ranged chemical attractions and longer-ranged, anisotropic elastic interactions could lead to novel patterns, for example by changing the wavelength of spatially modulated order. This could certainly be a fertile direction for future research. Yet, even the limited parameter space we have explored thus far has revealed intriguing behaviors that echo those seen in experiments.

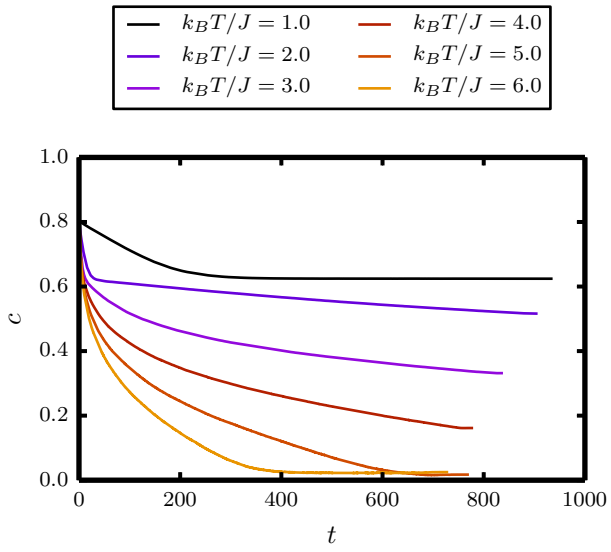

Figure 5.13: Temperature dependence of dynamics with only chemical interactions. Recall that the critical temperature of the triangular lattice Ising model is $T_c \approx 3.64$ [Fisher 1967].

5.4 Conclusion

Our model for cation exchange admittedly has limitations. We have not been able to reproduce exactly the striped nanorod structures which served a significant source of inspiration for this work. Our model does not resolve the individual anion and cation sublattices, and hence cannot explain the intriguing observation that many cation exchange reactions result in drastic compositional change of the cations yet leaves the geometry of the anion sublattice intact, even when the resulting structure is no longer the thermodynamically stable one [71, 72]. Indeed, it contains no reference to charge at all – and hence cannot account for charged defects that have been thought to be important for these reactions [90]. Nor can our model distinguish between vacancy- and interstitial-mediated mechanisms for ion transport [69]. In a sense, our model is coarse-grained: we have integrated out explicit vibrational motion, and moreover our "atoms" are really probably better thought of as unit cells. It may be feasible to resolve atomic details within our KMC framework by employing a more realistic force field for common semiconductor nanocrystals. Lastly, we have not allowed for the possibility of bond breaking or forming. The occurrence of point defects or even dislocations could profoundly impact the elastic energy associated with compositional change and hence the pathways taken during reactions. Finally, we have made no attempt in our model to resolve the organic ligands which usually coat the surfaces of nanoparticles. The density of ligands often varies from one facet of a nanocrystal surface to another [55], which could result in the exchange rate varying from one facet to another. In lieu of explicitly representing the ligands, one might be able to capture this effect simply by making k_{ex} depend on crystal

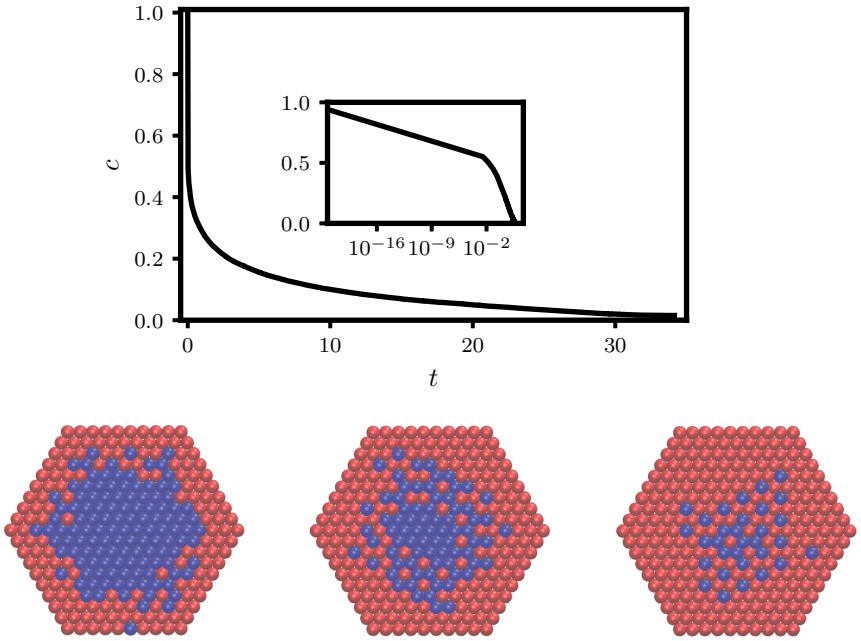

Figure 5.14: Composition vs. time, averaged over 100 independent trajectories, and representative configurations for the elastic interaction-only case. Here $k_BT/\epsilon = 0.2$, $h = -5\epsilon$, $k^0_{\text{diff}}/k^0_{\text{ex}} = 10^{-2}$, $N = 271$. Inset is a semilog plot of the same data. Configurations shown are from a single trajectory at times $t \approx 5, 130, 900$ from left to right.

facet.

Despite these limitations, our model has produced a rich phenomenology. Importantly, it has recapitulated some key features of real-world ion exchange reactions. An advantage of our model's simplicity, in addition to giving us access to long time and length scales, is that it allows us to explain those features in a transparent manner. Moreover, it suggests how one might change certain parameters in an attempt to achieve a desired heterostructure. For example, if one wants to create a Janus structure, one might select a dopant with high mobility within the host lattice (increasing the rate of diffusion relative to exchange.) In addition to further exploration of parameter space, the aforementioned elaborations of our model designed to enhance its realism should provide fertile ground for future investigations.

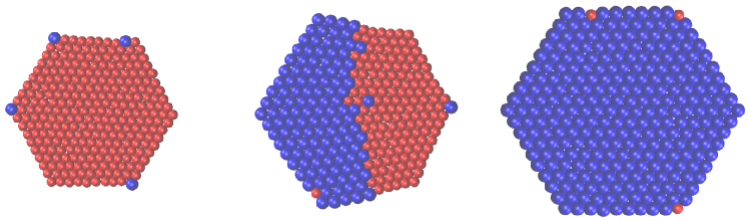

Figure 5.15: Equilibrium configurations taken from umbrella sampling simulations [113] of an elastic Ising nanocrystal with $h = 0$, $k_B T/\epsilon = 2$, $N = 271$. We used the full elastic Hamiltonian, Eq. 3.2 in Ch. 3, for these simulations. Configurations were taken from windows centered at $c \approx 0.02, 0.5, 0.98$ from left to right. Note the significant distortion apparent in the phase-separated $c \approx 0.5$ configuration. Periodic boundary conditions (appropriate to a bulk crystal) or a very stiff outer "shell" preclude such deformation at equilibrium (see Ch. 3.) Nonequilibrium conditions in our KMC simulations can evidently skirt phase separation as well.

Bibliography

[1] S. Alexander. "Lattice gas transition of He on Grafoil. A continuous transition with cubic terms". In: *Physics Letters A* 54.5 (1975), pp. 353–354. ISSN: 03759601. DOI: 10.1016/0375-9601(75)90766-5. URL: https://linkinghub.elsevier.com/retrieve/pii/0375960175907665.

[2] A. P. Alivisatos. "Semiconductor Clusters, Nanocrystals, and Quantum Dots". In: *Science* 271.5251 (1996), pp. 933–937. ISSN: 0036-8075. DOI: 10.1126/science.271.5251.933. URL: https://www.sciencemag.org/lookup/doi/10.1126/science.271.5251.933.

[3] A. Paul Alivisatos et al. "Organization of 'nanocrystal molecules' using DNA". In: *Nature* 382.6592 (1996), pp. 609–611. ISSN: 0028-0836. DOI: 10.1038/382609a0. URL: http://www.nature.com/articles/382609a0.

[4] George A. Baker and John W. Essam. "Effects of Lattice Compressibility on Critical Behavior". In: *Physical Review Letters* 24.9 (1970), pp. 447–449. ISSN: 0031-9007. DOI: 10.1103/PhysRevLett.24.447. URL: https://link.aps.org/doi/10.1103/PhysRevLett.24.447.

[5] George A. Baker and John W. Essam. "Statistical Mechanics of a Compressible Ising Model with Application to β Brass". In: *The Journal of Chemical Physics* 55.2 (1971), pp. 861–879. ISSN: 0021-9606. DOI: 10.1063/1.1676156. URL: http://aip.scitation.org/doi/10.1063/1.1676156.

[6] Brandon J. Beberwyck, Yogesh Surendranath, and A. Paul Alivisatos. "Cation Exchange: A Versatile Tool for Nanomaterials Synthesis". In: *The Journal of Physical Chemistry C* 117.39 (2013), pp. 19759–19770. ISSN: 1932-7447. DOI: 10.1021/jp405989z. URL: https://pubs.acs.org/doi/10.1021/jp405989z.

[7] K. Binder. "Critical Properties from Monte Carlo Coarse Graining and Renormalization". In: *Physical Review Letters* 47.9 (1981), pp. 693–696. ISSN: 0031-9007. DOI: 10.1103/PhysRevLett.47.693. URL: https://link.aps.org/doi/10.1103/PhysRevLett.47.693.

[8] Ishtvan Boldog et al. "Spin-Crossover Nanocrystals with Magnetic, Optical, and Structural Bistability Near Room Temperature". In: *Angewandte Chemie International Edition* 47.34 (2008), pp. 6433–6437. ISSN: 14337851. DOI: 10.1002/anie.200801673. URL: http://doi.wiley.com/10.1002/anie.200801673.

[9] Kamel Boukheddaden et al. "Dynamical model for spin-crossover solids. I. Relaxation effects in the mean-field approach". In: *Physical Review B* 62.22 (2000), pp. 14796–14805. ISSN: 0163-1829. DOI: 10.1103/PhysRevB.62.14796. URL: https://link.aps.org/doi/10.1103/PhysRevB.62.14796.

[10] R.P. Brent. *Algorithms for Minimization Without Derivatives*. Englewood Cliffs, NJ: Prentice-Hall, 1973. Chap. 3–4. ISBN: 0-13-022335.

[11] Joka Buha and Liberato Manna. "Solid State Intercalation, Deintercalation, and Cation Exchange in Colloidal 2D Bi 2 Se 3 and Bi 2 Te 3 Nanocrystals". In: *Chemistry of Materials* 29.3 (2017), pp. 1419–1429. ISSN: 0897-4756. DOI: 10.1021/acs.chemmater.6b05440. URL: http://pubs.acs.org/doi/10.1021/acs.chemmater.6b05440.

[12] F.C. Burton, W.K.; Cabrera, N.; Frank. "The growth of crystals and the equilibrium structure of their surfaces". In: *Philosophical Transactions of the Royal Society of London. Series A, Mathematical and Physical Sciences* 243.866 (1951), pp. 299–358. ISSN: 0080-4614. DOI: 10.1098/rsta.1951.0006. URL: https://royalsocietypublishing.org/doi/10.1098/rsta.1951.0006.

[13] John W. Cahn. "Phase Separation by Spinodal Decomposition in Isotropic Systems". In: *The Journal of Chemical Physics* 42.1 (1965), pp. 93–99. ISSN: 0021-9606. DOI: 10.1063/1.1695731. URL: http://aip.scitation.org/doi/10.1063/1.1695731.

[14] Alessandro Campa, Thierry Dauxois, and Stefano Ruffo. "Statistical mechanics and dynamics of solvable models with long-range interactions". In: *Physics Reports* 480.3-6 (2009), pp. 57–159. ISSN: 03701573. DOI: 10.1016/j.physrep.2009.07.001. URL: https://linkinghub.elsevier.com/retrieve/pii/S0370157309001586.

[15] Sergio A. Cannas, A. C. N. de Magalhães, and Francisco A. Tamarit. "Evidence of exactness of the mean-field theory in the nonextensive regime of long-range classical spin models". In: *Physical Review B* 61.17 (2000), pp. 11521–11528. ISSN: 0163-1829. DOI: 10.1103/PhysRevB.61.11521. URL: https://link.aps.org/doi/10.1103/PhysRevB.61.11521.

[16] H.W. Capel, L.W.J. Den Ouden, and J.H.H. Perk. "Stability of critical behaviour, critical-exponent renormalization and first-order transitions". In: *Physica A: Statistical Mechanics and its Applications* 95.3 (1979), pp. 371–416. ISSN: 03784371. DOI: 10.1016/0378-4371(79)90024-4. URL: https://linkinghub.elsevier.com/retrieve/pii/0378437179900244.

[17] John Cardy. *Scaling and Renormalization in Statistical Physics*. Cambridge: Cambridge University Press, 1996. Chap. 1.

[18] David Chandler. *Introduction to Modern Statistical Mechanics*. New York: Oxford University Press, 1987. Chap. 5. ISBN: 9780195042771.

[19] Qian Chen et al. "Interaction Potentials of Anisotropic Nanocrystals from the Trajectory Sampling of Particle Motion using in Situ Liquid Phase Transmission Electron Microscopy". In: *ACS Central Science* 1.1 (2015), pp. 33–39. ISSN: 2374-7943. DOI: 10.1021/acscentsci.5b00001. URL: https://pubs.acs.org/doi/10.1021/acscentsci.5b00001.

[20] Seon-Myeong Choi, Seung-Hoon Jhi, and Young-Woo Son. "Effects of strain on electronic properties of graphene". In: *Physical Review B* 81.8 (2010), p. 081407. ISSN: 1098-0121. DOI: 10.1103/PhysRevB.81.081407. URL: https://link.aps.org/doi/10.1103/PhysRevB.81.081407.

[21] D. Frenkel and B. Smit. *Understanding molecular simulation: from algorithms to applications*. 2nd. San Diego: Academic Press, 2001. Chap. 7. ISBN: 9780122673511.

[22] D. Dantchev and J. Rudnick. "Subleading long-range interactions and violations of finite size scaling". In: *The European Physical Journal B* 21.2 (2001), pp. 251–268. ISSN: 1434-6028. DOI: 10.1007/s100510170201. URL: http://link.springer.com/10.1007/s100510170201.

[23] Wheeler P. Davey. "Precision Measurements of the Lattice Constants of Twelve Common Metals". In: *Physical Review* 25.6 (1925), pp. 753–761. ISSN: 0031-899X. DOI: 10.1103/PhysRev.25.753. URL: https://link.aps.org/doi/10.1103/PhysRev.25.753.

[24] Luca De Trizio and Liberato Manna. "Forging Colloidal Nanostructures via Cation Exchange Reactions". In: *Chemical Reviews* 116.18 (2016), pp. 10852–10887. ISSN: 0009-2665. DOI: 10.1021/acs.chemrev.5b00739. URL: http://pubs.acs.org/doi/10.1021/acs.chemrev.5b00739.

[25] Denis O. Demchenko et al. "Formation Mechanism and Properties of CdS-Ag 2 S Nanorod Superlattices". In: *ACS Nano* 2.4 (2008), pp. 627–636. ISSN: 1936-0851. DOI: 10.1021/nn700381y. URL: http://pubs.acs.org/doi/10.1021/nn700381y.

[26] Tony DeSimone, Richard M. Stratt, and Jan Tobochnik. "Some developments in the theory of modulated order. II. Deformable-lattice models and the axial next-nearest-neighbor Ising model as a random magnet". In: *Physical Review B* 32.3 (1985), pp. 1549–1557. ISSN: 0163-1829. DOI: 10.1103/PhysRevB.32.1549. URL: https://link.aps.org/doi/10.1103/PhysRevB.32.1549.

[27] C. Domb. "Specific Heats of Compressible Lattices and the Theory of Melting". In: *The Journal of Chemical Physics* 25.4 (1956), pp. 783–783. ISSN: 0021-9606. DOI: 10.1063/1.1743060. URL: http://aip.scitation.org/doi/10.1063/1.1743060.

[28] B. Dünweg and D. P. Landau. "Phase diagram and critical behavior of the Si-Ge unmixing transition: A Monte Carlo study of a model with elastic degrees of freedom". In: *Physical Review B* 48.19 (1993), pp. 14182–14197. ISSN: 0163-1829. DOI: 10.1103/PhysRevB.48.14182. URL: https://link.aps.org/doi/10.1103/PhysRevB.48.14182.

[29] Cristian Enachescu and William Nicolazzi. "Elastic models, lattice dynamics and finite size effects in molecular spin crossover systems". In: *Comptes Rendus Chimie* 21.12 (2018), pp. 1179–1195. ISSN: 16310748. DOI: 10.1016/j.crci.2018.02.004. URL: https://linkinghub.elsevier.com/retrieve/pii/S1631074818300547.

[30] Cristian Enachescu et al. "Shape effects on the cluster spreading process of spin-crossover compounds analyzed within an elastic model with Eden and Kawasaki dynamics". In: *Physical Review B* 91.10 (2015), p. 104102. ISSN: 1098-0121. DOI: 10.1103/PhysRevB.91.104102. URL: https://link.aps.org/doi/10.1103/PhysRevB.91.104102.

[31] Zhaochuan Fan et al. "A transferable force field for CdS-CdSe-PbS-PbSe solid systems". In: *The Journal of Chemical Physics* 141.24 (2014), p. 244503. ISSN: 0021-9606. DOI: 10.1063/1.4904545. URL: http://aip.scitation.org/doi/10.1063/1.4904545.

[32] Zhaochuan Fan et al. "Atomistic understanding of cation exchange in PbS nanocrystals using simulations with pseudoligands". In: *Nature Communications* 7.1 (2016), p. 11503. ISSN: 2041-1723. DOI: 10.1038/ncomms11503. URL: http://www.nature.com/articles/ncomms11503.

[33] Michael E. Fisher and Robert J. Burford. "Theory of Critical-Point Scattering and Correlations. I. The Ising Model". In: *Physical Review* 156.2 (1967), pp. 583–622. ISSN: 0031-899X. DOI: 10.1103/PhysRev.156.583. URL: https://link.aps.org/doi/10.1103/PhysRev.156.583.

[34] Michael E. Fisher, Shang-keng Ma, and B. G. Nickel. "Critical Exponents for Long-Range Interactions". In: *Physical Review Letters* 29.14 (1972), pp. 917–920. ISSN: 0031-9007. DOI: 10.1103/PhysRevLett.29.917. URL: https://link.aps.org/doi/10.1103/PhysRevLett.29.917.

[35] Houcem Fourati et al. "Interplay between a crystal's shape and spatiotemporal dynamics in a spin transition material". In: *Physical Chemistry Chemical Physics* 20.15 (2018), pp. 10142–10154. ISSN: 1463-9076. DOI: 10.1039/C8CP00868J. URL: http://xlink.rsc.org/?DOI=C8CP00868J.

[36] P. Fratzl and O. Penrose. "Ising model for phase separation in alloys with anisotropic elastic interaction—I. Theory". In: *Acta Metallurgica et Materialia* 43.8 (1995), pp. 2921–2930. ISSN: 09567151. DOI: 10.1016/0956-7151(95)00005-G. URL: http://linkinghub.elsevier.com/retrieve/pii/095671519500005G.

[37] P. Fratzl and O. Penrose. "Ising model for phase separation in alloys with anisotropic elastic interaction—II. A computer experiment". In: *Acta Materialia* 44.8 (1996), pp. 3227–3239. ISSN: 13596454. DOI: 10.1016/1359-6454(95)00422-X. URL: http://linkinghub.elsevier.com/retrieve/pii/135964549500422X.

[38] Layne B. Frechette, Christoph Dellago, and Phillip L. Geissler. "Consequences of Lattice Mismatch for Phase Equilibrium in Heterostructured Solids". In: *Physical Review Letters* 123.13 (2019), p. 135701. ISSN: 0031-9007. DOI: 10.1103/PhysRevLett.123.135701. arXiv: 1906.08304. URL: https://link.aps.org/doi/10.1103/PhysRevLett.123.135701.

[39] Layne B. Frechette, Christoph Dellago, and Phillip L. Geissler. "The Origin of Mean-Field Behavior in an Elastic Ising Model". In: (2020). arXiv: 2004.10373. URL: http://arxiv.org/abs/2004.10373.

[40] Paul A. Gabrys et al. "Lattice Mismatch in Crystalline Nanoparticle Thin Films". In: *Nano Letters* 18.1 (2018), pp. 579–585. ISSN: 1530-6984. DOI: 10.1021/acs.nanolett.7b04737. URL: http://pubs.acs.org/doi/10.1021/acs.nanolett.7b04737.

[41] Daniel T. Gillespie. "Exact stochastic simulation of coupled chemical reactions". In: *The Journal of Physical Chemistry* 81.25 (1977), pp. 2340–2361. ISSN: 0022-3654. DOI: 10.1021/j100540a008. URL: https://pubs.acs.org/doi/abs/10.1021/j100540a008.

[42] Daniel T. Gillespie, Andreas Hellander, and Linda R. Petzold. "Perspective: Stochastic algorithms for chemical kinetics". In: *The Journal of Chemical Physics* 138.17 (2013), p. 170901. ISSN: 0021-9606. DOI: 10.1063/1.4801941. URL: http://aip.scitation.org/doi/10.1063/1.4801941.

[43] Roy J. Glauber. "Time-Dependent Statistics of the Ising Model". In: *Journal of Mathematical Physics* 4.2 (1963), pp. 294–307. ISSN: 0022-2488. DOI: 10.1063/1.1703954. URL: http://aip.scitation.org/doi/10.1063/1.1703954.

[44] Esther Groeneveld et al. "Tailoring ZnSe–CdSe Colloidal Quantum Dots via Cation Exchange: From Core/Shell to Alloy Nanocrystals". In: *ACS Nano* 7.9 (2013), pp. 7913–7930. ISSN: 1936-0851. DOI: 10.1021/nn402931y. URL: http://pubs.acs.org/doi/10.1021/nn402931y.

[45] Michael Grünwald et al. "Transferable pair potentials for CdS and ZnS crystals". In: *The Journal of Chemical Physics* 136.23 (2012), p. 234111. ISSN: 0021-9606. DOI: 10.1063/1.4729468. URL: http://aip.scitation.org/doi/10.1063/1.4729468.

[46] Iurii Gudyma, Victor Ivashko, and Andrej Bobák. "Surface and Size Effects in Spin-Crossover Nanocrystals". In: *Nanoscale Research Letters* 12.1 (2017), p. 101. ISSN: 1931-7573. DOI: 10.1186/s11671-017-1844-z. URL: http://nanoscalereslett.springeropen.com/articles/10.1186/s11671-017-1844-z.

[47] H Gupta. "Microscopic computer simulations of directional coarsening in face-centered cubic alloys". In: *Acta Materialia* 49.1 (2001), pp. 53–63. ISSN: 13596454. DOI: 10.1016/S1359-6454(00)00303-7. URL: https://linkinghub.elsevier.com/retrieve/pii/S1359645400003037.

[48] Rajan Gupta and Pablo Tamayo. "CRITICAL EXPONENTS OF THE 3-D ISING MODEL". In: *International Journal of Modern Physics C* 07.03 (1996), pp. 305–319. ISSN: 0129-1831. DOI: 10.1142/S0129183196000247. URL: https://www.worldscientific.com/doi/abs/10.1142/S0129183196000247.

[49] P Gutlich, V KsenofontovS, and A Gaspar. "Pressure effect studies on spin crossover systems". In: *Coordination Chemistry Reviews* 249.17-18 (2005), pp. 1811–1829. ISSN: 00108545. DOI: 10.1016/j.ccr.2005.01.022. URL: https://linkinghub.elsevier.com/retrieve/pii/S0010854505000305.

[50] M. Z. Hasan and C. L. Kane. "Colloquium : Topological insulators". In: *Reviews of Modern Physics* 82.4 (2010), pp. 3045–3067. ISSN: 0034-6861. DOI: 10.1103/RevModPhys.82.3045. URL: https://link.aps.org/doi/10.1103/RevModPhys.82.3045.

[51] Andreas Hauser et al. "Cooperative phenomena and light-induced bistability in iron(II) spin-crossover compounds". In: *Coordination Chemistry Reviews* 190-192 (1999), pp. 471–491. ISSN: 00108545. DOI: 10.1016/S0010-8545(99)00111-3. URL: https://linkinghub.elsevier.com/retrieve/pii/S0010854599001113.

[52] Matthew R. Hauwiller et al. "Unraveling Kinetically-Driven Mechanisms of Gold Nanocrystal Shape Transformations Using Graphene Liquid Cell Electron Microscopy". In: *Nano Letters* 18.9 (2018), pp. 5731–5737. ISSN: 1530-6984. DOI: 10.1021/acs.nanolett.8b02337. URL: https://pubs.acs.org/doi/10.1021/acs.nanolett.8b02337.

[53] Shinya Hayami et al. "Iron(III) Spin-Crossover Compounds with a Wide Apparent Thermal Hysteresis around Room Temperature". In: *Journal of the American Chemical Society* 123.47 (2001), pp. 11644–11650. ISSN: 0002-7863. DOI: 10.1021/ja0017920. URL: https://pubs.acs.org/doi/10.1021/ja0017920.

[54] Nikhil R. Jana. "Shape Effect in Nanoparticle Self-Assembly". In: *Angewandte Chemie International Edition* 43.12 (2004), pp. 1536–1540. ISSN: 1433-7851. DOI: 10.1002/anie.200352260. URL: http://doi.wiley.com/10.1002/anie.200352260.

[55] Jacek Jasieniak and Paul Mulvaney. "From Cd-Rich to Se-Rich - the Manipulation of CdSe Nanocrystal Surface Stoichiometry". In: *Journal of the American Chemical Society* 129.10 (2007), pp. 2841–2848. ISSN: 0002-7863. DOI: 10.1021/ja066205a. URL: https://pubs.acs.org/doi/10.1021/ja066205a.

[56] C. Jayaprakash and W. F. Saam. "Thermal evolution of crystal shapes: The fcc crystal". In: *Physical Review B* 30.7 (1984), pp. 3916–3928. ISSN: 0163-1829. DOI: 10.1103/PhysRevB.30.3916. URL: https://link.aps.org/doi/10.1103/PhysRevB.30.3916.

[57] E. Jones, E. Oliphant, P. Peterson, et al. *SciPy: Open Source Scientific Tools for Python*. 2001–. URL: http://www.scipy.org/.

[58] Yolanda Justo et al. "Less Is More. Cation Exchange and the Chemistry of the Nanocrystal Surface". In: *ACS Nano* 8.8 (2014), pp. 7948–7957. ISSN: 1936-0851. DOI: 10.1021/nn5037812. URL: https://pubs.acs.org/doi/10.1021/nn5037812.

[59] M. Kac, G. E. Uhlenbeck, and P. C. Hemmer. "On the van der Waals theory of the vapor-liquid equilibrium. I. Discussion of a one-dimensional model". In: *Journal of Mathematical Physics* 4.2 (1963), pp. 216–228. ISSN: 00222488. DOI: 10.1063/1.1703946. URL: https://aip.scitation.org/doi/pdf/10.1063/1.1703946?class=pdf.

[60] C. L. Kane and T. C. Lubensky. "Topological boundary modes in isostatic lattices". In: *Nature Physics* 10.1 (2014), pp. 39–45. ISSN: 1745-2473. DOI: 10.1038/nphys2835. URL: http://www.nature.com/articles/nphys2835.

[61] Kyozi Kawasaki. "Diffusion Constants near the Critical Point for Time-Dependent Ising Models. I". In: *Physical Review* 145.1 (1966), pp. 224–230. ISSN: 0031-899X. DOI: 10.1103/PhysRev.145.224. URL: https://link.aps.org/doi/10.1103/PhysRev.145.224.

[62] C.P. Köhler et al. "Nature of the phase transition in spin crossover compounds". In: *Journal of Physics and Chemistry of Solids* 51.3 (1990), pp. 239–247. ISSN: 00223697. DOI: 10.1016/0022-3697(90)90052-H. URL: https://linkinghub.elsevier.com/retrieve/pii/002236979090052H.

[63] Maksym V. Kovalenko et al. "Prospects of Nanoscience with Nanocrystals". In: *ACS Nano* 9.2 (2015), pp. 1012–1057. ISSN: 1936-0851. DOI: 10.1021/nn506223h. URL: https://pubs.acs.org/doi/10.1021/nn506223h.

[64] Joachim Krug. "Introducton to Step Dynamics and Step Instabilities". In: *Multiscale Modeling in Epitaxial Growth*. Ed. by Alex Voigt. Basel: Birkhäuser Basel, 2004, pp. 69–95.

[65] Shankar Kumar et al. "The weighted histogram analysis method for free-energy calculations on biomolecules. I. The method". In: *Journal of Computational Chemistry* 13.8 (1992), pp. 1011–1021. ISSN: 0192-8651. DOI: 10.1002/jcc.540130812. URL: http://doi.wiley.com/10.1002/jcc.540130812.

[66] D. P. Landau. "Critical and multicritical behavior in a triangular-lattice-gas Ising model: Repulsive nearest-neighbor and attractive next-nearest-neighbor coupling". In: *Physical Review B* 27.9 (1983), pp. 5604–5617. ISSN: 0163-1829. DOI: 10.1103/PhysRevB.27.5604. URL: https://link.aps.org/doi/10.1103/PhysRevB.27.5604.

[67] L.D. Landau and E.M. Lifshitz. *Theory of Elasticity*. 3rd. Butterworth-Heinemann, 1986. Chap. 1. ISBN: 9780750626330.

[68] Hyunjoo Lee et al. "Morphological Control of Catalytically Active Platinum Nanocrystals". In: *Angewandte Chemie International Edition* 45.46 (2006), pp. 7824–7828. ISSN: 14337851. DOI: 10.1002/anie.200603068. URL: http://doi.wiley.com/10.1002/anie.200603068.

[69] Vladimir Lesnyak et al. "Cu Vacancies Boost Cation Exchange Reactions in Copper Selenide Nanocrystals". In: *Journal of the American Chemical Society* 137.29 (2015), pp. 9315–9323. ISSN: 0002-7863. DOI: 10.1021/jacs.5b03868. URL: https://pubs.acs.org/doi/10.1021/jacs.5b03868.

[70] Jean-François Létard et al. "Critical temperature of the LIESST effect in iron(II) spin crossover compounds". In: *Chemical Physics Letters* 313.1-2 (1999), pp. 115–120. ISSN: 00092614. DOI: 10.1016/S0009-2614(99)01036-2. URL: https://linkinghub.elsevier.com/retrieve/pii/S0009261499010362.

[71] Hongbo Li et al. "Sequential Cation Exchange in Nanocrystals: Preservation of Crystal Phase and Formation of Metastable Phases". In: *Nano Letters* 11.11 (2011), pp. 4964–4970. ISSN: 1530-6984. DOI: 10.1021/nl202927a. URL: http://pubs.acs.org/doi/abs/10.1021/nl202927a.

[72] Joseph M. Luther et al. "Synthesis of PbS Nanorods and Other Ionic Nanocrystals of Complex Morphology by Sequential Cation Exchange Reactions". In: *Journal of the American Chemical Society* 131.46 (2009), pp. 16851–16857. ISSN: 0002-7863. DOI: 10.1021/ja906503w. URL: https://pubs.acs.org/doi/10.1021/ja906503w.

[73] F. Rossi M. Galassi, J. Davies, J. Theiler, B. Gough, G. Jungman, P. Alken, M. Booth. *GNU Scientific Library Reference Manual*. 3rd. Network Theory Ltd., 2009. ISBN: 0954612078. URL: http://www.gnu.org/software/gsl/.

[74] L D Marks and L Peng. "Nanoparticle shape, thermodynamics and kinetics". In: *Journal of Physics: Condensed Matter* 28.5 (2016), p. 053001. ISSN: 0953-8984. DOI: 10.1088/0953-8984/28/5/053001. URL: http://stacks.iop.org/0953-8984/28/i=5/a=053001?key=crossref.b811f882d99ecc7f5eeafdbf4e06fde7.

[75] Makoto Matsumoto and Takuji Nishimura. "Mersenne twister: a 623-dimensionally equidistributed uniform pseudo-random number generator". In: *ACM Transactions on Modeling and Computer Simulation* 8.1 (1998), pp. 3–30. ISSN: 10493301. DOI: 10.1145/272991.272995. URL: http://portal.acm.org/citation.cfm?doid=272991.272995.

[76] J.W. Matthews and A.E. Blakeslee. "Defects in epitaxial multilayers". In: *Journal of Crystal Growth* 27 (1974), pp. 118–125. ISSN: 00220248. DOI: 10.1016/S0022-0248(74)80055-2. URL: https://www.sciencedirect.com/science/article/pii/S0022024874800552.

[77] N.D. Mermin, N.W. and Ashcroft. *Solid State Physics*. Philadelphia, PA: Saunders College, 1976. Chap. 5. ISBN: 978-0030839931.

[78] Mirko Mikolasek et al. "Phase Stability of Spin-Crossover Nanoparticles Investigated by Synchrotron Mössbauer Spectroscopy and Small-Angle Neutron Scattering". In: *The Journal of Physical Chemistry Letters* 10.7 (2019), pp. 1511–1515. ISSN: 1948-7185. DOI: 10.1021/acs.jpclett.9b00335. URL: https://pubs.acs.org/doi/10.1021/acs.jpclett.9b00335.

[79] Seiji Miyashita et al. "Realization of the mean-field universality class in spin-crossover materials". In: *Physical Review B* 77.1 (2008), p. 014105. ISSN: 1098-0121. DOI: 10.1103/PhysRevB.77.014105. URL: https://journals.aps.org/prb/pdf/10.1103/PhysRevB.77.014105https://link.aps.org/doi/10.1103/PhysRevB.77.014105.

[80] Seiji Miyashita et al. "Threshold phenomena under photoexcitation of spin-crossover materials with cooperativity due to elastic interactions". In: *Physical Review B - Condensed Matter and Materials Physics* 80.6 (2009), pp. 1–6. ISSN: 10980121. DOI: 10.1103/PhysRevB.80.064414.

[81] Takashi Mori. "Analysis of the exactness of mean-field theory in long-range interacting systems". In: *Physical Review E* 82.6 (2010), p. 060103. ISSN: 1539-3755. DOI: 10.1103/PhysRevE.82.060103. URL: https://link.aps.org/doi/10.1103/PhysRevE.82.060103.

[82] Takashi Mori. "Nonadditivity in Quasiequilibrium States of Spin Systems with Lattice Distortion". In: *Physical Review Letters* 111.2 (2013), p. 020601. ISSN: 0031-9007. DOI: 10.1103/PhysRevLett.111.020601. URL: https://link.aps.org/doi/10.1103/PhysRevLett.111.020601.

[83] John A. Moriarty. "Total Energy of Copper, Silver, and Gold". In: *Physical Review B* 6.4 (1972), pp. 1239–1252. ISSN: 0556-2805. DOI: 10.1103/PhysRevB.6.1239. URL: https://link.aps.org/doi/10.1103/PhysRevB.6.1239.

[84] Taro Nakada et al. "Critical temperature and correlation length of an elastic interaction model for spin-crossover materials". In: *Physical Review B* 85.5 (2012), p. 054408. ISSN: 1098-0121. DOI: 10.1103/PhysRevB.85.054408. URL: https://link.aps.org/doi/10.1103/PhysRevB.85.054408.

[85] Taro Nakada et al. "Crossover between a short-range and a long-range Ising model". In: *Physical Review B* 84.5 (2011), p. 054433. ISSN: 1098-0121. DOI: 10.1103/PhysRevB.84.054433. URL: https://link.aps.org/doi/10.1103/PhysRevB.84.054433.

[86] W. Nicolazzi and S. Pillet. "Structural aspects of the relaxation process in spin crossover solids: Phase separation, mapping of lattice strain, and domain wall structure". In: *Physical Review B* 85.9 (2012), p. 094101. ISSN: 1098-0121. DOI: 10.1103/PhysRevB.85.094101. URL: https://link.aps.org/doi/10.1103/PhysRevB.85.094101.

[87] Masamichi Nishino et al. "Simple Two-Dimensional Model for the Elastic Origin of Cooperativity among Spin States of Spin-Crossover Complexes". In: *Physical Review Letters* 98.24 (2007), p. 247203. ISSN: 0031-9007. DOI: 10.1103/PhysRevLett.98.247203. URL: https://link.aps.org/doi/10.1103/PhysRevLett.98.247203.

[88] Jae Dong Noh and Doochul Kim. "Phase Boundary and Universality of the Triangular Lattice Antiferromagnetic Ising Model". In: *International Journal of Modern Physics B* 06.17 (1992), pp. 2913–2924. ISSN: 0217-9792. DOI: 10.1142/S0217979292002309. URL: http://www.worldscientific.com/doi/abs/10.1142/S0217979292002309.

[89] J Oitmaa and M N Barber. "On the critical behaviour of an Ising system with lattice coupling". In: *Journal of Physics C: Solid State Physics* 8.21 (1975), pp. 3653–3663. ISSN: 0022-3719. DOI: 10.1088/0022-3719/8/21/036. URL: http://stacks.iop.org/0022-3719/8/i=21/a=036?key=crossref.7282b82f7376b87d59e6ec1bb824ac76.

[90] Florian D. Ott et al. "Microscopic Theory of Cation Exchange in CdSe Nanocrystals". In: *Physical Review Letters* 113.15 (2014), p. 156803. ISSN: 0031-9007. DOI: 10.1103/PhysRevLett.113.156803. URL: https://link.aps.org/doi/10.1103/PhysRevLett.113.156803.

[91] D W Oxtoby. "Homogeneous nucleation: theory and experiment". In: *Journal of Physics: Condensed Matter* 4.38 (1992), pp. 7627–7650. ISSN: 0953-8984. DOI: 10.1088/0953-8984/4/38/001. URL: http://stacks.iop.org/0953-8984/4/i=38/a=001?key=crossref.3ff56e53666fa0d49dbc74dae3306661.

[92] Miguel Paez-Espejo, Mouhamadou Sy, and Kamel Boukheddaden. "Unprecedented Bistability in Spin-Crossover Solids Based on the Retroaction of the High Spin Low-Spin Interface with the Crystal Bending". In: *Journal of the American Chemical Society* 140.38 (2018), pp. 11954–11964. ISSN: 0002-7863. DOI: 10.1021/jacs.8b04802. URL: https://pubs.acs.org/doi/10.1021/jacs.8b04802.

[93] Jungwon Park et al. "Direct Observation of Nanoparticle Superlattice Formation by Using Liquid Cell Transmission Electron Microscopy". In: *ACS Nano* 6.3 (2012), pp. 2078–2085. ISSN: 1936-0851. DOI: 10.1021/nn203837m. URL: https://pubs.acs.org/doi/10.1021/nn203837m.

[94] R. People and J. C. Bean. "Calculation of critical layer thickness versus lattice mismatch for Ge x Si 1- x /Si strained-layer heterostructures". In: *Applied Physics Letters* 47.3 (1985), pp. 322–324. ISSN: 0003-6951. DOI: 10.1063/1.96206. URL: http://aip.scitation.org/doi/10.1063/1.96206.

[95] Vitor M. Pereira and A. H. Castro Neto. "Strain Engineering of Graphene's Electronic Structure". In: *Physical Review Letters* 103.4 (2009), p. 046801. ISSN: 0031-9007. DOI: 10.1103/PhysRevLett.103.046801. URL: https://link.aps.org/doi/10.1103/PhysRevLett.103.046801.

[96] Rob Phillips, Jane Kondev, and Julie Theriot. *Physical Biology of the Cell*. 1st. Garland Science, 2009. Chap. 10.

[97] Eran Rabani. "An interatomic pair potential for cadmium selenide". In: *The Journal of Chemical Physics* 116.1 (2002), p. 258. ISSN: 00219606. DOI: 10.1063/1.1424321. URL: http://scitation.aip.org/content/aip/journal/jcp/116/1/10.1063/1.1424321.

[98] José Antonio Real, Ana Belén Gaspar, and M. Carmen Muñoz. "Thermal, pressure and light switchable spin-crossover materials". In: *Dalton Transactions* 12 (2005), p. 2062. ISSN: 1477-9226. DOI: 10.1039/b501491c. URL: http://xlink.rsc.org/?DOI=b501491c.

[99] Sidney Redner. *A Guide to First-Passage Processes*. 1st. Cambridge, UK: Cambridge University Press, 2001. ISBN: 978-0521652483.

[100] O. K. Rice. "Thermodynamics of Phase Transitions in Compressible Solid Lattices". In: *The Journal of Chemical Physics* 22.9 (1954), pp. 1535–1544. ISSN: 0021-9606. DOI: 10.1063/1.1740453. URL: http://aip.scitation.org/doi/10.1063/1.1740453.

[101] Jessy B. Rivest and Prashant K. Jain. "Cation exchange on the nanoscale: an emerging technique for new material synthesis, device fabrication, and chemical sensing". In: *Chem. Soc. Rev.* 42.1 (2013), pp. 89–96. ISSN: 0306-0012. DOI: 10.1039/C2CS35241A. URL: http://xlink.rsc.org/?DOI=C2CS35241A.

[102] R. D. Robinson et al. "Spontaneous Superlattice Formation in Nanorods Through Partial Cation Exchange". In: *Science* 317.5836 (2007), pp. 355–358. ISSN: 0036-8075. DOI: 10.1126/science.1142593. URL: http://www.sciencemag.org/cgi/doi/10.1126/science.1142593.

[103] S. Schneider et al. "Atomic surface diffusion on Pt nanoparticles quantified by high-resolution transmission electron microscopy". In: *Micron* 63 (2014), pp. 52–56. ISSN: 09684328. DOI: 10.1016/j.micron.2013.12.011. URL: https://linkinghub.elsevier.com/retrieve/pii/S0968432813002126.

[104] B. J. Schulz et al. "Suppression of capillary wave broadening of interfaces in binary alloys due to elastic interactions". In: *Physical Review Letters* 95.9 (2005), pp. 1–4. ISSN: 00319007. DOI: 10.1103/PhysRevLett.95.096101. URL: https://journals.aps.org/prl/pdf/10.1103/PhysRevLett.95.096101.

[105] H. W. Sheng et al. "Highly optimized embedded-atom-method potentials for fourteen fcc metals". In: *Physical Review B* 83.13 (2011), p. 134118. ISSN: 1098-0121. DOI: 10.1103/PhysRevB.83.134118. URL: https://link.aps.org/doi/10.1103/PhysRevB.83.134118.

[106] Ahmed Slimani et al. "Microscopic spin-distortion model for switchable molecular solids: Spatiotemporal study of the deformation field and local stress at the thermal spin transition". In: *Physical Review B* 87.1 (2013), p. 014111. ISSN: 1098-0121. DOI: 10.1103/PhysRevB.87.014111. URL: https://link.aps.org/doi/10.1103/PhysRevB.87.014111.

[107] Andrew M. Smith, Aaron M. Mohs, and Shuming Nie. "Tuning the optical and electronic properties of colloidal nanocrystals by lattice strain". In: *Nature Nanotechnology* 4.1 (2009), pp. 56–63. ISSN: 1748-3387. DOI: 10.1038/nnano.2008.360. URL: http://www.nature.com/articles/nnano.2008.360.

[108] D. H. Son et al. "Cation Exchange Reactions in Ionic Nanocrystals". In: *Science* 306.5698 (2004), pp. 1009–1012. ISSN: 0036-8075. DOI: 10.1126/science.1103755. URL: http://www.sciencemag.org/cgi/doi/10.1126/science.1103755.

[109] H Spiering and N Willenbacher. "Elastic interaction of high-spin and low-spin complex molecules in spin-crossover compounds. II". In: *Journal of Physics: Condensed Matter* 1.50 (1989), pp. 10089–10105. ISSN: 0953-8984. DOI: 10.1088/0953-8984/1/50/011. URL: http://stacks.iop.org/0953-8984/1/i=50/a=011?key=crossref.f013d5938620f2eb1cf75d0faa8393ca.

[110] Elias M. Stein and Rami Shakarchi. *Complex Analysis*. 1st. Princeton, New Jersey: Princeton University Press, 2003. ISBN: 9780691113852.

[111] Roman Süsstrunk and Sebastian D. Huber. "Classification of topological phonons in linear mechanical metamaterials". In: *Proceedings of the National Academy of Sciences* 113.33 (2016), E4767–E4775. ISSN: 0027-8424. DOI: 10.1073/pnas.1605462113. URL: http://www.pnas.org/lookup/doi/10.1073/pnas.1605462113.

[112] M. F. Thorpe and E. J. Garboczi. "Elastic properties of central-force networks with bond-length mismatch". In: *Physical Review B* 42.13 (1990), pp. 8405–8417. ISSN: 0163-1829. DOI: 10.1103/PhysRevB.42.8405. URL: https://link.aps.org/doi/10.1103/PhysRevB.42.8405.

[113] G.M. Torrie and J.P. Valleau. "Nonphysical sampling distributions in Monte Carlo free-energy estimation: Umbrella sampling". In: *Journal of Computational Physics* 23.2 (1977), pp. 187–199. ISSN: 00219991. DOI: 10.1016/0021-9991(77)90121-8. URL: http://linkinghub.elsevier.com/retrieve/pii/0021999177901218.

[114] Mark Tuckerman. *Statistical Mechanics: Theory and Molecular Simulation*. New York: Oxford University Press, 2010.

[115] E. Vandeworp and Kathie E. Newman. "Coherent alloy phase separation: Differences in canonical and grand canonical ensembles". In: *Physical Review B - Condensed Matter and Materials Physics* 55.21 (1997), pp. 14222–14229. ISSN: 1550235X. DOI: 10.1103/PhysRevB.55.14222. URL: https://journals.aps.org/prb/pdf/10.1103/PhysRevB.55.14222.

[116] Benjamin B. Vollmayr-Lee and Erik Luijten. "Kac-potential treatment of nonintegrable interactions". In: *Physical Review E - Statistical Physics, Plasmas, Fluids, and Related Interdisciplinary Topics* 63.3 (2001), pp. 1–8. ISSN: 1063651X. DOI: 10.1103/PhysRevE.63.031108. URL: https://journals.aps.org/pre/pdf/10.1103/PhysRevE.63.031108.

[117] George M. Whitesides. "Nanoscience, Nanotechnology, and Chemistry". In: *Small* 1.2 (2005), pp. 172–179. ISSN: 1613-6810. DOI: 10.1002/smll.200400130. URL: http://doi.wiley.com/10.1002/smll.200400130.

[118] N Willenbacher and H Spiering. "The elastic interaction of high-spin and low-spin complex molecules in spin-crossover compounds". In: *Journal of Physics C: Solid State Physics* 21.8 (1988), pp. 1423–1439. ISSN: 0022-3719. DOI: 10.1088/0022-3719/21/8/017. URL: http://stacks.iop.org/0022-3719/21/i=8/a=017?key=crossref.0955fad160f988e576c6e42ab71438d3.

[119] G. Wulff. "XXV. Zur Frage der Geschwindigkeit des Wachsthums und der Auflösung der Krystallflächen". In: *Zeitschrift für Kristallographie - Crystalline Materials* 34.1-6 (1901). ISSN: 2196-7105. DOI: 10.1524/zkri.1901.34.1.449. URL: http://www.degruyter.com/view/j/zkri.1901.34.issue-1-6/zkri.1901.34.1.449/zkri.1901.34.1.449.xml.

[120] Younan Xia, Xiaohu Xia, and Hsin-Chieh Peng. "Shape-Controlled Synthesis of Colloidal Metal Nanocrystals: Thermodynamic versus Kinetic Products". In: *Journal of the American Chemical Society* 137.25 (2015), pp. 7947–7966. ISSN: 0002-7863. DOI: 10.1021/jacs.5b04641. URL: https://pubs.acs.org/doi/10.1021/jacs.5b04641.

[121] Xingchen Ye et al. "Single-particle mapping of nonequilibrium nanocrystal transformations". In: *Science* 354.6314 (2016), pp. 874–877. ISSN: 0036-8075. DOI: 10.1126/science.aah4434. URL: https://www.sciencemag.org/lookup/doi/10.1126/science.aah4434.

[122] Jong Min Yuk et al. "High-Resolution EM of Colloidal Nanocrystal Growth Using Graphene Liquid Cells". In: *Science* 336.6077 (2012), pp. 61–64. ISSN: 0036-8075. DOI: 10.1126/science.1217654. URL: https://www.sciencemag.org/lookup/doi/10.1126/science.1217654.

[123] You Zhai, Joseph C. Flanagan, and Moonsub Shim. "Lattice Strain and Ligand Effects on the Formation of Cu 2– x S/I-III-VI 2 Nanorod Heterostructures through Partial Cation Exchange". In: *Chemistry of Materials* 29.14 (2017), pp. 6161–6167. ISSN: 0897-4756. DOI: 10.1021/acs.chemmater.7b02392. URL: https://pubs.acs.org/doi/10.1021/acs.chemmater.7b02392.

[124] R. K. P. Zia, Edward F. Redish, and Susan R. McKay. "Making sense of the Legendre transform". In: *American Journal of Physics* 77.7 (2009), pp. 614–622. ISSN: 0002-9505. DOI: 10.1119/1.3119512. URL: http://aapt.scitation.org/doi/10.1119/1.3119512.

[125] Lianfeng Zou et al. "Dislocation nucleation facilitated by atomic segregation". In: *Nature Materials* 17.1 (2018), pp. 56–63. ISSN: 1476-1122. DOI: 10.1038/nmat5034. URL: http://www.nature.com/articles/nmat5034.

Appendix A

Appendix for "Etching: A Nonequilibrium Route to New Nanocrystal Shapes"

A.1 Choice of Microscopic Dynamics

Here we compare Glauber dynamics [43] to Metropolis dynamics [114] and to the kinetic Glauber scheme described in Chap. 2. Metropolis dynamics is implemented in a way nearly identical to Glauber dynamics; for Metropolis dynamics, though, the acceptance probabilities are given by:

$$A_{\text{insert}}(C \to C') = \min\left[1, \frac{N_{\text{vac}}(C)}{N_{\text{surf}}(C')} e^{-\beta\Delta\mathcal{H}}\right], \tag{A.1}$$

$$A_{\text{delete}}(C \to C') = \min\left[1, \frac{N_{\text{surf}}(C)}{N_{\text{vac}}(C')} e^{-\beta\Delta\mathcal{H}}\right], \tag{A.2}$$

$$\Delta\mathcal{H} = \mathcal{H}(C') - \mathcal{H}(C). \tag{A.3}$$

When the chemical potential is set to $\mu/\epsilon = -6.5$ (for the Glauber and Metropolis dynamics), the etching structures that result from the three different algorithms appear nearly identical; quantification of the h-index over time shows that they are statistically indistinguishable (Fig. A.1.) The appearance of a THH during etching thus appears to be robust to the choice of dynamics.

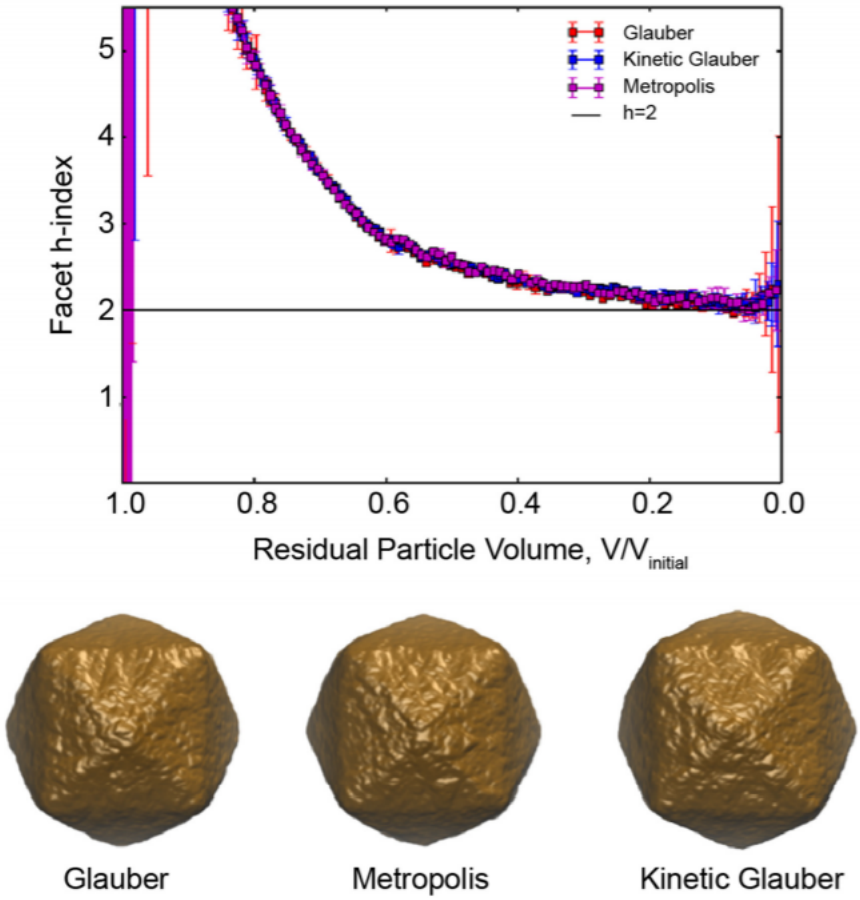

Figure A.1: Plot of h versus remaining volume, as well as snapshots from etching trajectories, for the three different choices of dynamics.

A.2 Detailed Balance

In order to sample an equilibrium ensemble, the acceptance probability A must satisfy detailed balance:

$$P(C)P_{\text{gen}}(C \to C')A(C \to C') = P(C')P_{\text{gen}}(C' \to C)A(C' \to C), \tag{A.4}$$

where $P_{\text{gen}}(C \to C')$ is the probability of generating the proposed move from C to C' and $P(C)$ is the equilibrium Boltzmann probability of observing configuration C. Once choice for A which satisfies Eq. A.4 is that of Metropolis [114]:

$$P_{\text{acc}}(C \to C') = \min\left[1, \frac{P_{\text{gen}}(C' \to C)}{P_{\text{gen}}(C \to C')} e^{-\beta(\mathcal{H}(C')-\mathcal{H}(C))}\right]. \tag{A.5}$$

Another satisfactory choice is due to Glauber [43]:

$$P_{\text{acc}}(C \to C') = \frac{1}{1 + \frac{P_{\text{gen}}(C \to C')}{P_{\text{gen}}(C' \to C)} e^{\beta(\mathcal{H}(C') - \mathcal{H}(C))}}. \tag{A.6}$$

Let us focus on the Glauber acceptance probability. Suppose that we are attempting an atom insertion move. In this case, the generation probability is just the probability of selecting a particular surface vacancy:

$$P_{\text{gen}}(C \to C') = \frac{1}{N_{\text{vac}}(C)}, \tag{A.7}$$

and the generation probability of the reverse move is:

$$P_{\text{gen}}(C \to C') = \frac{1}{N_{\text{surf}}(C')}, \tag{A.8}$$

where $N_{\text{surf}}(C)$ and $N_{\text{vac}}(C)$ denote the number of surface atoms and surface vacancies, respectively, in configuration C. The acceptance probability for insertion moves can thus be written as:

$$P_{\text{acc}}(C \to C') = \frac{1}{1 + \frac{N_{\text{surf}}(C')}{N_{\text{vac}}(C)} e^{\beta(\mathcal{H}(C') - \mathcal{H}(C))}}. \tag{A.9}$$

Acceptance probabilities for other kinds of moves are derived similarly.

A.3 FCC Crystal Facets

Crystal facets are conveniently described using Miller indices [77]. Given a set of real space vectors $\mathbf{a}_i$, $i = 1, 2, 3$ for the crystal's unit cell, the reciprocal space vectors $\mathbf{b}_i$ are defined by $\mathbf{a}_i \cdot \mathbf{b}_j = 2\pi\delta_{ij}$. Any other reciprocal space vector $\mathbf{q}$ can then be written as:

$$\mathbf{q} = h\mathbf{b}_1 + k\mathbf{b}_2 + l\mathbf{b}_3. \tag{A.10}$$

The integers h, k, l are Miller indices. The notation (h, k, l) refers to the plane to which the vector $\mathbf{q}$ is perpendicular; $\{h, k, l\}$ refers to all such planes which are equivalent by lattice symmetry. The related notation $[hkl]$ refers to the direction in real space given by the plane's outward normal vector. For cubic lattices, such as the FCC lattice, it is conventional to choose the vectors $\mathbf{a}_i$ to be the Cartesian basis vectors, i.e. $\mathbf{a}_1 = \hat{\mathbf{x}}$, $\mathbf{a}_2 = \hat{\mathbf{y}}$, $\mathbf{a}_3 = \hat{\mathbf{z}}$.

Cutting a crystal along different lattice planes exposes surfaces with different geometries. Of particular importance is the coordination number of surface atoms. In Fig. A.2 we depict the geometry of selected facets of an FCC lattice. Clearly, both the arrangement of atoms and their coordination is sensitive to the particular facet. So-called "vicinal" facets present more spatially heterogeneous distributions of atoms. The (210) and (310) facets of an FCC lattice exhibit "steps" which are just one atom thick, as shown in Fig. A.3.

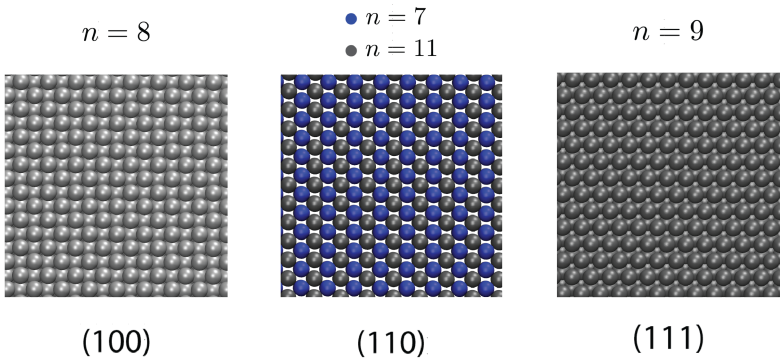

Figure A.2: Different facets of the FCC lattice. The coordination number n as well as the precise local arrangement of atoms on the surface varies with facet.

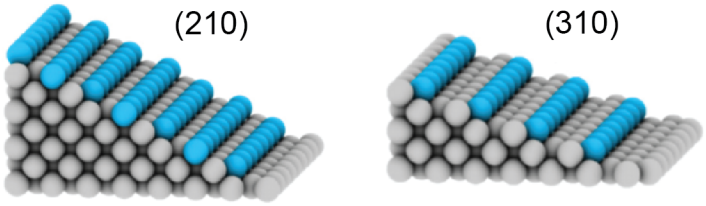

Figure A.3: Different vicinal facets of the FCC lattice. Light blue atoms have $n = 6$, while gray atoms have $n \geq 8$.

A.4 Calculation of h index

We used simple geometry to calculate the h-index in our simulations. Consider the vectors $\mathbf{v}_{100}$, $\mathbf{v}_{010}$ and $\mathbf{v}_{110}$, which extend from the center of a THH nanoparticle to its surface in the [100], [010], and [110] directions, respectively. We define the h vector as $\mathbf{v}_h = \mathbf{v}_{100} - \mathbf{v}_{110}$. Also defining the unit vectors $\hat{\mathbf{v}}_{100} = \mathbf{v}_{100}/|\mathbf{v}_{100}|$ and $\hat{\mathbf{v}}_{010} = \mathbf{v}_{010}/|\mathbf{v}_{010}|$, we compute h as:

$$h = \left(\frac{\mathbf{v}_h \cdot \hat{\mathbf{v}}_{100}}{\mathbf{v}_h \cdot \hat{\mathbf{v}}_{010}} \right)^{-1}. \tag{A.11}$$

Our reported values of h were computed by averaging the result of Eq. A.11 over 24 permutations of indices (6 pyramidal features, 4 faces on each pyramid.)

A.5 Surface Relaxation Moves

We considered three different types of diffusion moves: "local" diffusion moves, where a surface atom can hop to a nearest-neighbor vacancy; "global" diffusion moves, where a surface atom can move to any unoccupied surface site on the nanoparticle; and an intermediate type

of move, where a surface atom can hop to a nearest-neighbor vacancy or a second nearest-neighbor vacancy. We call this last type of move a "2-local" move.

To execute a local or global diffusion move, a surface atom is selected at random and a vacancy (chosen in a way appropriate to the type of diffusion that is being used) is also selected at random. (2-local moves are chosen in a somewhat different manner, which will be explained separately). These trial moves are then accepted with probabilities that preserve detailed balance; for local moves the probability is:

$$A_{\text{local}}(C \to C') = \frac{1}{1 + (d_l(C, C'))^{-1}}, \tag{A.12}$$

where:

$$d_l(C, C') = \frac{N_{\text{surf}}(C) n_{\text{vac}}(i)}{N_{\text{surf}}(C') n_{\text{vac}}(j)} e^{-\beta \Delta E}, \tag{A.13}$$

$$\Delta E = E(C') - E(C) = -\epsilon \Delta n. \tag{A.14}$$

Here, $n_{\text{vac}}(i)$ is the number of vacancies adjacent to atom i of configuration C and Δn is the total change in the number of contacts between occupied sites ("bonds") in going from C to C'. The ratio of Ns and ns in d_l is chosen so as to preserve detailed balance. For global moves the probability is:

$$A_{\text{global}}(C \to C') = \frac{1}{1 + (d_g(C, C'))^{-1}}, \tag{A.15}$$

where:

$$d_g(C, C') = \frac{N_{\text{surf}}(C) N_{\text{vac}}(C)}{N_{\text{surf}}(C') N_{\text{vac}}(C')} e^{-\beta \Delta E}, \tag{A.16}$$

$$\Delta E = E(C') - E(C) = -\epsilon \Delta n. \tag{A.17}$$

Again, Δn is the total change in the number of bonds.

For 2-local moves, surface atoms are still selected at random, but the vacancies are selected slightly differently. In particular, instead of selecting a single vacancy from a list of all eligible vacancies, one of the nearest neighbors of the selected atom is chosen at random (regardless of whether that neighboring site is occupied or unoccupied), and then a neighbor of that site is chosen at random (again, regardless of whether that neighbor is occupied or unoccupied). This site is rejected if it is not a surface vacancy, i.e. a vacancy that is a nearest neighbor of a surface atom.[1] If the site is a surface vacancy, then the diffusion move is accepted with probability:

$$A_{\text{2-local}}(C \to C') = \frac{1}{1 + (d_{2l}(C, C'))^{-1}}, \tag{A.18}$$

[1]For a given atom in an FCC lattice there are 12×12=144 ways to a select a nearest or next-nearest neighbor site. Many of these sites will not be surface vacancies and so a number of them will be rejected; nevertheless, we found this approach simpler than explicitly finding and listing all the nearest and next-nearest neighbor surface vacancies.

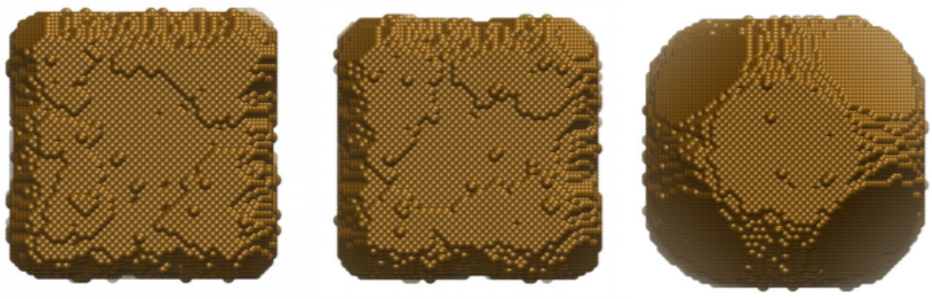

Figure A.4: Relaxation to the equilibrium fcc nanocrystal shape.

where:

$$d_{2l}(C, C') = \frac{N_{\text{surf}}(C)}{N_{\text{surf}}(C')} e^{-\beta \Delta E}, \tag{A.19}$$

$$\Delta E = E(C') - E(C) = -\epsilon \Delta n. \tag{A.20}$$

We performed MC simulations using each of the three different surface relaxation moves. Snapshots from these simulations for an initially cube-shaped nanocrystal containing ≈130,000 atoms at a temperature $\beta\epsilon \approx 2.5$ are shown in Fig. A.4 All simulations were run for 10^9 MC sweeps. All the simulations show that the nanoparticles approaching a truncated octahedron shape – the corners disappear resulting in {111} facets while the {100} faces of the cube shrink in surface area but accumulate additional layers. However, it is clear that global diffusion is the most effective move for reaching the equilibrium TO shape in a given number of sweeps.

A.6 Effect of Varying System Size

We performed etching simulations at several system sizes to check the robustness of our conclusions about shape changes. The largest such simulation consisted (initially) of ≈ 55 million atoms, corresponding to a cube of about 100nm. Simulations at different system sizes and $\mu/\epsilon = -6.5$ all produced THH intermediates, shown in Fig. A.5. Perhaps not surprisingly, the largest nanocrystal exhibited a transient THH shape most clearly.

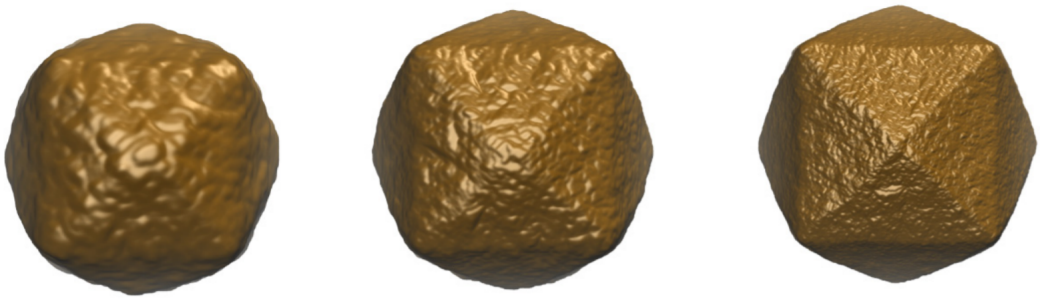

Figure A.5: Left to right: snapshots from etching simulations at $\mu/\epsilon = -6.5$ of initially ≈ 1 million-, 7 million-, and 55 million-atom cubic nanocrystals.

Appendix B

Appendix for "Consequences of Lattice Mismatch for Phase Equilibrium in Heterostructured Solids"

B.1 Numerical evidence for accuracy of small-mismatch approximation

Our elastic model is described by the Hamiltonian:

$$\mathcal{H}/\epsilon = 4\sum_{\mathbf{R},\hat{\boldsymbol{\alpha}}}\left[\frac{a}{\Delta}\left|\hat{\boldsymbol{\alpha}}+\left(\frac{\Delta}{a}\right)(\bar{\mathbf{u}}_{\mathbf{R}}-\bar{\mathbf{u}}_{\mathbf{R}+a\hat{\boldsymbol{\alpha}}})\right|-\left(\frac{l_{AB}}{\Delta}+\frac{1}{2}(\sigma_{\mathbf{R}}+\sigma_{\mathbf{R}+a\hat{\boldsymbol{\alpha}}})\right)\right]^2. \tag{B.1}$$

However, an approximate form of this Hamiltonian which assumes that the quantity $\boldsymbol{\delta} = (\Delta/a)(\bar{\mathbf{u}}_{\mathbf{R}} - \bar{\mathbf{u}}_{\mathbf{R}+a\hat{\boldsymbol{\alpha}}})$ is small captures the energetics very accurately when compared to Monte Carlo simulations. This approximate Hamiltonian - the small-mismatch Hamiltonian - is given by:

$$\bar{\mathcal{H}} \approx 4\sum_{\mathbf{R},\hat{\boldsymbol{\alpha}}}\left(\hat{\boldsymbol{\alpha}}\cdot(\bar{\mathbf{u}}_{\mathbf{R}}-\bar{\mathbf{u}}_{\mathbf{R}+a\hat{\boldsymbol{\alpha}}})-\frac{1}{2}(\delta\sigma_{\mathbf{R}}+\delta\sigma_{\mathbf{R}+a\hat{\boldsymbol{\alpha}}})\right)^2. \tag{B.2}$$

In the scaled units we have adopted, this Hamiltonian is independent of the mismatch Δ. To test how well this approximation works, we can measure the (minimum) energy of different configurations. A plot of the small-mismatch prediction for the energy of a superlattice ($E/N\epsilon = 8/3$) versus the energy measured by performing numerical energy minimization of a superlattice configuration governed by the full Hamiltonian is shown in Fig. B.1. The agreement is excellent: there is no visible difference between the predictions on the scale of the plot. An analogous plot, corresponding to an average over 1000 random configurations

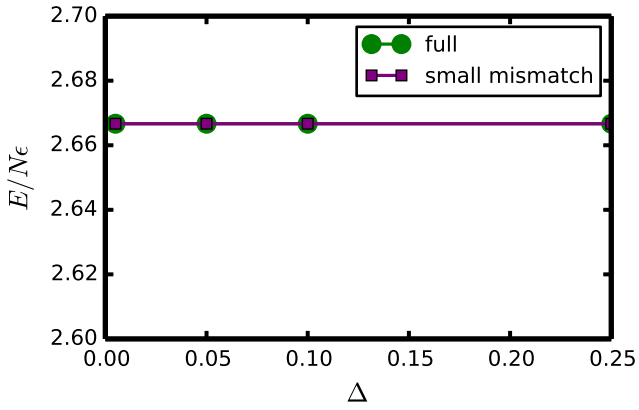

Figure B.1: Superlattice energy as a function of mismatch, $\Delta = (l_{AA} - l_{BB})/2$.

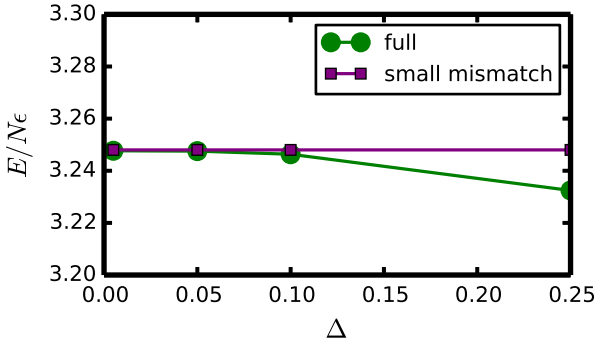

Figure B.2: Average energy of 1000 randomly initialized configurations with a composition $c = 1/3$ as a function of Δ. The small mismatch approximation predicts $E/N\epsilon = 8V_0/9$.

with the same composition, is shown in Fig. B.2. Here, the energy does have a visible dependence on mismatch (amounting to roughly a percent of the energy.) Additionally, the average energy of the random configurations changes upon global spin flips (although the effect is small; see Fig. B.3) while the superlattice energy does not (it is *symmetric* with respect to global spin flips.) Why does the superlattice do better than the random configurations?

The answer can be found by looking at the displacement fields of these configurations. As Fig. B.4 shows, the displacement field for the superlattice vanishes. This configuration nevertheless has energy because the bonds are still strained relative to their local, naturally-preferred lengths. This is illustrated in Fig. B.5. There is no guarantee of the random configuration's displacement field vanishing, a fact emphasized by Fig. B.6 (the corresponding strain field is shown in Fig. B.7.) Nevertheless, the magnitude of the displacement field

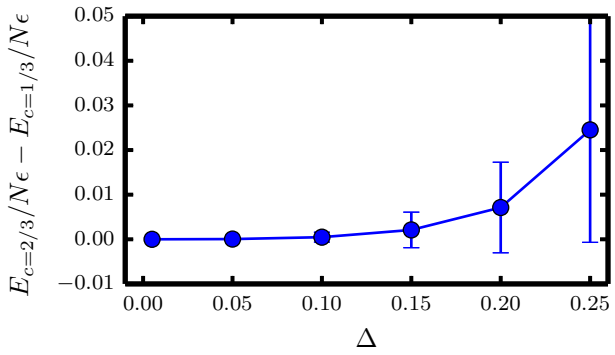

Figure B.3: Average energy difference between 1000 randomly initialized configurations with $c = 1/3$ and their globally spin-flipped counterparts. Error bars represent the standard deviation and reflect variability in the energy differences of different configurations. The small mismatch approximation predicts that this energy difference is zero. The anharmonicity of the Hamiltonian evidently favors B-rich compositions ($c = 1/3$) over A-rich compositions ($c = 2/3$.)

for the random configuration is still not huge.

The leading order correction to the small-mismatch approximation can be straighforwardly obtained by keeping terms first order in Δ. To be explicit, note that:

$$|\hat{\boldsymbol{\alpha}} + \boldsymbol{\delta}| = \sqrt{1 + 2\hat{\boldsymbol{\alpha}} \cdot \boldsymbol{\delta} + \boldsymbol{\delta}^2} \tag{B.3}$$

$$= 1 + \hat{\boldsymbol{\alpha}} \cdot \boldsymbol{\delta} + \frac{1}{2}\boldsymbol{\delta}^2 - \frac{1}{2}(\hat{\boldsymbol{\alpha}} \cdot \boldsymbol{\delta})^2 + \mathcal{O}(\boldsymbol{\delta}^3). \tag{B.4}$$

The small-mismatch approximation entails keeping only the first-order term in $\boldsymbol{\delta}$. When plugged back into the Hamiltonian, this term will be zero-th order in Δ (due to our scaling of variables.) If we keep the terms second-order in $\boldsymbol{\delta}$, we will get terms first-order in Δ in the Hamiltonian. Doing so, and noting that we can write:

$$\frac{1}{2}\left(\boldsymbol{\delta}^2 - (\hat{\boldsymbol{\alpha}} \cdot \boldsymbol{\delta})^2\right) = \frac{1}{2}\boldsymbol{\delta} \cdot (\mathbb{1} - \hat{\boldsymbol{\alpha}}\hat{\boldsymbol{\alpha}}) \cdot \boldsymbol{\delta}, \tag{B.5}$$

where $\mathbb{1}$ is the identity matrix, we have:

$$\bar{\mathcal{H}} \approx 4 \sum_{\mathbf{R},\hat{\boldsymbol{\alpha}}} \left(\hat{\boldsymbol{\alpha}} \cdot \mathbf{v}_{\mathbf{R},\hat{\boldsymbol{\alpha}}} + \frac{1}{2}\frac{\Delta}{a} \mathbf{v}_{\mathbf{R},\hat{\boldsymbol{\alpha}}} \cdot (\mathbb{1} - \hat{\boldsymbol{\alpha}}\hat{\boldsymbol{\alpha}}) \cdot \mathbf{v}_{\mathbf{R},\hat{\boldsymbol{\alpha}}} - \frac{1}{2}(\delta\sigma_{\mathbf{R}} + \delta\sigma_{\mathbf{R}+a\hat{\boldsymbol{\alpha}}}) \right)^2. \tag{B.6}$$

where we have defined $\mathbf{v}_{\mathbf{R},\hat{\boldsymbol{\alpha}}} = \bar{\mathbf{u}}_{\mathbf{R}} - \bar{\mathbf{u}}_{\mathbf{R}+a\hat{\boldsymbol{\alpha}}}$. The new (second) term in the above equation has a nice physical interpretation. The first term, present in the small-mismatch approximation, corresponds to energy due to *longitudinal* fluctuations, parallel to the bond vectors $\hat{\boldsymbol{\alpha}}$. The

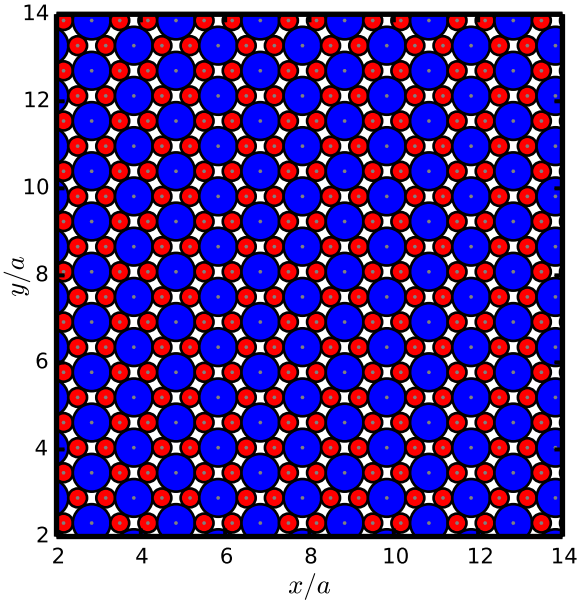

Figure B.4: The displacement field (indicated in gray) is zero for the superlattice. Here the mismatch is 20% (the result is the same for 50%.)

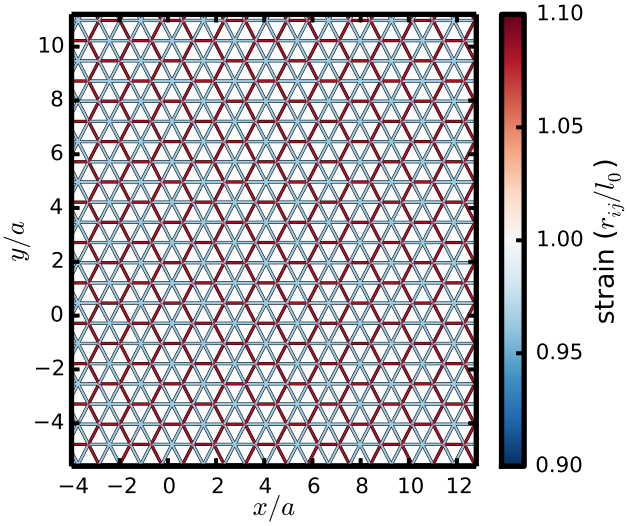

Figure B.5: Strain in the bonds of the superlattice with 20% mismatch, which results in a nonzero total energy.

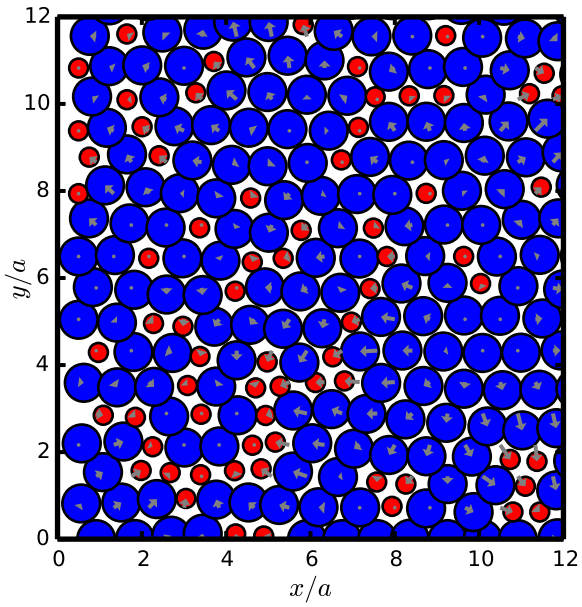

Figure B.6: The displacement field (indicated with gray arrows) for a random configuration with $c = 1/3$. The mismatch here is 50%.

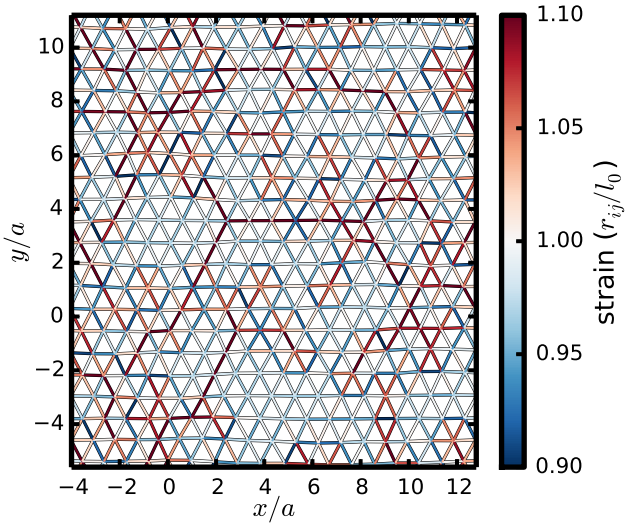

Figure B.7: Strain in the bonds of the random configuration with 20% mismatch.

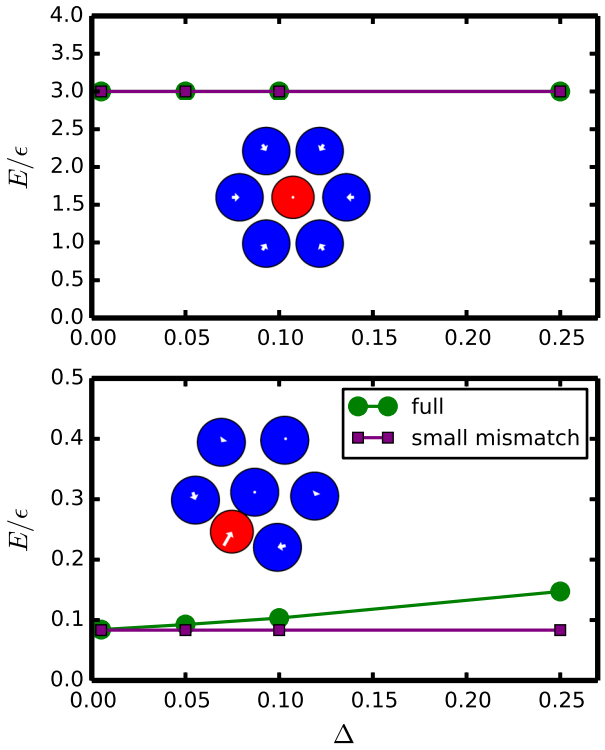

Figure B.8: Energies, as a function of mismatch Δ, of a 7-atom crystal with a compositional defect (red) placed either at the center or at a corner. The displacement fields, shown with white arrows, are for a mismatch of $\Delta = 0.25$ (50%.)

second term represents *transverse* fluctuations - those perpendicular to the bond vectors, a fact which can be deduced from the projection-operator-like form of this term. This is nicely illustrated with an example. In Fig. B.8 we show the energies and displacement fields of a 7-atom crystal with a single compositional impurity placed either at the center or at a corner. When the compositional defect is placed in the center, the small-mismatch approximation works very well, reflecting the fact that in this case the displacement vectors all point along the bond vectors. A compositional defect placed at a corner, though, generates a displacement field with a significant transverse component. The resulting energy is hence more sensitive to the value of the mismatch.

B.2 Asymptotic Scaling of Effective Potential

In the low-q limit, Taylor expansion of our effective potential yields leading order terms $\sim 4 - a(\hat{\mathbf{q}})q^2$, where a is a function of the direction of $\mathbf{q}$ but not its magnitude. The inverse Fourier transform is anisotropic, but scales as $\sim 1/R^4$ [34]. We confirmed this scaling by

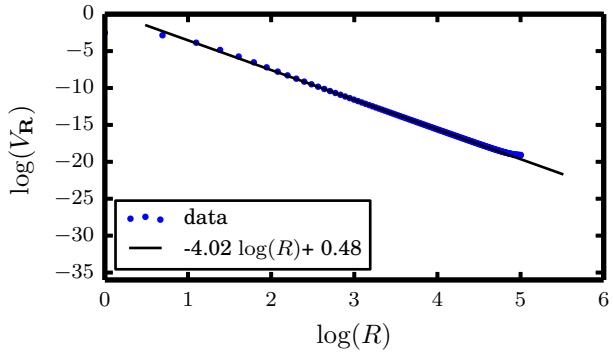

Figure B.9: Effective potential along the direction defined by the unit vector $\hat{\mathbf{a}} = (1, 0)$. Data was obtained from the numerical inverse Fourier transform of $\tilde{V}_{\mathbf{q}}$ on a 300 by 300 unit cell triangular lattice. The solid black line is a fit to the data, excluding the first 10 points and last 90 points (which are sensitive to the finite size of the lattice.)

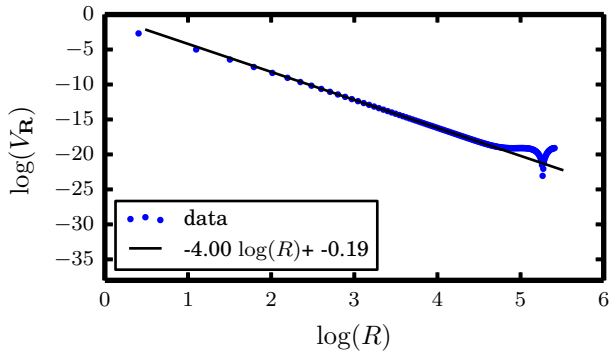

Figure B.10: Effective potential along the direction defined by the unit vector $\hat{\mathbf{a}} = (\sqrt{3}/2, 1/2)$. Data was obtained from the numerical inverse Fourier transform of $\tilde{V}_{\mathbf{q}}$ on a 300 by 300 unit cell triangular lattice. The solid black line is a fit to the data, excluding the first 10 points and last 90 points (which are sensitive to the finite size of the lattice.)

plotting the numerical inverse Fourier transform of $\tilde{V}_{\mathbf{q}}$ along different directions. Figs. B.9 and B.10 show the magnitude of the effective potential along two different lattice directions (one along one of the six principal lattice directions, here $\hat{\mathbf{a}} = (1, 0)$ and another along a vector halfway between two principal lattice directions, $\hat{\mathbf{a}} = (\sqrt{3}/2, 1/2)$. In both cases, fits to the tail of the energy yield a power law with exponent -4, consistent with our theoretical prediction.

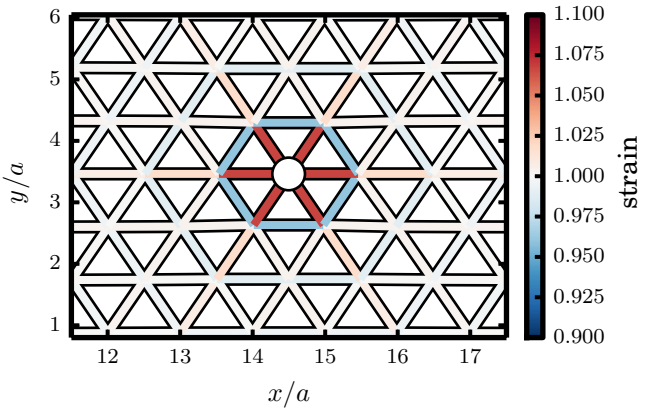

Figure B.11: Strain (defined as $|\mathbf{r}_{\mathbf{R}} - \mathbf{r}_{\mathbf{R}+a\hat{\boldsymbol{\alpha}}}|/l(\sigma_{\mathbf{R}}, \sigma_{\mathbf{R}+a\hat{\boldsymbol{\alpha}}})$) of bonds due to the presence of a single B defect surrounded by A atoms.The defect is denoted with a white circle.

B.3 Energetics of Impurity Configurations

The effective potential arises from the microscopic strain required to accommodate atoms of different sizes in the same lattice. Here we plot configurations of bonds, along with their associated strain, for a few "impurity" configurations, in which one or two atoms of type B have been substituted in an otherwise perfect A crystal. These zero-temperature configurations were generated by performing energy minimization via gradient descent.

Fig. B.11 shows a single B atom surrounded by A atoms. The "inner shell" of bonds emanating from the B atom have natural length l_{AB}, but in this minimum-energy configuration they do not achieve this length. They are instead stretched out by A atoms, which prefer a longer bond length. Meanwhile, the "second shell" of bonds connecting those of the inner shell are compressed relative to their natural length of l_{AA}.

Fig. B.12 shows the result of making two such impurities nearest neighbors. The bond connecting them has a natural length $l_{BB} < l_{AB}$. Evidently, minimizing the total energy means that this bond is far from its natural length. Lattice strain is highly localized in this bond and its immediate neighbors to the left and right. The resulting large energy contribution disfavors this configuration relative to a configuration in which the B atoms are very far apart. This is a consequence of the fact that a pair of B atoms prefers a bond distance l_{BB} that is smaller than either l_{AA} or l_{AB}. This preference is strongly frustrated when adjacent B defects are surrounded by an excess of A atoms, making this arrangement especially costly. The two defects are more readily accommodated on next-nearest neighbor sites. In this configuration, the energy is lower than that of infinite separation (see Fig. B.13). Similarly, two A defects in a B-rich environment can mitigate the cost of local expansion by sharing an intervening B neighbor. Inspection of the configuration reveals that the "second shell" bond shared by the B atoms bears a significant amount of strain, although

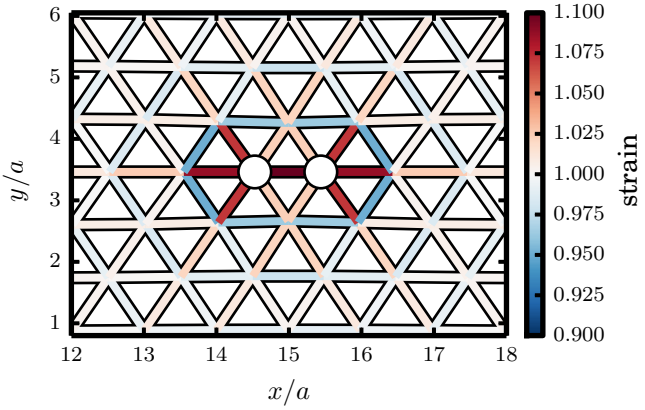

Figure B.12: Strain due to the presence of two nearest-neighbor B defects surrounded by A atoms.

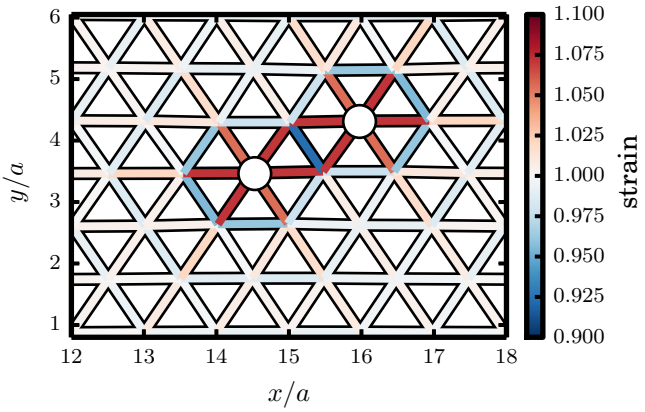

Figure B.13: Strain due to the presence of two next-nearest-neighbor B defects surrounded by A atoms.

much less than the $B - B$ bond in the nearest-neighbor configuration. Additional strain appears to be shared more equitably (compared to the nearest-neighbor configuration) among neighboring bonds, resulting in a lower total energy. Despite the more even distribution of strain, compression of the shared second shell bond appears to be necessary for the energetic favorability of this configuration; if we fix bond's length to the value it would have if the impurity were isolated, then the next-nearest neighbor configuration becomes energetically unfavorable compared to two isolated impurities. This reasoning allows us to microscopically rationalize the anisotropy of our effective potential.

B.4 Fourier-space representation of the square wave

Writing the square wave in Fourier space requires some care. Let us start by choosing a basis in which to evaluate it. The standard choice is:

$$\mathbf{a}_1 = (1, 0) \tag{B.7a}$$

$$\mathbf{a}_2 = \left(\frac{1}{2}, \frac{\sqrt{3}}{2}\right). \tag{B.7b}$$

The corresponding reciprocal lattice vectors are:

$$\mathbf{b}_1 = \left(2\pi, -\frac{2\pi}{\sqrt{3}}\right) \tag{B.8a}$$

$$\mathbf{b}_2 = \left(0, \frac{4\pi}{\sqrt{3}}\right). \tag{B.8b}$$

If the stripes have normal vectors parallel to the y direction $\hat{\mathbf{y}}$, then $\mathbf{b}_2$ is parallel to those normal vectors, which makes life easier. Restricting ourselves to the first Brillouin zone of reciprocal space, we write:

$$\mathbf{q} = \frac{k_1}{N_1}\mathbf{b}_1 + \frac{k_2}{N_2}\mathbf{b}_2 \tag{B.9}$$

$$\mathbf{r} = n_1\mathbf{a}_1 + n_2\mathbf{a}_2. \tag{B.10}$$

So, $s(\mathbf{r})$ is indexed by (n_1, n_2) and $\tilde{s}(\mathbf{q})$ is indexed by (k_1, k_2). For stripes along $\hat{\mathbf{y}}$, we have:

$$s(n_1, n_2) - s(n_1, n_2 - 1) = \begin{cases} -1, & n_2 = 2\lambda, 4\lambda, \dots \\ 1, & n_2 = \lambda, 3\lambda, \dots \\ 0, & \text{otherwise,} \end{cases} \tag{B.11}$$

where λ is the width of the stripe. Making the definitions:

$$\tilde{s}(k_1, k_2) = \sum_{n_1, n_2} s(n_1, n_2) e^{2\pi i\left(\frac{n_1 k_1}{N_1} + \frac{n_2 k_2}{N_2}\right)} \tag{B.12}$$

$$s(n_1, n_2) = \frac{1}{N_1 N_2} \sum_{k_1, k_2} \tilde{s}(k_1, k_2) e^{-2\pi i\left(\frac{n_1 k_1}{N_1} + \frac{n_2 k_2}{N_2}\right)}, \tag{B.13}$$

we can write:

$$\begin{aligned} s(n_1, n_2) - s(n_1, n_2 - 1) &= \frac{1}{N_1 N_2} \sum_{k_1, k_2} \tilde{s}(k_1, k_2) \left(e^{-2\pi i\left(\frac{n_1 k_1}{N_1} + \frac{n_2 k_2}{N_2}\right)} - e^{-2\pi i\left(\frac{n_1 k_1}{N_1} + \frac{(n_2 - 1) k_2}{N_2}\right)} \right) \\ &= \frac{1}{N_1 N_2} \sum_{k_1, k_2} \tilde{s}(k_1, k_2) e^{-i\mathbf{q}\cdot\mathbf{r}} (1 - e^{2\pi i k_2 / N_2}). \end{aligned} \tag{B.14}$$

At the same time, we can write:

$$\begin{aligned} s(n_1, n_2) - s(n_1, n_2 - 1) &= \delta(n_2, \lambda) - \delta(n_2, 2\lambda) + \delta(n_2, 3\lambda) - \cdots \\ &= \frac{1}{N_2} \sum_{k_2} \left(e^{-2\pi i k_2 (n_2 - \lambda)/N_2} - e^{-2\pi i k_2 (n_2 - 2\lambda)/N_2} + \cdots \right) \\ &\quad \times \frac{1}{N_1} \sum_{k_1} e^{-2\pi i k_1 n_1 / N_1} N_1 \delta(k_1, 0). \end{aligned} \tag{B.15}$$

Comparing eqs. B.14 and B.15, we have:

$$\tilde{s}(k_1, k_2)(1 - e^{2\pi i k_2/N_2}) = N_1 \delta(k_1, 0) \left(e^{2\pi i k_2 \lambda / N_2} - e^{2\pi i k_2 (2\lambda)/N_2} + \cdots \right)$$

$$\implies \boxed{\tilde{s}(k_1, k_2) = (1 - e^{2\pi i k_2/N_2})^{-1} \delta(k_1, 0) \frac{N_1 N_2}{\lambda} \sum_{j = \pm 1, \pm 3, \ldots}^{\lambda} -\delta\left(k_2, \frac{N_2 j}{2\lambda}\right).}$$

If, on the other hand, the stripes are parallel to the x direction $\hat{\mathbf{x}}$, then the previous choice of basis is awkward because neither reciprocal lattice vector is parallel to $\hat{\mathbf{x}}$. (It is very convenient to describe a spatial modulation when one of the reciprocal lattice vectors points in the direction of that modulation.) Instead we pick a new basis:

$$\mathbf{a}_1 = \left(\frac{1}{2}, \frac{\sqrt{3}}{2} \right) \tag{B.16a}$$

$$\mathbf{a}_2 = \left(0, \sqrt{3} \right), \tag{B.16b}$$

in which the corresponding reciprocal lattice vectors are:

$$\mathbf{b}_1 = (4\pi, 0) \tag{B.17a}$$

$$\mathbf{b}_2 = \left(-2\pi, \frac{2\pi}{\sqrt{3}} \right). \tag{B.17b}$$

(Note that $\mathbf{a}_2$ is not normalized.) Now $\mathbf{b}_1$ is parallel to $\hat{\mathbf{x}}$, which is the direction of modulation. Again, we write:

$$\mathbf{q} = \frac{k_1}{N_1} \mathbf{b}_1 + \frac{k_2}{N_2} \mathbf{b}_2 \tag{B.18}$$

$$\mathbf{r} = n_1 \mathbf{a}_1 + n_2 \mathbf{a}_2. \tag{B.19}$$

Now, our square wave will satisfy:

$$s(n_1, n_2) - s(n_1 - 1, n_2) = \begin{cases} -1, & n_1 = 2\lambda, 4\lambda, \ldots \\ 1, & n_1 = \lambda, 3\lambda, \ldots \\ 0, & \text{otherwise,} \end{cases} \tag{B.20}$$

Pulling the same computational tricks as before, we arrive at:

$$\boxed{\tilde{s}(k_1,k_2) = (1-e^{2\pi i k_1/N_1})^{-1}\delta(k_2,0)\frac{N_1N_2}{\lambda}\sum_{j=\pm1,\pm3,\ldots}^{\lambda} -\delta\left(k_1,\frac{N_1 j}{2\lambda}\right).} \tag{B.21}$$

This is essentially the same form we had before, but we have switched the role of $\mathbf{b}_1$ and $\mathbf{b}_2$.

B.5 Exact energy of phase separation

We can compute the energy of (zero-temperature) phase separation exactly by taking the limit $\lambda \to \infty$. Focusing on unstructured domains and abbreviating $E_{\text{unstruct+unstruct}}$ as E_{ps}, we have:

$$E_{\text{ps}}/N = \lim_{\lambda\to\infty}\frac{2\Delta\bar{\sigma}^2}{\lambda^2}\sum_{j=1,3\ldots}^{\lambda}\frac{\tilde{V}\left(\frac{N_1 j}{2\lambda},0\right)}{2-2\cos\left(\pi j/\lambda\right)}. \tag{B.22}$$

For large λ, we Taylor expand the denominator:

$$2-2\cos\left(\pi j/\lambda\right) = (\pi j/\lambda)^2 + (\pi j/\lambda)^4/12 + \mathcal{O}(\lambda^{-6}). \tag{B.23}$$

So:

$$\begin{aligned} E_{\text{ps}}/N &= 2\Delta\bar{\sigma}^2\lim_{\lambda\to\infty}\sum_{j=1,3,\ldots}^{\lambda}\frac{\tilde{V}\left(\frac{N_1 j}{2\lambda},0\right)}{\lambda^2\left[(\pi j/\lambda)^2+(\pi j/\lambda)^4/12+\mathcal{O}(\lambda^{-6})\right]} \\ &= 2\Delta\bar{\sigma}^2\lim_{\lambda\to\infty}\sum_{j=1,3,\ldots}^{\lambda}\frac{\tilde{V}\left(\frac{N_1 j}{2\lambda},0\right)}{(\pi j)^2+(\pi j)^4/\lambda^2/12+\mathcal{O}(\lambda^{-4})} \\ &= 2\Delta\bar{\sigma}^2\sum_{j=1,3,\ldots}^{\infty}\frac{\lim_{q\to0}\tilde{V}(q,0)}{\pi^2 j^2}. \end{aligned} \tag{B.24}$$

We have made the last step by noting that when j is small only the first term in the denominator contributes significantly to the value of the denominator, but when j is large (comparable to λ) the denominator diverges while the numerator stays bounded, so large-j terms contribute negligibly to the sum. Using the identity:

$$\sum_{j\,\text{odd}}^{\infty}\frac{1}{j^2} = \frac{\pi^2}{8}, \tag{B.25}$$

we can write:

$$E_{\text{ps}}/N = \frac{\Delta\bar{\sigma}^2}{4}\lim_{q\to0}\tilde{V}(q,0). \tag{B.26}$$

For $\Delta\bar{\sigma} = 2$, which is the case for compositionally pure unstructured phases ($\bar{\sigma} = \pm1$), this simplifes to:

$$E_{\text{ps}}/N = \lim_{q\to0}\tilde{V}(q,0) = 4, \tag{B.27}$$

in agreement with our numerical result.

B.6 Fratzl-Penrose-Style Mean Field Theory

Here we perform a mean field theory in the style of Fratzl and Penrose (which we refer to as MFT-2) [36], and compare it to the results of our mean field theory described in the previous section (which we refer to as MFT-1). The mean field free energy is given by:

$$F_{\mathrm{MF}} = E - TS \tag{B.28}$$

$$= \sum_{\mathbf{R},\mathbf{R}'\neq\mathbf{R}} V_{\mathbf{R},\mathbf{R}'}\sigma_{\mathbf{R}}\sigma_{\mathbf{R}'} + k_B T \sum_{\mathbf{R}} \left(\frac{1+\sigma_{\mathbf{R}}}{2} \log\left(\frac{1+\sigma_{\mathbf{R}}}{2}\right) + \frac{1-\sigma_{\mathbf{R}}}{2} \log\left(\frac{1-\sigma_{\mathbf{R}}}{2}\right)\right). \tag{B.29}$$

Noting that $\sum_{\mathbf{R},\mathbf{R}'\neq\mathbf{R}} V_{\mathbf{R},\mathbf{R}'}\sigma_{\mathbf{R}}\sigma_{\mathbf{R}'} = \sum_{\mathbf{R},\mathbf{R}'} \sigma_{\mathbf{R}}(V_{\mathbf{R},\mathbf{R}'} - V_0\delta_{\mathbf{R},\mathbf{R}'})\sigma_{\mathbf{R}'}$, and setting the derivative with respect to the spin field to zero,

$$0 = \frac{\delta F_{\mathrm{MF}}}{\delta \sigma_{\mathbf{R}}} = k_B T \frac{1}{2} \log\left(\frac{1+\sigma_{\mathbf{R}}}{1-\sigma_{\mathbf{R}}}\right) + 2\sum_{\mathbf{R}'} \sigma_{\mathbf{R}'}(V_{\mathbf{R},\mathbf{R}'} - V_0\delta_{\mathbf{R},\mathbf{R}'}). \tag{B.30}$$

Some algebra shows that:

$$\frac{1}{2}\log\left(\frac{1+\sigma_{\mathbf{R}}}{1-\sigma_{\mathbf{R}}}\right) = -\tanh^{-1}(-\sigma_{\mathbf{R}}), \tag{B.31}$$

and so:

$$\sigma_{\mathbf{R}} = \tanh\left(-2\beta\sum_{\mathbf{R}'} \sigma_{\mathbf{R}'}(V_{\mathbf{R},\mathbf{R}'} - V_0\delta_{\mathbf{R},\mathbf{R}'})\right). \tag{B.32}$$

Now we write the spin field as:

$$\sigma_{\mathbf{R}} = \bar{m} + \Delta m \cos(\Delta\mathbf{G}\cdot\mathbf{R}), \tag{B.33}$$

where $\Delta\mathbf{G}$ is the wavevector on which superlattice ordering occurs. We will write eq. B.32 in terms of Δm, anticipating that at high temperatures in the absence of order, Δm will be zero, whereas at low temperatures it will be nonzero. Plugging eq. B.33 into eq. B.32, writing cosine as a sum of complex exponentials, writing V in terms of its Fourier coefficients, and simplifying, we find:

$$\bar{m} + \Delta m = \tanh\left[2\beta\left((V_0 - \tilde{V}_0)\bar{m} + \Delta m(V_0 - \tilde{V}_{\Delta\mathbf{G}})\right)\right]. \tag{B.34}$$

Unless $\bar{m} = 0$ eq. B.34 will not have $\Delta m = 0$ as a solution (as can be seen by taking the first term in a Taylor series expansion of the right hand side.) This is unphysical, because at high enough temperature there must be a solution $\Delta m = 0$ corresponding to a disordered phase. However, if we take $\bar{m} = 0$, we have:

$$\Delta m = \tanh\left[2\beta\Delta m(V_0 - \tilde{V}_{\Delta\mathbf{G}})\right]. \tag{B.35}$$

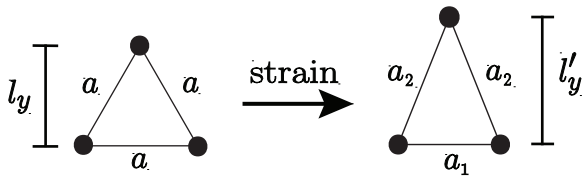

Figure B.14: Illustration of a triangular plaquette undergoing a deformation applied in the y (vertical) direction.

The transition will occur when $2\beta(V_0 - \tilde{V}_{\Delta\mathbf{G}}) = 1$, or:

$$k_B T_c = 2(V_0 - \tilde{V}_{\Delta\mathbf{G}}). \tag{B.36}$$

For our triangular lattice, $V_0 \approx 3.654$ and $\tilde{V}_{\Delta\mathbf{G}} = 3$. Therefore,

$$k_B T_c \approx 1.307. \tag{B.37}$$

This agrees quite well with our MFT-1 result:

$$k_B T_c \approx 1.308. \tag{B.38}$$

Hence, while MFT-2 cannot work for compositions other than $c = 1/2$, it actually quantitatively agrees with MFT-1 at $c = 1/2$.

B.7 Microscopic Expression for Young's Modulus

It is possible to derive the Young's Modulus, and hence the energy of phase separation, microscopically. To do so, we decompose the triangular lattice into *plaquettes* - three-bond triangular loops. When phase separation occurs, two macroscopic domains with different natural sizes need to be stretched (or compressed) in order to have the same length. As long as we can think of the resultant strain in an individual domain as being uniform across plaquettes, we can obtain the energy associated with phase separation simply by evaluating the energy of an individual plaquette. Consider a triangle with side lengths a_1 (lying along the x-axis) and $a_2 = a_3$ (with components in both x and y.) When unstrained, these lengths are all equal to the lattice constant a. We denote the height of this triangle as $l_y = \sqrt{3}a/2$. When a uniform strain is applied to the elastic domain in, say, the y direction, the bonds in the plaquettes will adopt new lengths in order to minimize the elastic energy. This situation is illustrated in Fig. B.14. Given a lattice mismatch Δ between the two coexisting elastic domains, the new height l'_y is given by:

$$l'_y = \frac{\sqrt{3}}{2}(a + \Delta). \tag{B.39}$$

Our task now is to find the strained values of a_1, a_2, and a_3. We do so by minimizing the energy of the strained plaquette. The energies of the individual bonds are given by:

$$\epsilon_1 = \frac{K}{2}(a_1 - a)^2 \tag{B.40}$$

$$\epsilon_2 = \epsilon_3 = \frac{K}{2}(a_2(a_1) - a)^2, \tag{B.41}$$

where, by geometry, we have written a_2 as a function of a_1:

$$a_2(a_1) = \sqrt{\left(\frac{a_1}{2}\right)^2 + \frac{3}{4}(a + \Delta)^2}. \tag{B.42}$$

The total energy of the plaquette is then given by:

$$\epsilon_{\text{tot}} = \epsilon_1 + \epsilon_2 + \epsilon_3 \tag{B.43}$$

$$= \frac{K}{2}\left[(a_1 - a)^2 + 2(a_2(a_1) - a)^2\right]. \tag{B.44}$$

To obtain the minimum energy and associated bond lengths, we minimize ϵ_{tot} with respect to a_1:

$$0 = \frac{\partial \epsilon_{\text{tot}}}{\partial a_1} = K(a_1 - a) + 2K(a_2(a_1) - a)\frac{\partial a_2}{\partial a_1} \tag{B.45}$$

$$\implies 0 = a_1\left(1 + \frac{1}{2}\left(\frac{a_2 - a}{a_2}\right)\right) - a. \tag{B.46}$$

Rearranging, we obtain a self-consistent equation for a_1:

$$a_1 = \frac{a}{\frac{3}{2} - \frac{a}{2a_2(a_1)}} \tag{B.47}$$

Assuming that a_1 is not too different from a, we can linearize the self-consistent equation about $a_1 = a$. Expanding the resulting expression to first order in Δ (assumed to be small,) we find:

$$a_1 \approx a - \frac{\Delta}{3}. \tag{B.48}$$

Plugging this expression into the equation for a_2 and again expanding to first order in Δ, we have:

$$a_2 \approx a + \frac{2}{3}\Delta. \tag{B.49}$$

The plaquette energy is therefore:

$$\epsilon_{\text{tot}} \approx \frac{K}{2}\Delta^2. \tag{B.50}$$

Multiplying by N, the total number of plaquettes, gives the total energy of phase separation. To extract the Young's modulus, compare this expression for the energy of phase separation with Eq. 3.77. This yields:

$$Y = \frac{2}{3}K, \tag{B.51}$$

which agrees with the value of Y we infer by applying mechanical deformation in a simulated, zero-temperature elastic domain and measuring the resulting elastic energy as a function of deformation. In terms of the energy unit $\epsilon = K\Delta^2/8$, we have $Y\Delta l^2 = 16$.

B.8 Construction of MC Phase Diagram

Previous work by D. Landau [66] showed that a triangular lattice spin model with nearest-neighbor attraction and next-nearest neighbor repulsion (henceforth referred to as the "Landau model,") produces rich phase behavior. Of particular interest is the fact that mean field theory fails to capture some major features of the phase diagram. While mean field theory accounts for the low temperature phases and their coexistence scenarios, it entirely misses a higher-temperature region which exhibits critical lines with 3-state Potts universality and which end in tricritical points, as well as a line of Kosterlitz-Thouless critical points. We have determined a very similar phase diagram for our elastic model. In this section, we outline how we established various features of the phase behavior.

3-State Potts Critical Lines

As previously mentioned, Landau found that for compositions $c \neq 1/2$ there are critical lines separating a high-temperature disordered phase and lower-temperature modulated-order ("superlattice") phases. Symmetry arguments have been advanced which state that in models like Landau's such critical lines should have three-state Potts universality [1]. This phase behavior is also very similar to that of the triangular lattice antiferromagnet in an external field. Transfer matrix results for that model are also consistent with three-state Potts universality [88]. We used finite-size scaling methods in order to locate critical lines in our model and to show that these critical lines have three-state Potts universality.

A common method for locating critical points involves computation of the Binder cumulant [7]:

$$U_N = 1 - \frac{\langle \Delta m^4 \rangle}{3\langle \Delta m^2 \rangle^2}, \tag{B.52}$$

where Δm is the order parameter. One can identify the critical point as the point of intersection of Binder cumulants for different system sizes. We used this technique to locate the critical lines. For several different fixed compositions, we computed U_N as a function of temperature for several different system sizes. This is illustrated for a composition $c = 1/3$ in Fig. B.15.

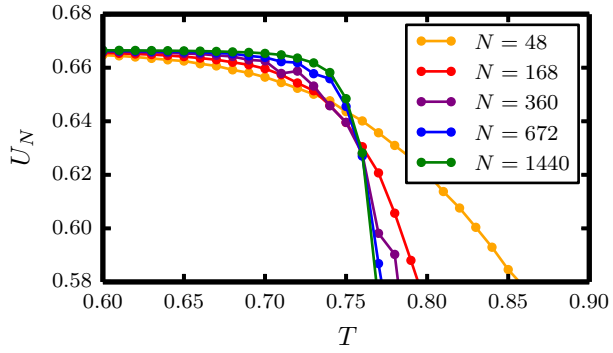

Figure B.15: Binder cumulants as a function of temperature for different system sizes at a fixed composition $c = 1/3$. Averages were taken over 10^6 MC sweeps. The transition temperature was identified as $T_c \approx 0.76$.

We also used finite-size scaling to confirm that the critical points located with the Binder cumulants have the critical exponents associated with the 3-state Potts model. Near a critical point, thermodynamic quantities like the specific heat $C = \left(\langle E^2\rangle - \langle E\rangle^2\right)/(Nk_BT^2)$, the susceptibility $\chi = \langle \Delta m^2\rangle$, and the correlation length ξ exhibit power-law dependencies on the reduced temperature $t = (T - T_c)/T_c$ [17]:

$$C \propto |t|^{-\alpha} \tag{B.53a}$$
$$\Delta m \propto |t|^{\beta} \tag{B.53b}$$
$$\chi \propto |t|^{-\gamma} \tag{B.53c}$$
$$\xi \propto |t|^{-\nu}. \tag{B.53d}$$

For the two-dimensional three-state Potts model, $\alpha = 1/3$, $\beta = 1/9$, $\gamma = 13/9$, and $\nu = 5/6$ [66]. Extracting these exponents directly from measurements of these thermodynamic quantities in simulations is complicated by finite-size effects. Rather than trying to estimate these quantities directly, we can take advantage of finite-size scaling theory to confirm the values of the critical exponents. Specifically, one can write finite-size scaling expressions for thermodynamic quantities [66]:

$$C = L^{\alpha/\nu} f_1(x) \tag{B.54a}$$
$$\Delta m = L^{-\beta/\nu} f_2(x) \tag{B.54b}$$
$$\chi = L^{\gamma/\nu} f_3(x), \tag{B.54c}$$

where $x = tL^{1/\nu}$ is a scaled temperature and the functions f_1, f_2, and f_3 depend only on x. Therefore, the quantities $L^{-\alpha/\nu}C$, $L^{\beta/\nu}\Delta m$, and $L^{-\gamma/\nu}\chi$ as functions of x are independent of system size. When plotted, data for different system sizes should therefore lie on top of each

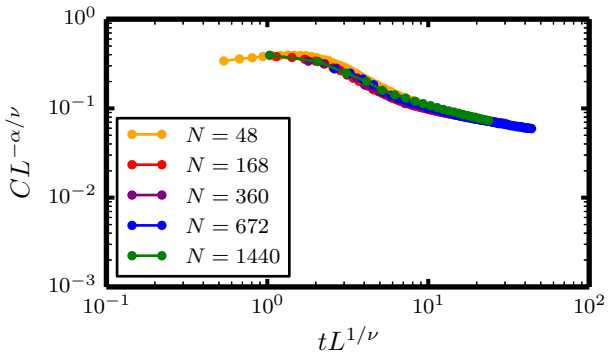

Figure B.16: Heat capacity for different system sizes at $c = 1/3$. Averages were taken over 10^6 MC sweeps.

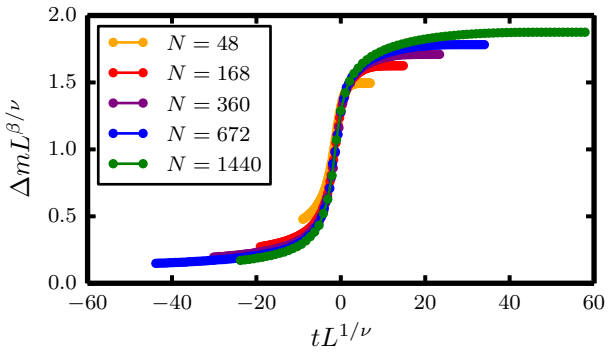

Figure B.17: Order parameter for different system sizes at $c = 1/3$. Averages were taken over 10^6 MC sweeps.

other close to $t = 0$. (This is known as "data collapse.") We made such plots to confirm that our critical lines indeed obey 3-state Potts universality. Examples are shown in Figs. B.16, B.17, and B.18.

Kosterlitz-Thouless Transition Line

At a composition $c = 1/2$ the Landau model exhibits a line of Kosterlitz-Thouless transitions, with upper critical temperature T_c^{upper} and lower critical temperature T_c^{lower}. Near such a transition, the correlation length diverges exponentially [66]:

$$\xi = \xi_0 \exp(at^{-1/2}). \tag{B.55}$$

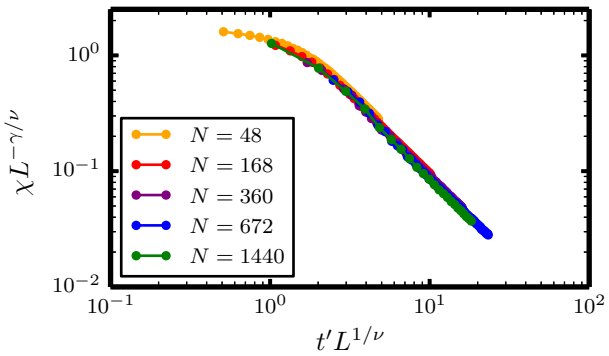

Figure B.18: Susceptibility for different system sizes at $c = 1/3$. Here, $t' = |1 - T_c/T|$. Averages were taken over 10^6 MC sweeps.

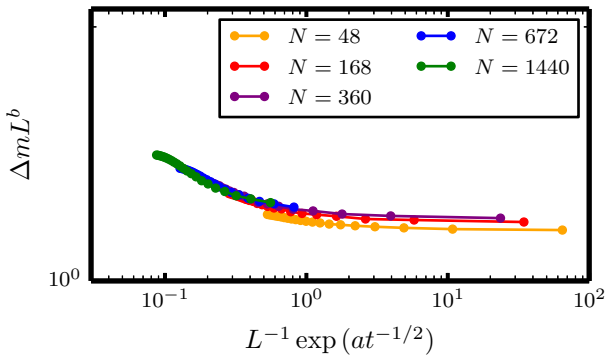

Figure B.19: Order parameter for different system sizes at $c = 1/2$. Here, $t = (T - T_c^{\text{lower}})/T_c^{\text{lower}}$. Data collapse is observed for all but the smallest system size. Averages were taken over 10^6 MC sweeps.

This leads to finite-size scaling expressions:

$$\Delta m = L^{-b} g_1(L^{-1} \exp(at^{-1/2})) \tag{B.56a}$$

$$\chi = L^c g_2(L^{-1} \exp(at^{-1/2})), \tag{B.56b}$$

where the functions g_1 and g_2 depend only on the quantity $L^{-1} \exp(at^{-1/2})$. Landau states that $a = 0.9$, $b = 0.095$, and $c = 1.72$. Using these values, we observed reasonable data collapse for $T_c^{\text{upper}} \approx 0.56$ and $T_c^{\text{lower}} \approx 0.46$. Plots of the scaled susceptibility and order parameter are shown in Figs. B.19 and B.20.

We confirmed that the correlation length upon approaching T_c^{upper} scales as Eq. B.55 by computing correlation functions at $c = 1/2$ for various temperatures and fitting these to the

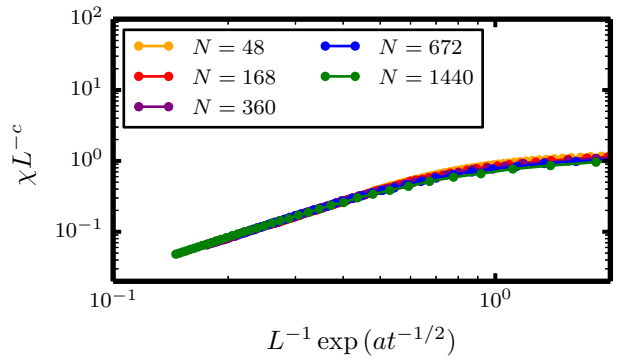

Figure B.20: Susceptibility for different system sizes at $c = 1/2$. Here, $t = (T - T_c^{\text{upper}})/T_c^{\text{upper}}$. Averages were taken over 10^6 MC sweeps.

form:

$$c(r) = \frac{Ae^{-r/\xi}}{r^{\eta}}. \tag{B.57}$$

Finite size effects cause an apparent divergence of ξ prior to our independently measured value of T_c^{upper}. Nevertheless, the scaling of Eq. B.55 appears to be satisfied, as shown in Fig. B.21. Between T_c^{lower} and T_c^{upper}, Landau states that while the correlation function should have power law behavior, the associated exponent will depend on temperature, i.e. $\eta = \eta(T)$. To confirm this, we fit correlation functions between T_c^{lower} and T_c^{upper} to a power law. A plot of the resulting exponent versus temperature is shown in Fig. B.22, confirming that η is indeed temperature-dependent.

Coexistence Regions

To identify low-temperature coexistence regions (which are reasonably well-described by mean field theory combined with the quadratic construction,) we performed umbrella sampling simulations of our effective Hamiltonian at various temperatures. (Because the effective Hamiltonian contains only composition variables and not mechanical variables, it is easier to sample than the full Hamiltonian.) We then subtracted off the energy associated with coexistence at zero temperature, $E_{\text{coex}}(c)$. This simply consists of parabolic segments with curvature -16 connecting compositions $c = 0$ to $c = 1/3$, $c = 1/3$ to $c = 2/3$, and $c = 2/3$ to $c = 1$. These special compositions have energies $E(c = 0) = E(c = 1) = 0$ and $E(c = 1/3) = E(c = 2/3) = 8/3$. A plot of the free energies is shown in Fig. B.23. There are clearly three distinct regions in this plot: $0 < c < 1/3$, $1/3 < c < 2/3$, and $2/3 < c < 1$, each of which, taken individually, develop non-convexities as temperature decreases. We associated these regions with coexistence. Specifically, we identified coexistence lines as the boundaries of these non-convex regions, which we located with the standard double-tangent

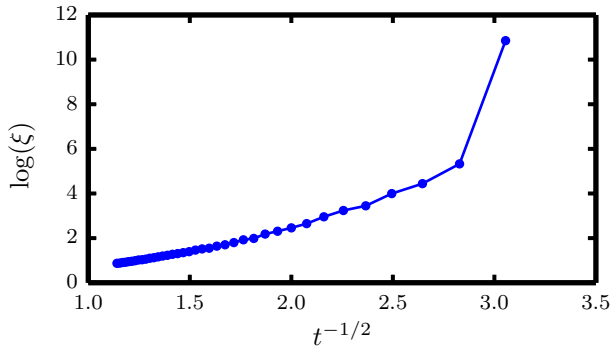

Figure B.21: Correlation lengths extracted from fit to $c(r)$. These correlation functions were obtained from MC simulations of an $N = 1440$ system at $c = 1/2$ using 10^7 configurations for averaging. The linear behavior of the plot as $t \to 0$ indicates that the scaling of Eq. B.55 is satisfied.

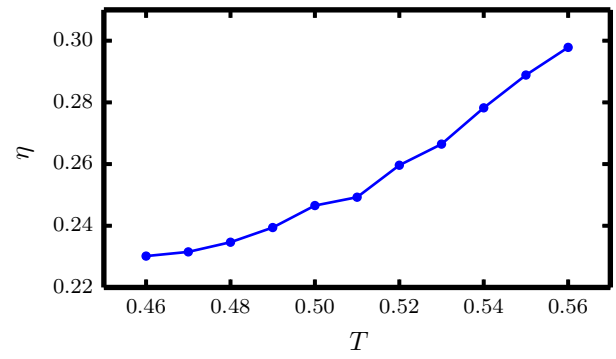

Figure B.22: Power law exponent η extracted from fit to $c(r)$ between T_c^{lower} and T_c^{upper}.

construction. We justify this procedure as follows. Recall our expression for the free energy of elastic coexistence:

$$f(c) = f(c_1) - \frac{\Delta c_1}{\Delta c_2 - \Delta c_1}\Delta f - Y\Delta l^2 \Delta c_1 \Delta c_2. \tag{B.58}$$

Non-convexity in the thermodynamic limit stems from the last term. We can remove this non-convexity by defining:

$$\tilde{f}(c) = f(c) + Y\Delta l^2 (c_1^* - c)(c_2^* - c), \tag{B.59}$$

where c_1^*, c_2^* are the compositions of coexisting phases at zero temperature. We wish to prove that for $\tilde{f}(c)$, coexistence regions $[c_1, c_2]$ satisfy the conditions of the double tangent construction. To do so, we must show:

$$\left.\frac{\partial \tilde{f}}{\partial c}\right|_{c_1} = \left.\frac{\partial \tilde{f}}{\partial c}\right|_{c_2} \tag{B.60a}$$

$$\tilde{f}(c_2) - \tilde{f}(c_1) = \left.\frac{\partial \tilde{f}}{\partial c}\right|_{c_1} \Delta c. \tag{B.60b}$$

Eq. B.60a is easy to demonstrate. The necessary derivative is:

$$\begin{aligned}\frac{\partial \tilde{f}}{\partial c} &= \frac{\partial f}{\partial c} + Y\Delta l^2 \left(2c - (c_1^* + c_2^*)\right) \\ &= \frac{\Delta f}{\Delta c} - Y\Delta l^2 \left[(c_1^* + c_2^*) - (c_1 + c_2)\right],\end{aligned} \tag{B.61}$$

which is independent of c, proving the equality. Eq. B.60b is also straightforward to prove. The left hand side can be written:

$$\begin{aligned}\tilde{f}(c_2) - \tilde{f}(c_1) &= \Delta f + Y\Delta l^2 \left[(c_1^* - c_2)(c_2^* - c_2) - (c_1^* - c_1)(c_2^* - c_1)\right] \\ &= \Delta f + Y\Delta l^2 \left(-c_2 c_2^* - c_1^* c_2 + c_2^2 + c_1 c_2^* + c_1^* c_1 - c_1^2\right),\end{aligned}$$

as can the right hand side:

$$\begin{aligned}\left.\frac{\partial \tilde{f}}{\partial c}\right|_{c_1} \Delta c &= \Delta f - Y\Delta l^2 \left[(c_1^* + c_2^*) - (c_1 + c_2)\right](c_2 - c_1) \\ &= \Delta f + Y\Delta l^2 \left[-(c_1^* + c_2^*)(c_2 - c_1) + (c_1 + c_2)(c_2 - c_1)\right] \\ &= \Delta f + Y\Delta l^2 \left(-c_1^* c_2 - c_2 c_2^* + c_1^* c_1 + c_1 c_2^* + c_2^2 - c_1^2\right).\end{aligned}$$

The right and left hand sides are clearly equal, showing that the conditions of the double tangent construction are indeed satisfied. For any finite-sized system, the free energy will not be strictly convex – surface tension will result in a non-convex contribution to $f(c)$ scaling as $O(N^{-1/2})$ (in two dimensions.) Knowing that in the thermodynamic limit this contribution vanishes and the free energy of coexistence satisfies the above conditions, we applied the double tangent construction to the finite system free energy and took the coexisting compositions thus inferred as proxies for the coexisting compositions for an infinite system.

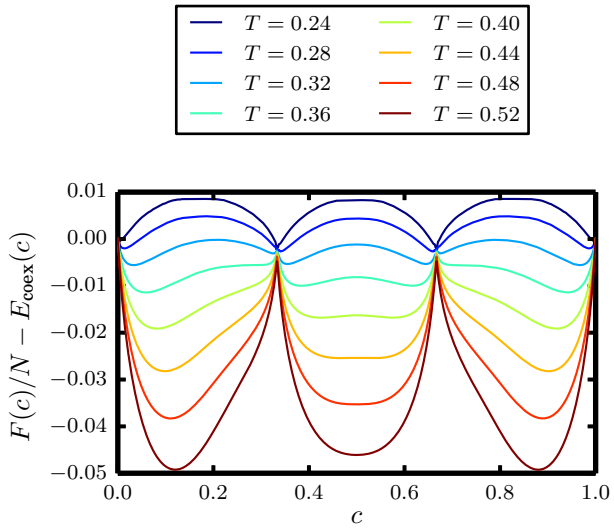

Figure B.23: Free energy minus the coexistence energy for different temperatures. Free energies were obtained for systems with $N = 360$ atoms, using umbrella sampling with 100 evenly-spaced harmonic windows. In each window, we performed 10^7 MC sweeps of equilibration and subsequently collected data every sweep for 10^7 MC sweeps.

B.9 Modulated Order in a Core-Shell Nanocrystal

To test the extent to which bulk phase behavior influences pattern formation in nanocrystals, we performed MC simulations of a model "core-shell" nanocrystal. Specifically, we simulated a hexagonal excerpt of an infinite triangular lattice. In our caricature the perimeter of this hexagonal crystal is comprised of atoms whose identity is consistent with a natural bond length of l_{AB}, and that bonds connecting these atoms are infinitely stiff. These atoms comprise the "shell." Such atoms have composition variables $\sigma_{\mathbf{R}} = 0$ and bonds with other atoms follow the simple mixing rule $l(\sigma_{\mathbf{R}}, \sigma_{\mathbf{R}'}) = l_{AB} + \Delta(\sigma_{\mathbf{R}} + \sigma_{\mathbf{R}'})/2$. The "core" consists of a mixture of A and B atoms with a net composition $c = 2/3$. Starting from a random initial configuration of core atoms, we performed MC sampling to obtain representative configurations. The nanocrystal core quickly (within a few thousand sweeps) rearranged to yield configurations closely resembling the bulk superlattice phase, as shown in Fig. B.24.

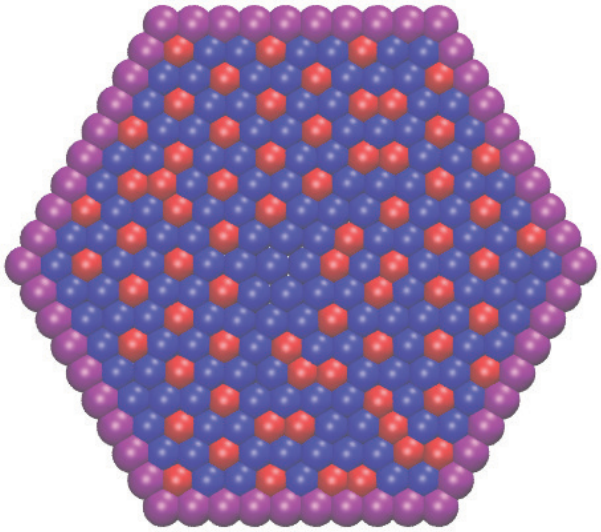

Figure B.24: "Core-shell" nanocrystal configuration obtained from an MC simulation consisting of 2×10^4 sweeps at a temperature $T = 0.6$.

B.10 Impact of Lattice Geometry on Phase Behavior

Following the same procedure we used for the two-dimensional triangular lattice, we obtained an effective potential for the three-dimensional FCC lattice. The bond vectors are:

$$\hat{\boldsymbol{\alpha}}_1 = \begin{pmatrix} 1/\sqrt{2} \\ 1/\sqrt{2} \\ 0 \end{pmatrix} \tag{B.62a}$$

$$\hat{\boldsymbol{\alpha}}_2 = \begin{pmatrix} 1/\sqrt{2} \\ 0 \\ 1/\sqrt{2} \end{pmatrix} \tag{B.62b}$$

$$\hat{\boldsymbol{\alpha}}_3 = \begin{pmatrix} 0 \\ 1/\sqrt{2} \\ 1/\sqrt{2} \end{pmatrix} \tag{B.62c}$$

$$\hat{\boldsymbol{\alpha}}_4 = \begin{pmatrix} 0 \\ -1/\sqrt{2} \\ 1/\sqrt{2} \end{pmatrix} \tag{B.62d}$$

$$\hat{\boldsymbol{\alpha}}_5 = \begin{pmatrix} -1/\sqrt{2} \\ 0 \\ 1/\sqrt{2} \end{pmatrix} \tag{B.62e}$$

$$\hat{\boldsymbol{\alpha}}_6 = \begin{pmatrix} -1/\sqrt{2} \\ 1/\sqrt{2} \\ 0 \end{pmatrix}, \tag{B.62f}$$

(as well as their additive inverses) and the effective potential is:

$$\tilde{V}_{\mathbf{q}} = A(\mathbf{q})/B(\mathbf{q}), \tag{B.63}$$

where now $\mathbf{q} = (q_x, q_y, q_z)$ and:

$$\begin{aligned}
A(\mathbf{q}) = 4\Bigg(&8\cos\left(\frac{q_z}{\sqrt{2}}\right)\cos\left(\frac{q_x-q_y}{2\sqrt{2}}\right)\left(-41\cos\left(\frac{q_x}{\sqrt{2}}\right)\cos\left(\frac{q_y}{\sqrt{2}}\right)+\cos\left(\sqrt{2}q_x\right)\right.\\
&\left.\times\left(\cos\left(\sqrt{2}q_y\right)+3\right)+3\cos\left(\sqrt{2}q_y\right)+64\right)\\
&\times\cos\left(\frac{q_x+q_y}{2\sqrt{2}}\right)+8\cos\left(\frac{3q_z}{\sqrt{2}}\right)\cos\left(\frac{q_x-q_y}{2\sqrt{2}}\right)\left(\cos\left(\frac{q_x}{\sqrt{2}}\right)\cos\left(\frac{q_y}{\sqrt{2}}\right)+1\right)\\
&\times\cos\left(\frac{q_x+q_y}{2\sqrt{2}}\right)+\cos\left(\sqrt{2}q_z\right)\\
&\times\left(\cos\left(\frac{q_x-3q_y}{\sqrt{2}}\right)-34\cos\left(\frac{q_x-q_y}{\sqrt{2}}\right)+6\cos\left(\sqrt{2}(q_x-q_y)\right)+\cos\left(\frac{3q_x-q_y}{\sqrt{2}}\right)\right.\\
&-34\cos\left(\frac{q_x+q_y}{\sqrt{2}}\right)+6\cos\left(\sqrt{2}(q_x+q_y)\right)+\cos\left(\frac{3q_x+q_y}{\sqrt{2}}\right)+\cos\left(\frac{q_x+3q_y}{\sqrt{2}}\right)\\
&\left.-4\cos\left(\sqrt{2}q_x\right)-4\cos\left(\sqrt{2}q_y\right)-36\right)+3\cos\left(\frac{q_x-3q_y}{\sqrt{2}}\right)\\
&+90\cos\left(\frac{q_x-q_y}{\sqrt{2}}\right)-2\cos\left(\sqrt{2}(q_x-q_y)\right)+3\cos\left(\frac{3q_x-q_y}{\sqrt{2}}\right)+90\cos\left(\frac{q_x+q_y}{\sqrt{2}}\right)\\
&-2\cos\left(\sqrt{2}(q_x+q_y)\right)+3\cos\left(\frac{3q_x+q_y}{\sqrt{2}}\right)+3\cos\left(\frac{q_x+3q_y}{\sqrt{2}}\right)\\
&-36\cos\left(\sqrt{2}q_x\right)-36\cos\left(\sqrt{2}q_y\right)-276\Bigg),
\end{aligned} \tag{B.64}$$

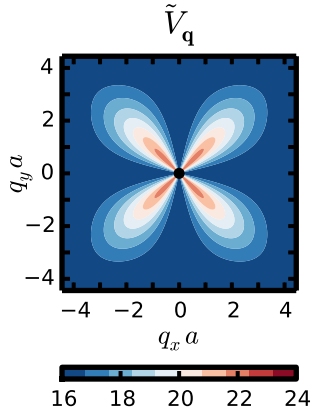

Figure B.25: Cross section of $\tilde{V}_{\mathbf{q}}$ for the FCC lattice at $q_z = 0$. The color indicates the magnitude of $\tilde{V}_{\mathbf{q}}$. The black dot in the center indicates the fact that the potential is zero at $\mathbf{q} = 0$.

$$
\begin{aligned}
B(\mathbf{q}) = 2\cos\left(\frac{q_z}{\sqrt{2}}\right)\Bigg(&\cos\left(\frac{q_x}{\sqrt{2}}\right)\left(22 - 8\cos\left(\sqrt{2}q_y\right)\right) + \cos\left(\frac{q_y}{\sqrt{2}}\right)\Big(-8\cos\left(\sqrt{2}q_x\right) \\
&+2\cos\left(\sqrt{2}q_y\right) + 21\Big) \\
&+ \cos\left(\frac{3q_x}{\sqrt{2}}\right)\Bigg) + 2\cos\left(\frac{3q_z}{\sqrt{2}}\right)\left(\cos\left(\frac{q_x}{\sqrt{2}}\right) + \cos\left(\frac{q_y}{\sqrt{2}}\right)\right) \\
&+ 4\cos\left(\sqrt{2}q_z\right)\Bigg(-4\cos\left(\frac{q_x}{\sqrt{2}}\right)\cos\left(\frac{q_y}{\sqrt{2}}\right) \\
&+ \cos\left(\sqrt{2}q_x\right)\cos\left(\sqrt{2}q_y\right) - 3\Bigg) + \cos\left(\frac{q_x - 3q_y}{\sqrt{2}}\right) + 22\cos\left(\frac{q_x - q_y}{\sqrt{2}}\right) \\
&+ \cos\left(\frac{3q_x - q_y}{\sqrt{2}}\right) + 22\cos\left(\frac{q_x + q_y}{\sqrt{2}}\right) + \cos\left(\frac{3q_x + q_y}{\sqrt{2}}\right) + \cos\left(\frac{q_x + 3q_y}{\sqrt{2}}\right) \\
&- 12\cos\left(\sqrt{2}q_x\right) - 12\cos\left(\sqrt{2}q_y\right) - 64.
\end{aligned}
\tag{B.65}
$$

A plot is shown in Fig. B.25. The potential discourages spatial modulations of the composition which do not lie along the $\hat{\mathbf{x}}$, $\hat{\mathbf{y}}$, or $\hat{\mathbf{z}}$ directions. However, it is equally permissive of modulations of any wavelength along these principal directions, owing to the fact that the potential is essentially flat along these directions. This vast degeneracy could in principle be broken by the introduction of an additional spatially short-ranged interaction or, alternatively, the addition of next-nearest-neighbor springs [47]. We also computed the effective potential for a simple cubic lattice, on which next-nearest-neighbor springs are required to

provide resistance to shear [5]. The nearest-neighbor bond vectors in that case are:

$$\hat{\boldsymbol{\alpha}}_1 = \begin{pmatrix} 1 \\ 0 \\ 0 \end{pmatrix} \tag{B.66a}$$

$$\hat{\boldsymbol{\alpha}}_2 = \begin{pmatrix} 0 \\ 1 \\ 0 \end{pmatrix} \tag{B.66b}$$

$$\hat{\boldsymbol{\alpha}}_3 = \begin{pmatrix} 0 \\ 0 \\ 1 \end{pmatrix}, \tag{B.66c}$$

as well as additive inverses, and the next-nearest-neighbor bond vectors $\{\hat{\boldsymbol{\beta}}_j\}$ are identical to the nearest-neighbor bond vectors on the FCC lattice. The associated effective potential is given by:

$$\tilde{V}_{\mathbf{q}} = 4\left(C(\mathbf{q}) - \frac{D_1(\mathbf{q}) + D_2(\mathbf{q}) + D_3(\mathbf{q})}{E(\mathbf{q})}\right), \tag{B.67}$$

where:

$$\begin{aligned} C(\mathbf{q}) &= \cos(q_x - q_y) + \cos(q_x + q_y) + \cos(q_x - q_z) \\ &\quad + \cos(q_x + q_z) + \cos(q_x) + \cos(q_y - q_z) + \cos(q_y + q_z) + \cos(q_y) + \cos(q_z) + 9 \end{aligned} \tag{B.68a}$$

$$\begin{aligned} D_1(\mathbf{q}) &= 2\sin^2(q_z)\left(\sqrt{2}\cos(q_x) + \sqrt{2}\cos(q_y) + 1\right) \\ &\quad \times \Big(4\sin^2(q_x)\left(\sqrt{2}\cos(q_y) + \sqrt{2}\cos(q_z) + 1\right)(\cos(q_y)(\cos(q_x) + \cos(q_z) + 1) \\ &\quad + \sin^2(q_y) - 3\Big) \\ &\quad + 4\sin^2(q_y)\left(\sqrt{2}\cos(q_x) + \sqrt{2}\cos(q_z) + 1\right) \times (\cos(q_x)(\cos(q_y) + \cos(q_z) + 1) \\ &\quad + \sin^2(q_x) - 3\Big) \\ &\quad + \left(\sqrt{2}\cos(q_x) + \sqrt{2}\cos(q_y) + 1\right)((2\cos(q_y)(\cos(q_x) + \cos(q_z) + 1) - 6) \\ &\quad \times (2\cos(q_x)(\cos(q_y) + \cos(q_z) + 1) - 6) - 4\sin^2(q_x)\sin^2(q_y))\Big) \end{aligned} \tag{B.68b}$$

$$\begin{aligned} D_2(\mathbf{q}) &= 2\sin^2(q_y)\left(\sqrt{2}\cos(q_x) + \sqrt{2}\cos(q_z) + 1\right) \\ &\quad \times \Big(4\sin^2(q_x)\left(\sqrt{2}\cos(q_y) + \sqrt{2}\cos(q_z) + 1\right)(\cos(q_z)(\cos(q_x) + \cos(q_y) + 1) \\ &\quad + \sin^2(q_z) - 3\Big) \\ &\quad + 4\sin^2(q_z)\left(\sqrt{2}\cos(q_x) + \sqrt{2}\cos(q_y) + 1\right)(\cos(q_x)(\cos(q_y) + \cos(q_z) + 1) \\ &\quad + \sin^2(q_x) - 3\Big) \\ &\quad + \left(\sqrt{2}\cos(q_x) + \sqrt{2}\cos(q_z) + 1\right)((2\cos(q_z)(\cos(q_x) + \cos(q_y) + 1) - 6) \\ &\quad \times (2\cos(q_x)(\cos(q_y) + \cos(q_z) + 1) - 6) - 4\sin^2(q_x)\sin^2(q_z))\Big) \end{aligned} \tag{B.68c}$$

$$\begin{aligned} D_3(\mathbf{q}) &= 2\sin^2(q_x)\left(\sqrt{2}\cos(q_y) + \sqrt{2}\cos(q_z) + 1\right) \\ &\quad \times \Big(4\sin^2(q_y)\left(\sqrt{2}\cos(q_x) + \sqrt{2}\cos(q_z) + 1\right)(\cos(q_z)(\cos(q_x) + \cos(q_y) + 1) \\ &\quad + \sin^2(q_z) - 3\Big) \\ &\quad + 4\sin^2(q_z)\left(\sqrt{2}\cos(q_x) + \sqrt{2}\cos(q_y) + 1\right)(\cos(q_y)(\cos(q_x) + \cos(q_z) + 1) \\ &\quad + \sin^2(q_y) - 3\Big) \\ &\quad + \left(\sqrt{2}\cos(q_y) + \sqrt{2}\cos(q_z) + 1\right)((2\cos(q_z)(\cos(q_x) + \cos(q_y) + 1) - 6) \\ &\quad \times (2\cos(q_y)(\cos(q_x) + \cos(q_z) + 1) - 6) - 4\sin^2(q_y)\sin^2(q_z))\Big) \end{aligned} \tag{B.68d}$$

$$\begin{aligned} E(\mathbf{q}) &= 8\sin^2(q_y)\sin^2(q_z)\left(\cos(q_x)(\cos(q_y) + \cos(q_z) + 1) + \sin^2(q_x) - 3\right) \\ &\quad + 8\sin^2(q_x)\sin^2(q_z)\left(\cos(q_y)(\cos(q_x) + \cos(q_z) + 1) + \sin^2(q_y) - 3\right) \\ &\quad + (6 - 2\cos(q_z)(\cos(q_x) + \cos(q_y) + 1)) \\ &\quad \times ((2\cos(q_y)(\cos(q_x) + \cos(q_z) + 1) - 6)(2\cos(q_x)(\cos(q_y) + \cos(q_z) + 1) - 6) \\ &\quad - 4\sin^2(q_x)\sin^2(q_y)\Big) \end{aligned} \tag{B.68e}$$

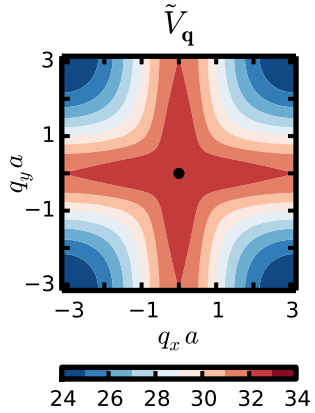

Figure B.26: Cross section of $\tilde{V}_{\mathbf{q}}$ for the simple cubic lattice at $q_z = 0$. The color indicates the magnitude of $\tilde{V}_{\mathbf{q}}$. The black dot in the center indicates the fact that the potential is zero at $\mathbf{q} = 0$.

A plot is shown in B.26. Unlike the FCC lattice, the minima here occur at isolated, nonzero, points. This suggests that finite-wavelength modulated order is energetically favorable on the simple cubic lattice, which we confirm with an exploratory MC simulation. In Fig. B.27 we show a configuration taken from one such MC simulation of atoms interacting via the effective potential Eq. B.67. The simulation consisted of 10^5 MC sweeps on a $10 \times 10 \times 10$ simple cubic lattice at a temperature $T = 0.5$ and fixed composition $c = 1/2$. Starting from a random initial configuration, the system quickly reorganized into what we surmise is a modulated order ground state for this value of c, consisting of single-species columns of atoms arranged in an alternating "checkerboard" pattern.

We obtained phase diagrams for the cubic lattice from both MFT and MC using the same techniques described in Ch. 3.8 and App. B.8. Here we describe modulated order by imagining the cubic lattice to be composed of four interpenetrating sublattices (rather than three as on the triangular lattice,) allowing for unstructured phases U_1 and U_2, modulated phases S_1 and S_2 in which one sublattice is enriched in one species relative to the three others which are enriched in the other species, and a modulated "checkerboard" phase S_3 in which two sublattices are enriched in one species and the other two sublattices are enriched in the other species. The phase diagrams are shown in Fig. B.28 Unlike for the triangular lattice, here MFT and MC are in qualitative agreement at all temperatures. Both predict first order phase boundaries separating coexisting modulated and unstructured phases, terminating in a single critical point. Finite-size scaling analysis indicates that the MC critical point lies in the Ising universality class (see Fig. B.29.)

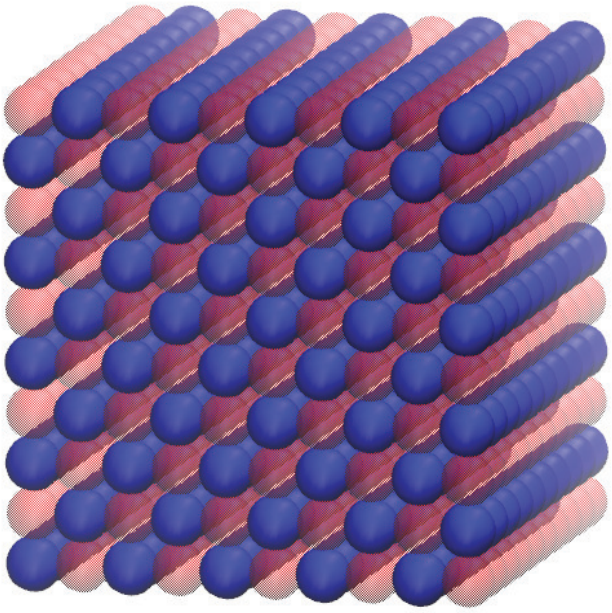

Figure B.27: Configuration taken from an MC simulation of atoms interacting according to the pair potential in Eq. B.67. Columns of single-color (-species) stripes alternate in a checkerboard pattern. Red atoms (species B) are made translucent for clarity.

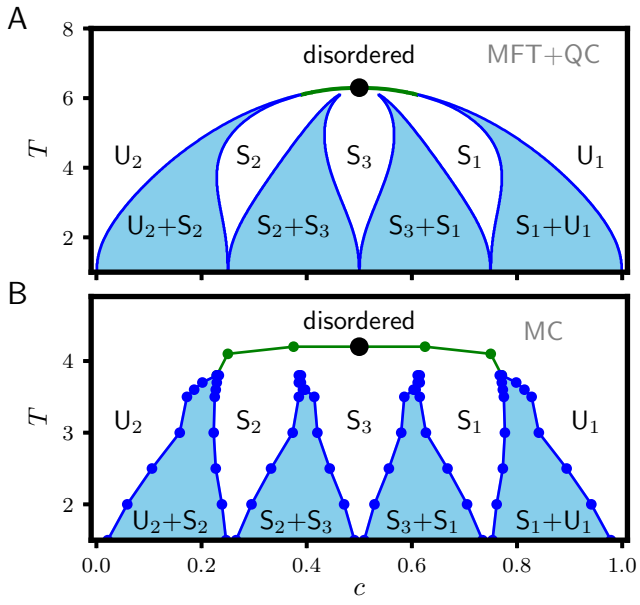

Figure B.28: Phase diagram for our elastic model on the three-dimensional simple cubic lattice in the plane of temperature and composition. **A**: Mean-field prediction resulting from the quadratic construction of Eq. 3.82. Black circle indicates a critical point at $T \approx 6.1$; elsewhere, lines indicate first-order transitions. Green lines represent phase boundaries where no coexistence could be found withing the tolerance of our self-consistent algorithm. Blue lines bound coexistence regions, which are shaded in light blue. **B**: Numerically exact results from Monte Carlo sampling. There is an Ising critical point at $T \approx 4.2$; colors have the same meaning as in Panel A.

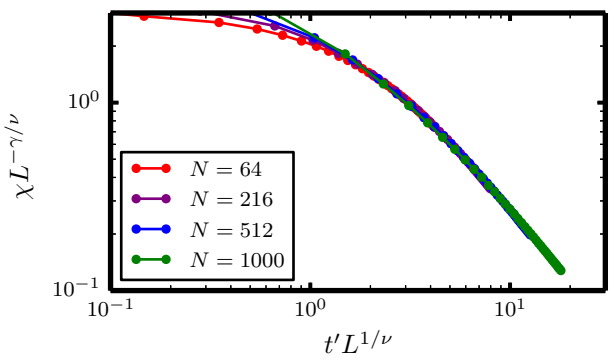

Figure B.29: Susceptibility of the cubic lattice for different system sizes at $c = 1/2$. Here, $t' = |1 - T_c/T|$. Averages were taken over 10^6 MC sweeps. The critical exponents $\gamma \approx 1.24$ and $\nu \approx 0.63$ are those of the 3d Ising model [48].

Appendix C

Appendix for "The Origin of Mean-Field Behavior in an Elastic Ising Model"

C.1 Pressure in the Small-Mismatch Limit

In the small-mismatch limit, we can simplify the pressure-volume contribution to our Hamiltonian, which we label here as $E(pV)$:

$$E(pV) = pcNa^d. \tag{C.1}$$

To begin, we use the the fact that $a = \delta a + l_{AB}$:

$$E(pV) = pcN(\delta a + l_{AB})^d \tag{C.2}$$

$$= pcNl_{AB}^d + pcNdl_{AB}^{d-1}\delta a + \mathcal{O}(\Delta^2), \tag{C.3}$$

since δa is of order Δ. Dropping the constant first term and the terms of order $\mathcal{O}(\Delta^2)$, which vanish in the small-mismatch limit, we arrive at:

$$E(pV) \approx pcNdl_{AB}^{d-1}\delta a, \tag{C.4}$$

in agreement with our small-mismatch Hamiltonian in Ch. 4.

C.2 MC Simulation Details

We used MC simulations to compute both equilibrium and dynamic properties of our elastic model. We used a value of $\Delta = 0.1$ for the lattice mismatch. For simulations of bulk crystals consisting of $N = N_x N_y$ atoms, periodic boundary conditions were imposed in the x and y (and for three-dimensional simulations, z) directions. Simulations of nanocrystals employed

hexagonal systems with open boundary conditions. Bulk equilibrium properties were computed by performing simulations of Eq. 4.2 in the isothermal-isobaric (NPT) ensemble. As in Ch. 3, this ensemble was sampled using two basic MC moves: spin flips and displacement moves. In both cases, an atom at lattice site $\mathbf{R}$ was selected at random. An attempt was then made to change either its spin, $\sigma_{\mathbf{R}} \to -\sigma_{\mathbf{R}}$, or its position, $\mathbf{R} + \mathbf{u}_{\mathbf{R}} = \mathbf{r}_{\mathbf{R}} \to \mathbf{r}_{\mathbf{R}} + \boldsymbol{d}$, where $\boldsymbol{d} = (d_x, d_y)$ is a two dimensional vector. The components of the vector were selected uniformly at random from an interval $[-0.1, 0.1]$. Random numbers were generated using the Mersenne Twister algorithm [75] as implemented in the GNU Scientific Library (GSL) [73]. A Metropolis criterion was used to accept or reject proposed moves, ensuring detailed balance: [21]:

$$P(C \to C') = \min\left[1, e^{-\beta(\mathcal{H}(C)-\mathcal{H}(C'))}\right], \tag{C.5}$$

where C and C' represent configurations $\{\sigma_{\mathbf{R}}\}, \{\mathbf{r}_{\mathbf{R}}\}$ before and after the proposed move, respectively. Simulation runs consisted of performing a large number of MC sweeps. A single MC sweep consisted of N attempted spin flips and N attempted displacement moves. Constant pressure was maintained using a standard algorithm in which attempts to change the system's volume were proposed and then accepted or rejected according to a Metropolis criterion [21]. Proposed volume moves consisted of changing the total volume by an amount δV, selected uniformly at random from the interval $[-\delta V_{\max}, \delta V_{\max}]$. We chose $\delta V_{\max} = 0.01 V_0$, where V_0 is the volume at the beginning of a simulation run. Such volume moves were performed once every MC sweep. Initial configurations consisted of atoms arranged on a perfect triangular lattice, with a random distribution of spins, and with a volume consistent with the net composition. Before obtaining statistics, we equilibrated the system by running at least 100 MC sweeps without collecting any data. Data was then recorded for different observables once every sweep. Umbrella sampling simulations [113], used in combination with WHAM [65] to compute the equilibrium free energy, employed $n_{window} = 50$ (100 for the largest systems studied) evenly spaced harmonic biases with spring constants of strength 0.1ϵ. Dynamical bulk properties were computed *via* simulations of Eq. 4.12 in the canonical ensemble, employing the spin-flip moves and Metropolis criterion described previously. Properties of the nanocrystals were computed using simulations of the effective Hamiltonian (Eq. 4.34) in the canonical ensemble. Spin-flip moves and the Metropolis criterion were used as in bulk simulations. Umbrella sampling simulations for the nanocrystals used spring constants of strength 0.2ϵ for the 50 evenly spaced harmonic biases.

C.3 Critical Temperature and Scaling on Different Lattices

Here we assess mean-field predictions for the critical temperature (T_c) and exponents of spontaneous symmetry breaking of the elastic Ising model on different lattices. Mean-field scaling as measured by critical exponents should hold for each lattice (as long as there is a gap at $\mathbf{q} = 0$,) since mean-field exponents are known to be robust to the addition

of short-ranged interactions [16, 85]. However, since it is a non-universal quantity, the accuracy of mean-field predictions for T_c will depend on the lattice structure, in particular the magnitude of short-ranged interactions compared to the long-ranged interaction. We examine five different lattices, spanning one to three spatial dimensions, and show that each exhibits mean-field critical exponents, as expected. Mean field theory (MFT) predicts T_c with reasonable accuracy for all lattices except the one-dimensional (1d) lattice. This is likely a consequence of the significant magnitude of short-ranged interactions for that lattice.

Theory & Methods

As argued in Ch. 4, MFT predicts that the critical temperature for spontaneous symmetry breaking of the magnetization m is given by:

$$T_c = 2\bar{V}, \tag{C.6}$$

$$\bar{V} = -\sum_{\mathbf{R}\neq 0} V_{\mathbf{R}}/2. \tag{C.7}$$

The mean-field potential $\bar{V}$ is composed of a long-ranged part $\bar{V}^{\mathrm{LR}} = \lim_{\mathbf{q}\to 0} \tilde{V}_{\mathbf{q}}/2$ and a short-ranged part $\bar{V}^{\mathrm{SR}} = \bar{V} - \bar{V}^{\mathrm{LR}}$. If the magnitude of $\bar{V}^{\mathrm{SR}}$ is small compared to that of $\bar{V}^{\mathrm{LR}}$ then we expect MFT to give a reasonable estimate for T_c. MFT also predicts [79] that the average squared magnetization $\langle m^2 \rangle$ obeys:

$$\langle m^2 \rangle = N^{-1/2} f_1(tN^{1/2}), \tag{C.8}$$

where $t = (T - T_c)/T_c$ and N is the system size, and the Binder cumulant $U = 1 - \langle m^4 \rangle / (3\langle m^2 \rangle^2)$ obeys:

$$U = f_2(tN^{1/2}). \tag{C.9}$$

The scaling functions f_1 and f_2 depend only on the scaled temperature $tN^{1/2}$, and hence plots of $N^{1/2}\langle m^2 \rangle$ and U versus $tN^{1/2}$ for different system sizes should fall on top of one another. Additionally, in MFT the Binder cumulant attains a universal value of ≈ 0.27 at T_c [79].

To verify these relationships, we employ MC simulations using the effective Hamiltonian for each lattice, which improves sampling since we do not have to explicitly evolve mechanical degrees of freedom. With these simulations, we compute the quantities U and $\langle m^2 \rangle$ as functions of temperature for several system sizes. At each temperature and system size we equilibrate the system for 10^3 MC sweeps (1 sweep is N attempts to flip a spin) and then collect data every sweep for 10^6 sweeps. The MC estimate for T_c is given by the intersection of Binder cumulants for different system sizes.

1d Lattice

MFT does not accurately predict T_c for the 1d lattice (with both nearest- and next-nearest-neighbor springs):

$$T_c^{\mathrm{MF}} \approx 3.57 \tag{C.10}$$

$$T_c^{\mathrm{MC}} \approx 2.79. \tag{C.11}$$

See Fig. 1. That is because $\bar{V}^{\mathrm{LR}} = 0.8$ is comparable to $\bar{V}^{\mathrm{SR}} = 0.987$ ($\bar{V}^{\mathrm{SR}}$ is $\approx 55\%$ of $\bar{V}$.) When U and $\langle m^2 \rangle$ are scaled using T_c^{MF}, data collapse is poor; however, when they are scaled using T_c^{MC}, data collapse is excellent (see Figs. 2 and 3.) Thus the critical exponents of the 1d lattice have mean-field scaling, as expected.

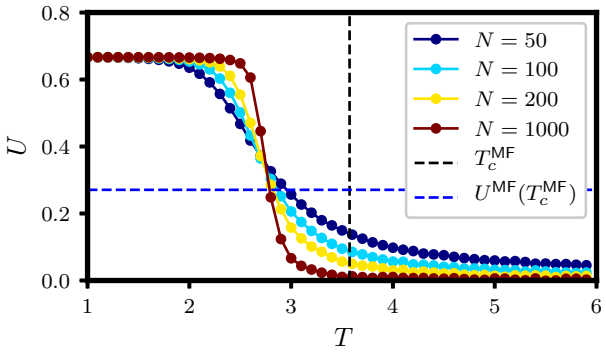

Figure C.1: Binder cumulants for the 1d lattice.

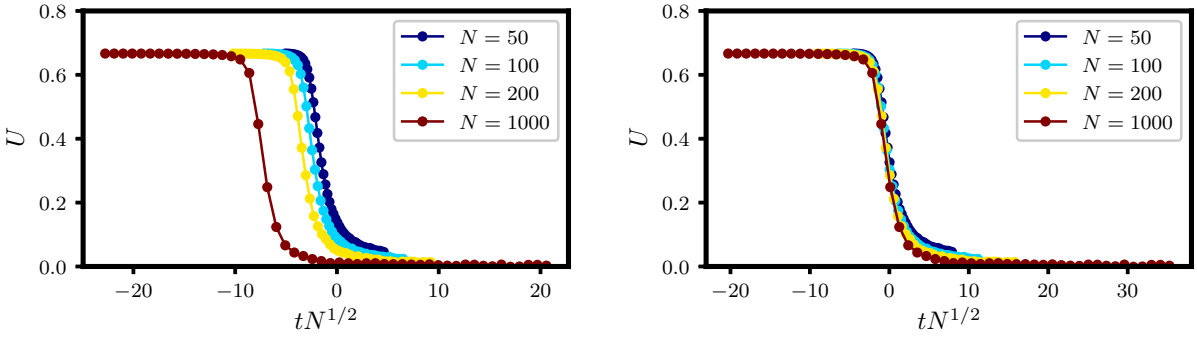

(a) T_c computed from MFT.

(b) T_c computed from MC.

Figure C.2: Scaling of U for different choices of T_c on the 1d lattice.

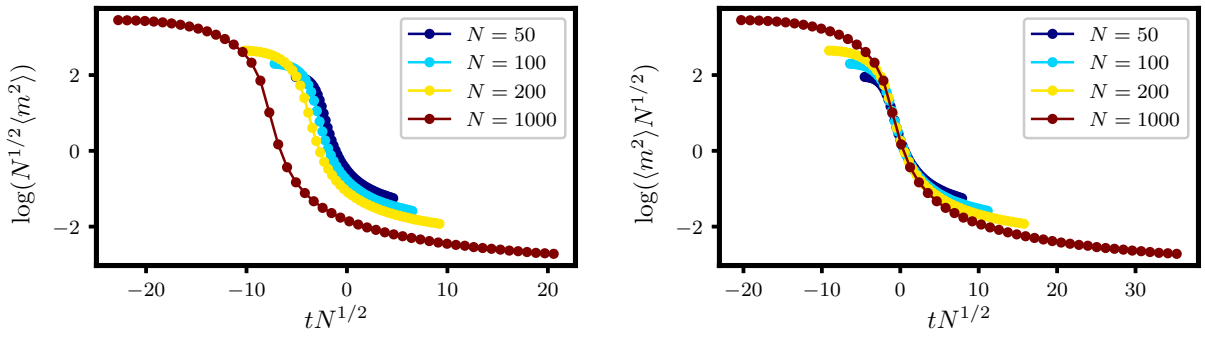

(a) T_c computed from MFT.

(b) T_c computed from MC.

Figure C.3: Scaling of $\langle m^2 \rangle$ for different choices of T_c on the 1d lattice.

Triangular Lattice

MFT accurately predicts T_c for the 2d triangular lattice:

$$T_c^{\mathrm{MF}} \approx 7.31 \tag{C.12}$$

$$T_c^{\mathrm{MC}} \approx 7.20. \tag{C.13}$$

See Fig. 4. That is because $\bar{V}^{\mathrm{LR}} = 4.0$ is much larger in magnitude than $\bar{V}^{\mathrm{SR}} = -0.346$ ($\bar{V}^{\mathrm{SR}}$ is $\approx 8.7\%$ of $\bar{V}$.) When U and $\langle m^2 \rangle$ are scaled using T_c^{MF}, data collapse is excellent (see Figs. 5 and 6.)

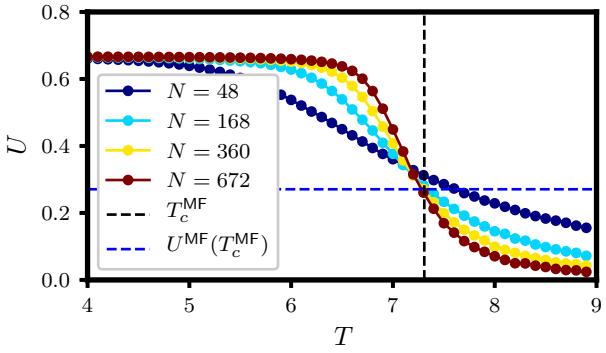

Figure C.4: Binder cumulants for the triangular lattice.

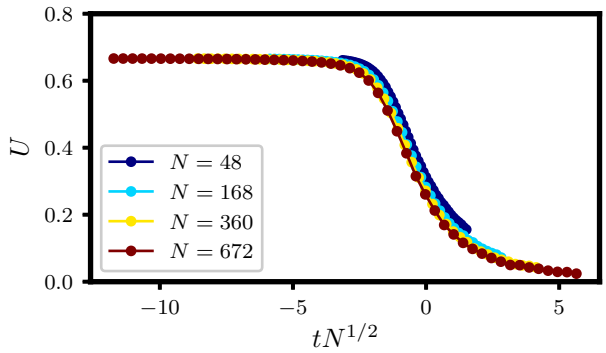

Figure C.5: Scaling of U for the triangular lattice.

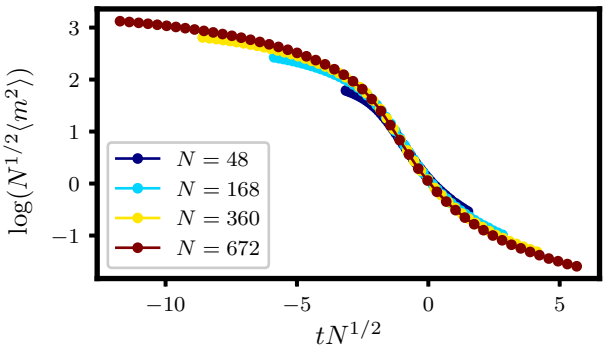

Figure C.6: Scaling of $\langle m^2 \rangle$ for the triangular lattice.

Square Lattice

MFT predicts T_c for the 2d square lattice (with nearest- and next-nearest-neighbor springs) with reasonable accuracy:

$$T_c^{\mathrm{MF}} \approx 11.1 \tag{C.14}$$

$$T_c^{\mathrm{MC}} \approx 10.6. \tag{C.15}$$

See Fig. 7. That is because $\bar{V}^{\mathrm{LR}} = 4.34$ is fairly large in magnitude compared to $\bar{V}^{\mathrm{SR}} = 1.20$ ($\bar{V}^{\mathrm{SR}}$ is $\approx 21.6\%$ of $\bar{V}$.) When U and $\langle m^2 \rangle$ are scaled using T_c^{MF}, data collapse is good (see Figs. 8 and 9.)

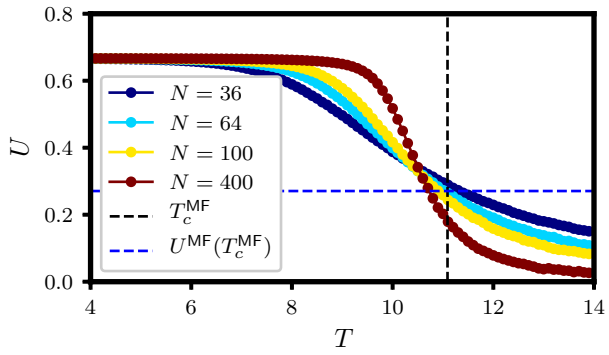

Figure C.7: Binder cumulants for the square lattice.

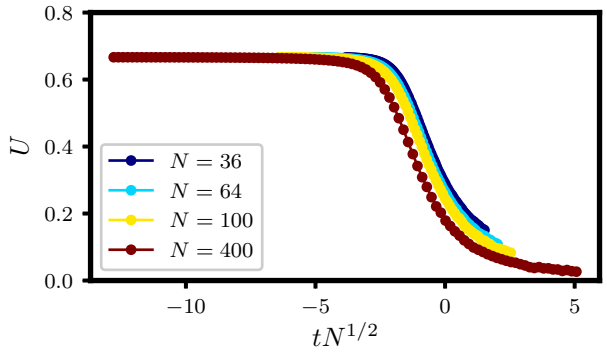

Figure C.8: Scaling of U for the square lattice.

FCC Lattice

MFT accurately predicts T_c for the 3d FCC lattice:

$$T_c^{\mathrm{MF}} \approx 18.3 \tag{C.16}$$

$$T_c^{\mathrm{MC}} \approx 18.0. \tag{C.17}$$

See Fig. 10. That is because $\bar{V}^{\mathrm{LR}} = 8$ is much larger in magnitude than $\bar{V}^{\mathrm{SR}} = 1.13$ ($\bar{V}^{\mathrm{SR}}$ is $\approx 14.1\%$ of $\bar{V}$.) When U and $\langle m^2 \rangle$ are scaled using T_c^{MF}, data collapse is excellent (see Figs. 11 and 12.)

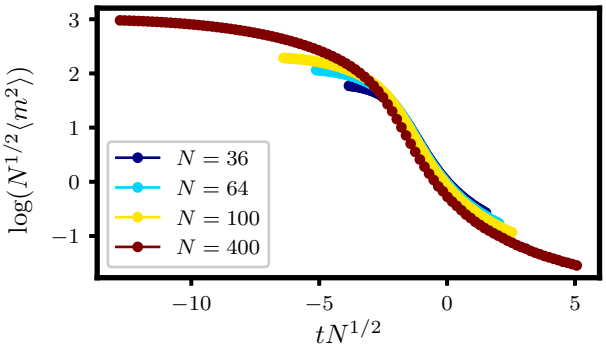

Figure C.9: Scaling of $\langle m^2 \rangle$ for the square lattice.

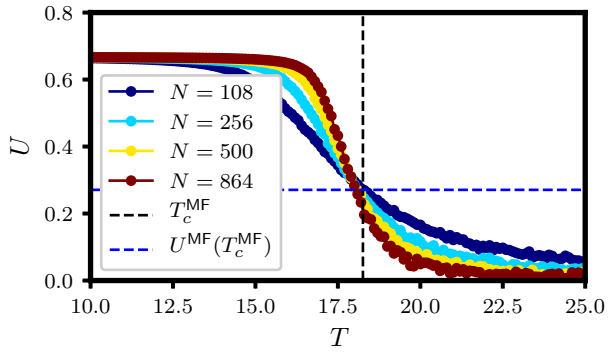

Figure C.10: Binder cumulants for the FCC lattice.

Simple Cubic Lattice

MFT accurately predicts T_c for the 3d simple cubic lattice (with nearest- and next-nearest-neighbor springs):

$$T_c^{\mathrm{MF}} \approx 30.3 \tag{C.18}$$

$$T_c^{\mathrm{MC}} \approx 29.8. \tag{C.19}$$

See Fig. 13. That is because $\bar{V}^{\mathrm{LR}} = 16.5$ is much larger in magnitude than $\bar{V}^{\mathrm{SR}} = -1.31$ ($\bar{V}^{\mathrm{SR}}$ is $\approx 7.9\%$ of $\bar{V}$.) When U and $\langle m^2 \rangle$ are scaled using T_c^{MF}, data collapse is excellent (see Figs. 14 and 15.)

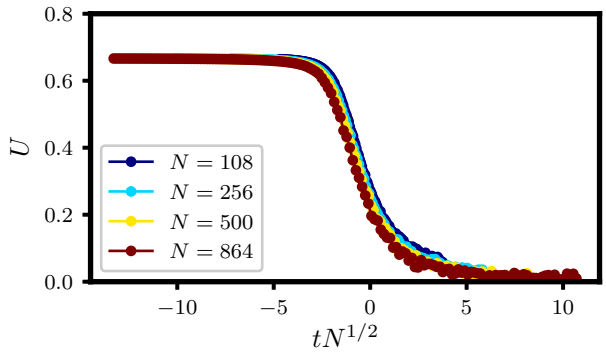

Figure C.11: Scaling of U for the FCC lattice.

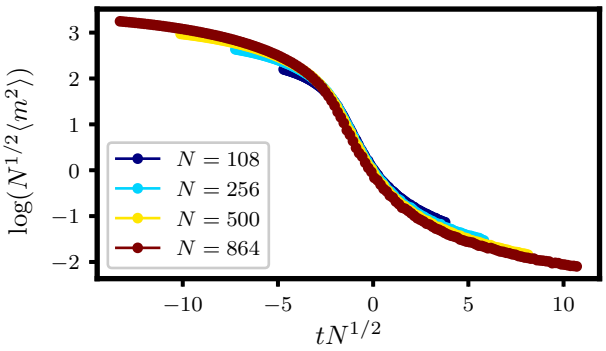

Figure C.12: Scaling of $\langle m^2 \rangle$ for the FCC lattice.

C.4 Mean-Field Dynamics

Here we compare two methods for propagating mean-field dynamics: explicit MC simulation of a mean-field Hamiltonian, and numerical solution of a mean-field Master equation.

The most straightforward way to study the relaxation dynamics is simply to harvest many MC trajectories of a mean-field Hamiltonian. We label this approach "MFMC." We harvested 10^5 such trajectories for a mean-field Hamiltonian:

$$\mathcal{H}_{\mathrm{MF}} = -\frac{\bar{V}}{N} \sum_{\mathbf{R},\mathbf{R}'} \sigma_{\mathbf{R}} \sigma_{\mathbf{R}'}, \tag{C.20}$$

where $\bar{V} = \sum_{\mathbf{R}} V_{\mathbf{R}}/2$. Trajectories were initialized at configurations sampled from an equilibrium distribution $\propto \exp(-\beta\mathcal{H})$ at fixed magnetization $m = -0.7$, inverse temperature $\beta = 1/6$, and external field $h = 0.5$. Each trajectory consisted of 100 sweeps (a sweep

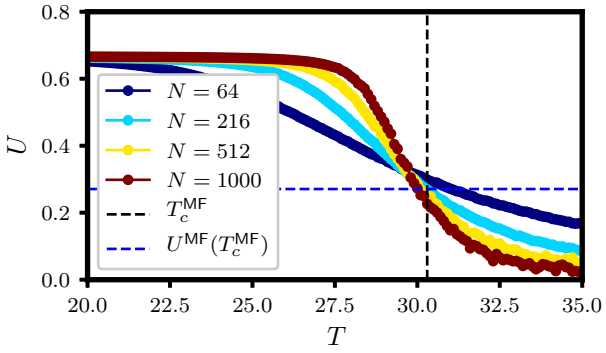

Figure C.13: Binder cumulants for the simple cubic lattice.

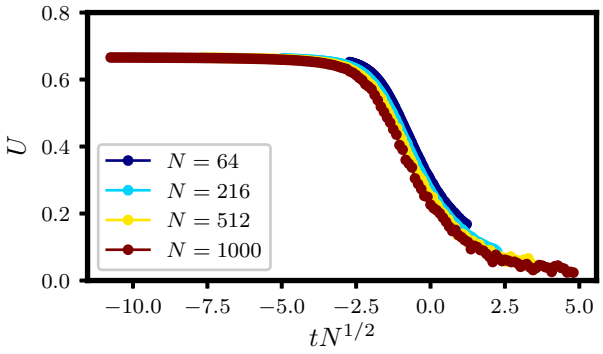

Figure C.14: Scaling of U for the simple cubic lattice.

consists of N attempted spin flips.)Rather than harvesting many trajectories, one could compute the first passage time distribution by solving a mean-field master equation for the time-dependent magnetization probability distribution, $p(m,t)$ (as we have done in Chapter 4.) We compare the MFMC and master equation approaches to dynamics in Figs. C.16 and C.17. Excellent agreement is evident for both the average magnetization versus time and the mean first passage time distribution.

C.5 Single-Site MFT

Standard MFT assumes that the order parameter m is spatially uniform. This assumption is a poor one in systems such as nanocrystals which are intrinsically spatially non-uniform. It is more appropriate to consider a spatially-resolved order parameter $m(\mathbf{R})$ which is capable

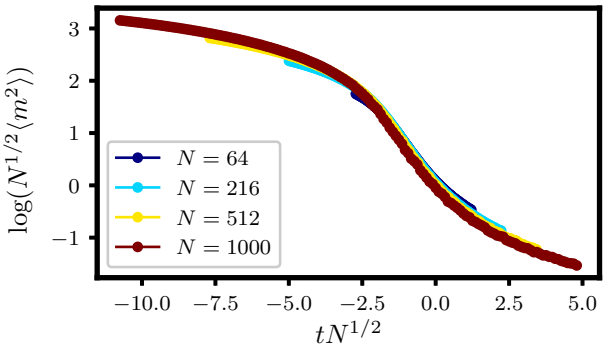

Figure C.15: Scaling of $\langle m^2 \rangle$ for the simple cubic lattice.

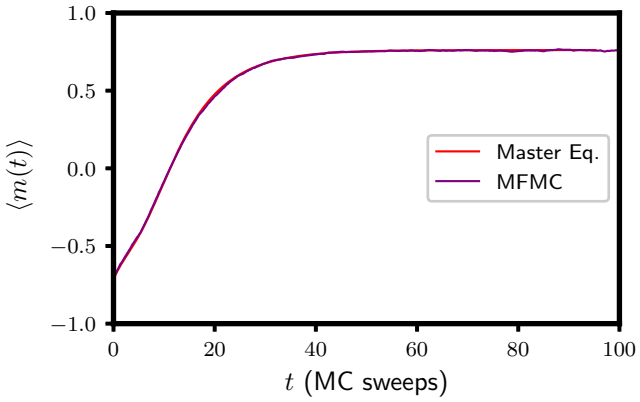

Figure C.16: Average magnetization versus time. MFMC results were obtained averaged over 10^5 Monte Carlo trajectories.

of capturing spatial inhomogeneities. With this in mind, consider a spin Hamiltonian with pair interactions:

$$\mathcal{H} = \sum_{\mathbf{R},\mathbf{R}'\neq\mathbf{R}} \frac{1}{2}\sigma_{\mathbf{R}} V_{\mathbf{R},\mathbf{R}'}\sigma_{\mathbf{R}'}, \tag{C.21}$$

where we have excluded self-interactions for the purpose of our theory. As our mean-field *ansatz* we take a one-body Hamiltonian with spatially-varying field:

$$\mathcal{H}_0 = -\sum_{\mathbf{R}} h_{\mathbf{R}}\sigma_{\mathbf{R}}. \tag{C.22}$$

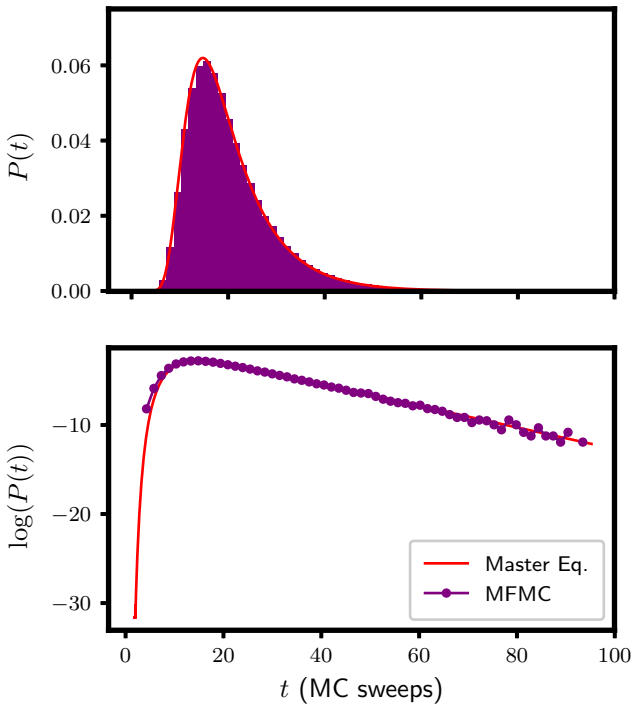

Figure C.17: First passage time distributions. MFMC histogram was made from 10^5 Monte Carlo trajectories.

The associated partition function is:

$$\begin{aligned} Q_0 &= \sum_{\{\sigma_{\mathbf{R}}\}} \exp(-\beta \mathcal{H}_0) \\ &= \sum_{\sigma_1} \exp\left(\beta h_1 \sigma_1\right) \sum_{\sigma_2} \exp\left(\beta h_2 \sigma_2\right) \cdots \\ &= \prod_{\mathbf{R}} 2 \cosh \beta h_{\mathbf{R}}. \end{aligned} \tag{C.23}$$

The spatially-varying magnetization is easily extracted:

$$\begin{aligned} m(\mathbf{R}) = \langle \sigma_{\mathbf{R}} \rangle_0 &= \frac{\partial \log Q_0}{\partial \beta h_{\mathbf{R}}} \\ &= \tanh \beta h_{\mathbf{R}}. \end{aligned}$$

To obtain the optimal value of $h_{\mathbf{R}}$, we apply the Gibbs-Bogoliubov-Feynman bound [18]:

$$Q_{\text{est}} = Q_0 e^{-\beta \langle \Delta \mathcal{H} \rangle_0}, \tag{C.24}$$

where $\Delta\mathcal{H} = \mathcal{H} - \mathcal{H}_0$. We variationally optimize $h_{\mathbf{R}}$ by setting the derivative of (the logarithm of) this partition function to zero:

$$\begin{aligned} 0 &= \frac{\partial \log Q_{\text{est}}}{\partial \beta h_{\mathbf{R}}} \\ &= \frac{\partial \log Q_0}{\partial \beta h_{\mathbf{R}}} - \frac{\partial}{\partial \beta h_{\mathbf{R}}} \beta \langle \Delta\mathcal{H} \rangle_0 \end{aligned}$$

The necessary average is given by:

$$\langle \Delta\mathcal{H} \rangle_0 = \frac{1}{2} \sum_{\mathbf{R},\mathbf{R}'} V_{\mathbf{R},\mathbf{R}'} \langle \sigma_{\mathbf{R}} \rangle_0 \langle \sigma_{\mathbf{R}'} \rangle_0 + \sum_{\mathbf{R}} h_{\mathbf{R}} \langle \sigma_{\mathbf{R}} \rangle_0. \tag{C.25}$$

Evaluating the derivative,

$$\frac{\partial}{\partial h_{\mathbf{R}}} \langle \Delta\mathcal{H} \rangle_0 = \left(\sum_{\mathbf{R}'} V_{\mathbf{R},\mathbf{R}'} \langle \sigma_{\mathbf{R}'} \rangle_0 + h_{\mathbf{R}} \right) \frac{\partial \langle \sigma_{\mathbf{R}} \rangle_0}{\partial h_{\mathbf{R}}} + \langle \sigma_{\mathbf{R}} \rangle_0. \tag{C.26}$$

Using the fact that $\partial \log Q_0 / \partial \beta h_{\mathbf{R}} = \langle \sigma_{\mathbf{R}} \rangle_0$, we find an expression for the optimal field:

$$h_{\mathbf{R}} = -\sum_{\mathbf{R}'} V_{\mathbf{R},\mathbf{R}'} \langle \sigma_{\mathbf{R}'} \rangle_0. \tag{C.27}$$

This finally yields a self-consistent equation for the spatially-varying order parameter:

$$m(\mathbf{R}) = \tanh \left(-\beta \sum_{\mathbf{R}'} V_{\mathbf{R},\mathbf{R}'} m(\mathbf{R}') \right). \tag{C.28}$$

Appendix D

Appendix for "Ion Exchange Dynamics"

D.1 Maximally Localized Eigenvectors

A consequence of of having a set of degenerate, zero-eigenvalue modes is that the associated eigenvectors are not unique. Consequently, the eigenvectors located by a standard matrix diagonalization algorithm show no obvious symmetries and are thus difficult to interpret. Bearing in mind the potential analogy with topological insulators, in which special modes are exponentially localized to the surface, we sought that orthonormal set of zero modes which both span the degenerate subspace and maximize a localization functional:

$$\Omega = \sum_{\alpha} \left[\sum_{R} (\xi_R^{(\alpha)})^2 R^2 - \left| \sum_{R} (\xi_R^{(\alpha)})^2 \boldsymbol{R} \right|^2 \right], \tag{D.1}$$

where $\xi_R^{(\alpha)}$ is the component of the αth degenerate eigenvector at lattice site $\boldsymbol{R}$.

To be explicit, let us imagine that we begin with a set of "scrambled" eigenvectors contained in a matrix U_{iR}. The entry in the ith row and Rth column of this matrix is the Rth component of the ith scrambled eigenvector. We seek a new set of "unscrambled" eigenvectors:

$$\xi_R^{(\alpha)} = \sum_i c_i^{(\alpha)} U_{iR}, \tag{D.2}$$

which satisfy the orthonormality constraint:

$$\begin{aligned}\delta_{\alpha\beta} &= \sum_R \xi_R^{(\alpha)}\xi_R^{(\beta)} \\ &= \sum_{i,j}\sum_R c_i^{(\alpha)}c_j^{(\beta)}U_{iR}U_{jR} \\ &= \sum_{i,j} c_i^{(\alpha)}c_j^{(\beta)}\delta_{ij} \\ &= \sum_i c_i^{(\alpha)}c_i^{(\beta)}. \end{aligned} \tag{D.3}$$

The functional Ω can be rewritten in terms of these coefficients:

$$\Omega = \sum_\alpha \left(\sum_{ij} c_i^{(\alpha)}c_j^{(\alpha)} \left[R^2\right]_{ij} - \sum_{ijkl} c_i^{(\alpha)}c_j^{(\alpha)}c_k^{(\alpha)}c_l^{(\alpha)} \left[\boldsymbol{R}\right]_{ij}\cdot\left[\boldsymbol{R}\right]_{kl} \right) \tag{D.4}$$

where we have defined:

$$\left[f(\boldsymbol{R})\right]_{ij} = \sum_R U_{iR} f(\boldsymbol{R}) U_{jR} \tag{D.5}$$

for an arbitrary function f. Were there no constraint, one could locate the desired coefficients through simple application of gradient descent: updating the coefficients *via*

$$c_i^{(\alpha)} \to c_i^{(\alpha)} + \epsilon \Delta c_i^{(\alpha)}, \tag{D.6}$$

where ϵ is small and

$$\Delta c_i^{(\alpha)} = -\frac{\partial\Omega}{\partial c_i^{(\alpha)}} = -2\sum_j c_j^{(\alpha)}\left[R^2\right]_{ij} + 4\sum_{jkl} c_j^{(\alpha)}c_k^{(\alpha)}c_l^{(\alpha)}\left[\boldsymbol{R}\right]_{ij}\cdot\left[\boldsymbol{R}\right]_{kl}, \tag{D.7}$$

and iterating until convergence. In order to ensure orthonormality of the coefficients, one could introduce Lagrange multipliers, but the resulting nonlinear eigenvalue problem is unwieldy. Alternatively, one can project out components of the gradient which violate the constraint to first order in Δc. To do so, note that preservation of orthonormality under Eq. D.6 requires that:

$$\delta_{\alpha\beta} = \delta_{\alpha\beta} + \sum_i c_i^{(\alpha)}\Delta c_i^{(\beta)} + \sum_i c_i^{(\beta)}\Delta c_i^{(\alpha)} + \mathcal{O}(\Delta c^2). \tag{D.8}$$

Thus our constraint, to first order in Δc, can be written as:

$$\mathcal{C}_{\alpha\beta} = \sum_i c_i^{(\alpha)}\Delta c_i^{(\beta)} + \sum_i c_i^{(\beta)}\Delta c_i^{(\alpha)} = 0. \tag{D.9}$$

A vector normal to the constraint is given by the gradient:

$$n_{\alpha\beta}^{(j\gamma)} = \frac{\partial \mathcal{C}_{\alpha\beta}}{\partial \Delta c_j^{(\gamma)}} = \delta_{\beta\gamma} c_j^{(\alpha)} + \delta_{\alpha\gamma} c_j^{(\beta)}. \tag{D.10}$$

As written, this vector is not normalized. In fact,

$$\sum_{j\gamma} n_{\alpha\beta}^{(j\gamma)} n_{\alpha\beta}^{(j\gamma)} = 2(1 + \delta_{\alpha\beta}). \tag{D.11}$$

We define the normalized normal vector as:

$$\hat{n}_{\alpha\beta}^{(j\gamma)} = (2(1 + \delta_{\alpha\beta}))^{-1/2} \, n_{\alpha\beta}^{(j\gamma)}. \tag{D.12}$$

Finally, we can define a modified gradient descent step:

$$\tilde{\Delta} c_i^{(\varepsilon)} = \Delta c_i^{(\varepsilon)} - \hat{n}_{\alpha\beta}^{(i\varepsilon)} \left(\sum_{j\gamma} \Delta c_j^{(\gamma)} \hat{n}_{\alpha\beta}^{(j\gamma)} \right), \tag{D.13}$$

where the subtraction is carried out sequentially for each α and β. This modified step is guaranteed to satisfy the orthonormality constraint to first order in Δc.

In practice, the finite size of a gradient descent step means that deviations from orthonormality of order $\mathcal{O}(\Delta c^2)$ will accumulate and eventually become significant. A simple remedy is to simply re-orthogonalize the vectors after every step (or every few steps,) for example using a Gram-Schmidt algorithm. Additionally, one ought to re-compute the eigenvectors U_{iR} and reset the coefficients $c_i^{(\gamma)}$ after each step.

In Fig. D.1 we plot three "scrambled" eigenvectors alongside three "unscrambled" eigenvectors produced by the algorithm outlines above. The unscrambled eigenvectors show clear surface localization. The extent of localization appears to be independent of system size, which we demonstrate in Fig. D.2.

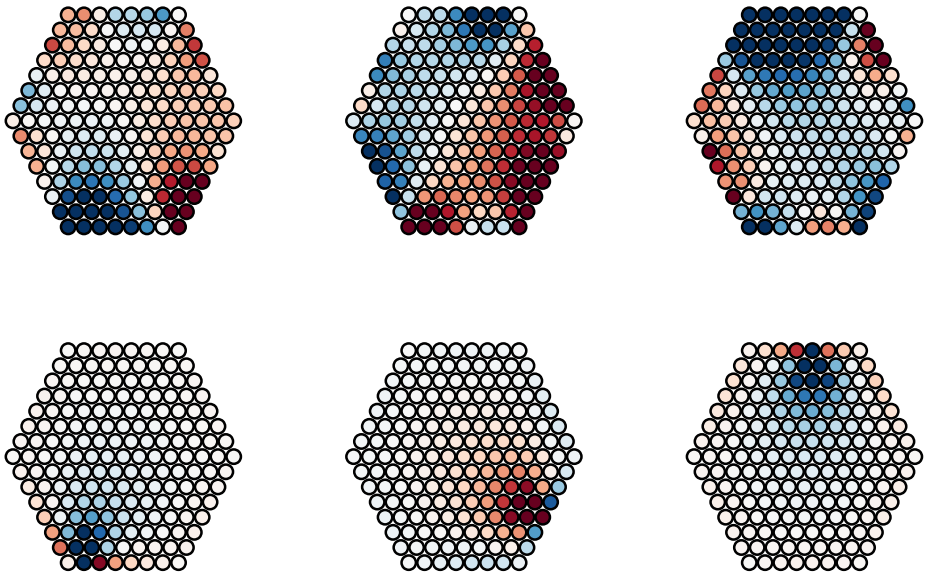

Figure D.1: Zero-mode eigenvectors for a 169-atom nanocrystal on the triangular lattice. Red corresponds to $\sigma_{\mathbf{R}} > 0$; blue corresponds to $\sigma_{\mathbf{R}} < 0$; white corresponds to $\sigma_{\mathbf{R}} = 0$. Top row: three "scrambled" eigenvectors. Bottom row: three "unscrambled" eigenvectos.

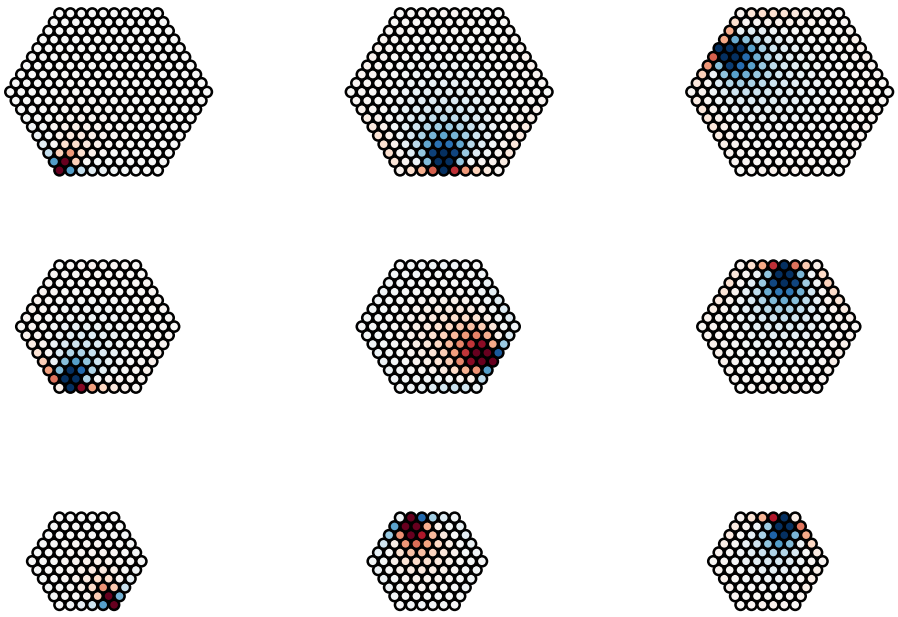

Figure D.2: Zero-mode eigenvectors for 271-atom (top row,) 169-atom (middle row,) and 91-atom (bottom row) nanocrystals on the triangular lattice.